Molecular structure and early age behaviour of metakaolin geopolymers: insights from nanoscale modelling.

Francesca Lolli

Doctor of Philosophy

School of Engineering

Supervisors: Dr. Enrico Masoero, Dr. Fabio Cucinotta,
Prof. David Manning, Prof. Maria Chiara Bignozzi

July 2019

Abstract

Growing demand for sustainable building materials is driving research in alternative cements, but their applicability in the construction field is still limited by an insufficient understanding of their durability. Geopolymers belong to this group of materials, since their production involves less carbon dioxide emissions than traditional cement. Geopolymers are aluminosilicate raw materials (*e.g.* metakaolin) activated with an alkali solution. Their binding phase commonly consists in sodium-alumino-silicate hydrate (N-A-S-H), which provides strength at the macroscale. Hence, understanding how mechanical properties emerge during the formation of N-A-S-H is crucial to control the macroscale performance of geopolymers. This dissertation discusses the results obtained with an integrated approach combining nanoscale modelling and experiments to clarify chemo-mechanical behaviour of N-A-S-H, especially at early age. This work delivers two main contributions. First, it presents a new molecular model of N-A-S-H, obtained by atomistic simulations. The uniqueness of this model lie in its ability to capture both amorphous and crystalline features displayed by literature data, whereas the other existing models only focus on either amorphous or crystalline structures, hence not fully explaining experimental observations. Second, this work quantifies for the first time the volumetric changes of geopolymers in the first stages of their formation, addressing the current lack of literature data on the so-called ”chemical shrinkage” of geopolymers. The results in this work, actually, indicate that geopolymers undergo chemical expansion, and not shrinkage, and a theoretical model is proposed to explain this uncommon behaviour. Finally, preliminary considerations on understanding ageing in geopolymers are presented. In particular, a mesoscale model based on aggregated nanoparticles is discussed, together with long term experiments on drying shrinkage and creep behaviour. Overall, this dissertation provides insights into the development of mechanical properties in geopolymers at early age, addressing some gaps whose limited understanding is a current barrier for the standardisation and commercialisation of geopolymers.

Acknowledgments

Completing a PhD dissertation is definitely challenging, but it would not have been possible without the direct and indirect support of the following people:

First, I would like to thank my supervisors: Dr. Enrico Masoero, Dr. Fabio Cucinotta, Prof. David Manning and Prof. Maria Chiara Bignozzi, for their technical guidance, and insightful suggestions during these three years. Special thanks to Enrico, for having spent almost every afternoon of my first year trying to teach me the principles of molecular dynamics simulations, and for always having supported my desire to travel. I would like to thank Fabio for all our meetings at *Quilliam Brothers* and for his patience and support. Thanks to Prof. Bignozzi, for her guidance for all the experiments carried out at the University of Bologna and at Centro Ceramico, and for sending me that email in 2015 with the following subject “PhD opportunity in Newcastle”.

Thanks to my “non-official supervisors”, Prof. Kimberly Kurtis, for her advice, support, and availability during the year spent at the Georgia Institute of Technology, and Dr. Jeff Thomas, for our weekly conversations and his brilliant suggestions.

I would like to thank all my friends, for the amazing support in every part of the world in which I had the opportunity to live during the last three years. Thanks to my friends from Bologna, in particular Elena and Diletta, who were always ready for an international call. Even at distance we have been able to share a lot: graduations, new jobs and even weddings. Thanks to my Newcastle’s family: Giada, Fulvio, Thomas, Maria and Riccardo. Thanks for all the evening conversations, laughs and trips around UK. Thanks for the morning teas and chats in the coffee room, for all the lunches and pizzas that we shared together, and for letting me store my boxes for a whole year in the living room while I was in the US. Thanks to my American friends, the GTech material group. The advantages of being part of a big group are many: there is always

somebody to chat to, have a coffee or a walk with, or have trips around the US. And of course, sharing ideas and insightful discussion on cryptic experimental results.

A special thanks to Leo, for his unconditioned support in some of the most stressful moment of my life, publishing a journal paper and writing a PhD dissertation. He has been more helpful than he probably think, and he has always found the right way to celebrate an “accomplishment”. I would always remember those pastries after the paper submission. Thank you.

Un enorme grazie alla mia famiglia. Grazie a mia nonna Giovanna, perché tornare e trovare un enorme piatto di cappelletti ad aspettarmi non ha prezzo, così come sentirla parlare a voce più alta al telefono per contrastare la distanza via Whatsapp. Grazie al mio nonno ultracentenario Orazio, per le mille domande sulla mia ricerca e perché mi ha sempre spronato ad essere indipendente e seguire la mia strada. Grazie a papà, mamma e Marghe, sempre presenti anche a distanza e sempre pronti a raggiungermi in giro per il mondo. Grazie per avermi supportato e sopportato e accettato l’idea che non sarei stata vicina per un bel po’ di tempo. E per farmi sentire sempre “a casa” con gli aggiornamenti nel gruppo *Family*.

Finally, I would like to thank you because you are about to read this thesis, or just part of it.

Francesca

Contents

List of Figures

List of Tables

1

Introduction

Contents

1.1 Why geopolymer cements?

Three quarters of the worldwide energy consumption come from urban areas [43] and by 2050, 2.5 billion people more than today are expected to live in cities, bringing 68% of the world population to metropolitan areas [44]. Accommodating this transformation will be challenging, especially for developing countries, that will have to address an increasing need for new infrastructure, housing and energy systems. Fig. 1.1 shows the expected percentage of population moving from rural to urban areas in China and India. Concurrently, also the rest of the world will face increased pressure on existing infrastructure, since more people are expected to move to denser urban areas and the existing infrastructures will need to be upgraded both with new constructions and regular maintenance. All this will cause an increased consumption of building materials. Data from 2015, reproduced in Fig. 1.2, show that the construction sector is already the main consumer of extracted materials, accounting for over 45% of the total consumption, three times more than the percentage allocated for the extraction of fossil fuels, which is commonly considered the main responsible for new extracted materials.

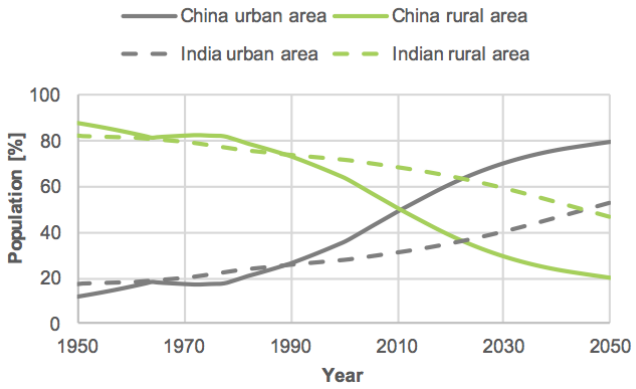

Figure 1.1: Urban and rural population in China and India as a percentage of the total population (data from 1950 to 2050) (after United Nations [1]).

Two thirds of the construction materials are cement-based, which represents ca. 30% of the total worldwide extraction of raw materials [45]. Furthermore, the building sector is also responsible for ca. 10% of the global anthropogenic CO_2 emission [43], 85% of which is directly caused by the production of cement [46]. The main source of CO_2 emission in the production of Portland cement, which is the main cementitious material today, is the production of clinker (ca. 60% of CO_2 in mass) [46, 47]. During clinker production, calcium carbonate is transformed in calcium oxide, which releases one CO_2 molecule per molecule of product. The fact that CO_2 release is intrinsic to the chemical

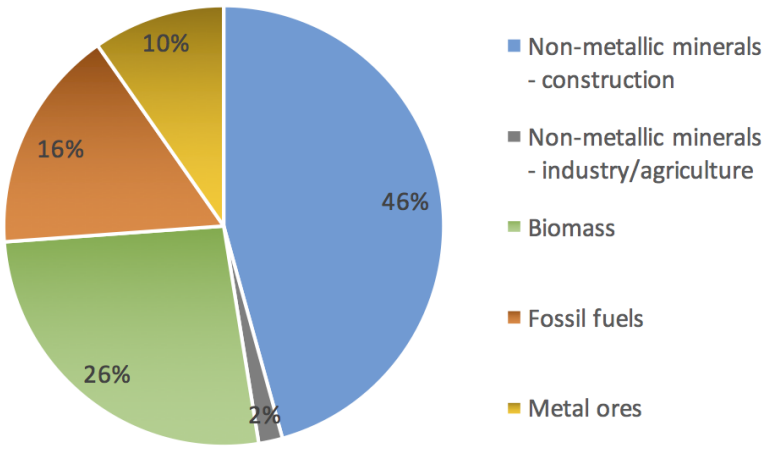

Figure 1.2: Worldwide extractions by material category in 2015. Data from Global Material flows database of the UN International Resource Panel [2].

reaction to produce clinker means that improving the efficiency of cement kilns only, e.g. transitioning to almost carbon-neutral biofuels, would only have a limited impact on the overall CO_2 footprint of cement production. This poses a serious challenge, given that the international target for the year 2050 is an 80% reduction of greenhouse gas emissions, compared to 1990 [48]. Hence, the chemical composition of cement needs to be fundamentally transformed to be able to produce cements with intrinsically lower CO_2 emissions (e.g. drastically reducing the reliance on calcination of calcium carbonate). This however raises another issues, having to do with costs.

Currently, cement is used in a wide range of applications, from structural purposes such as reinforced concrete (25% of its use), mortars (40%), and other cement based products like roof tiles, pavements and blocks (35% of its use) [45]. The production cost of cement is relatively low (U.S. price 113 USD/tonne [49] or 85 GBP/tonne) and, as a result, finding alternative solutions, which can compete on the market, is even more challenging. Current research efforts are considering a range of solutions that could be grouped into two complementary approaches: carbon capture and storage (CCS) or usage (CCU), and new material-based solutions. The latter, which is the main focus area of this dissertation, encompasses: (i) improvement of cement sustainability by replacing part of the traditional cement, based on tricalcium silicate, with less CO_2-intensive supplementary cementitious materials (SCM). In this case the traditional cement is still the main component of the binder, providing mechanical strength and controlling durability; (ii) complete substitution of cement with alternative, more sustainable binders. Geopolymers are major players in this second category and are the focus of

this dissertation. In Australia, geopolymers are currently transitioning from a research domain to industrial applications, such as airport geopolymer concrete pavement (Brisbane West Wellcamp airport) [50], and precast panels used for suspended geopolymer concrete floors (Queensland's University GCI building) [51]. Being a novel material necessitates that every technological improvement of geopolymers must be scalable for production. This entails both an environmental impact assessment of the new material, and the development of standards that regulates the application of geopolymers in different fields.

1.2 Dissertation layout

This dissertation is organised in five chapters. After this introductory first chapter, Chapter 2 explores available literature data on metakaolin geopolymer pastes, starting from an overview of geopolymerisation chemistry, continuing with a review of existing molecular dynamics simulations of calcium silicate hydrate products (C-S-H) and geopolymers, and concluding with production cycle and sustainability analyses. Chapter 3 introduces aims and objectives of this dissertation. Chapter 4 provides an overview of the methodology used for the experiments, together with the methodology applied to build the molecular scale and mesoscale models of the sodium aluminate silicate hydrate (N-A-S-H) geopolymerisation product. Chapter 5 presents results from the molecular scale model, from a theoretical model of volume changes during geopolymer formation, and from experiments, as well as first results from the mesoscale model. Finally, the main conclusions and contributions of this work are drawn in Chapter 5.

1.3 Dissemination

The following contributions are the result of a PhD course started in September 2015. One journal paper has been published in June 2018 and a second one, on the "Early age volume stability of metakaolin geopolymers" is currently in preparation. In addition, an award-winning poster has been presented at an international conference and three conference papers have also been published. The following manuscripts are the results of this work, and can be found in the Appendix.

Publications

- *Journal papers:*
    - F. Lolli, H. Manzano, J.L. Provis, M.C. Bignozzi, E. Masoero ”Atomistic simulations of geopolymer models: the impact of disorder on structure and mechanics.”, *ACS Applied Materials and Interfaces*, 2018.
    - *In progress* F. Lolli, J.J. Thomas, K.E. Kurtis, F. Cucinotta, E. Masoero ”Early age volume stability of metakaolin geopolymers”.
- *Conference papers:*
    - F. Lolli, E. Masoero, F. Cucinotta, M. C. Bignozzi, S. Manzi ”Experiments and nanoscale simulations of geopolymers: porosity and molecular structure.”, *36th Cement and Concrete Science Conference*, Cardiff (UK), 2016
    - F. Lolli, E. Masoero ”Towards a mesoscale model of geopolymers: interaction potential from the molecular scale.”, *EURO-C Computational modelling of concrete and concrete structures*, Bad Hofgastein (AU). CRC Press / Balkema Taylor and Francis Group, 2018.
    - F. Lolli, E. Masoero ”A defective crystal model for the molecular structure of geopolymers: disorder, structure, and mechanics.”, *ICCC 15th International Conference on the Chemistry of Cement*, Prague (CZ), 16-20 September 2019.
- *Posters:*
    - **Gold prize for best technical poster** DTU-COST-RILEM doctoral course: Service life of cement-based materials and structures. Lyngby, Copenhagen (DK), 2016.

Conference presentations

- 2016: Presentation *Experiments and nanoscale simulations of geopolymers: porosity and molecular structure*. 36th Cement and Concrete Science Conference (Cardiff - UK).
- 2017: Presentation *Nanoscale modelling and simulation of metakaolin geopolymer binders.* Engineering Mechanics Institute conference (San Diego - USA).

- 2017: Presentation *Nanoscale modelling and simulation of metakaolin geopolymer binders.* American Ceramic Society conference (Atlanta - USA).
- 2018: Presentation *Towards a mesoscale model of geopolymers: interaction potential from the molecular scale.* EURO-C conference - Computational Modelling of concrete and Concrete Structures (Bad Hofgastein - Austria).
- 2018: Presentation *Molecular model of geopolymers with increasing level of disorder in the atomic structure.* ECI conference - Alkali Activated Materials and Geopolymers: Versatile Materials Offering High Performance and Low Emissions (Tomar - Portugal).

Collaborations

- April 2016 and March 2017: University of Bologna (DICAM and Centro Ceramico) (IT). Experimental measurements on metakaolin geopolymers: water sorption, MIP, XRD. Supervisors: Prof. Maria Chiara Bignozzi, Dr. Stefania Manzi.
- June 2017 - May 2018: Georgia Institute of Technology (School of Civil and Environmental Engineering) (Atlanta - USA). Durability tests on metakaolin geopolymers: creep test, chemical shrinkage, autogenous shrinkage, calorimetry tests. Advisor: Prof. Kimberly Kurtis.

Workshops and training

- 2015: Wienerberger Sustainable Building Academy (WiSBA and TU Graz, AU). Five international workshops focused on the study of a change of function scenario of Building 2226 by Baumschlager Eberle and in particular about LCC analysis.
- 2016: Engineering YES competition (Brighouse, Leeds, UK). Training experience for research students and staff that introduces participants to setting up a technology start-up. Awarded Best Teamwork from the Sheffield Rotary Club during Leeds heat.
- 2016: DTU-COST-RILEM doctoral course. Service life of cement-based materials and structures.
- 2017: 5th Marseille Winter School on Multi-Scale Porous Materials.

2

Literature review

Contents

2.1 Metakaolin geopolymers

In this dissertation the term geopolymer will be used as synonym of low-calcium alkali activated materials.[1] In particular:

Definition 1

Geopolymers are the product of the activation of an aluminosilicate raw material through an aqueous alkaline solution at ambient temperature. They are a sub-class of alkali-activated materials (AAMs) and their distinguishing feature is an overall amount of silica and alumina greater than 80% in mass as shown in Fig. 2.1.

Definition 2

Alkali activated materials (AAMs) is a term that refers to inorganic binders resulting from the activation of an aluminosilicate source with an alkaline solution typically sodium hydroxide, sodium silicate, and potassium silicates.

Two main components are required to synthesise geopolymers via the so-called "geopolymerisation" reaction: a raw material and an activating solution.

- *Raw materials*. The raw materials commonly used to create geopolymers include aluminosilicate by-products such as coal fuel ashes and industrial slags, or calcined clays such as metakaolin. These precursors provide Si and Al ions.
- *Activating solution*. The activating solution is obtained by mixing a silicate solution (waterglass) and an alkali hydroxide solution (usually sodium or potassium based). The role of the solution is first to dissolve the raw material and then to provide alkali ions that contribute to the formation of the geopolymer.

2.1.1 Metakaolin

Metakaolin is a common raw material for geopolymer synthesis, owing to its large content of silica SiO_2 and alumina Al_2O_3 (typically more than 90%w in total [52,53]) and

[1] There is an open discussion in the scientific community regarding the definition of the term "geopolymer". Frequently it is considered a synonym of alkali-aluminosilicate materials, and it is widely used in the literature and in industry to describe this type of cements. A more appropriate alternative phrasing is "low-calcium alkali-activated aluminosilicate cement", however, this lacks some of the conciseness and catchiness of the term "geopolymer".

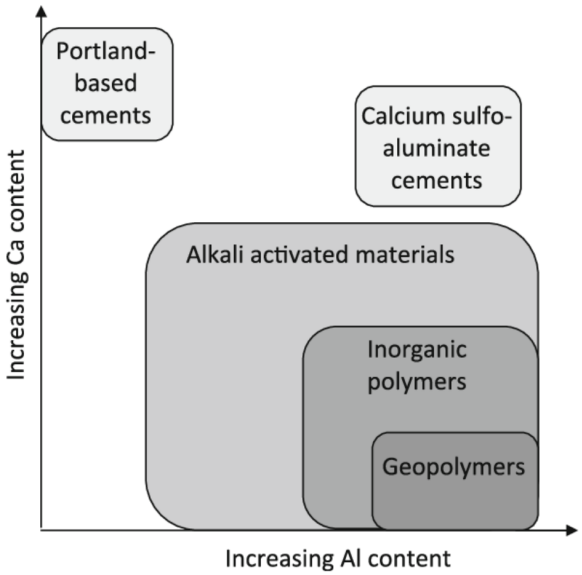

Figure 2.1: Qualitative classification of alkali activated materials and comparison with PC and calcium sulfo-aluminate cements (after van Deventer [3]).

its high reactivity. Metakaolin is produced by calcination of kaolin clay ($Al_2Si_2O_5 \cdot (OH)_4$), a thermal treatment during which the water contained in the kaolin is expelled from the structure. The resulting material is an amorphous aluminosilicate known as metakaolin ($Al_2O_3 \cdot SiO_2$). This process, called dehydroxylation, is described in Eq. 2.1 and it usually occurs in the 600-800 ℃ temperature range [54]. This temperature allows the removal of the bound water, but it is also sufficiently low to avoid the formation of unreactive mullite ($3\,Al_2O_3 \cdot 2\,SiO_2$ in crystalline phase) [55, 56].

$$\mathrm{Al_2Si_2O_5 \cdot (OH)_4 \rightarrow Al_2O_3 \cdot 2SiO_2 + 2H_2O} \tag{2.1}$$

The reactivity of metakaolin depends on the presence of strained Al sites. The dehydroxylation of kaolinite involves a reorganisation of the Si-O-Al network in which the Si-O network remains mostly unchanged while the Al-O network is rearranged from octahedral Al to esa, penta and tetracoordinated Al [56]. Aluminium is therefore readily available for dissolution and its release does not depend on the activating solution used, contrary to what happens for fly ash where the Al is not as strained, causing lower reactivity [55, 57].

Prior to final storage, the industrial process of calcination involves three phases as shown in Fig. 2.2:

1. *Sourcing kaolin.* Kaolin is an abundant natural clay, practically classified as “avail-

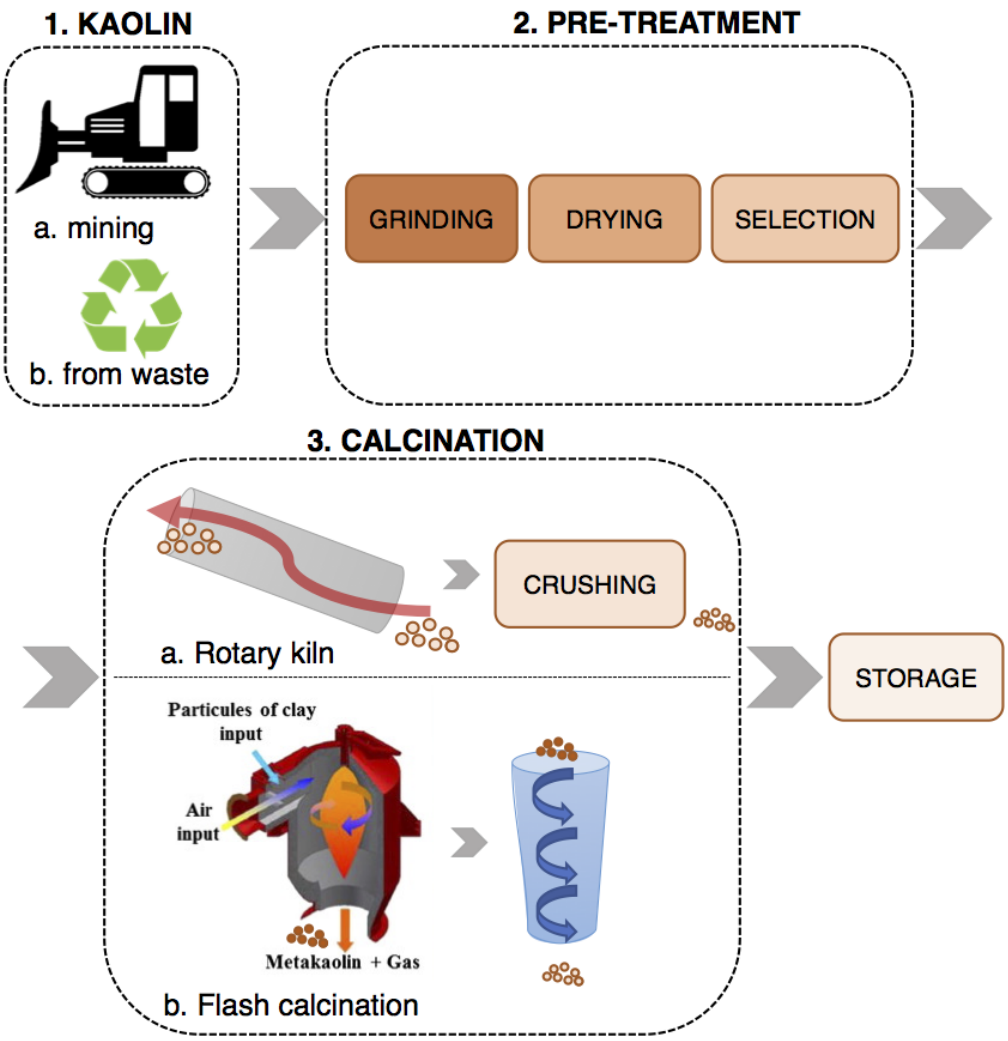

Figure 2.2: Schematic of the industrial production cycle of metakaolin.

able in infinite amount" on the Earth surface [45]. Kaolin can be extracted by mining natural deposits at a depth of ca. 60 m [58]. It is a soft white clay commonly known as "China clay" and it is used for a wide range of applications from paper production (ca. 50%) to ceramics (ca. 30%) and other mixed uses [59]. Kaolin can also be sourced from paper industry waste and mine tailings. The final product may have a different particle size and crystallinity depending on its origin, but this does not influence its applicability for metakaolin production for geopolymer binder systems [55].

2. *Grinding, drying and selection.* During this phase kaolin is separated from other impurities, e.g. sand, and is ground and dried to obtain a powder.

3. *Calcination.* Two different methodologies are currently available: traditional rotary kiln calcination and flash calcination.

   Rotary kiln calcination. The raw material (clay) is processed in pellet form and calcined in cylindrical rotary kilns, 60 to 90 m long, with a diameter of 4-6 m and inclined from the horizontal plane [52]. The material is calcined for approximately 5 hours at ca. 750 ℃ with hot gases being flown in the opposite direction to the flux of the material. This procedure is followed by crushing the resulting pellets (5 - 10 cm in diameter) to obtain the desired particle size.

   Flash calcination. The kaolin clay is selected across a 200 μm sieve, and forced by a hot air stream directly into the calciner. In the calciner the clay particles flow in a spiral around a high temperature flame (1000-1200℃; see 3b in Fig. 2.2) for a few tenths of a second and then are cooled at a rate of 10^3 to 10^5 ℃ per second in an air cooling cyclone [52]. Final crushing is not needed since the particles do not have time to agglomerate. With this technology, production companies also claim that it is possible to recycle the calcination energy, allowing a reduction of 40% energy consumption compared to the rotary kiln method [32] and a 80% reduction compared to the cement production [52]. The advantages of flash calcination, compared to traditional calcination in rotary kilns, are the following:

   - Flash calcination is less energy intensive;
   - The machinery is compact and therefore it can be installed in the proximity of the mining site or near the usage site;
   - Flash calcined metakaolin is less expensive because of the savings in energy consumption, that have an effect on the final price [60];
   - Flash calcined metakaolin is characterised by spherical particles with an average diameter of 10 μm [52]. This particular shape and dimension lead to aqueous pastes that are significantly more workable than pastes of traditionally calcined metakaolin, hence enabling a significant reduction of water demand, which is usually high in traditionally calcined metakaolin due to its fineness and the plate like morphology [55,57]. As a direct consequence, the workability of the binder is improved both for geopolymers and for cementitious binder with metakaolin used as SCM (supplementary cementitious material).

2.1.2 Activators

In order to obtain geopolymers, the raw material has to be dissolved with an activating solution obtained by mixing an alkali hydroxide solution (sodium or potassium hydroxide) with an alkali silicate solution. The concentration of alkalis in solution is usually very high, with a resulting high pH, and this enables the dissolution of metakaolin. Some important details of the main components of typical activating solutions are described as follows.

- *Sodium hydroxide solution*
  Sodium hydroxide (NaOH), commonly known as caustic soda, is a strong base (pH $\geq$ 14) usually preferred to potassium hydroxide for geopolymer production both because of its wider availability and lower cost. NaOH is commercially produced via the chloralkali process [4], which consists in the electrolysis of brine (aqueous sodium chloride) to form sodium hydroxide, hydrogen and chlorine as in Eq. 2.2.

  $$2\mathrm{NaCl} + 2\mathrm{H_2O} \rightarrow \mathrm{Cl_2} + 2\mathrm{NaOH} + \mathrm{H_2} \tag{2.2}$$

  Three technologies are currently available for this process: membrane, mercury cell and diaphragm. Until early 2000s the mercury cell technology was the predominant technology (55% of the European production [4]), with concerning environmental implications linked to the mercury itself. For this reason, in 2010 the Industrial Emission Directive regarding regulation of pollution and emissions from industry [61], concluded that mercury technology could not be used anymore in chloralkali process starting from 2018. At present, the least polluting technology is the membrane cell process, accounting today for ca. 64% of European production, and described in Fig. 2.3 In the membrane chloralkali process, when an electric current is passed through a concentrated solution of sodium chloride, chloride ions are attracted to the anode while hydrogen ions move towards the cathode. Chlorine gas and hydrogen gas are formed in proximity of the two poles while the sodium ions pass through the membrane and react with hydroxide groups in solution forming sodium hydroxide.

  The resulting NaOH is commercially available in solid form at ambient temperature (pellets or drops), it is highly hygroscopic and it is used as activator in aqueous solutions with typical concentrations ranging between 5 and 15 M. The resulting solution is characterised by a low viscosity, in the same order as the viscosity of water even for high concentrations. Considering that high molarities

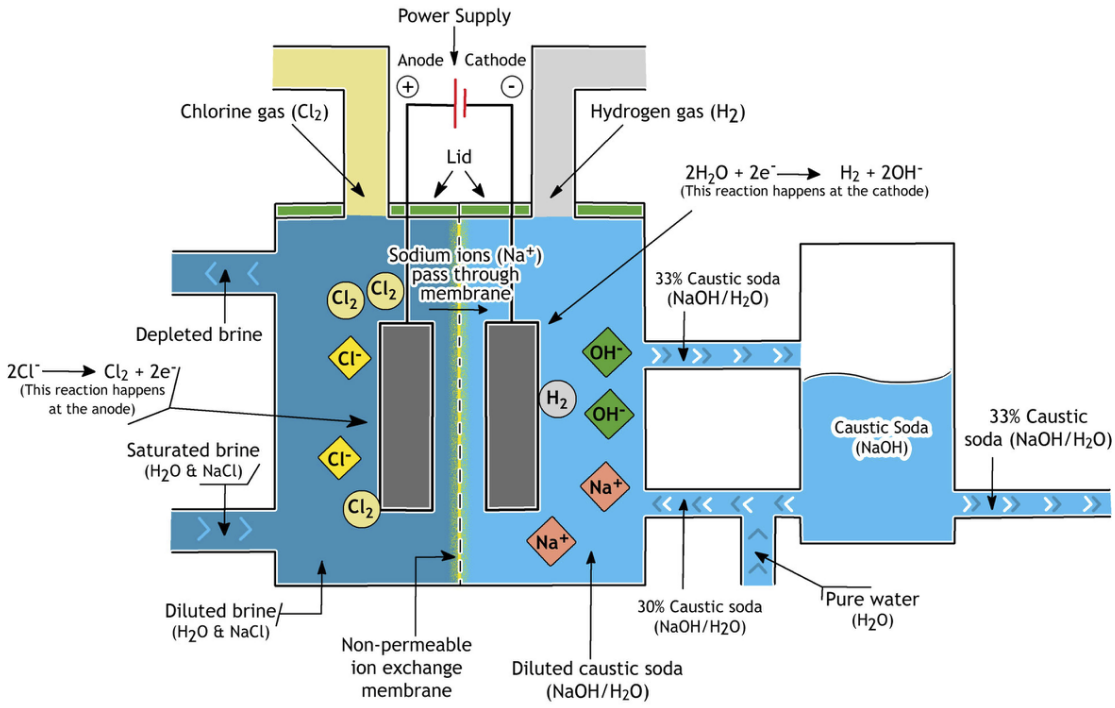

Figure 2.3: Membrane cell chloralkali process (after Euro Chlor [4]).

and pH are required, attention must be paid to safety during the production of the solution. Sodium hydroxide is highly corrosive and releases a large amount of heat upon dissolution in water: having an enthalpy of dissolution of ca. - 45 kJ/mol at infinite dilution leads to ca. 90 ℃ increase of temperature during the mixing phase of a 10 M solution prepared at 25℃ [55]. One of the main issues of using NaOH solution as the only activator, is efflorescence on the surface of the final geopolymer sample. This is due to the leftover unreacted alkali combining with the CO_2 in the surrounding environment, to form white carbonate and bicarbonate crystals.

- *Sodium silicate solution*
  Soluble silicates are chemically defined as $M_2(SiO_2)_nO$ (M is the alkali ion: Na or K), with pH between 10 and 13, depending on the SiO_2 / M_2O ratio. Sodium silicate is commercially available in form of dried powder, glass or aqueous solutions of glass [5] with SiO_2:Na_2O ratio between 2 and 2.85 or between 2.85 and 3.75. The process to produce sodium silicate involves calcination at 1000℃ of pure silica sand (SiO_2) and sodium carbonate (Na_2CO_3), followed by dissolution in water of the resulting sodium silicate lumps at the desired ratio of H_2O:Na, as

described in Eq. 2.3[2] [5].

$$Na_2CO_3 + nSiO_2 + mH_2O \rightarrow Na_2O{\cdot}\, nSiO_2 + CO_2 \uparrow + mH_2O \tag{2.3}$$

The raw material Na_2CO_3 can either be produced through the Solvay process or directly sourced by mining carbonate salt deposits. Direct mining technology involves up 10 times less production of CO_2 than the Solvay process [62]. Fig. 2.4 summarises the production process.

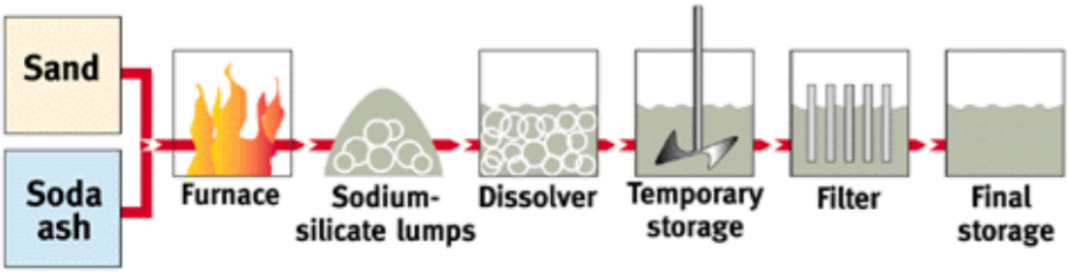

Figure 2.4: Sodium silicate solution production process (after CEES [5]). Soda ash is sodium carbonate Na_2CO_3.

2.1.3 The chemistry of geopolymers and the chemistry of cement

First research on geopolymers started in the early 1980s, by Davidovits [6, 63], with the aim of creating an inorganic material with fireproof properties after a series of ruinous fires in France in the early 1970s. It soon become clear that the field of application of geopolymers was partially overlapping with that of Portland cement and, for this reason, these two materials are now often compared to each other, even if their chemistry is fundamentally different. Portland cement binders develop as a result of the hydration process of calcium oxide and silicon dioxide, while the geopolymerisation reaction is more similar to the formation of an aluminosilicate gel [64].

Definition 3

Cement is a common term used to indicate a material with binding properties. Portland cement consists of calcium silicate and calcium aluminate minerals with main

[2]The upward-pointing arrow in Eq. 2.3 indicates that CO_2 is released in gaseous form.

phases, described in Table 2.1. In contact with water, the anhydrous cement dissolves and precipitates new hydration products, resulting in a new material called cement paste [65].

Table 2.1: Typical composition of a Type I Portland cement.

Compound	Chemical formula	Cement chemistry notation	% by weight [65]
Alite or tricalcium silicate	Ca_3SiO_5	C_3S	50%
Belite or dicalcium silicate	Ca_2SiO_4	C_2S	25%
Tricalcium aluminate	$Ca_3Al_2O_6$	C_3A	12%
Tetracalcium aluminoferrite	$Ca_4Al_2Fe_2O_{10}$	C_4AF	8%
Gypsum	$CaSO_4$	$C\overline{S}$	3.5%

The mechanical behaviour of hardened cement paste depends on the physical and chemical changes occurring during hydration. Hydration consists of dissolution of chemical compounds in Table 2.1 and precipitation of new phases. The overall transformations are usually summarised by the following equations (Eqs. 2.4–2.9) [65], in which $Q\uparrow$ is heat released[3]:

$$\mathrm{C_3S} + (1.3 + \mathrm{x})\mathrm{H} \rightarrow \mathrm{C_{1.7}SH_x} + 1.3\mathrm{CH} + \mathrm{Q}\uparrow \tag{2.4}$$

$$\mathrm{C_2S} + (0.3 + \mathrm{x})\mathrm{H} \rightarrow \mathrm{C_{1.7}SH_x} + 0.3\mathrm{CH} + \mathrm{Q}\uparrow \tag{2.5}$$

$$\mathrm{C_3A} + 3\mathrm{C\overline{S}H_2} + 26\mathrm{H} \rightarrow \mathrm{C_3A \cdot 3C\overline{S}H_{32}} + \mathrm{Q}\uparrow \tag{2.6}$$

$$2\mathrm{C_3A} + \mathrm{C_6A\overline{S}_{32}H_{32}} + 4\mathrm{H} \rightarrow 3\mathrm{C_4A\overline{S}H_{12}} + \mathrm{Q}\uparrow \tag{2.7}$$

$$\mathrm{C_3A} + 6\mathrm{H} \rightarrow \mathrm{C_3A_2H_6} + \mathrm{Q}\uparrow \tag{2.8}$$

$$\mathrm{C_4AF} + 13\mathrm{H} \rightarrow \mathrm{C_4(A_2F)H_{13}} + \mathrm{Q}\uparrow \tag{2.9}$$

The final product of traditional cement hydration mainly consists of calcium silicate hydrate $C_{1.7}SH_x$ (C-S-H) and calcium hydroxide (CH), respectively 50%-60% and 20%-25% in volume. C-S-H is the main binding phase of the cement paste and it is responsible for macroscale properties such as strength, permeability and volume changes.

[3] Eqs. 2.4–2.9 adopt an oxide notation, common in cement chemistry. The main oxides are abbreviated as follows: C is CaO, S is SiO_2, A is Al_2O_3, F is Fe_2O_3, $\overline{S}$ is SO_3 and H is H_2O. Table 2.1 identifies the main compounds.

C-S-H is often described as a colloidal gel with high surface area and characteristic pore size in the order of few nanometres (gel pores). The calcium hydroxide phase does not contribute significantly to the mechanical properties but is key to maintaining the pH of the aqueous solution in the pores to approximately 12.5, thus passivating the corrosion of steel rebars.

The chemical structure of geopolymers is intrinsically different from that of a cement paste. The binding phase in a geopolymer is a highly cross-linked aluminosilicate gel [55] that presents similarities with zeolite-type structures [66–70]. At the early stages of research on geopolymers, Davidovits proposed the term, *geopolymer*, defining it as a three dimensional structure of silicon (SiO_4) and aluminum tetrahedra (AlO_4) [63]. This nomenclature describes three oligomeric building units of silicon-oxo-aluminate, *sialates*, illustrated in Fig. 2.5 and with empirical formula in Eq. 2.10 [64]:

$$\mathrm{M_x\{(SiO_2)_zAlO_2\}_x \cdot wH_2O} \tag{2.10}$$

where *x* is the polycondensation degree, *z* is variable from 1 to 3 and *w* indicates the amount of water. A geopolymer is hence defined as an assembly of such building units.

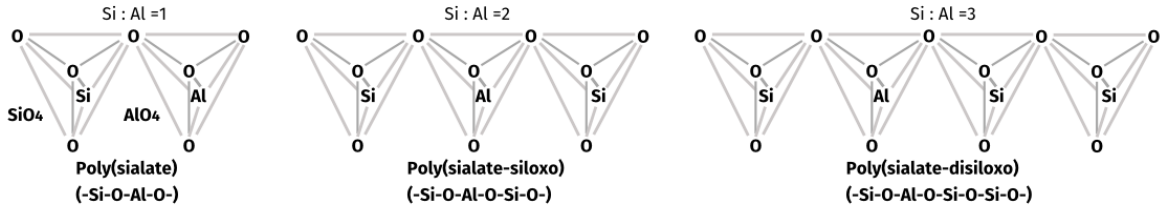

Figure 2.5: Molecular building blocks in geopolymers [6].

Considering these building units one might assume that geopolymers have a bidimensional chain-like organisation, however in the work of Davidovits [6] the final structure is described as a three-dimensional network with polysialate structures ranging from amorphous to semi-crystalline, and with alkali cations (Na^+) balancing the negative charge of tetracoordinated Al sites [57]. The building blocks in Fig. 2.5 do not allow for the presence of Al-O-Al, in accordance with the Loewenstein's principle [71]. Although thermodynamically unfavourable, the Al-O-Al linkage can sometimes be found in zeolites, [72] and a study by Duxson et al. [64] showed evidence of Al-O-Al bonds also in geopolymers, although in minimal proportion (0.18% of the bonds for sodium activated geopolymers and 1% for potassium activated ones).

In 1982 [73] a new nomenclature was introduced to describe different types of alu-

minosilicate systems, making it applicable both to crystalline aluminosilicates (zeolites) and structurally disordered geopolymers. Eq. 2.11 describes a silicon atom linked to *n* nearby atoms via oxygen bonds, of which neighbours *m* are Al atoms and *n-m* are Si atoms.

$$\mathrm{Q^n(mAl)} \tag{2.11}$$

This notation matches the type of information provided by ^{29}Si solid state Nuclear Magnetic Resonance (NMR). Both ^{29}Si NMR and ^{27}Al NMR were used by Davidovits [74] to provide the first general understanding of the geopolymer structure. First investigations by ^{29}Si NMR reported a single broad peak at -94.5 ppm, which was interpreted as containing all possible silicon tetrahedra species Q^4(mAl), hence the Si atoms with coordination 4 were convoluted into a single peak that did not differentiate between different numbers (*m*) of Al atoms coordinated to them [75]. More recent studies, however, deconvoluted the Q^4(mAl) silicon peak identifying one peak for each different value of *m* [76, 77]. Deconvoluted results indicated that the proportion of Al neighbours for the tetracoordinated silicon is highly dependent on the Si:Al ratio of the geopolymer, but also on the type of activator used, with sodium favouring Q^4(4Al), while potassium Q^4(3Al). ^{27}Al NMR allowed instead to determine the degree of reaction of the geopolymer gel [74]. Metakaolin contains Al(IV) (tetra-coordinated Al), Al(V) (penta-coordinated Al) and Al(VI) (esa-coordinated Al), but during the geopolymerisation Al(V) and Al(VI) peaks disappear while the intensity of the Al(IV) peak increases, meaning that during the geopolymerisation all reactive aluminum atoms become arranged into tetrahedral structures [78].

In 2005, Provis [79] analysed previous literature results and proposed a more detailed explanation for the physicochemical nature of the geopolymer gel phase. The binder network was described as constituted by nanosized zeolite-like units embedded in the geopolymer gel (called N-A-S-H: sodium-aluminosilicate hydrate) with the additional presence of crystalline zeolites structures within the gel. This model is referred to as the pseudo-zeolitic model [79] and evidences of these crystalline structural units were found experimentally: faujasite, sodalite and zeolite A were identified through X-Ray Diffraction (XRD) [80], short-range peaks were clearly recognisable in X-ray pair distribution function [37], and TEM images [81] showed crystalline domains. In particular crystalline domains were shown to be favoured at high temperature and high water content and for Na-activated MK-geopolymers. Small amounts of calcium inhibit the crystallisation of zeolites [79], and for this reason fly ash geopolymers have a lower tendency to present crystalline domains. For geopolymers activated with sodium

hydroxide, the identified crystalline species were mainly belonging to the hydrosodalite-hydroxysodalite family and to the zeolite family (zeolite A and faujasites) [79].

While hypotheses on the molecular structure were confirmed experimentally, various models for the evolution of the geopolymer from unreacted material to binder have been proposed over the years, but are still a less resolved matter of debate. Duxson et al. [24] proposed the geopolymerisation model described in Fig. 2.6. The aluminosili-

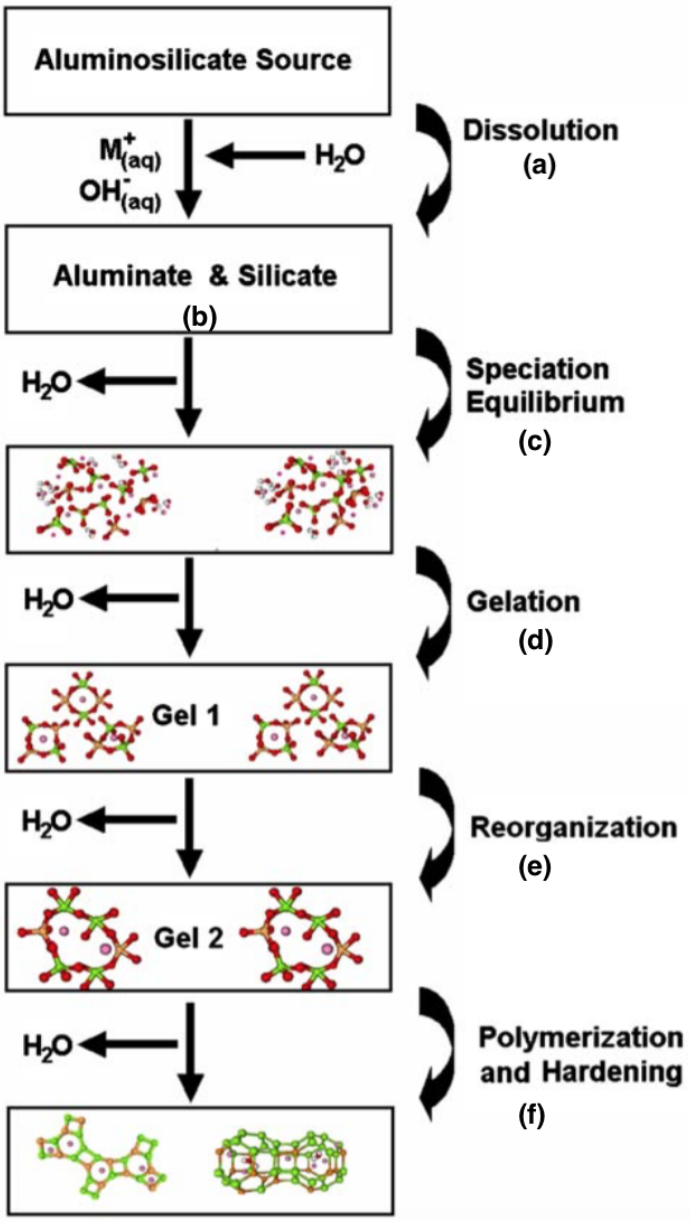

Figure 2.6: Model for geopolymerisation (after Duxson et al. [7]).

cate precursor is dissolved by a highly alkaline solution (a) and releases monomers (b),

which condense into oligomers expelling water from the skeletal structure and reaching equilibrium (c). The aluminosilicate solution undergoes gelation (d) forming the so-called *gel 1*, rich in Si-O-Al bonds, which reorganises to form a more complex gel (*gel 2*) (e). Depending on the type of activator, precursors, and curing temperature, *gel 2* undergoes partial crystallisation and zeolite-like structures emerge from the amorphous gel (f). This model implied a linear process while, realistically, dissolution and polymerisation occur simultaneously. Additionally this model refers to a general aluminosilicate as raw material, whereas it is known that, for different kinds of aluminosilicate sources, e.g. fly ash rather than slag, would lead to different geopolymer structures or even different phases, the structure of the gel can be different, e.g. with the formation of C-N-A-S-H gel.

A more complex model, in Fig. 2.7, was proposed by Provis and van Deventer [8] in 2007. This model describes simultaneous processes, with the different monomeric

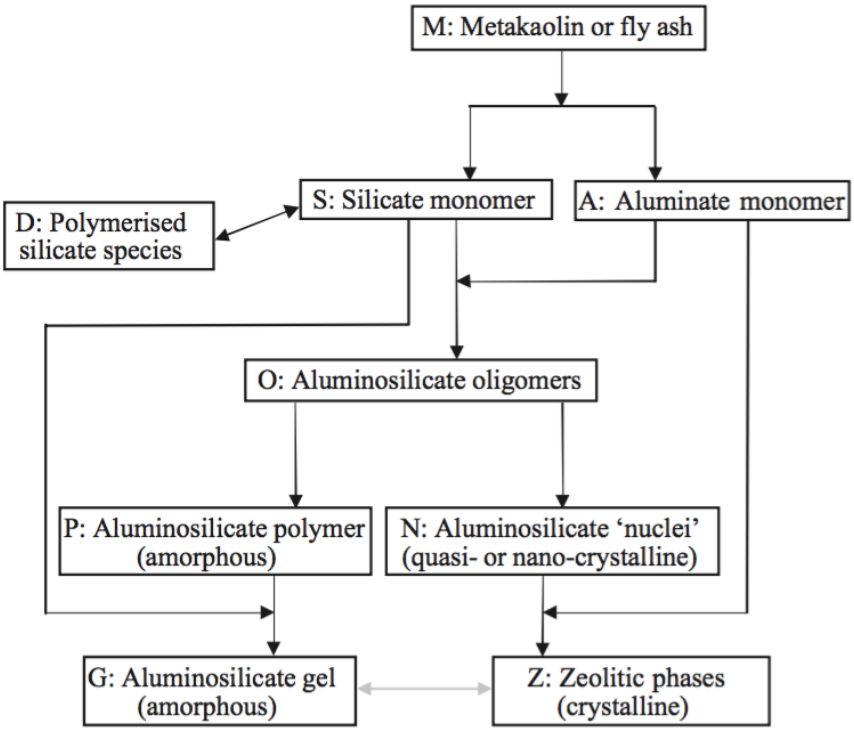

Figure 2.7: Conceptual model of geopolymerisation (after Provis and van Deventer [8]).

species formed after dissolution, and a parallel formation of polymerised silicate species and aluminosilicate oligomers. Each of the different stages of these proposed reaction was confirmed through experimental results from energy dispersive X-Ray diffraction and impedance spectroscopy. However, also with this model some questions remain

unanswered. First, the role of water in the structure of the N-A-S-H is still unclear, and it is not defined if some of the water used for dissolution still remains in the skeletal structure of the N-A-S-H. In addition, it is not clarified if the water expelled from the N-A-S-H influences macroscale properties.

The mechanisms discussed so far addressed the formation of the geopolymer gel focusing on the molecular scale. To discuss how these molecular processes translate into a microstructural evolution model during the geopolymerisation reaction, Fernández-Jiménez et al. [9], proposed a microstructural model for the sodium hydroxide activation of fly ash, in Fig. 2.8. The same model can be applied to flash calcined metakaolin, also characterised by spherical particle size due to the production process.The model describes the formation of reaction products both on the surface of the fly ash particle and inside the fly ash particle. The result is a microstructure with embedded spherical particles and possible spherical cavities at different stages of reaction.

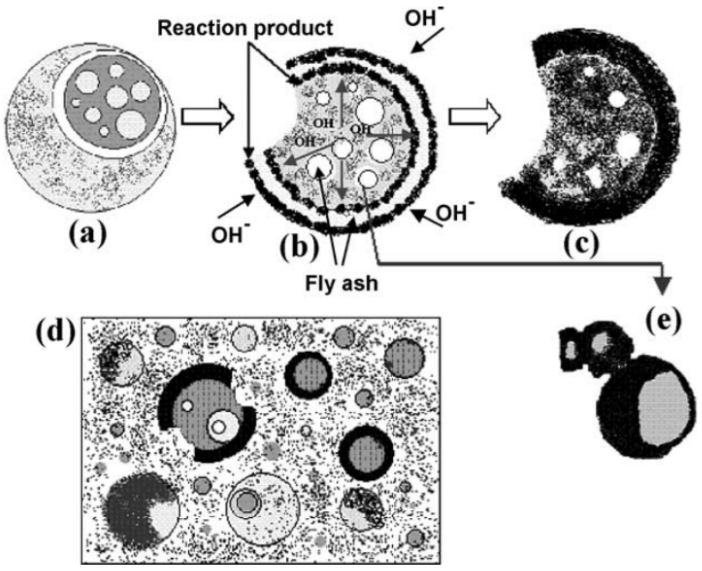

Figure 2.8: Descriptive model of sodium hydroxide activation of fly ash (after Fernández-Jiménez [9]).

To summarise, several techniques have been employed to characterise the geopolymer gels and to model the geopolymerisation reaction. Nuclear magnetic resonance was used to assess the coordination of Al and Si species, X-ray diffraction has been used to distinguish crystalline and amorphous domains and to elaborate descriptive models [9]. The pseudo-crystalline conceptual model provides a detailed explanation for the co-existence of both crystalline and amorphous domains. However, due to the qualitative nature of this model, the linkage between chemical composition and

structural properties of N-A-S-H is still not understood. Molecular and nanoscale simulations, can help clarify this point, thus the current state of the art on molecular and mesoscale models of geopolymers will be discussed later in Section 2.2.

2.1.4 Microstructure and long-term mechanics of geopolymer cements

Civil constructions must be designed and tested to maintain physical and mechanical properties for their entire service life. Hence, the environment to which the structure will be exposed has crucial importance in the choice of the materials used. The primary causes for ageing may be of chemical origin, or derived from mechanical stresses. Premature ageing might be initiated when concrete structures are exposed to aggressive environments, e.g. acid exposure or marine environment. For this reason there are specific design standards indicating the amount of chemical elements that can have an impact of the durability of concrete, e.g. the amount of chlorides. However chemical attack is only one of the factors affecting the durability of a structure. Mechanical stresses may also affect the service life performance of concrete. These stresses are due to a combination of sustained loads, e.g. causing creep, and capillary pressure in the pore structure, e.g. causing drying shrinkage. Both shrinkage and creep depend on water content in the solid and in the pores, hence they both depend on the mechanisms and rate of water transport, and thus on the structure of the pore network determining it [82, 83]. There is therefore a strong connection between microstructure and durability. This part of the literature review summarises studies on the microstructure, with a focus on porosity, since the transport mechanisms which can degrade the concrete are a function of the pore dimension, continuing with data on shrinkage and creep.

Microstructure. Microstructure and permeability of Portland cement have been studied widely [84–86] and its pore structure has been analysed with various laboratory techniques targeting multiple scales. Each technique enables the characterisation of a specific range of pore sizes. Fig. 2.9 summarises some of the methodologies that are currently used and relates them to the range of pore sizes that they address. Mercury intrusion porosimetry (MIP) and nitrogen sorption tests (Barret-Joyner-Halenda, BJH) are based on a fluid (respectively mercury or nitrogen) permeating the pore network, and on measuring the volume of the fluid absorbed. These tests enable the calculation of the pore size distribution using standardised models that typically assume cylindrical

pore shapes [87]. Another technique, water vapour adsorption, is also used to define the pore size distribution and the connectivity of the pore network. This test relates relative humidity in the environment to weight changes in the samples to pore sizes, focusing on micro and mesoporosity (pores with a diameter up to 50 nm). Scanning electron microscopy (SEM) and transmission electron microscopy (TEM) instead allow a visual inspection of the microstructures in two dimensional projections.

Following the IUPAC classification [88], pores can be classified in micropores ($<$ 2 nm in diameter), mesopores (between 2 nm and 50 nm) and macropores ($>$ 50 nm), therefore according to Fig. 2.9 nitrogen adsorption is able to capture micropores and MIP can detect both mesopores and macropores.

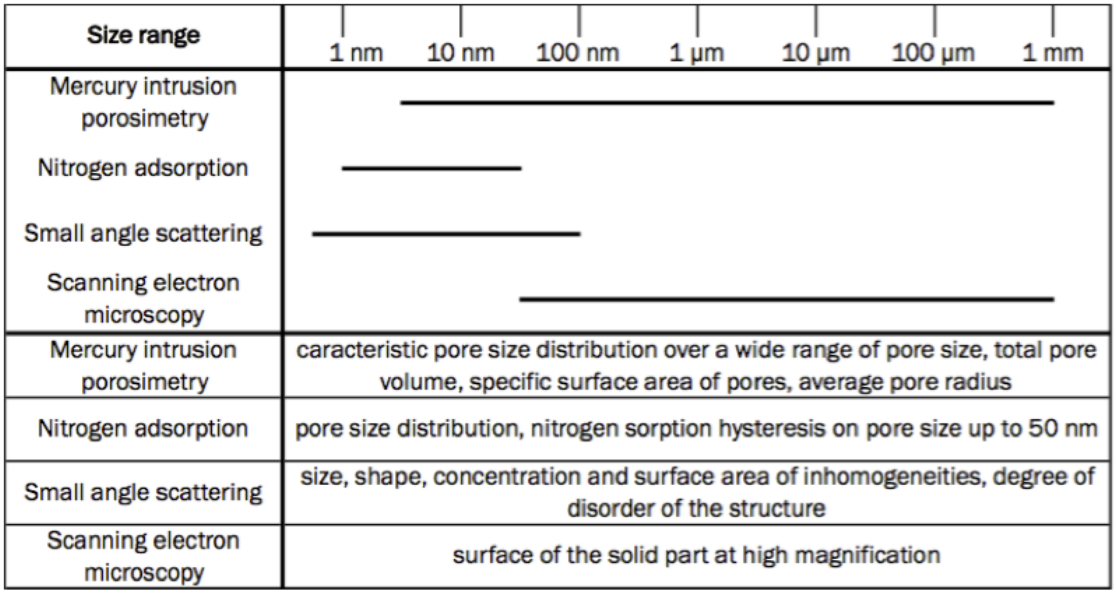

Figure 2.9: Porosity study methods and applicable range of pore size.

The porosity of geopolymers has been extensively studied using the same techniques as for ordinary cement. Geopolymers are commonly described as mesoporous materials [89, 90] therefore with majority of pores ranging between 2 and 50 nm. Benavent et al. [10] combined different techniques, including small-angle X-ray scattering, BET and MIP, to analyse the pore structure of geopolymers at different scales. The comparison of different methods allowed an estimation of closed porosity (between 1.2% to 2.7%) and the appreciation of an open mesoporous network with pore sizes between 5 and 15 nm, depending on the activator used (see TEM image in Fig. 2.10 a.). Particles and pores between 5 and 10 nm were also identified by Kriven et al. [81] using the same technique. Gharzouni et al. [91] tested different types of metakaolin

pastes activated with two types of activators, based on sodium and potassium, cured at ambient temperature (25 °C). The open porosity for sodium activated samples tested with MIP was between 20 and 30% in volume, with mean pore size between 25 nm and 56 nm. The same mix design activated with potassium was found to be more porous but with a smaller mean pore size (between 10 and 30 nm), and results were confirmed by literature comparison. The different pore sizes for sodium and potassium activated geopolymers are related to the different mobility and size of the cations Na^+ and K^+. In particular, sodium induces first the formation of a low-density, highly polycondensated structure with low porosity in the mesopore range, followed then by a densification of the solid which causes agglomeration of small pores, eventually leading to larger mean sizes of the mesopores. A SEM micrograph of sodium activated geopolymer is shown in Fig. 2.10 b. Analogous porosity ranges were determined by Kamseu et al. [92] for metakaolin pastes activated with sodium silicate solution obtained mixing sodium hydroxide and rice husk ash. In Kamseu et al. the average porosity calculated with MIP was between 25 and 35% increasing with the concentration of the sodium hydroxide solution.

Pouhet and Cyr [93] instead calculated the open porosity of flash calcined metakaolin geopolymer concrete using water permeability which, alongside MIP, is often considered a simpler approach to estimate the open porosity. They found that for geopolymer concrete the calculated open porosity ranged between 12 and 19% of the total volume.

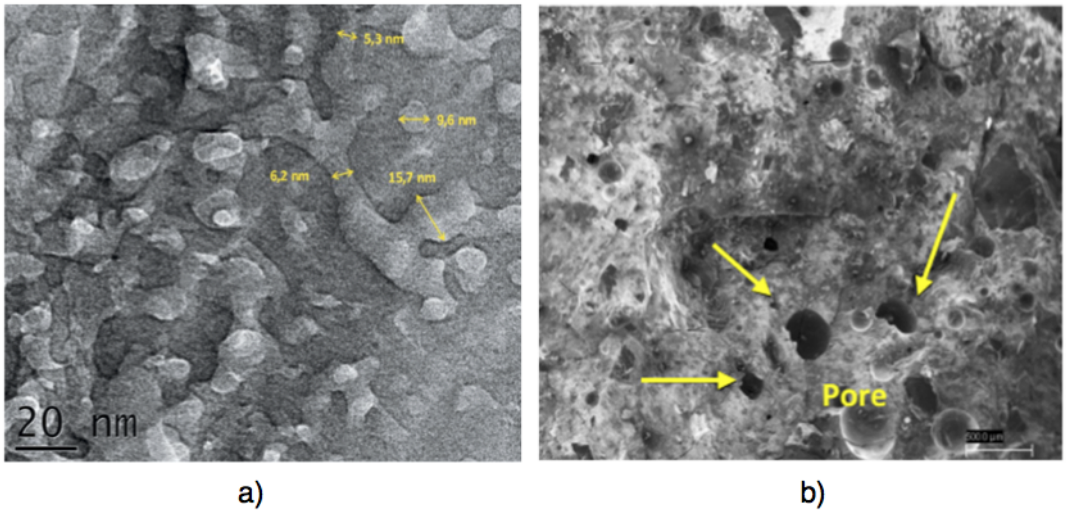

Figure 2.10: Micrographs showing geopolymers microstructure a) TEM (after Benavent et al. [10]) b) SEM (after Silva Rocha et al. [11]).

Ferone et al. [13] analysed the effect of different Si:Al compositions on the pore structure, concluding that the higher silicon content leads to a microstructure with lower total porosity and with a smaller mean particle size. The effect of curing temperature on porosity and therefore on the mechanical properties of geopolymer was analysed by GascaTirado et al. [94]. Metakaolin pastes with Si:Al = 1.67 were investigated using nitrogen adsorption, and their pore size distributions were reconstructed using the BJH analysis. Geopolymers were dried for 2 hours at 40 ℃ and then cured in sealed containers at temperatures between 40 and 90 ℃ for 24 hours. When increasing the curing temperature from 60 ℃ to 90 ℃, the mesoporosity decreased from 75% to 60% while the macroporosity increased from 26% to 35% porosity. Microporosity was detected only in the samples cured at 90 ℃.

Finally, the increasing understanding of the microstructure of geopolymers, is promoting a new field of study, aiming to create new geopolymer-zeolite materials to obtain a final product which combines the microporosity of zeolites with the mesoporosity of geopolymers [95]. As explained in Section 2.1.3 geopolymers present similarities with zeolites, therefore the combination of these materials can be achieved. The objective is to rely on the catalytic and adsorbents zeolite properties and mechanical properties of geopolymers. Because of their cage like structure, zeolites are currently studied for CO_2 adsorption, encapsulation of waste material or purification of contaminated water, therefore their combination with geopolymers can promote these applications in civil engineering.

To summarise the N-A-S-H gel can be defined as constituted by nanoparticles ranging from 5 to 50 nm and a mesoporous network ranging from 2 to 50 nm. Understanding the microstructure of geopolymers is a crucial step in clarifying the mechanisms of degradation.

Shrinkage

Definition 4

Chemical shrinkage For traditional Portland cement, it is defined as the molar volume change resulting from cement hydration, caused by the fact that the products of hydration have a smaller molar volume than the reactants [96].

Definition 5

Autogenous shrinkage is the dimensional change occurring in cementitious materials during their hydration at constant temperature, in a sealed environment, and without the action of external forces, such as load [34].

Definition 6

Drying shrinkage is the dimensional change occurring in cementitious materials due to the loss of capillary water. The loss of water in capillary pores causes an increase of internal tensile stresses, resulting in macroscopic contraction and, in certain cases, cracking [97].

Fresh and hardened cement pastes, mortars and concretes have been extensively tested for shrinkage. The current testing methods allow addressing separately one mechanism of shrinkage at the time, hence distinguishing between drying (ASTM C490-11 [97]) autogenous (ASTM C1608-09 [34]) and chemical shrinkage (ASTM C1608-17 [96]). The testing methods for geopolymer cements have been adopted from those of traditional cements, and several studies report results from such tests applied to fly ash and slag geopolymers mortars. However, to date, geopolymer shrinkage has been tested under conditions that do not allow to separately asses the individual types of shrinkage defined above (e.g., a young still reacting geopolymer paste is exposed to external drying, thus combining together autogenous and drying shrinkage). To the author's knowledge, no research has been directed yet to the chemical or autogenous shrinkage of metakaolin geopolymers.

Some general indications however have been drawn from the shrinkage tests conducted thus far. One of these is that geopolymers from fly ash usually shrink less than traditional PC [55]. Conversely, metakaolin geopolymers are known to shrink significantly [14,55], with evident formation of cracks as shown in Fig. 2.11. However, there is still a significant lack of quantitative data on shrinkage beyond mere visual inspection. As a consequence, the shrinkage mechanisms of metakaolin geopolymer are not yet understood.

Ferone et al. [13] analysed the shrinkage of geopolymers samples with several Si:Al compositions, concluding that the high silicon content leads to higher shrinkage. This was explained analysing the microstructure: a higher amount of silicon in the mix design leads to a microstructure with lower open porosity, constituted by pores with a

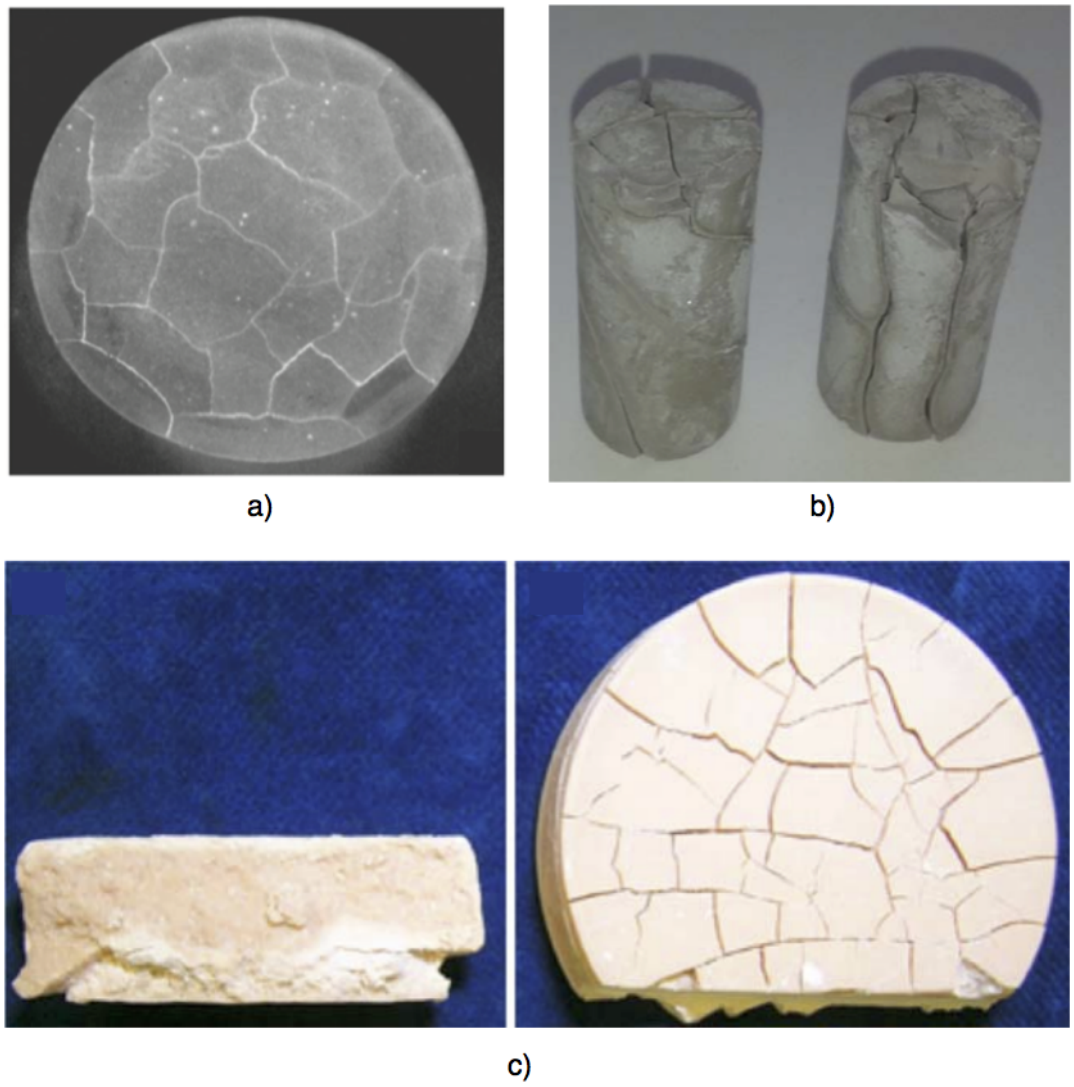

Figure 2.11: Cracking of metakaolin geopolymer pastes due to drying shrinkage a) (after Kuenzel et al [12]) b) (after Ferone et al. [13]) c) (after Perera et al. [14]).

mean pore size below 10 nm. Pores with this dimension in concrete are classified as small gel pores and small capillary pores. The open porosity allows the evaporation of water in pores of this size, but during the evaporation the strong menisci formed between the pore wall cause higher capillary stresses which result in higher shrinkage. The extent of shrinkage was determined by visual inspection, see Fig. 2.11 b. Palumbo et al. [98] analysed the autogenous and drying shrinkage (combined together into a single measure) using fibre Bragg gratings (FBG) embedded in the metakaolin geopolymer pastes. These sensors were able to monitor internal temperature develop-

ment and shrinkage strain for different types of metakaolin. Measurements were taken in an environmental chamber at 40 ℃ for 330 hours and all samples reached thermal equilibrium after the initial exothermic reaction. All mix designs displayed an initial expansion that was associated with the exothermic reaction, except for the paste from flash calcined metakaolin, which shrank instead. The authors acknowledged that the results obtained for the flash calcined metakaolin were with minor significance, probably due to an issue related to the mix design. The results on autogenous shrinkage that will be presented in this dissertation will show instead an expansive behaviour, in line with observations on different metakaolins.

The effect of blending precursors, i.e. flash calcined metakaolin, fly ash and slag, in different proportions was studied by Samson et al. [15]. Several geopolymers with same water to binder ratio were analysed and their shrinkage compared to reference geopolymers cast using only one precursor at the time. The test was performed in environmental conditions starting from one day after casting (RH=50% T=20 ℃). After 2 days the pure metakaolin binder showed the highest shrinkage, equal to 2.2%, percentage that remained comparable (2.4%) after 28 days. Additionally, metakaolin geopolymers with a higher Si:Al and Na:Al ratios, showed more shrinkage considering the same mass loss (2.4% versus 1.4% at 10% mass loss), as displayed in Fig. 2.12 a. This was associated to a possible increase in autogenous shrinkage for geopolymers with a higher activation rate. Finally, Kuenzel et al. [12] carried out an extensive study on the onset of drying shrinkage at ambient temperature and its relation with water content. A range of metakaolin geopolymer pastes, with various water contents and Si:Al ratios were compared. All the samples with Si:Al 2 started experiencing drying shrinkage when the molar water content remaining in the sample, after drying at ambient temperature, was equal to 3 moles per sodium atom (irrespective of the initial water content of the mix), as displayed in Fig. 2.12 b. Lowering the Si:Al ratio decreased the molar water content at the onset of shrinkage, for example for Si:Al 1.6, H_2O/Na was equal to 2, see Fig. 2.12 c.

Creep

Definition 7

Creep is the gradual deformation of a material under constant mechanical load, typically a compression [99].

For concrete structures creep effects should be considered during the design phase,

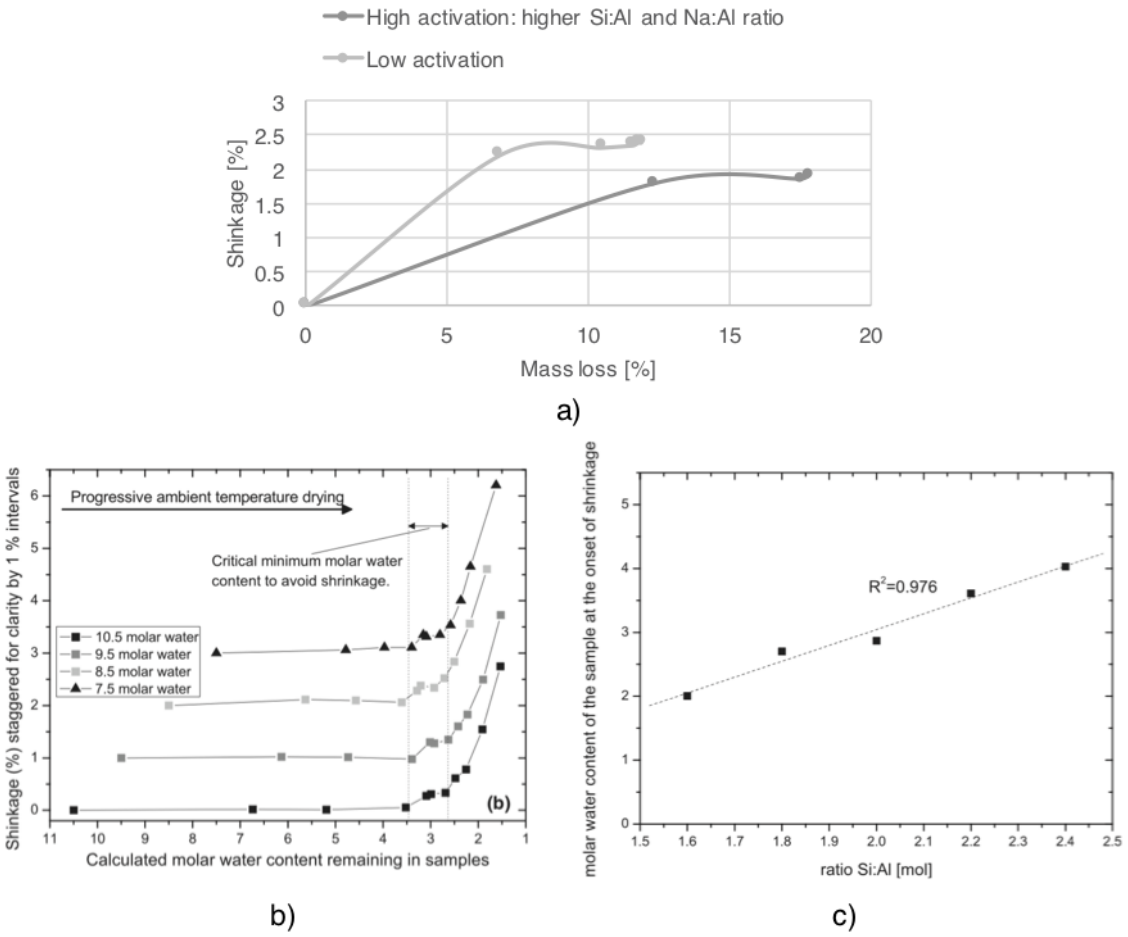

Figure 2.12: a) Drying shrinkage versus mass loss in metakaolin activated geopolymers paste (after Samson et al. [15]). b) Drying shrinkage at ambient temperature versus molar water content of the sample at the onset of shrinkage, for samples with Si:Al 2 and different water content (after Kuenzel et al. [12]). c) Si:Al molar ratio versus molar water content at the onset of shrinkage (after Kuenzel et al. [12]).

for two main reasons. First, the creep deformation can relax stresses induced by thermal gradients or shrinkage, having therefore a positive effect on the structure [100]. Second, if the superposition of creep deformation and external stress is not well calculated, it might enhance the formation of cracks, triggering a series of possible durability issues, from chloride penetration to acid attacks. It is therefore important to understand the creep mechanisms in order to predict excessive deformations and allow for maximisation of the benefits while eliminating the negative effects. Testing for creep requires several months up to years and, for this reason, shorter term experimental results are often combined with predictive models to estimate, rather than directly measure, long

term effects [55, 101]. As discussed previously, the chemistry and microstructure of geopolymers and calcium-based cements are not the same, meaning that also the development of mechanical properties in time does not follow the same mechanisms. Hence, the application of creep theories for concrete and cement mortars to geopolymers has to be considered carefully.

Creep of geopolymers and of alkali activated materials is a field of ongoing research. To the best of the author's knowledge, there is currently no literature available on the creep of metakaolin geopolymers. A small number of studies is instead available for fly ash based systems and their main conclusions are presented as follows.

Wallah [102] investigated the creep behaviour of fly ash-based geopolymer concrete comparing four mixes characterised by two different types of initial curing (dry and steam curing for 7 days) and different water contents. The mix with a higher water content displayed lower compressive strength at 7 days compared to the analogously cured samples containing less water: 47 MPa versus 67 MPa for the dry cured samples, 40 MPa versus 57 MPa for the steam cured ones. These results were used to calibrate the load for the creep test, and a load equal to 40% of the 7^{th} day compressive strength was applied. After one year, the fly-ash geopolymer concrete underwent lower creep than the creep predicted for PC concrete, and for a compressive strength of 40 to 67 MPa the specific creep (or creep compliance, namely creep strain per unit of stress applied) ranged from 29 to 15 x 10^{-6}/MPa, resulting in values that are about 50% of the values obtained with a prediction model for PC concrete [103]. A similar timeframe was analysed by Shekhovtsova et al. [104], who compared long-term creep of a PC-fly ash concrete with fly ash concretes activated with a sodium hydroxide solution. After one year of testing, the creep strain for the reference concrete (PC - fly ash concrete) was three times higher than the AA fly-ash concrete, this latter being equal to 200 μm/m. The test was performed under a sustained stress of 40% of the 28^{th} day compressive strength for both mixes. A different approach was applied instead by Castel et al. [105], opting for a short test of 90 days combined with predictive models from Eurocode 2 [106]. Also in this case the geopolymer concrete (85% fly-ash and 15% GGBS) showed less creep than PC concrete. The conclusion was that the creep of geopolymer developed with a different coefficient[4] compared to the PC. For the first 50 days PC and geopolymer displayed a comparable creep coefficient, but starting from day 50 the creep coefficient of the PC was higher than that of the geopolymer concrete. Finally, a very recent study focused on the contribution on creep behaviour of the dif-

[4]The creep coefficient is the ratio between creep strain and elastic strain, see Section 4.3.1 for details.

ferent phases of alkali activated fly-ash [107]. Nanoindentation technique coupled with statistical analysis allowed to identify, between the three main reaction products (N-A-S-H, partly-activated and non-activated phases) those which had the main effect on creep. Differently from cement pastes, where creep originates mostly in the hydration product (C-S-H), in the geopolymer paste the partly-activated and non-activated phases seemed to induce more creep deformation, and this was enhanced when a higher amount of liquid was used in the mix design.

Overall, there is still a fundamental lack of research on the creep behaviour of metakaolin geopolymers that needs to be addressed. Long-term experimental tests should be compared to predictive models as has been done for fly ash geopolymer, but an important support to understand of the link between microstructure (porosity and particle size) and mechanical performance might also come from modelling at the molecular and mesoscale, as it has happened in the field of traditional cement science.

2.2 Modelling across scales

Several models have been developed, in the field of traditional cement science, to understand the impact of chemical composition on the microstructure and on the pore structure, and therefore on degradation mechanisms related to creep and shrinkage. Linking chemical composition with the mechanisms responsible for long term deformations requires an in-depth analysis of a material at the nanoscale. Analysing the structure of disordered materials at such scales is an open challenge in materials science. Despite a few experimental techniques targeting those scales exist (e.g. H NMR to study the water in nanopores, or quasi elastic neutron scattering), atomistic and nanoscale modelling and simulation are, to date, useful assets to better understand fundamental structures and processes. This Section presents molecular and mesoscale models of C-S-H in traditional cements, and continues with an overview of very recent models of N-A-S-H in geopolymers.

2.2.1 Modelling C-S-H

In the field of traditional cement science, High Performance Computing (HPC) simulations provided significant insights into the microscopic mechanisms governing the macroscale properties of Portland cement pastes.

In 2009, Pellenq et al. [16] proposed the first molecular structure of C-S-H to be used in atomistic simulations (2 to 3 nm), as shown in Fig. 2.13 a. The model was built using molecular dynamics (MD) simulations starting from tobermorite, a layered structure of calcium and silicon. Tobermorite was then modified to incorporate more calcium, causing distortion in the layered structure, and the amount of structural water in the C-S-H was determined by free energy minimisation, via the so called "Grand Canonical Monte Carlo" (GCMC) approach. The resulting structures were able to capture experimental data on chemical composition ($C_{1.65}$-S-$H_{1.75}$), structural order (radial distribution function, X-ray diffraction) density, and mechanical properties at the nanoscale (nanoindentation modulus and hardness). This model was used by various authors to investigate the effect of order and chemistry on mechanical properties. Qomi et al. [108] created a database of atomic configurations using the Pellenq et al.'s model [16] as a baseline. Qomi et al.'s work presented a wide range of C-S-H chemical compositions, obtained by varying the Ca:Si molar ratio, and for each of them mechanical properties and medium range environment was calculated. The Ca:Si ratio was then identified as a quantification of defects in the structure (with possible vacancies in the silicate network), together with medium range environment for Si-O and Ca-O network (first peak in the X-ray pair distribution function). It was found that in addition to the well known correlation between structural propertied and Ca:Si ratio, also the position of the medium range environment for Si-O and Ca-O affects mechanical properties.

The relationship between long term mechanical response and molecular structure of C-S-H was instead studied by Bauchy et al. [109] introducing creep deformations in C-S-H caused by activation by stress fluctuations on creep deformations. This work was then developed further by Morshedifard et al. [110]. Morshedifard et al. used an incrementally stress-marching (ISM) technique that simulates ageing phenomena, such as creep and viscoelastic deformation, *via* the acceleration of thermal fluctuation. Creep was determined to be related to the water content at the molecular level. The implications of the water behaviour in the interlayers of C-S-H was also analysed by Manzano et al. [111]. In this work the authors studied the effects of water dissociation in the C-S-H layered confined environment via MD simulations, using a reactive force field (ReaxFF). ReaxFF [112] specifies interaction forces between atoms that simulate the chemical bonds, also allowing to simulate the occurrence of the chemical reactions, including those that are responsible for water dissociation in the micropores of the C-S-H, and for the formation of Si-OH and Ca-OH groups. The results indicated that

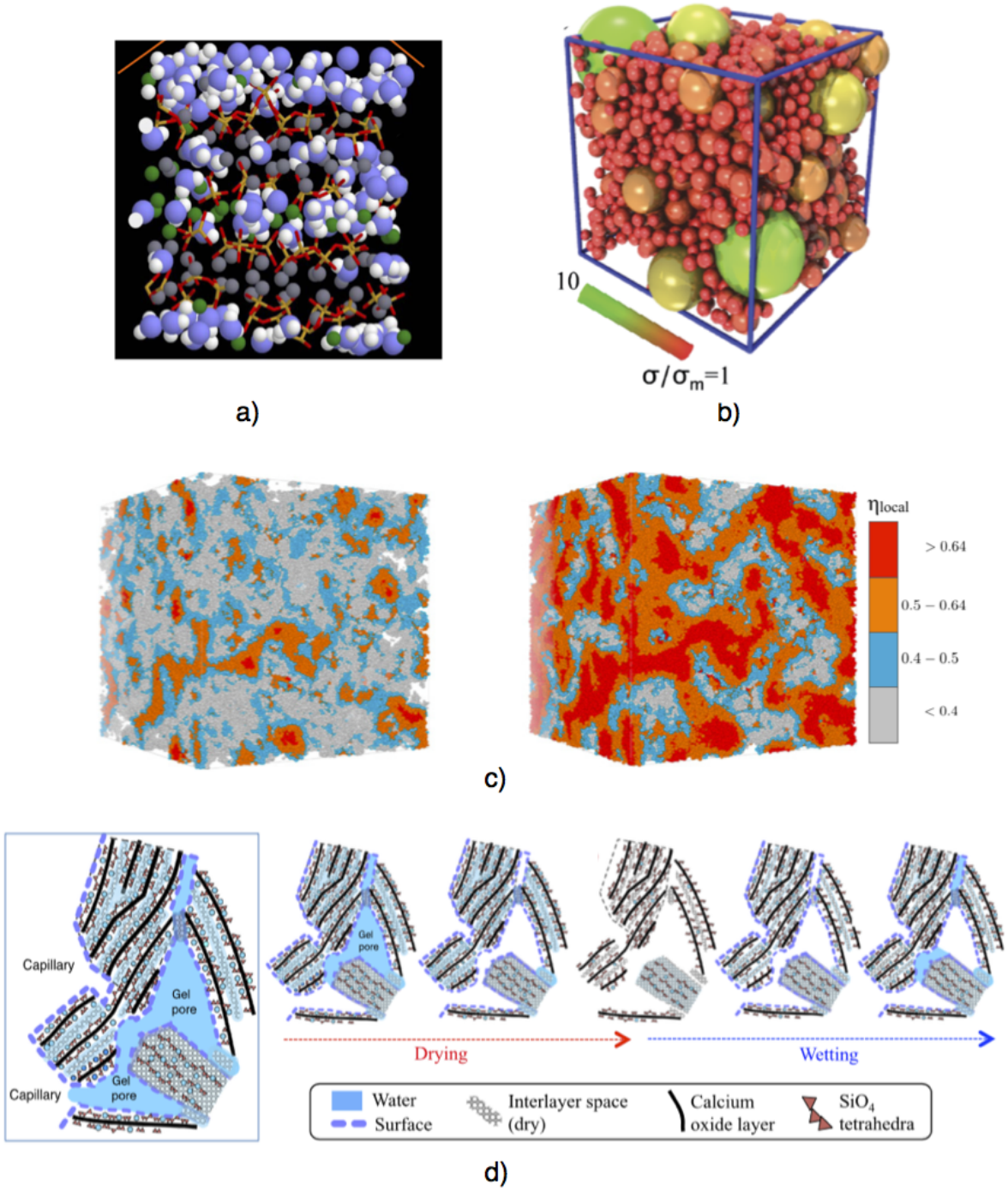

Figure 2.13: Snapshots of the molecular and mesoscale structure of the C-S-H a) (after Pellenq et al. [16]) b) (after Masoero et al. [17]) c) (after Ioannidou et al. [18]) d) (after Pinson et al. [19]).

the elastic properties of the C-S-H were not affected by the dissociation of water and results such as nanoindentation modulus and elastic tensor were comparable to those obtained by Pellenq et al. [16]. Conversely, the shear behaviour of the C-S-H gel changed before and after water dissociation. Manzano et al. focused also on the effect of the water content on large range shear strain [113], clarifying which molecular mechanisms is responsible for relaxation and stress accumulation at the molecular scale. Two different systems were considered, a highly ordered one (tobermorite), and a highly amorphuos one (glassy C-S-H). For both systems the shear deformation was localised in the interlayer sites rich in confined water, which can be interpreted as interfacial regions between solid units of C-S-H, supporting a description of the material that is based on the agglomeration of nanoparticles to form a so-called gel [114]. This implied that the C-S-H gel can be defined as constituted of nanoparticles aggregating via strong interactions, having water-rich regions at their interface.

The concept of modelling C-S-H as an agglomeration of nanoparticles is at the basis of several mesoscale models [17, 18, 115]. In these models, particles interact *via* effective interaction potentials obtained from molecular simulations. In Masoero et al. [17] stress-strain curves derived from atomistic simulations of C-S-H, were used to define a modified version of the Lennard-Jones potential, making it particle size dependent. The configuration in Fig. 2.13 b, was generated starting with an empty cubic box, which is progressively filled by inserting new particles. The possible sizes of the particles were predefined and ranging from 3 to 15 nm. Throughout the simulation the nanoparticles were inserted randomly to create the C-S-H structure with a range of particle size polydispersities, which permitted to analyse the effect of heterogeneities on the mesoscale properties. Using this model it was possible to predict realistic mechanical properties such as indentation modulus and creep [116]. Ioannidou et al. [18] showed that a combination of different potentials can be used to model the formation of the C-S-H gel structure from early age structures to aged material. Fig. 2.13 c, shows the C-S-H mesoscale structure obtained. Different densities represented the evolution of the gel in time, and for each packing fraction, microstructure characterisation (small angle neutron scattering, SANS, and pore size distribution) and mechanical properties were calculated, and showed good agreement with experimental results. Another example of mesoscale model built starting from inputs at the molecular scale, is described in Fig. 2.13 d. The model, by Pinson et al. [19], is not based on simulations of nanoparticle aggregation, but it is rather a semi-analytical description of water vapour sorption, and related capillary stresses in an interconnected network of mesopores.

Pinson et al. explained the implication for durability and transport properties due to the interactions between cement and water in the environment. In this case, the molecular model was used to distinguish the sorption effect due to the interaction between water and C-S-H in the micropores, from the interaction due to capillary forces in the mesopores (gel pores). Structural parameters from the mesoscale model of sorption were used to model reversible drying shrinkage, providing new understanding of the role of microstructure in the development of shrinkage. Lastly, Shvab et al. [117], developed an off-lattice Kinetic Monte Carlo simulation to explicitly account for the chemical reactions taking place when a particle of C-S-H nucleates, i.e. when it is inserted in a simulation box during a simulation. The authors used data from molecular simulations and experiments to inform the model, and they were able to mimic several possible mechanisms of C-S-H precipitation.

Overall, molecular and mesoscale models clarified different aspects of the C-S-H structure and mechanical properties, e.g. nanoindentation and creep moduli. This outcome would be desirable also for geopolymers, however geopolymer modelling is still in its infancy.

2.2.2 Models of geopolymers

To date, most of the of the research on geopolymers is still exclusively based on experiments, while only a few very recent studies have attempted modelling the N-A-S-H gel and the microstructure of these materials. The first nanoscale simulations of geopolymer systems focused on the dissolution of metakaolin and subsequent formation of the three dimensional geopolymer network, but until 2018 only a few authors attempted to model the N-A-S-H structure. 2018 was a prolific year for simulations of geopolymer structures, with seven models being presented at the same time. One of these models, in the Appendix, is by the author of the present dissertation, and will be discussed in detail in the next chapters. The other models are briefly reviewed here.

Modelling the geopolymerisation reaction. White et al. [118] simulated the geopolymerisation reaction for the first time, and provided insights into the fundamental mechanisms controlling the reaction. In this model the cubic lattice sites represented metakaolin particles, and coarse grained Monte Carlo simulations allowed to transforms sites from metakaolin to Si:Al oligomers, to geopolymer. The probability of phase transformation at each site depended on interaction energy with neighbouring

site: these interactions were parametrised based on the free energy of the polymerisation of silicate species calculated by density functional theory (DFT, viz. predictive calculations to approximate the solution of Schroedinger's equation in the framework of quantum mechanics.) [119]. Different Si:Al systems were compared, simulating the activation of metakaolin both from silicate and sodium hydroxide solutions. The main conclusion was that the silica in the activating solution decreased the dissolution of metakaolin, and that the gel resulting from reactions in solutions containing more silica precipitated preferentially on the surface of the metakaolin particle. Instead, when metakaolin was activated only with sodium hydroxide, it was possible to obtain full dissolution of the metakaolin, and the N-A-S-H gel formed by homogeneous nucleation everywhere in the simulation box, with eventual percolation of clusters of aluminosilicates to form the gel. The evolution of the gel structure at the mesoscale (between 1 and 100 nm) was investigated in 2016 using the same model [120], but studying two different precursors morphologies, a round one, representing a fly ash particle, and a cubic one to represent metakaolin. The effect of the silicon in the activating solution on the growth of the gel structure was confirmed, but the new simulations indicated that the shape of the initial particle does not affect the morphology of the gel nor its kinetics growth. In 2018 Zhang et al. [121], used a combination of DFT and effective potentials to perform atomistic simulations of the reaction between oligomers as part of the geopolymerisation reaction. The result was a completely amorphous N-A-S-H gel.

Link between chemical composition and mechanical properties for the N-A-S-H gel. Parallel to the simulations of geopolymerisation, some modelling effort has been devoted to linking the chemical composition of geopolymers at the molecular scale with mechanical properties. In 2015, Sadat et al. [21] used MD to propose a molecular model of N-A-S-H gel based on a completely amorphous structure of silicate and aluminate tetrahedra, simulating different Si:Al ratios. The calculated Young's modulus for structures with Si:Al 2 was ca. 75 GPa, the ultimate tensile stress was ca. 9.5 GPa. The final structure, shown in Fig. 2.14 b, was not fully polymerised, presenting penta-coordinated aluminum, and non-bridging oxygen atoms, which were identified as the main cause for failure under test. One year later the same authors [42] presented a different N-A-S-H gel model based on poly-sialate, poly-siloxo-sialate and poly-disiloxo sialate building blocks, with addition of different percentages of water molecules. The model still presented a completely amorphous structure with aluminum

in penta-coordination, but this time the failure under mechanical tensile test was initiated by Al-O bonds breakage. Kolezynski et al. [20] proposed a N-A-S-H model based on predefined oligomeric building blocks and clusters resulting from the combination of the original oligomer, shown in Fig. 2.14 a. The authors found that increasing the size and order of the clusters (hence heading towards more crystalline structures) showed a better agreement with experimental results of FT-IR spectroscopy. The ordered clusters were similar to zeolites and therefore this kind of polymeric structure was expected to be found in geopolymers.

Modelling the performance of N-A-S-H at high temperatures. In addition, MD simulations allow the study of structural changes originated by external extreme environmental conditions, often difficult to test experimentally. For instance, one of the most studied application field for geopolymers is their resistance at high temperature, and therefore MD simulation was firstly used in 2013 [122] to compare different kinds of geopolymers subjected to high temperature (up to 4000 °C). By using MD, Kupwade et al. [122] modelled the N-A-S-H and potassium-aluminosilicate-hydrate K-A-S-H gel. The initial structures were completely amorphous sodium-aluminosilicate chains without structural water. Different Si:Al ratio were studied finding that the N-A-S-H gel was more stable at elevated temperatures than the K-A-S-H gel. The mechanical behaviour of the N-A-S-H gel at temperatures up to ca. 1200 °C was also presented in a recent paper by Hou et al. [22]. In this work, the initial non-hydrated structure, in Fig. 2.14 c, was build through a series of heating/quenching cycles and the MD simulations using the ReaxFF potential, which led to a sodium aluminosilicate glass. Water was then statistically introduced via energy minimisation by Monte Carlo, achieving the final hydrated N-A-S-H. The result was a gel structure with 23.4% Al(V), hence not fully reacted, a density of 2.59 g/cm^3, higher than experimental values (between 2.3 and 2.4 g/cm^3 [40]), and 7.64% in weight of water molecules. The simulated Young's modulus was in the order of ca. 80 GPa at room temperature, dropping to 40 GPa at 1200 °C, in line with experimental trends showing a decrease in Young's modulus at temperatures over 500 °C.

Interaction between N-A-S-H and other elements. A combined approach involving MC and MD was also adopted by Bagheri et al. [123] to study chloride sorption in the gel structure. The starting structure was an alumino - silicate network with oxygen bonds, like in zeolites and geopolymers, but with protons instead of alkali atoms

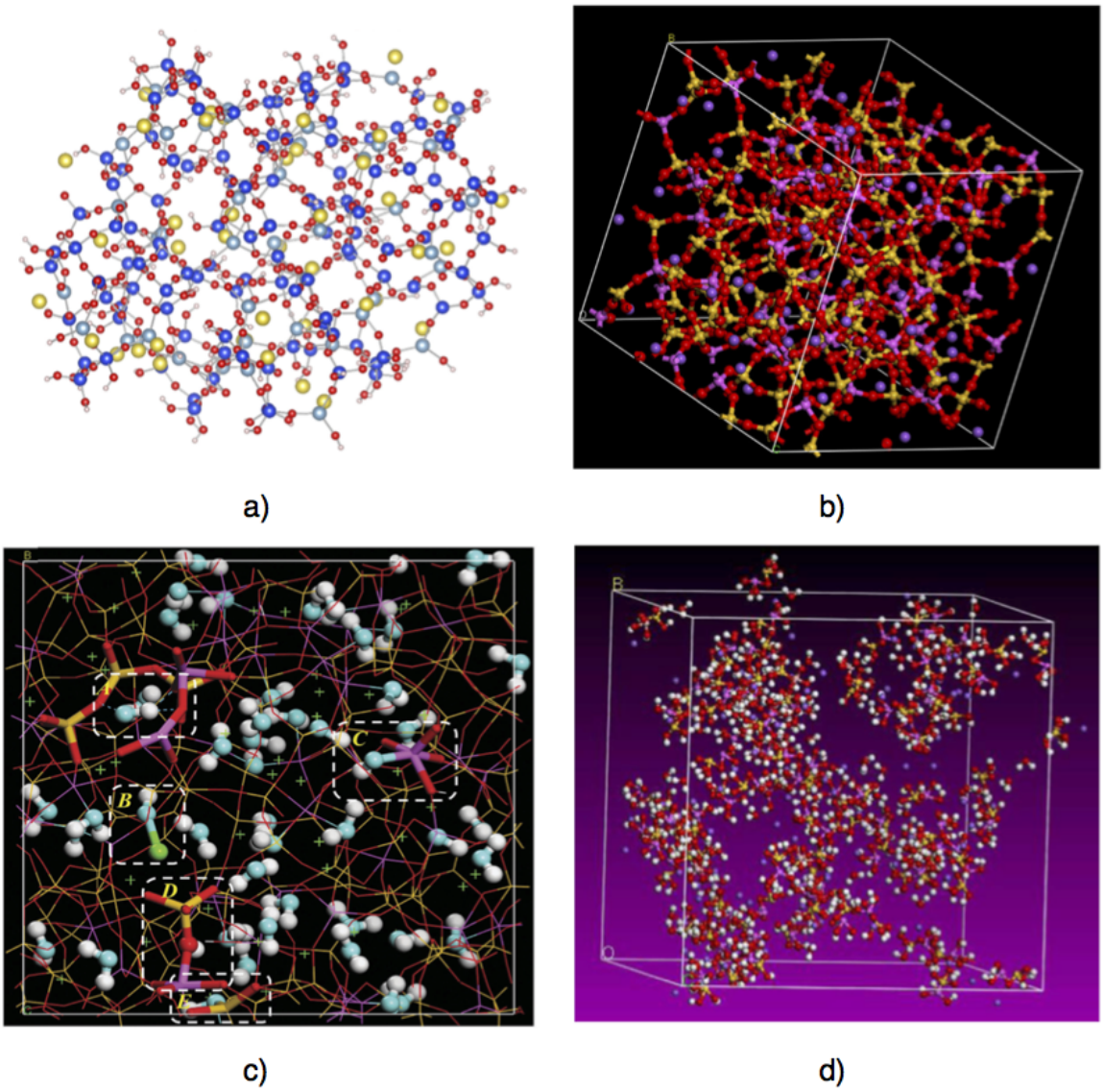

Figure 2.14: Snapshots showing the order level of different molecular structure of the N-A-S-H a) (after Kolezynski et al. [20] Legend: O in red, Si in blue, Al in light blue, Na in yellow and H in pink) b) (after Sadat et al. [21]) c) (after Hou et al. [22]) d) (after Bagheri et al. [23]).

balancing the charge (so-called A-S-H). Hence, only the A-S-H skeleton was considered as representative of geopolymer and used to study the water and chloride ions absorption, without considering the effect of Na or Ca on the structure. The absorption of both water and ions in the nanopores, was found to be dependent on the equilibrium state (function of temperature and pressure). Furthermore the absorption of

chloride and water into A-S-H was exothermic, with the amount of heat raising while increasing the concentration of chloride ions. The same authors [23] applied MD to explore the nanoscale mechanical performances of geopolymers activated with alternative solutions, such as boric acid. The initial structure, in Fig. 2.14 d, was a polysialate amorphous structure, with water added in 5% in weight and the substitution of boric acid required the use of a different force field.The results showed that the simulated mechanical properties of geopolymers activated with boric acid presented an elastic modulus of 35 GPa, smaller compared to the 42 GPa simulated by the same authors for geopolymers activated with sodium silicate solution.

Modelling different geopolymerisation precursors and composite systems. The same approaches as those discussed in this Section thus far, can also be applied to study different kinds of precursors containing different elements such as calcium, hence modelling C-A-S-H instead of N-A-S-H. A few authors focused their research on the study of the C-A-S-H gel comparing it with C-S-H [124, 125]. The introduction of Al in the C-S-H layered structure improved the tensile strength of the material, in particular in the direction perpendicular to the plane of the C-S-H layers. Finally, composite systems of C-S-H and N-A-S-H binders were studied by Sadat et al. [126] with a focus on the failure mode of this material. The composite failed at the interface between the two binders and failure was caused by the breaking of the O-Si bonds in the C-S-H.

Despite the recent interest in molecular modelling of the N-A-S-H gel, all the models reviewed in this Section have shortfalls. First, the role of the order at the nanoscale is still not clarified yet. The majority of the studies are based on completely amorphous structures [22, 23, 121, 122], not fully polymerised and displaying penta-coordinated aluminum [21, 42] in partial contrast with the experimental data that show traces of crystalline features and full tetracoordination of the Al in the geopolymer phase (see Section 2.1.3 for reference). Only one study is based on a zeolite structure [123] and only Kolezynski et al. [20] discussed the importance of crystalline features when comparing to the experimental results. However these studies overlook the experimentally observed contribution to structure and properties coming from the amorphous regions. Second, the amount of structural water in the N-A-S-H is still unknown, as well as its influence on properties at the macroscale. Some models do not consider the presence of water at all [21, 122], while most studies that consider water introduces it with criteria (e.g. space-filling) that are not directly justified by experimental observations. Only Hou

et al. [22] used GCMC to obtain the amount of water in the structure from free energy minimisation, which is not necessarily matching the experiments but is at least a justified physical principle. On the other hand, Hou et al.'s structures were fully amorphous which is not realistic, hence also the resulting content of water is likely to be incorrect. Therefore more research is needed in relation to the water content of molecular models of N-A-S-H.

2.3 From material science to engineering implementation

As discussed in the previous Section, the research on geopolymers is still ongoing, with a series of challenges that still need to be addressed. Geopolymers are a relatively new material, therefore every scientific or technological improvement must be scalable to be introduced on the market. This requires an assessment of the impact of new cements on the environment, and the development of new standards allowing the implementation of these new materials.

2.3.1 Life Cycle Assessment of alkali activated cements and concretes

Life Cycle Assessment (LCA) [127] is an approach to evaluate the environmental impact of any material or system, including new concretes and cements. For cement based materials, LCA follows the "cradle to gate" approach, considering all the components of the production process but only until the product is released to the market, hence not considering the transportation, placement, maintenance and disposal of the product throughout its full life cycle. This is a common approach due to the fact that cement based materials and concrete can be part of various end-products. LCA allows to determine the impact of the material production through several impact categories, but for the construction sector, the global warming potential (GWP) category is the main issue that needs to be addressed, since cement production has an extensive impact on the global CO_2 production. At present, only a few research papers on LCA of alkali activated cements and concretes (AACC, of which geopolymers are a sub-class) have been published, and with contrasting outcomes.

A first LCA analysis of geopolymers and of their production, in 2007, predicted an 80% reduction of CO_2 compared to Portland cement (PC) binders [24]. This however considered only geopolymers obtained from industrial by-products, such as fly ash and ground granulated blast furnace slag, which do not require calcination or other pre-treatments. In the study, however, those by-products were still considered as waste products, hence the contribution of their production to the environmental impact was neglected. Thus, the almost totality of the environmental impact was attributed to the production of the activating silicate solution, which is a necessary component of the production process of geopolymer-based cements (see geopolymerisation chemistry in Section 2.1.3). In 2009, Weil et al. [25] published the first LCA of geopolymer considering three impact categories: global warming potential (GWP), abiotic deletion potential (ADP) and cumulative energy demand (CED). The global warming potential of geopolymer was three times lower than a reference Portland cement, while the impact on the other two categories was comparable. A more extensive study was carried out in 2011 [26] with the analysis of 10 different indicators. Also in this paper the GWP of geopolymers was lower than Portland cement, but the impact on other indicators, more related to the agricultural field [28], favoured cement production. The main responsible for the higher environmental impact on these categories was the production of the sodium silicate activating solution (see Section 2.1.2). In the 2011 study, the raw materials were considered by-product and not waste, with consequently attribution of an allocation coefficient, hence with embodied energy. In the same year, Mc Lellan et al. [27] compared the environmental impact of PC and geopolymer production in Australia, indicating a potential 44 to 64% reduction of greenhouse gas emissions for geopolymers compared to PC. In the results of Mc Lellan et al. [27], the transport of raw materials to the production site, and the transport of cement to the construction site, had a major impact on the total emission, but the novelty of this study was the comparison of different technologies to produce the activating solutions. Yang et al. in 2013, obtained similar values for reduction of CO_2 emissions comparing PC concrete and AAC concrete. Depending on the amount of activating solution in the mix design of the geopolymer, results varied from a 55 to a 75% reduction of greenhouse gas emissions compared to PC. All these results have been reviewed in a recent publication by Habert et al. [28] concluding that CO_2 emissions can be reduced by 75% compared to the production of concrete using PC, depending on the mix design used. However, this estimation includes only the production phase, without considering durability aspects. This is due to a general lack of durability data for alkali activated materials.

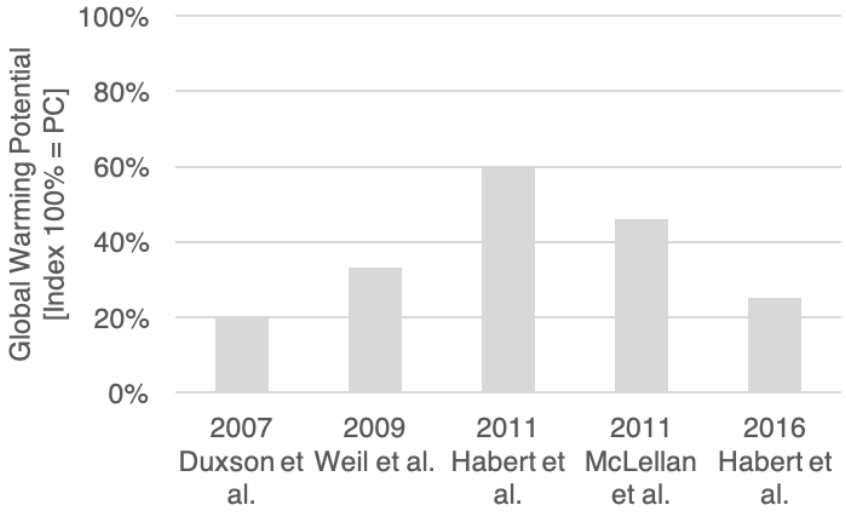

Figure 2.15: Summary of global warming potential (GWP) impact of geopolymers compared to PC. Data from Duxson et al. [24], Weil et al [25], Habert et al. [26], McLellan et al. [27], and Habert et al [28].

Overall all the LCA studies to date agree that geopolymers have a lower impact on global warming than Portland cement [24–27, 47, 128], and the main source of impact for geopolymers is the production of the sodium silicate solution. There are however uncertainties related to:

- *Transport*. Cement production is an established and consolidated market with a wide availability of production sites around the world. On the contrary, geopolymers are not produced extensively and for this reason their transport has a higher environmental impact [27]. The creation of a denser supply chain, therefore shorter geographical distances between production and construction sites, could reduce this environmental cost, creating also new opportunities for local business, favouring small and medium enterprises, and thus supporting the UK Engineering and Physical Sciences Research Council's (EPSRC) vision of a "local and bespoke" approach to growth [129];

- *Accuracy of available data*. The origin of the raw materials for the activating solution should be considered in order to reduce the impact of the final product. Data on sodium silicate production are not to date and difficult to estimate. The majority of studies mentioned above, consider data published in 1999 [130] based on 1995 production [47, 62]. It is likely that the efficiency of the production has improved during the last 25 years, see Section 2.1.2. Furthermore the conver-

sion of sodium carbonate (Na_2CO_3) and silica (SiO_2) to sodium silicate can be realised through various processes [62], e.g. producing Na_2CO_3 via the Solvay process (mainly in Europe) versus than directly mining it or obtaining it from trona (United States), see Section 2.1.2 for details. The Solvay process causes 5 to 10 times more CO_2 emissions compared to the mining process [62]. Data on metakaolin production are also conflicting and do not consider new production techniques such as flash calcination (see Section 2.1.1). The main variability on the CO_2 emissions related to kaolin calcination process to obtain metakaolin (see Section 2.1.1) is due to the type of fuel used. The impact can change considerably changing the GWP from 0.08 kg CO_{2eq}/m^2 of wood based fuel, to 0.57 kg CO_{2eq}/m^2 of coal fuel [28];

- *Lack of data on the durability of geopolymers*. The durability of geopolymers cannot be quantified efficiently since long-term data (50-100 years) are still scarce and research on this topic is still in its infancy compared to durability of traditional cement and concrete structures. With available data the LCA could be done considering also the use phase of the material.

- *Availability of raw materials*. It is necessary to consider the availability of raw material locally, therefore geographically specific LCA should be analised. For examples, while in Europe the availability of fly ash is limited with coal industry being phased out in many countries, in China or India, where most of the electricity is still produced by coal combustion, fly ash supply is not an issue. Metakaolin sources might be the best option to ensure robustness of supply, owing to extensive availability without reliance of primary market on which industrial by-products depend (coal for pulverised fuel ash, PFA, and ironmaking for slag).

All LCA studies available in the literature are comparing geopolymers to cement or concrete, however the applicability of geopolymers is wider and can provide alternatives also to other building materials. For example, a first estimation is that geopolymers bricks may have an embodied CO_2 content of 15.5 kg CO_{2eq}/m^2, while traditional masonry bricks have an environmental impact of 26-44 kg CO_{2eq}/m^2. Geopolymers bricks display, in addition, 150% higher compressive strength compared to traditional bricks [47].

To summarise, the international objective of an 80% reduction of greenhouse gas (GHG) emission by 2050 [131] cannot be achieved only by incremental improvements of traditional cement technology [62]. Alkali-activated materials may contribute to a

reduction of 45-75% of CO_2 emissions related to cement production, but the reduction percentage is strongly dependent on the mix design and content of activating solution. The main areas where significant gains in environmental performance can be achieved include:

1. Transitioning to flash calcined metakaolin. Metakaolin geopolymers from flash calcined metakaolin requires less activating solution because of a higher reactivity of metakaolin compared to fly ash.

2. Partial substitution of materials other than PC with geopolymers (e.g. bricks, pavements, tiles and mortar).

3. Advance science and technology of silicate solution production.

Operatively, the deployment of these relatively new materials requires new standards for each application, and further investigation, in particular concerning their durability.

2.3.2 Standards

To promote the commercialisation of AAM it is fundamental to develop standards setting the parameters for these materials to be deployed and applied. The current EU standards for cementitious materials are mainly prescriptive, both for the composition of the raw material (the cement), and for the mix design. Such standards are preventing the adoption of new binders, while favouring Portland cement (PC).

The first standards on AAM have been developed in Ukraine and former URSS, with the first standard published in 1961, followed by 60 revised updates. This considerable number of revisions is mainly due to the fact that all these standards were prescriptive, hence several updates have been redacted each time that a new formulation or a new raw material was considered. These standards regulate the type of material, the applications for which AAM can be used, as well as the manufacturing process. To facilitate the adoption of AAM, a better alternative to prescriptive standards would be performance based standards, which in principle could be applied to any cementitious materials (including AAM) as long as the required performances are met. The American ASTM C1157 [132] is a performance based standard for hydraulic cements. According to the principle for performance based standards in the ASTM C1157, there are no restrictions on the cement composition. Cements are classified only depending on their desired performance in: General Use (GU), High Early-Strength (HE),

Moderate Sulfate Resistance (MS), High Sulfate Resistance (HS), Moderate Heat of Hydration (MH), Low Heat of hydration (LH). This standard however, to date, is only adopted in 5 of the 50 American States, and at the European level performance based standards are yet not available.

The general lack of specification in Europe motivated the formation of the RILEM TC 224-AAM in 2007. The main aim of the committee was to outline standards that may be applicable to alkali activated materials. Due to the wide variability of applications and precursor constituents, the RILEM TC promoted a performance base standard over a prescription based one. This decision allows also the possibility for future technological innovation without the frequent reformulation of new standards. At the UK level, the result of this work is the British Standards Institute (BSI) Publicly Available Specification PAS 8820:2016 "Construction materials. Alkali-activated cementitious material and concrete - Specification" in 2016 [133]. PAS 8820 [133] specifies the performance requirements for alkali activated cements and concrete, including performance requirements for precursors. In addition, it is prescribed that the manufacturers of these materials develop a greenhouse gas life cycle assessment for each new material.

2.4 Open challenges

In order to consider geopolymers as an alternative to Portland cement, further research has to be done as underlined by this literature review, and the following summary addresses the challenges that are still open and arguably most pivotal in this field.

1. Optimising the content and origin of sodium silicate in the mix design or studying sodium silicate solutions from alternative sources to reduce the GWP index (*e.g.* rice husk ash could be used to produce sodium silicate [134]).

2. Understanding and provide a unique definition of geopolymer chemical structure at the molecular scale, with a particular focus on the interaction between amorphous and crystalline features in the N-A-S-H gel. In addition, definition and quantification of structural water at the molecular level still need to be provided. Such an understanding could be exploited to design geopolymer cements with optimum structures and properties.

3. The role of water in the geopolymerisation still need to be clarified, together with

its contribution on long term macroscale behaviour such as shrinkage (chemical, autogenous and drying).

4. Obtaining experimental durability data related to long-term performances. In particular data on shrinkage and creep of metakaolin geopolymers are still lacking.

5. Connecting shrinkage and creep mechanism to the microstructure of geopolymers to understand which parameters influence the development of long term properties, e.g. Si:Al ratio, type of activator, and water content.

6. Support experimental tests with molecular models to correlate and clarify the link between chemistry and mechanical properties.

3

Aim and objectives

Contents

3.1 Aim and objectives

The aim of this PhD work is to nano-engineer the early-age behaviour of more sustainable geopolymer-based cements, i.e. more than existing geopolymers, combining experiments with new theoretical models and simulations. The main objectives of this dissertation are:

- **O1**: To develop a reference computer model of metakaolin geopolymers at the molecular scale (up to 2 nm), to explain the experimental data that show a coexistence of amorphous and crystalline features at the molecular scale.
- **O2**: To build a set of experimental data on volume changes during early hydration (chemical and autogenous shrinkage); there are no such data available in the literature to date.
- **O3**: To identify the microstructural and chemical features of metakaolin geopolymers that correlate with volume changes: this will be done by combining the new experimental results from O2 with the new theoretical insights from the model from O1.
- **O4**: To develop a reference computer model of metakaolin geopolymers at the mesoscale between 1 nm and 1 μm, to be validated and refined with experiments on metakaolin geopolymers. The mesoscale model will especially aim to capture those features, such as nanopore structure and interaction with water, which are key to the durability of cementitious materials.

Fig. 3.1 illustrates schematically all of the objectives and their interconnections. The last objective, “Modelling creep of metakaolin geopolymers” represents a possible future development of the work presented in this thesis.

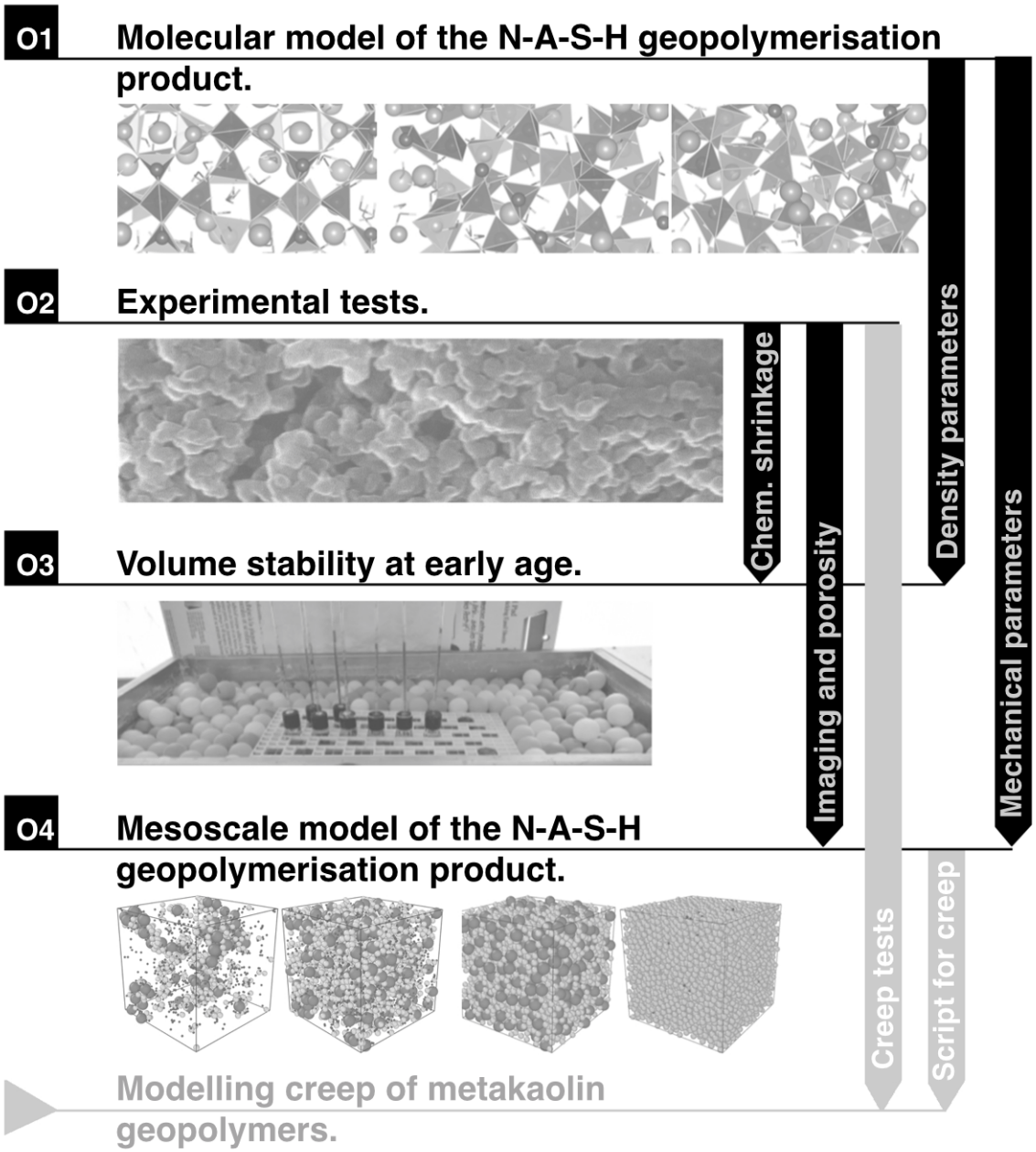

Figure 3.1: Schematic of the thesis objectives.

4

Methodology

Contents

4.1 Molecular scale model

Section 2.1.3 highlighted that the microstructure of geopolymers presents some features that are typical of crystalline structures and other that are typical of amorphous structures. This coexistence of features may be explained in two ways. One is that the molecular structure is homogeneous and everywhere intermediate between crystalline and amorphous. Alternatively, one may accept the pseudo-zeolitic model of Provis et al. [79], with crystalline regions embedded in an amorphous matrix. In this latter case, the interfacial zones between crystalline and amorphous domains would also be intermediate between the two. Therefore, in both the above assumptions, regions with intermediate order are likely to play a crucial role in determining properties, especially mechanical ones. None of the molecular models of geopolymers to date has quantitatively described such molecular structures with intermediate order between amorphous and crystalline. Hence, three molecular scale models, ranging from completely crystalline to completely amorphous, are presented in this Section. In particular, this Section introduces the methodology to design the molecular structure of geopolymers identified as the sodium-aluminium-silicate-hydrate geopolymerisation product, N-A-S-H. The content of this Section is from a recently published paper in *ACS Applied Materials and Interfaces* titled *Atomistic Simulations of Geopolymer Models: The Impact of Disorder on Structure and Mechanics*, Lolli et al. [31].

4.1.1 Introduction to molecular scale modelling

This Section presents a brief introduction to atomistic modelling and simulation, before discussing the methodology used for the molecular model of N-A-S-H in the following Sections.

In an atomistic model, an *atom* is represented as a pointwise particle characterised by a certain mass and by three spatial coordinates ($\mathbf{r}_i$), that define its position in a simulation cell. Each cell is a three dimensional volume which is, in many cases, repeated periodically in all three dimensions (periodic boundary condition, as displayed in Fig. 4.1 a.) During a simulation the atoms can move driven by interaction forces. For the generic atom *i*, the acceleration is defined by Eq. 4.1:

$$\ddot{\mathbf{r}} = \frac{d^2\mathbf{r}}{dt^2} = \frac{\mathbf{f}_i}{m_i} \tag{4.1}$$

The force field $\mathbf{f}_i$ can be derived from a potential energy function as shown in

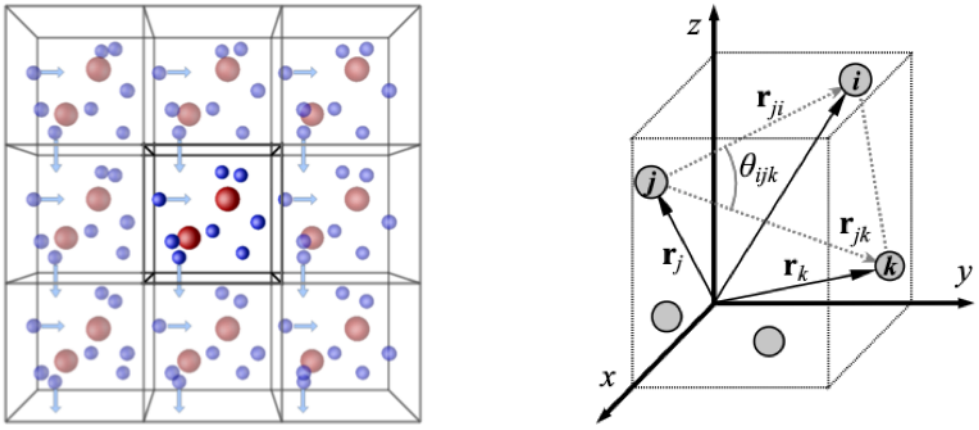

Figure 4.1: a) Representation of periodic boundary condition [29]. b) Schematic of interatomic distances **r** and angle θ between atoms.

Eq. 4.2. This is possible because at the atomic scale the atoms are typically considered to interact with each other via conservative potentials, that depend only on the positions of the atoms $U(\mathbf{r}_i)$. Under these conditions, the force fields is simply obtained as:

$$\mathbf{f}_i = -\frac{\delta U}{\delta \mathbf{r}_i} \tag{4.2}$$

Interatomic potentials. The potential energy function $U(\mathbf{r}_i)$ in Eq. 4.2 is typically expressed as a sum of interaction potentials between groups of few neighbouring atoms (a simple example of a pairwise interaction potential would be the harmonic potential, viz. a linear spring). Interatomic potentials are classified as two-body, or pair potentials, which depend only on the distance between pairs of atoms ($r_{i,j}$), three-body potentials, depending on distance and angle between triplets of atoms ($r_{i,j}$, $r_{i,k}$, $\theta_{i,j,k}$), and many-body potentials. Fig. 4.1 b. shows a representation of interatomic distance ($r_{i,j}$, $r_{i,k}$) and angle between atoms ($\theta_{i,j,k}$). In addition to being positions-dependent, interatomic potential are also functions of parameters that are specific to the types of interacting atoms. Different sets of parameters define different force fields, and a number of those are commonly used in the literature on molecular simulations. Two examples of force fields that are important in the cement and geopolymer literature are CLAY-FF [135], for systems containing Al, Si, Na, K, and C-S-H-FF [136]

for molecular models of C-S-H. Most of the existing force field are not able to predict chemical reactions, i.e. the breaking and formation of interatomic bonds. ReaxFF [112] instead can reproduce chemical reactions for a wide range of materials. For this reason ReaxFF has been chosen for the molecular model of geopolymer presented later in this manuscript.

Temperature. Statistical mechanics provides a relationship between temperature and kinetic energy, and thus velocity, of atoms in a simulation cell:

$$\sum_{i=1}^{N} \frac{1}{2} m \dot{\mathbf{r}}_i^2 = E_{kin} = \frac{3}{2} N k_B T \tag{4.3}$$

where E_{kin} is the total kinetic energy of the system of atoms, *N* is the number of atoms in the simulation cell, k_B is the Boltzmann constant equal to 1.3810^{-23} J/K, and *T* is the temperature in Kelvin. Hence, to set a specific temperature, the velocity of all atoms has to be such that the kinetic energy of the system is equal to $\frac{3}{2} N k_B T$. In molecular dynamics simulations an algorithm called "thermostat" can control and rescale the velocity of all atoms to meet the target temperature, and preserve it on average. In this dissertation T is usually assumed equal to 300 K (ambient temperature), except for when constructing the defective model during which the temperature is assumed equal to 1000 K, to enable a more effective relaxation of the structure.

Pressure. The pressure of the entire system of atoms can be obtained using the virial formula, which for a three-dimensional system can be defined as in Eq. 4.4 [137], given the positions $\mathbf{r}_i$ and forces $\mathbf{f}_i$ of all atoms.

$$P = \frac{N k_B T}{V} + \frac{1}{3V} \Big\langle \sum_{i=1}^{N} \mathbf{r}_i \mathbf{f}_i \Big\rangle \tag{4.4}$$

where *N* is the number of atoms in the system, k_B is the Boltzmann constant, and *V* is the volume of the simulation cell. In molecular dynamics simulations it is possible to fix the pressure of the system through a "barostat", which changes the size of the simulation cell thus changing interatomic distances until the target pressure is met. In this dissertation pressure is assumed equal to 1 atm. For completeness in Eq. 4.5 is reported the full expression of the stress tensor [137].

$$S_{ab} = -\Big[mv_a v_b + \frac{1}{2}\sum_{n=1}^{N_p}(r_{1a}F_{1b} + r_{2a}F_{2b}) + \frac{1}{2}\sum_{n=1}^{N_b}(r_{1a}F_{1b} + r_{2a}F_{2b}) + \frac{1}{3}\sum_{n=1}^{N_a}(r_{1a}F_{1b} + r_{2a}F_{2b} + r_{3a}F_{3b}) + \frac{1}{4}\sum_{n=1}^{N_d}(r_{1a}F_{1b} + r_{2a}F_{2b} + r_{3a}F_{3b} + r_{4a}F_{4b}) + \frac{1}{4}\sum_{n=1}^{N_i}(r_{1a}F_{1b} + r_{2a}F_{2b} + r_{3a}F_{3b} + r_{4a}F_{4b}) + Kspace(r_{ia}, F_{ib}) + \sum_{n=1}^{N_f} r_{ia}F_{ib}\Big] \quad (4.5)$$

where *a* and *b* take on values x, y, z to generate the six components of the symmetric tensor. N_p is the number of neighbours, r_i is the positions of the two atoms in the pairwise interaction, F_i the forces on the two atoms resulting from the interaction. N_b, N_a, N_d, N_i, N_f represent respectively bond contribution, angle contribution, dihedral contribution, improper interactions and internal constraints forces.

Simulations by energy minimisation or Molecular Mechanics simulations. This type of simulations are used to determine a configuration state of mechanical equilibrium in which the total forces on all atoms are balanced to zero, hence when the potential is minimised. The resulting configuration of atoms may represent a local or global potential energy minimum, depending on the type of interactions, on the density of the system, on the starting configuration, and on the algorithm used for the minimisation. These simulations are also called athermal simulations because the velocity is always zero, hence the temperature is implicitly assumed to be null. Energy minimisation is used at different steps of the formation of the molecular model, in particular each time that a structural or mechanical property is computed (see Fig. 4.9 for additional details).

Molecular Dynamics simulations. In MD simulations atoms move in time, due to initial velocities, thermal agitation and interaction forces. The types of MD simulations used in this dissertation are in the so-called “NVT” and “NPT” ensembles. In an NVT simulation the number of atoms is fixed and equal to *N*, the volume *V* is kept constant, and the temperature *T* is regulated through a thermostat. As a result, the only exchange between the simulation cell and the external environment is a heat exchange operated by the thermostat. Since the volume is constant but the atoms can move, the pressure can vary during the simulation, as described in Eq. 4.4. In an NPT simulation, the number of atoms *N* is fixed, *T* is fixed by a thermostat and the pressure *P* is fixed

by a barostat, hence the volume of the cell fluctuates. By combining NPT and NVT it is possible to measure stress-strain curves as explained in detail in Section 4.1.3. For completeness, it should be mentioned that it is also possible to vary the number of particles in a simulation cell (in the so-called μVT or grand canonical ensemble), but this type of simulation has not been applied to the model of geopolymers discussed in the following sections. Both NPT and NVT simulations are performed to obtain the molecular model of N-A-S-H gel presented in this dissertation (more details in Fig. 4.9).

Thousands of atoms are usually part of a simulation, interacting for millions of timesteps. The timestep is bound to be a fraction of the shortest natural period of the interactions between atoms, which is typically in the order of femtoseconds. Therefore a clear limitation of this type of models is the timescale that can be simulated. A typical molecular scale simulation that represent a few nanoseconds in real time, may take up to a few weeks of running time.

4.1.2 Siliceous baseline structures and N-A-S-H model constraints

Three types of structures are built: a fully crystalline, a fully amorphous, and a defective crystal structure, to allow for a comparative analysis on the impact of the degree of order on the structure. Each type of structure is then modelled with various Si:Al ratios, ranging from 1 to 2. The Si:Al ratios identified as targets are summarised in Table 4.1 together with the chemical formula of each structure and the distinctive parameters in each model, namely cell volume, number of atoms in each simulation cell and water content.

First of all, three baseline siliceous structure are built, containing only Si and O atoms. The reason behind this choice is that the addition of Al and Na atoms induces structural changes distorting the skeletal structure. Na atoms, being positively charged (cations) interact electrostatically with the Si-Al-O-Si environment, modifying the Si-Al-O-Si bond angles as a result of the equilibrium position of the Na atoms. Measuring structural properties on undistorted siliceous structures leads to results concerning the geometry and topology of the structures that are clearer to interpret. A summary of all the analysis undertaken on the molecular models is shown in Fig. 4.2, together with the software used to perform each test.

All the baseline Si-O structures are first energy-minimised at T= 0 K and P= 1 atm using the Polak-Ribiere version of the conjugate gradient method available in LAMMPS [137]. The interaction potential chosen is ReaxFF [112], since it can repro-

Table 4.1: Three molecular structures: amorphous (Am), crystalline (Cr) and defective (De). The Na:Al:H_2O molar ratio are set to 1:1:3 for all structures. *Total number of H and O atoms in water molecules divided by the total number of atoms in the cell. Table from [31].

Name	Si:Al molar ratio	Cell volume [nm^3]	No. of atoms	Water content [%] *
Am_1.5	1.5	41.26	4324	51.4
Am_2	2	38.73	3914	47.4
Cr_1	1	54.25	6144	56.3
Cr_1.4	1.4	50.07	5496	52.4
Cr_2	2	52.53	4856	47.4
De_1.5	1.5	44.95	4480	51.4
De_2	2	46.03	3840	45.0

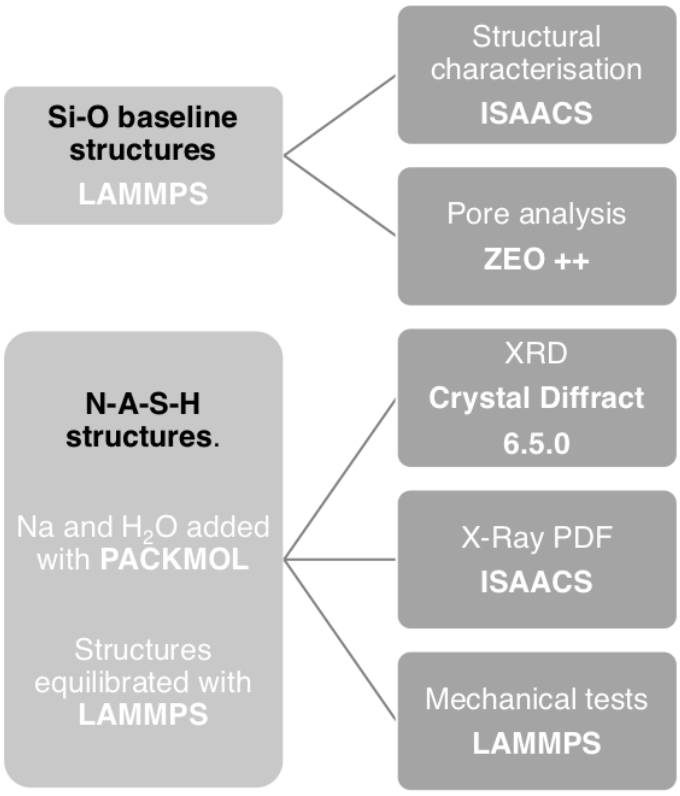

Figure 4.2: Schematic of the tests conducted in this Section and the corresponding software.

duce chemical reactions and include parameters for all chemical elements and chemical combinations involved in the geopolymerisation reaction. Furthermore ReaxFF can be applied to structures with different degree of order; for example Manzano et al. used it for both glasses and crystal structures of calcium silicate hydrates with the same set of parameters [113, 138]. A discussion of the appropriateness of the ReaxFF and its parameters for the N-A-S-H structures to be modelled here can be found in Lolli et al. [31]. Structural characterisations of the model siliceous baseline structures is then carried out using the software ISAACS [29], which provides the bond lengths and bond angles distributions (Fig. 4.3). ISAACS also provides the ring distribution, computed using the King's shortest path criterion. A ring is defined as a closed path of nodes

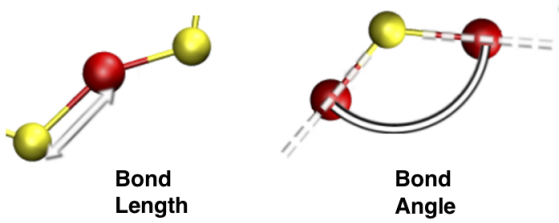

Figure 4.3: Simplified representation of bond length and bond angle [29].

(Si atoms) and links (Si-O-Si bonds) connected in sequence without overlap [29]; this gives information about structural organisation beyond the first neighbouring atoms, extending towards mesoscale organisation at the scale of a few nanometers. Finally the micropore size distribution is obtained using the software Zeo++ [139], that applies the method by Pinheiro et al. [140] based on the Voronoi tesselation. The parameters used to model the pore size distribution are a probe radius of 0.1 Å, and a number of Monte Carlo samples per unit cell equal to 50000. These parameters allowed to reach the expected pore distribution for the zeolite used as baseline for the crystalline structure (details on this structure can be found in Section 4.1.4).

To model the N-A-S-H structures starting from the Si-O baseline structures, some Si atoms are substituted with Al atoms (targeting the desired Si:Al ratio) and Na atoms and water are added at random locations using the software Packmol [141] until reaching the target water content. An example of the whole process is displayed in Fig. 4.4. For all structures the same principles have been followed:

1. The number of Na atoms equals the number of Al atoms, to satisfy charge neutrality. Al is tetracoordinated to oxygen and thus the Al-centred tetrahedron carries a

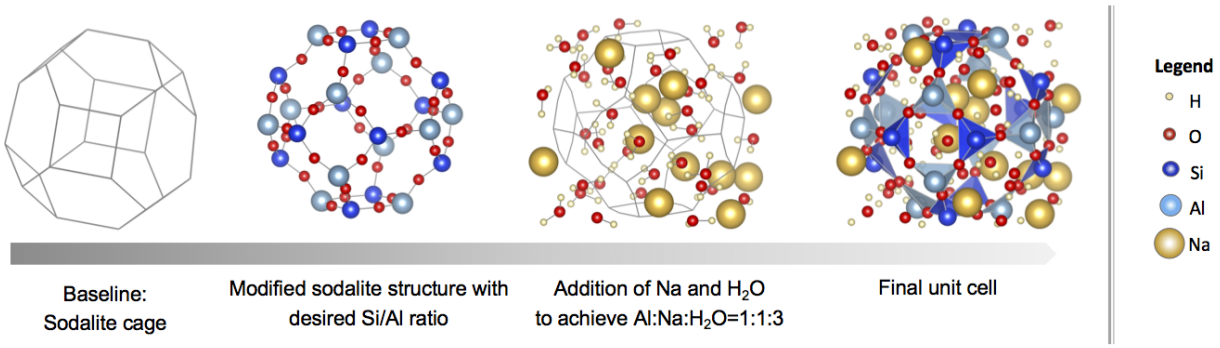

Figure 4.4: Simplified schematic of the construction process for a crystalline structure. All snapshots are obtained using VESTA [30] (after Lolli et al. [31]).

-1 net negative charge, which the Na cation balances.

2. The structural water considered at the molecular level is three molecules of water for each Na atom. If one defines structural water as the minimum amount of water below which the material undergoes microstructural changes leading to drying shrinkage and microcracks, then drying shrinkage experiments can be used as a reference to estimate the amount of water embedded in the skeletal structure. Experiments on metakaolin geopolymers paste with Si:Al = 1.15 - 2.15 dried at 150°C, indicate that the amount of non-evaporable water is equal to 3.3 - 4.4 H_2O:Na molar ratio [41]. Additionally Kuenzel et al. [12] showed that irrespectively of the initial amount of water in the sample, drying shrinkage starts only when the amount of water still in the sample decreases below 3 moles per mole of Na. Therefore in the models presented here, the amount of water is considered equal to H_2O:Na=3:1 molar ratio.

3. The Loewenstein's principle is always respected, therefore two Al tetrahedra cannot be linked by a single oxygen bond and each Al tetrahedron is always linked to four Si tetrahedra.

4. No edge-sharing tetrahedra. As described in Section 2.2.2, in the existing molecular simulations of geopolymers, some Al tetrahedra are linked through two oxygen bonds instead of one. The consequence of this edge-sharing is a deformation of the O-T-O (oxygen-tetrahedron-oxygen) angles that is unrealistic, *i.e* largely unfavourable from a thermodynamics point of view, when considering materials containing water and forming by chemical reactions at room temperature.

5. Full Q^4 polymerisation to represent more statistically relevant structures, in accordance with NMR experiments showing a majority of tetracoordinated Al, and only penta coordinated Al in small percentage, as explained in Section 2.1.3.

Finally, for all structures periodic boundary conditions are applied in all three directions.

4.1.3 Structural and mechanical characterisation

All the N-A-S-H structures are subjected to the following simulations and analyses:

1. First relaxation *via* energy minimisation, using the Polak-Ribiere version of the conjugate gradient method in LAMMPS [137].

2. Equilibration at P = 1 atm and T = 300 K *via* 1 ns of molecular dynamics in the NPT ensemble, using the Verlet time integration scheme and integration timestep of 0.1 fs in LAMMPS [137].

3. Check of the stability (on average and within fluctuations) of total interaction energy and pressure at T = 300 K *via* 1 ns of molecular dynamics in the NVT ensemble.

Once these three steps are completed, X-Ray diffraction patterns are simulated using the CrystalDiffract 6.5.0 program [142]. All generated patterns are corrected via peak broadening of 0.5^o full width at half-maximum, to better match experimental results. X-Ray Pair distributions are computed with ISAACS [29], obtained calculating the Fourier transform of the structure factor derived from the Debye equation. Mechanical tests are then simulated using LAMMPS [137]. A sequence of tensile deformation steps of 1% each is applied to one side of the cell while keeping constant the size of the simulation cell in the other two perpendicular directions. Step increments are applied until rupture, as schematically displayed in Fig. 4.5. The tensile test is then repeated also in the other two directions, to explore statistical uncertainty. The 1% strain increment per step has been chosen following a sensitivity analysis of deformation steps varying from 0.1% to 2.5%. Strain in the order of tenths of the percent are typical in molecular dynamics (MD) simulations, since at the molecular scale the structure can sustain higher strain and stresses than at the macroscale, owing to absence of macroscopic defects. After each deformation increment the structure is subjected to relaxation *via* energy minimisation. Having kept the cell fixed in the direction perpendicular to the loading, the

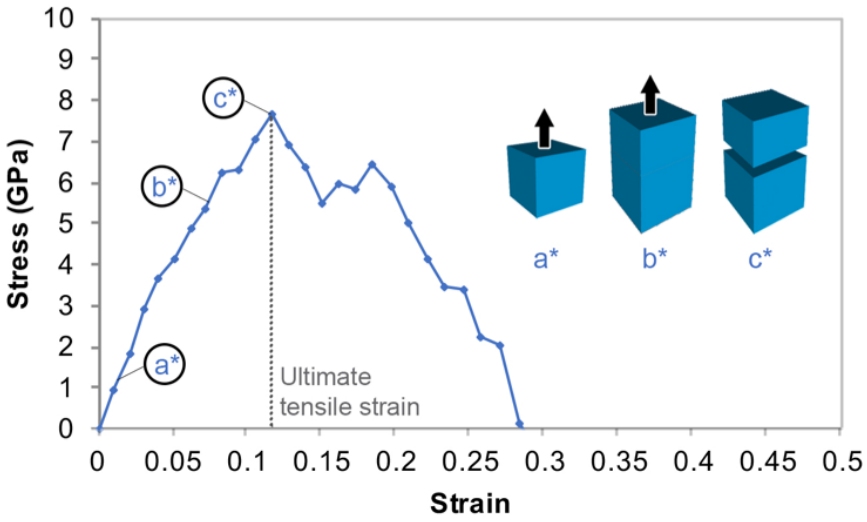

Figure 4.5: Simplified schematic of a stress-strain curve at the molecular scale.

resulting strain field is representative of nanoindentation experiments or AFM (atomic force microscopy) indentation tests. From the mechanical tests it is possible to obtain stress-strain curves, useful to compute elastic moduli and therefore to determine the amount of stress that produces a unit strain in the small-deformations regime, *viz.* when the strain tends to zero. The initial slope of the stress-strain curves obtained with this approach, is the indentation modulus M, which is related to the Young's elastic modulus (E) and Poisson's ratio ν by Eq. 4.6 [143].

$$E = \frac{M(1+\nu)(1-2\nu)}{(1-\nu)} \tag{4.6}$$

Eq. 4.6 is valid only for homogeneous, isotropic, linear elastic materials, but all the N-A-S-H structures satisfy these conditions when the strain tends to zero. The Poisson's ratio can be determined by monitoring the evolution of axial stresses in all three directions during the tensile test. Eq. 4.7 shows that the stress in the direction perpendicular to the loading direction (j and k) are related to the tensile stress applied in direction i via the Poisson's ratio [144]. The stresses in the three direction are calculated directly with LAMMPS at each step of the deformation, therefore the Poisson's ratio for each Si:Al and type of structure can be computed applying Eq. 4.7.

$$\sigma_{jj} = \frac{\nu}{1-\nu}\sigma_{ii}\ ; \qquad \sigma_{kk} = \frac{\nu}{1-\nu}\sigma_{ii} \tag{4.7}$$

The final parameter deducted from the tensile deformations of the molecular struc-

tures is the average non-affine displacements $\overline{\delta}_{na}$, described in Eq. 4.8.

$$\overline{\delta}_{na} = \frac{\sum_i^N |r_i(\varepsilon) - r_{i,aff}(\varepsilon)|}{N} \tag{4.8}$$

In Eq. 4.8 N is the number of atoms in the simulation box, r_i is the position of atom i at strain value ε after energy minimisation at that strain step, and the affine $r_{i,aff}$ is the position that the same atom i would have had at the same strain step ε in absence of minimisation performed during the tensile deformation test. Non-affine displacements are usually related to ductility and brittleness of a structure, with large non-affine displacements indicating plastic deformations.

4.1.4 Tuning the level of disorder

Several N-A-S-H structures with different levels of order have been created:

- *Crystalline structures.* All the crystalline models are based on a simple sodalite skeleton, framework type SOD [145], common in zeolites found in geopolymers (see Section 2.1.3). Sodalite is part of the building skeleton of both faujasite and Zeolite A and presents a cage structure of hexagonal and squared rings, as shown in the first snapshot of Fig. 4.4.

- *Amorphous structures.* The baseline for all amorphous structures is an amorphous silica glass molecular model built by Sheikholeslam et al. [146]. In this structure all the constraints listed in Section 4.1.2 are respected, namely the Loewenstein's principle, full Q^4 polymerisation and the absence of edge-sharing tetrahedra. The substitution of Si with Al has been performed using a specifically written Monte Carlo program which analyses the first and second neighbours of each atom, to satisfy the Loewenstein's principle. Due to the disorder in the amorphous structure, only Si:Al 1.5 and 2 could be achieved and analysed. The topological disorder does not allow Si:Al molar ratios equal to 1, while respecting Loewenstein's principle. Fig. 4.6 describes the construction process for the amorphous structure.

- *Defective structures.* Fig. 4.7 describes the construction process for the defective structures. The starting configuration is a crystalline sodalite one, previously equilibrate at P = 1 atm. Two SiO_2 units are randomly deleted from this structure,

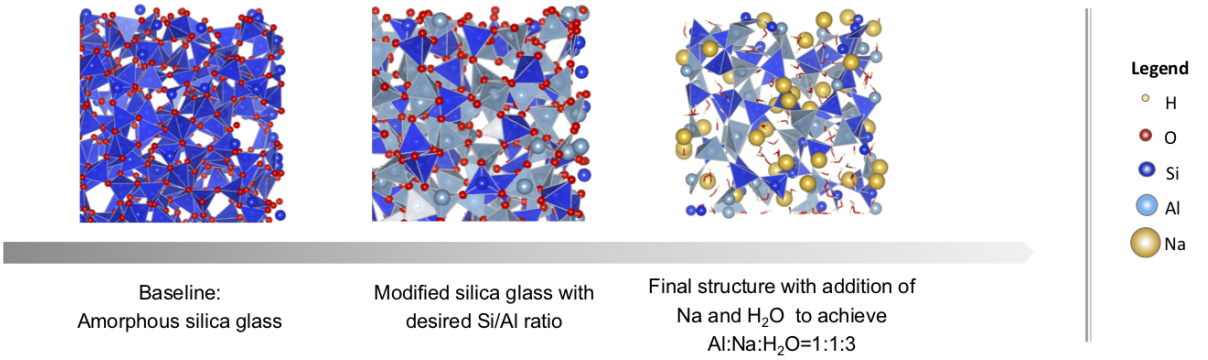

Figure 4.6: Simplified scheme of the construction process for an amorphous structure. All snapshots are obtained using VESTA [30]. *Some Si atoms are not visualised as tetrahedra due to the boundary conditions.

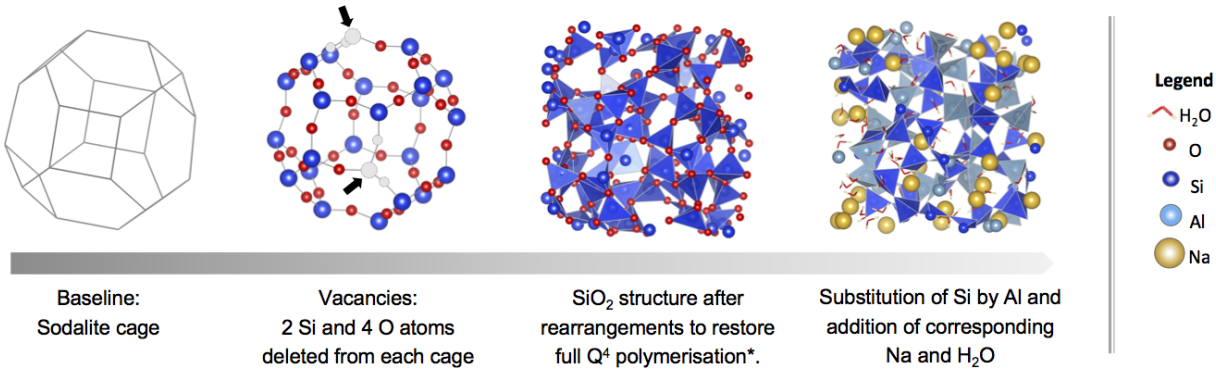

Figure 4.7: Simplified scheme of the construction process for a defective structure. All snapshots are obtained using VESTA [30]. *Some Si atoms are not visualised as tetrahedra due to the boundary conditions (after Lolli et al. [31]).

to create vacancies in the sodalite framework, and then the structure is equilibrated via MD simulations at P = 1 atm in the NPT ensemble for 0.01 ns at 300 K, followed by 0.01 ns in the NVT ensemble at 300 K. This process leads to a defective structure with some dangling oxygen atoms, and therefore individual atoms are slightly displaced by hand to restore the full Q^4 polymerisation. The NPT equilibration is then repeated (0.01 ns and T= 300K) and potential energy checked and found stable before the final MD simulation. Finally, MD simulations in the NVT ensemble are performed at T = 1000 K for 0.1 ns to enable a more effective relaxation of the structure, and reaching stabilisation of the structure before the introduction of Na and water molecules (energy minimisation is achieved, personal communication, April 2018). With this methodology some of the sym-

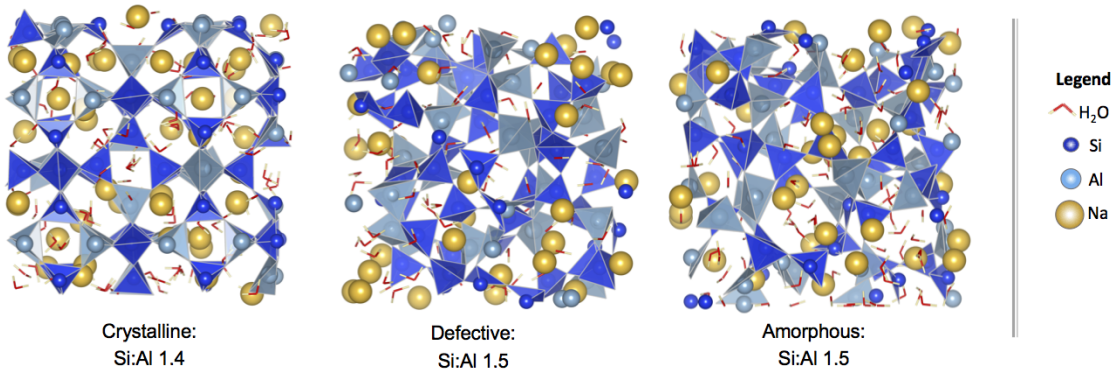

Figure 4.8: Structures with Si:Al = 1.4 - 1.5 and different degrees of disorder. The organisation of Al and Si tetrahedra is highlighted. All snapshots are obtained using VESTA [30] (after Lolli et al. [31]).

metry of the initial crystal is preserved, while at the same time some disorder emerges.

Seven model structures of N-A-S-H have been built varying the degree of order and the Si:Al ratio (see Table 4.1 in Section 4.1.2). Fig. 4.8 shows structures with comparable Si:Al ratio and an increasing level of disorder. Fig. 4.9 summarises the analysis process including the length of each simulation.

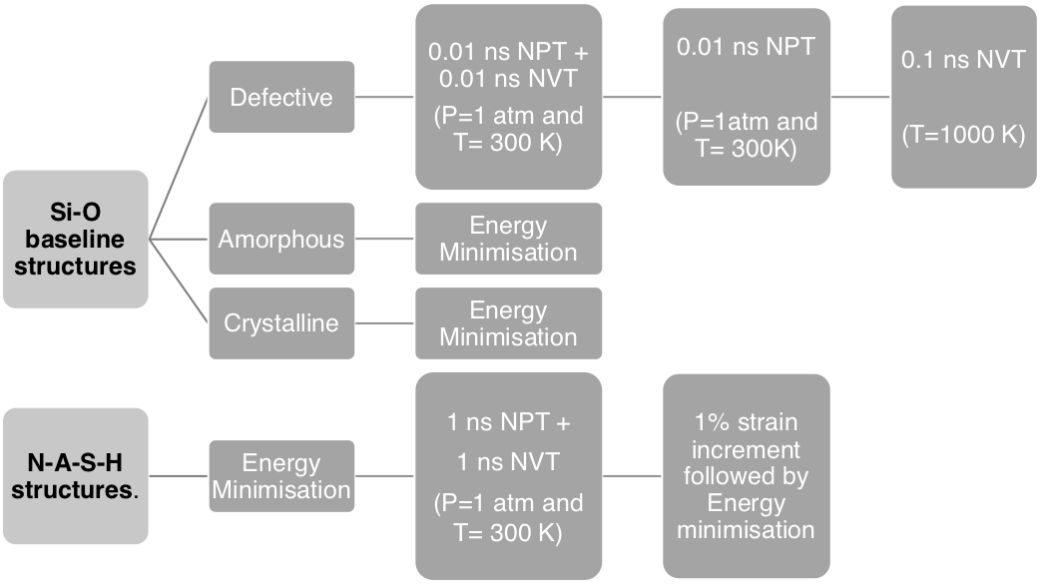

Figure 4.9: Schematic of the parameters used for each simulation.

4.2 Volume changes during geopolymer formation

The main aim of this Section is to present experimental techniques used to quantify volume changes at the early age of the geopolymerisation, and introduce theoretical models to better understand the experimental results by leveraging new information coming from the molecular model. In detail, Section 4.2.1 presents the materials used for casting geopolymer pastes, and Sections 4.2.2–4.2.4 describe several types of characterisation techniques: from imaging techniques to porosity measurements and reaction kinetics. Finally, Sections 4.2.5 and 4.2.6 report the methodology to study chemical expansion and autogenous shrinkage.

4.2.1 Materials

The materials used to prepare the samples are:

- *Metakaolin.* The metakaolin (MK) Argicem used in this study is sourced from ARGECO Développement (France), and it is a flash calcined metakaolin (see Section 2.1.1) characterised by a light pink colour as visible in Fig. 4.10, due to more than 3% in wt. of iron oxide as shown in Table 4.2. Table 4.2 lists the principal oxides composition of as per technical sheet, compared with literature data from Pouhet et al. [147], referencing the same metakaolin. Two additional analyses have been undertaken to characterise further this aluminosilicate source: particle size distribution and X-Ray Diffraction (XRD). The particle size distribution has been measured at Centro Ceramico (Bologna, IT) by a laser particle size

Figure 4.10: Picture of Argicem metakaolin [32].

Table 4.2: Comparison of the chemical composition of Argicem flash calcined metakaolin (% wt.).

	SiO_2	Al_2O_3	CaO	MgO	Fe_2O_3	TiO_2	SO_3	L.O.I.
ARGECO	93.16		0.36	0.04			0.14	1.63
Pouhet et al. [147]	68.10	24.10	0.91	0.22	3.73	1.14	0.03	1.83

analyser (Mastersizer 2000, Malvern Instruments, UK). The XRD has been carried out at the University of Bologna (IT) using an X-ray powder diffractometer PW 3710 (Philips) with Ni-filtered Cu Kα (λ=1.54 Å) radiation in the 5-80 ° 2θ range. The crystalline phases were identified by comparison with tabulate data on the JCPDS files. X-ray Diffraction is used to analyse the degree of crystallinity of a material. The relationship between the X-ray incident beam and the diffraction angle (characteristic of a specific crystalline structure) is governed by Eq. 4.9, also known as Bragg's law [148].

$$n\lambda = 2dsin\theta \tag{4.9}$$

where *n* is a positive integer, λ is the wavelength of the incident beam, θ is the angle between the wave vector of the incident plane wave and *d* is the distance between crystalline planes.

Fig. 4.11 shows the results of particle size distribution and X-ray Diffraction characterisation. The MK used in this work has an average particle size of 40 μm, hence it is coarser compared to other commercial metakaolins. Crystalline and therefore unreactive impurities are visible in the XRD spectrum: these include quartz (40% in weight), mullite (2% in weight), and anatase (1% in weight) [147].

- *Sodium hydroxide solution.* Sodium hydroxide solution at 8 M concentration is prepared dissolving sodium hydroxide pellets (supplied by Acros Organics, 98% extra pure) in ultrapure water. To obtain a concentration of 8 M, 320 g of sodium hydroxide pellets have been dissolved in one litre of solution. This quantity is obtained considering the molar mass of sodium hydroxide (39.997 g/mol) and the targeted concentration of the solution (8M). Eq. 4.10 relates molarity and volume of the solution.

$$Molarity = \frac{moles\,of solute}{volume\,of\,the\,solution} \tag{4.10}$$

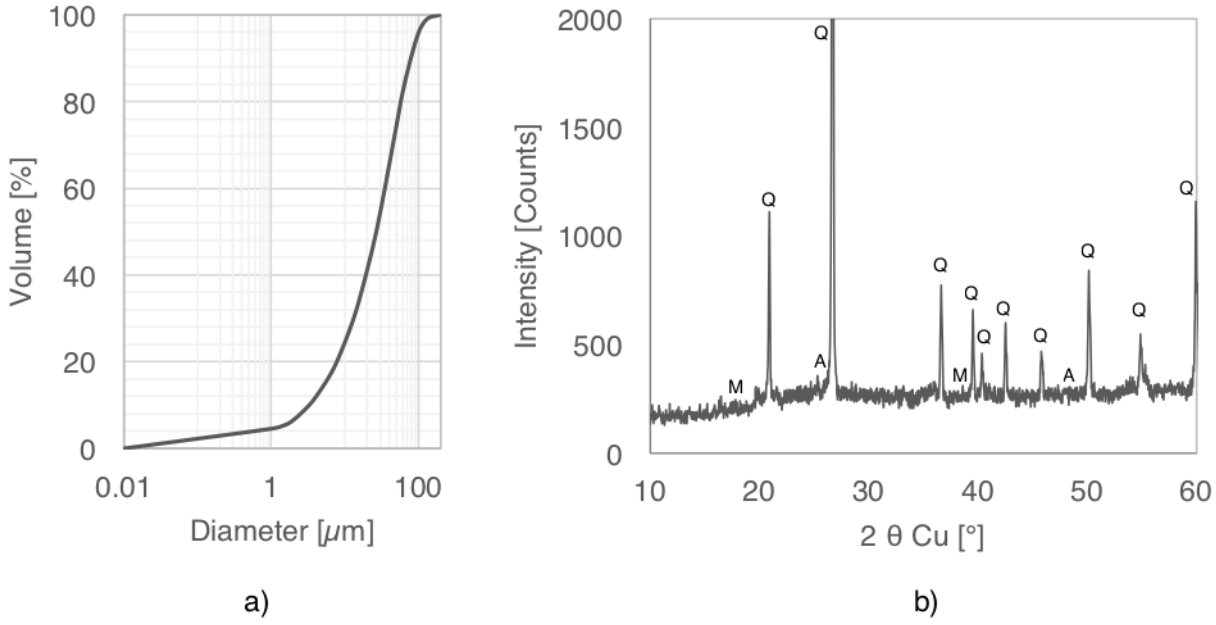

Figure 4.11: Characterisation of Argicem MK a) Particle size distribution b) Qualitative X-Ray diffraction, Legend: Q is quartz, M is mullite, A is anatase.

- *Sodium silicate solution.* Sodium silicate solution is provided by Ingessil S.r.l. (Italy) and has SiO_2:Na_2O = 1.71 molar ratio, Na_2O:H_2O = 0.93 molar ratio, and density at 20°C = 1.54 g/ml.

All the samples are prepared by mechanically mixing activating solutions and quantities of metakaolin according to the formulations described in Table 4.3. The samples are formulated in order to obtain Si:Al molar ratios of 1.5, 1.75 and 2 (see Table 4.3), and, for practicality reasons, the mixing procedure depends on the amount of material to be prepared. For small quantities (ca. 10 g of paste for calorimetry and chemical shrinkage test) the mixing procedure is carried out in a blender (Constant Speed Mixer, Fann Instrument Company). The two solutions are mixed one hour prior to the casting and then added to the metakaolin, mixing at 4000 rpm for 60 s and 10000 rpm for 30 s, eventually followed by a resting period of 150 s and final mixing at 10000 rpm for 30 s, obtaining a homogenous paste. For larger amounts (ca. 2 kg of paste for mechanical tests and drying shrinkage) the two solutions are mixed one hour prior to casting and then added to the metakaolin, mixing at low speed for 1 minute and then at high speed for 1 minutes, followed by 30 s of resting and final mixing for 1 minute. The size of the

sample depends on the test to be performed and more details will be provided in the Sections below.

Table 4.3: Percentage by weight of the components for the mix designs.

Si:Al	MK	Sodium silicate solution	Sodium hydroxide 8M	Water
1.5	54.5%	25.2%	19.1%	1.2%
1.75	53.1%	39.8%	5%	2.1%
2	49.3%	49.3%	0%	1.4%

4.2.2 Imaging characterisation techniques (SEM, TEM, HIM)

This Section outlines all the imaging techniques used to characterise the microstructure of geopolymers, and to visualise their pore structure at the sub-micrometer and nanometer level.

Scanning Electron Microscopy (SEM). SEM observations are performed on two sets of samples. Each set comprises samples with the three compositions in Table 4.3. The first set is cured at ambient temperature (23℃) and kept in sealed bags for 28 days prior to analysis. The second set is cured for 1 year at ambient temperature in sealed environment. The SEM analyses are conducted using a Zeiss EP EVO 40 microscope in Centro Ceramico (Italy), with 15kV acceleration voltage. Prior to the analyses the samples are pretreated with gold coating for 3 minutes to prevent charging of the specimen and to increase the signal to noise ratio.

Transmission Electron Microscopy (TEM). TEM imaging is performed on two samples with Si:Al 1.5 and Si:Al 2, and composition shown in Table 4.3. Samples are cured at ambient temperature (23℃) and kept in sealed bags for 13 days prior to the test. On the 14th day the samples are subjected to freeze-drying (for 24 hours) and crushed into a fine powder (mean size 60 μm). After this procedure, on the day of the test, the particles are suspended in water and a drop of this solution is placed on the sample grid holder. The grid is then dried and the sample holder inserted into the microscope. The analysis is conducted using a Philips CM100 Transmission EM at HV=100.0kV and a magnification of 92000x, available at EM Research Services (Newcastle University).

Helium Ion Microscopy (HIM). HIM images are produced with a Zeiss ORION NanoFab Helium Ion Microscope available at NEXUS (Newcastle University) on samples with Si:Al 1.5 cured at ambient temperature (23℃), kept in sealed bags for 28 days, and freeze dried prior to the test. HIM allows to achieve a similar magnification and resolution as the TEM, but obtaining clear images of the sample surface (like SEM), without overlapping planes like the TEM.

4.2.3 Porosity study (isotherms, MIP, TGA)

Several techniques have been used to analyse the pore structure of geopolymers at different scales. Water adsorption/desorption isotherms provide useful data regarding pores with size between 1 and 90 nm (nanoscale and mesoscale) and allow estimating the pore connectivity; Mercury Intrusion Porosimetry (MIP) captures pores between 5 and 200 nm (mesoscale and macroscale), finally Thermogravimetric Analysis (TGA) indicates how tightly water is bound to the structure.

Water adsorption-desorption isotherms. These tests measure changes in weight of the geopolymer paste due to changes of relative humidities, while keeping the samples at a constant temperature, here 23 ℃. Three types of pastes with Si:Al equal to 1.5, 1.75 and 2 are analysed one year after casting and the test is repeated twice for each Si:Al. It has been decided to undertake this test after one year, but because the pore structure of the sample is not changing considerably between early age (first week) and one year, the results obtained here will also be useful to discussion of the early age behaviours. Prior to the test, the pastes have been kept in sealed environment at 23 ℃. Two small discs are analysed for each mix design, weighing ca. 4 g each. The discs are placed in a sealed box with two foggers, and left there until their weight stabilises, to obtain a first measurement of mass at RH=100%. The saturated-surface dry (SSD) weights of the discs are measured after removing the excess surface water with a damp paper towel (M_{ssd}). The samples are then placed in a test environmental chamber at T=23 ℃ and RH=80%, which is the upper humidity limit of the environmental test chamber, and kept under constant humidity until the weight stabilises. The same procedure is applied decreasing the relative humidity in steps of 10% until RH = 10%, which is the lower limit of the test chamber. The weight of the sample is measured after each decrement of humidity. To obtain an additional measurement for RH$<$

10% the samples are placed in a sealed box containing silica gel until constant weight is reached. The adsorption curve follows the same procedure starting with the sample at RH$<$ 10%, and bringing it to 80% RH increasing the RH in steps of 10%. The whole procedure is repeated a second time to obtain a second desorption-adsorption isotherm, and capture any irreversible change of the pore structure that might have occured during the first cycle of drying and wetting. Finally, the samples are placed in an oven at 105℃ and kept there until the weight becomes constant, providing the dry mass (M_{dry}). The results of the experiments are plotted on a graph with the saturation degree on the vertical axis, and the RH on the horizontal axis. The degree of saturation is calculated with Eq. 4.11 in which M_t is the mass of the sample at an intermediate level of RH.

$$\mathrm{Saturation} = 1 - \frac{\mathrm{M_{ssd}} - \mathrm{M_t}}{\mathrm{M_{ssd}} - \mathrm{M_{dry}}} \tag{4.11}$$

The pore size distribution is then obtained applying the Kelvin-Laplace equation in Eq. 4.12. This equation relates the Kelvin pore radius (r_k) to the internal relative humidity of the sample (assumed to be at equilibrium with, and thus equal to the external RH), under the assumption of cylindrical pores.

$$\ln\frac{\mathrm{RH}}{100} = \frac{-2\gamma_\mathrm{w}\mathrm{V_w}}{\mathrm{r_k RT}} \tag{4.12}$$

where γ_w is the water surface tension (0.0738 N/m), V_w is the molar volume of liquid water (1.8 10^{-5} m^3/mol), *R* is the gas constant (8.314 J/molK), *T* is the temperature in Kelvin (296 K), and *RH* is the relative humidity in percentage. At T = 296 K, Eq. 4.12 predicts that it is possible to detect pore diameters ranging between 1 nm (RH =12 %) up to 90 nm (RH = 97 %). Fig. 4.12 shows the correlation between relative humidity and pore radius up to 30 nm, allowing a more detailed visualisation of the the mesopore range. It should be noted that between 95% RH and 97% the curve is asymptotical hence pores with radius between 20 nm and 45 nm corresponds to a narrow range of RH (2%). Additionally, the Kelvin-Laplace equation assumes equilibrium conditions but, in principle, neither adsorption nor desorption are at equilibrium. However, for materials with multi-scale porosity, like geopolymers, the adsorption curve is closer to equilibrium, since the desorption curve is affected by pore blocking effects [19]. Hence, in this manuscript, the adsorption curve is used to compute the pore size distribution.

The determination of the pore size distribution is achieved by applying a model developed by Masoero et al. [149], but considering the additional contribution of Lang-

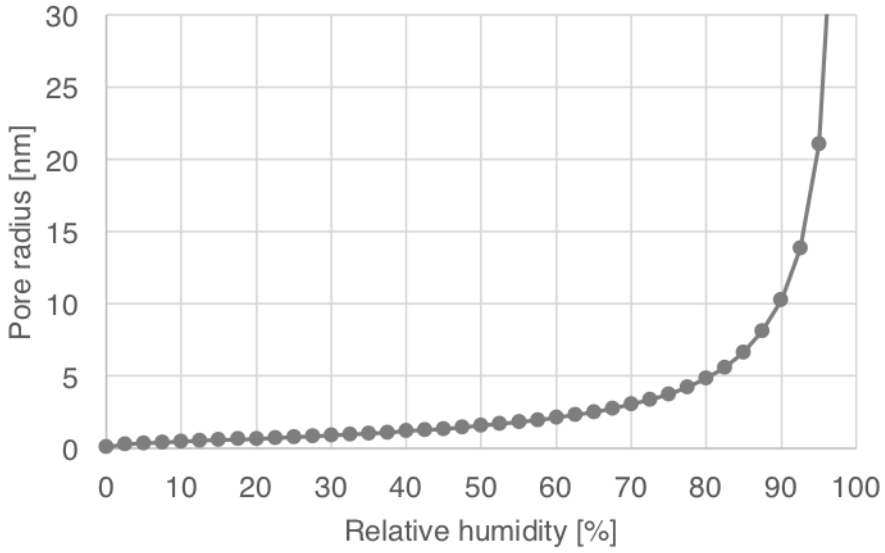

Figure 4.12: Relationship between internal relative humidity and pore radius, calculated with Kelvin-Laplace equation Eq. 4.12 at 296 K.

muir adsorption[1]. Masoero et al.'s [149] model incorporates as a constitutive law a sorption isotherm that is characteristic to adsorption and desorption within the molecular structure of C-S-H in traditional cements. This isotherm was obtained by molecular simulations of water adsorption in C-S-H model structures. Analogous results are not available to date for geopolymer pastes, thus this work employs the same characteristic isotherm for C-S-H at the sub-nanometre level as a first approximation of the sorption isotherm that might be characteristic of geopolymer at the molecular scale (i.e. pores below 1 nm). Hence, the pore size distribution obtained for geopolymers from the analysis of the isotherms should be considered as a first approximation where the water content at the molecular scale is accounted for only in a qualitative manner. In the model proposed by Masoero et al. [149] the mesopores (with size between 5 nm and

[1]Langmuir theory considers the contribution of one water layer on the surface of the pore, which is excluded from the calculation of the Kelvin radius. Langmuir is often used as an alternative to BET adsorption, which considers the formation of multiple adsorbed layers but neglects interactions between water molecules on the same layer, resulting in more precision at high humidity and less at low humidity. In a material with multiscale porosity reaching down to the the nanoscale, the contribution of adsorbed water layers to the overall sorption prevails on that from capillary condensation only at small humidity [19], hence this work employs the Langmuir rather than the BET adsorption theory.

50 nm as per IUPAC) are divided in two categories, each having a characteristic pore size distribution, the first with small mesopores (pertaining to the so-called "dense domain" of the C-S-H) and the second with larger mesopores (pertaining to the "loose domain" of the C-S-H). The same categorisation is employed here for geopolymers. For geopolymer paste with Si:Al 1.5, the characteristic pore size in the dense domains, is considered equal to 3 nm, value obtained from published literature data [10]. The characteristic pore size in the loose domains is instead determined from new MIP results for Si:Al 1.5 that will be shown later in this work (see Fig. 5.19), leading to a size of 10 nm. The model requires also an additional parameter called packing fraction, η=1-ϕ, where ϕ is the pore volume fraction in the gel (i.e. the total volume of mesopores divided by the total volume of gel, excluding pores larger than the mesopores and considering pores that are smaller than 3 nm as part of the solid volume). The packing fraction considered for geopolymers and resulting from MIP is equal to η=0.69, which is an approximated value since MIP data can be considered accurate only for pore sizes larger than 5 nm.

Mercury Intrusion Porosimetry (MIP). This technique provides information on the open porosity[2] for pore sizes larger than 5 nm, giving data on pore size distribution and on the average pore size of the sample. The tests have been carried out at the University of Bologna (IT) and consists of two steps, a first analysis of macropores (Macropores Unit 120, Fisons Instruments), and a second one of mesopores (Porosimeter 2000, Carlo Erba Strumentazione). The samples used for the test are obtained from the internal part of cylindrical samples and cut into a polygonal shape with a mass of *ca.* 1 gram. Prior to the MIP test, the samples are freeze dried for 24 hours in order to remove free water that may obstruct the pores and cause issues while creating vacuum for the test. Mercury is then forced into the pores by applying an external pressure, since it would not spontaneously wet and penetrate the sample by capillary action. The required pressure is inversely proportional to the pore diameter, therefore lower pressure are needed to characterise macropores, whereas the pressure reaches up to 2000 bar when sampling mesopores. Eq. 4.13, known as Washburn equation [150], describes this relation.

$$r_{pore} = \frac{-2\gamma cos\theta}{P} \tag{4.13}$$

where γ is the mercury surface tension (480 mN/m), θ is the mercury contact angle of

[2]The fraction of the pore volume connected with the external environment

intrusion (141.3°) and *P* is the mercury pressure.

Two types of paste samples with Si:Al equal to 1.5 and 2 are analysed with MIP at 5, 7 and 14 days after casting.

Thermogravimetric Analysis (TGA). Thermogravimetric Analysis (TGA) has been performed at the Georgia Institute of Technology (USA) on a Hitachi Thermal Analysis System (TG/DTA7300) with purge gas flow rate of 100 cm^3/min and the following heating profile. During the tests, the temperature is set to increase from 40℃ to 1000℃ with heating rate of 10℃/min, followed by 5 minutes at 1000℃. Cement paste samples are usually chemically pretreated with the main intent of stopping hydration, but in this case the samples are not subjected to chemical pretreatment since the test is performed one year after casting on fully reacted geopolymers. The samples are instead subjected to thermal pretreatment in the TGA at 25 ℃ for 15 minutes, followed by 75 minutes at 40 ℃ under stream of N_2 gas to prevent carbonation. A temperature of 40 ℃ has been chosen for the pretreatment, because some phases, such as C-S-H and N-A-S-H, start to lose bound water at temperatures just above 40 ℃. Three types of paste samples with Si:Al equal to 1.5, 1.75 and 2 are analysed one year after casting. During this time the pastes are kept in sealed environment at ambient temperature (23 ℃) and used for the autogenous shrinkage test. Prior to TGA testing, the samples are crushed and sieved in two steps, first through a sieve < 300 μm, then through a sieve < 75 μm. The results have been analysed plotting the mass loss, considered as water loss, versus temperature. The water in the sample has been qualitatively identified based on the temperature ranges in which the mass loss is most significant.

4.2.4 Reaction kinetics by calorimetry

The heat evolution of each geopolymer, during the geopolymerisation reaction and across setting, is analysed via isothermal calorimetry tests at the Georgia Institute of Technology (USA). The measurements are performed in a TAM Air isothermal conduction calorimeter (Thermometric TA Instruments) at 25 $^\circ$ C with heat flow rate recorded every 10 seconds. Two samples for each mix design (see Section 4.2.1 for formulations) have been analysed. This test monitors the heat released during the reaction, which is typically assumed to be proportional to the rate of the reaction (here, geopolymerisation). The rate and cumulative heat per gram of metakaolin are plotted versus time.

4.2.5 Chemical expansion: new experiments and modelling

Several macroscopic properties of cementitious materials, such as strength development and crack formation, are governed by the reaction rate at early age. Autogenous volume changes (discussed in Section 4.2.6) are the ultimate result of chemical reactions happening at the early age, reactions that cause volume changes between reactants and products. For traditional Portland cement the volume of the products is smaller than the volume of the reactants, causing the so-called “chemical shrinkage”, see Section 2.1.4. For geopolymers the literature lacks experimental data and for this reason this Section presents the methodology to measure for the first time the chemical shrinkage (or expansion) of geopolymer pastes.

Experimental methodology. Volume changes resulting from the geopolymerisation reaction have been measured following ASTM C1608 - 17 standard [96] and the setup is shown in Fig. 4.13.

Four geopolymer samples are prepared for each mix design and analysed in two batches. The experiment procedure is the following:

1. Geopolymers paste is carefully poured into a glass vial (0.025 l), reaching a height of ca. 10 mm and manually vibrating the sample to remove air bubbles.

2. The mass of the paste and the liquid to metakaolin ratio are recorded (indicated as l/mk).

3. Paraffin oil is added to the glass vial filling it to the top. ASTM C1608 - 17 standard [96] recommends the use of water instead of paraffin oil to quantify the volume change during the hydration of a cement paste. The choice of paraffin oil instead of water for geopolymers is because the ions in the activating solution would diffuse into the additional water, causing a decrease of the pH and thus a change of reactivity, affecting the dissolution of the metakaolin. On the contrary, oil does not interfere with the geopolymerisation reaction.

4. A rubber stopper with an inserted capillary tube is placed to seal the glass vial and further sealed with a layer of cyanoacrylates adhesive.

5. A drop of coloured paraffin oil, less dense than the transparent paraffin oil (to float atop) is placed on the surface of the capillary tube. The different color allows an easy reading of measures on the capillary tube.

6. The sample vials are placed into a constant temperature water bath at 23℃, and a camera is set to take a picture every 10 minutes for the first 6 hours, then every 30 minutes for further 2 days until conclusion of the experiment. The measure consists in reading the value corresponding to the meniscus in the capillary tube, and calculating the volume change between two successive measures. The first measure is after 60 minutes, so-called h(60 min), from the moment in which metakaolin and activating solution are in contact, to allow thermal equilibration of the sample vial with the water bath. The exposed surface of the thermal bath is covered with table tennis balls to create a layer of air insulation between water and laboratory environment.

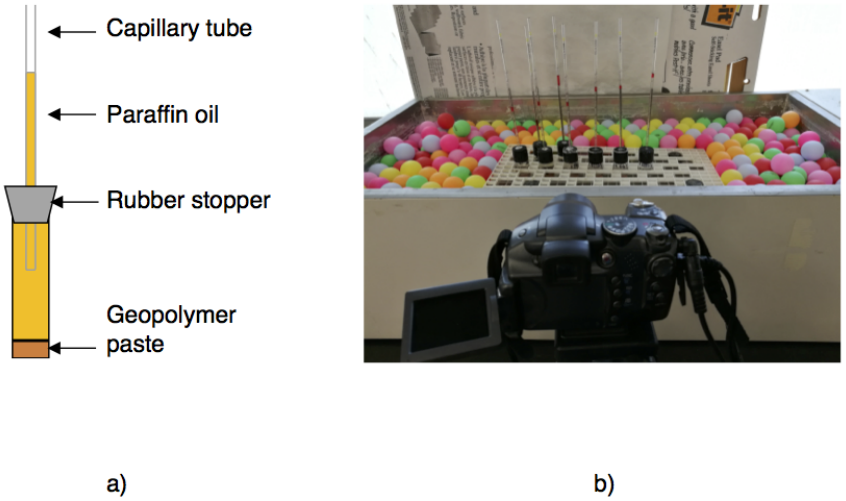

Figure 4.13: a) Description of the vial experimental setup b) Laboratory setup.

This method allows measuring volume changes with a resolution of 10 μl, which is the volume corresponding to each mark on the capillary tube. Considering an average metakaolin content in the paste of ca. 10 g, a change in reading of one mark corresponds to a chemical shrinkage or expansion of 1μl/g MK. This resolution is expected to be appropriate for cementitious materials, since typical values of chemical shrinkage for PC are in the range of 0.02 ml/g cement after 24 hours [151].

The chemical shrinkage (CS) data are then processed calculating the volume change

per gram of metakaolin at time t, applying Eq. 4.14 and Eq. 4.15.

$$M_{MK}[g] = \frac{M_{vial+paste} - M_{empty\ vial}}{1 + \frac{l}{mk}} \tag{4.14}$$

$$CS(t)[ml/g_{MK}] = \frac{h(t) - h(60\ min)}{M_{paste}} \tag{4.15}$$

In Eq. 4.14 M_{MK} is the mass of the metakaolin, $M_{vial+paste}$ is the mass of the glass vial plus the mass of the paste, $M_{empty\ vial}$ is the mass of the empty glass vial and l/mk is the ratio between liquid and metakaolin. In Eq. 4.15 $h(t)$ is the oil level in the capillary tube at time t measured in volume units (ml), hence each gradation in the capillary tube represents a volume change.

Theoretical model. The experimental results on geopolymer pastes, presented in the later Section 5.2.4, will indicate chemical expansion (not shrinkage, as usual in traditional calcium-based cements), meaning that the volume of the reaction products is greater than the volume of the reactants. Understanding this expansion requires an analysis of the specific volume (or molar volume) of reactants and products in the geopolymerisation reaction, as functions of the degree of reaction (from here onwards called DoR). The molar volume (MV) of reactants and products as a function of the DoR, is obtained by applying Eq. 4.16, which requires data on the molecular weight (MW) and density of each component.

$$\mathrm{MV}[\mathrm{cm}^3/\mathrm{mol}] = \frac{\mathrm{MW}[\mathrm{g/mol}]}{\mathrm{Density}[\mathrm{g/cm}^3]} \tag{4.16}$$

The calculations that follow assumes the activation of 1 mole of metakaolin, therefore all the other components of the geopolymerisation reaction, in Fig. 4.14, are normalised accordingly. As described in Section 4.2.1 the metakaolin used in the experiments is a flash calcined metakaolin with 45% in weight of unreactive material (mainly quartz, with traces of mullite and anatase), leaving a 55% in weight of reactive part.

To determine the molar ratio between reactive metakaolin and inert metakaolin a first approximation is introduced: that the inert component of metakaolin is approximated as quartz, with chemical formula SiO_2 and with molar weight of 60.08 g/mol. The reactive material is instead considered as pure metakaolin, with chemical formula $Al_2O_3 \cdot 2\,SiO_2$ and molar weight of 222.12 g/mol. The moles of quartz and metakaolin are calculated applying Eq. 4.17, obtaining that, for the composition in Fig. 4.14, for

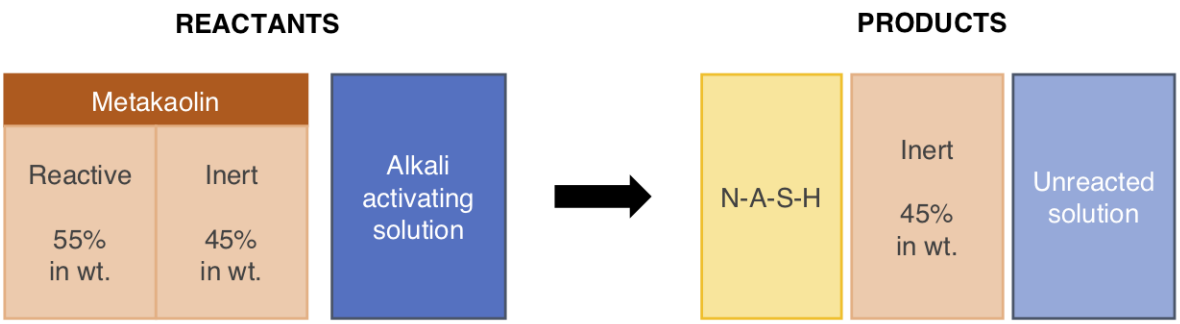

Figure 4.14: Schematic of the system considered for the geopolymerisation reaction.

each mol of metakaolin there are 3.02 mol quartz.

$$\text{Moles[mol]} = \frac{\text{M[g]}}{\text{MW[g/mol]}} \tag{4.17}$$

A second hypothesis concerns the composition of the main reaction product, the N-A-S-H. The methodology here will be explained referring to N-A-S-H with Si:Al 1.5 only, which will suffice to explain the observation of chemical expansion. Nevertheless, the theory presented here is equally applicable to any other Si:Al ratio, and the effect of changing Si:Al ratio will indeed be discussed in the results Section later on. A parameter β is introduced here to assess the impact that different water contents may have on the N-A-S-H structure. β is defined as the H_2O:Na molar ratio, and in this study it has been considered as variable between 0 and 3.

Under these hypotheses, the chemical formula of the N-A-S-H has H_2O:Na=β and Si:Al=1.5. The chemical reaction which represents the reaction of metakaolin to produce N-A-S-H, as per Fig. 4.14, is:

$$\begin{aligned} &1\mathrm{Al_2O_3 \cdot 2\,SiO_2\,(mk)} + 1\mathrm{Na_2O \cdot 0.87SiO_2 \cdot 12.3H_2O\,(solution)} + 3.02\mathrm{SiO_2(quartz)} \longrightarrow \\ &2\mathrm{Na(AlO_2 \cdot 1.5SiO_2)} \cdot \beta\mathrm{H_2O\,(N{-}A{-}S{-}H)} + (12.3 - 2\beta)\mathrm{H_2O\,(solution)} + 3.02\mathrm{SiO_2(quartz)} \end{aligned} \tag{4.18}$$

Another parameter α is then introduced to account for the DoR of the geopolymerisation; when α is 0 the DoR is equal to 0%, meaning that the reaction has not started yet. When α=1 the reaction is complete. At any given stage of the reaction (i.e. for any α between 0 and 1) the composition of the paste is given in Table 4.4.

Table 4.4: Summary of the parameters used to calculate volume needed for the chemical expansion (% wt.).

Material	**No. of moles**	**Density [g/cm^3]**
N-A-S-H	$\alpha \cdot [2\,Na \cdot (AlO_2 \cdot 1.5\,SiO_2) \cdot \beta H_2O]$	Table 4.5
Unreacted sol.	$[(1-\alpha) \cdot (1\,Na_2O \cdot 0.87\,SiO_2 \cdot (2\,\beta \cdot H_2O)] \cdot (12.3-2\,\beta)H_2O$	Fig. 4.16
Unreacted MK	$(1-\alpha) \cdot\ Al_2O_3 \cdot 2\,SiO_2$	2.55
Inert material	$3.02\,SiO_2$	2.65 [152]

Converting the molar relationships in Table 4.4 to volume changes requires consideration of densities. The density of the reactive metakaolin is 2.55 g/cm^3 obtained subtracting the inert mass, with density of 2.65 g/cm^3 typical for quartz, from the total mass of metakaolin, with density 2.59 g/cm^3 as per technical data sheet from the producer. The densities of the N-A-S-H and of the activating solution, instead, are more difficult to estimate.

The density of the N-A-S-H gel is taken from the defective molecular model described in Section 4.1. This means that densities for a range of Si:Al ratios and water contents can be read directly from the molecular model, which also allows checking whether the structure is expected to keep or lose its integrity at any given chemical composition. Six structures have been created varying β from 0 to 3, but maintaining Si:Al 1.5 constant, to consider the contribution of structural water content to the chemical expansion. Specifically, the values are β = H_2O:Na=0, 0.5, 1, 1.5, 2, 2.5, 3, and for each structure the density has been calculated. β=0 is experimentally impossible to reach, but this extrapolation has been useful to determine a theoretical bound value for density. For each structure the density is calculated after equilibrating the structure at P = 1 atm and T = 300 K via 0.1 ns of molecular dynamics in the NPT ensemble, followed by 0.1 ns in the NVT ensemble, to verify the stability of potential energy and pressure. All simulations are performed using LAMMPS [137] with Verlet time integration scheme and integration timestep of 0.1 fs. Density results are reported in Table 4.5 and the snapshots of three structures with different water contents are shown in Fig. 4.15.

The density of the activating solution instead, has been determined experimentally measuring its weight and volume, this latter read from a graduated cylinder, and considering the stoichiometric proportions in Table 4.3. The result is 1.36 g/ml. During the geopolymerisation reaction the ions in the solution are consumed until the solution

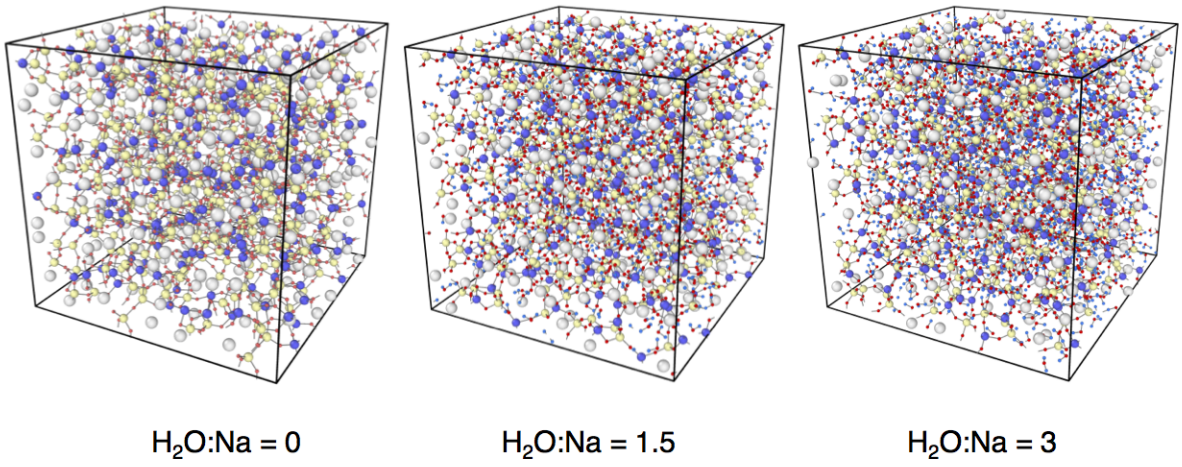

Figure 4.15: Snapshots of three different N-A-S-H structures with Si:Al =1.5 and water content variable from H_2O:Na= 0 to 3 molar ratio. Snapshots obtained with OVITO [33].

Table 4.5: Density values of the molecular model as a function of the structural water content.

H_2O:Na ratio	Density [g/cm^3]
0	2.998
0.5	2.30
1	2.288
1.5	2.253
2	2.225
2.5	2.227
3	2.198

reaches a theoretical concentration of zero (pure water with density 1 g/ml). To limit the number of assumptions, it has been decided to measure the density of the solution experimentally as a function of α, creating solutions with different concentrations that represented the activating solution at different α (0, 0.5, 0.75, 1), i.e. after a certain fraction of dissolved ions is expected to have been consumed by the reaction already. The results are shown in Fig. 4.16, as black dots. The solid curves in Fig. 4.16 are instead calculated theoretically, considering the density of the stoichiometric amounts of the sodium silicate solution from Ingessil S.r.l. (density from data sheet) and of the 8M NaOH solution. The equations used to plot the density curves are:

$$\rho_{sol} = \frac{M_{sol}}{V_{sol}} \tag{4.19}$$

$$M_{sol} = (1-\alpha)M_{NaSi} + (1-\alpha)M_{NaOH} + (1-\alpha)M_{\mathrm{H_2O}} + [\alpha m_{tot} - 2(\beta\alpha)]MW_{H_2O} \tag{4.20}$$

Here simplified as:

$$M_{sol} = x + y + z + k \tag{4.21}$$

$$V_{sol} = \frac{x}{\rho_{NaSi}} + \frac{y}{\rho_{NaOH}} + \frac{z+k}{\rho_{H_2O}} \tag{4.22}$$

where in the total mass of the solution (M_{sol}): M_{NaSi} is the mass of the sodium silicate solution, M_{NaOH} is the mass of the sodium hydroxide solution, $M_{\mathrm{H_2O}}$ is the mass of the water added to the mix design, m_{tot} the sum of moles of water from the sodium hydroxide solution, the sodium silicate solution, and the added water, and $MW_{\mathrm{H_2O}}$ = 18.02 g/mol is the molar mass of water. In the total volume of the solution (V_{sol}): ρ_{NaSi} is the density of the sodium silicate solution, ρ_{NaOH} is the density of the sodium hydroxide solution, $\rho_{\mathrm{H_2O}}$ is the water density.

At intermediate α, the density of the solution is expected to change non-linearly between the limit values at α 0 and α 1 since both the mass of the solution and the volume are function of α. From Eq. 4.19, when α=0 the density of the solution is 1.34 g/ml, while for α=1 the density is 1 g/ml meaning that all the Na and Si atoms in solution reacted to form N-A-S-H, hence only water remains available. It is possible to notice that the experimental value and the theoretical one for H_2O:Na=3 are comparable. Therefore, this theoretical approach (which is valid for any α, thus more general), has been applied to study the variation of the density of the activating solution for the geopolymerisation reaction assuming different N-A-S-H products.

To summarise, by using the parameters in Table 4.4 combined with the density values at the molecular scale, in Table 4.5, and the density of the solution, in Fig. 4.16, it is possible to predict the expected chemical shrinkage or expansion of geopolymers as a function of the degree of reaction.

4.2.6 Autogenous shrinkage

Autogenous shrinkage is defined as the dimensional change occurring when a cement paste hydrates in sealed conditions and at constant temperature. Autogenous shrinkage resulting from the geopolymerisation reaction has been measured following ASTM C1698 - 09 standard [34], with the autogenous strain measured from the time of

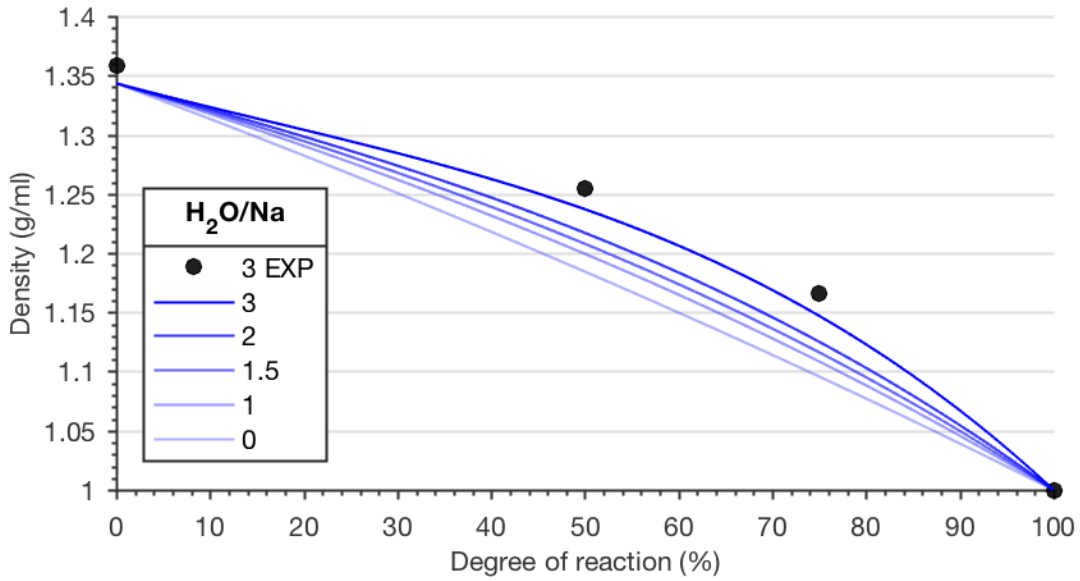

Figure 4.16: Density values of the activating solution during the geopolymerisation reaction, and as a function of the hypothesised content of water in the skeletal structure of the N-A-S-H.

final setting until a specific age. For the experiments in this dissertation measurements have been taken until 35 days after setting. Four specimens have been tested for each mix design, and the results have been averaged. The pastes are prepared according to the methodology described in Section 4.2.1 and poured into corrugated tubes (in Fig. 4.17a.), 420 mm long and with an outer diameter of 29 mm, made with flexible plastic that allows expansion and contraction in the longitudinal direction. The tubes are closed with plugs to ensure sealed conditions. Due to the flexibility of the tube, the casting procedure can be complex since it is necessary to avoid the formation of entrapped air. Hence, the corrugated tube has been placed into a graduated cylinder of approximately the same length, inclined and continuously rotated while being filled and vibrated on a vibrating table. The tube is filled to approximately 10 mm below the top end and then the paste inside the tube is gently compressed to bring it in contact with the plug before sealing the corrugated tube. All the samples and dilatometer, the latter used as a reference bar for each measure of sample length (see Fig. 4.17a.), are kept in a controlled environmental chamber at 23℃ and RH=50% for the entire duration of the test. After casting, the specimens are left untouched until final setting, when the first measure of sample length is taken (L_0). Table 4.6 reports the final setting times for each mix design.

Before each measurement the dilatometer is calibrated using a stainless steel ref-

Table 4.6: Final setting time for the geopolymer pastes.

Si:Al	Final setting time [hours]
1.5	2
1.75	4
2	7

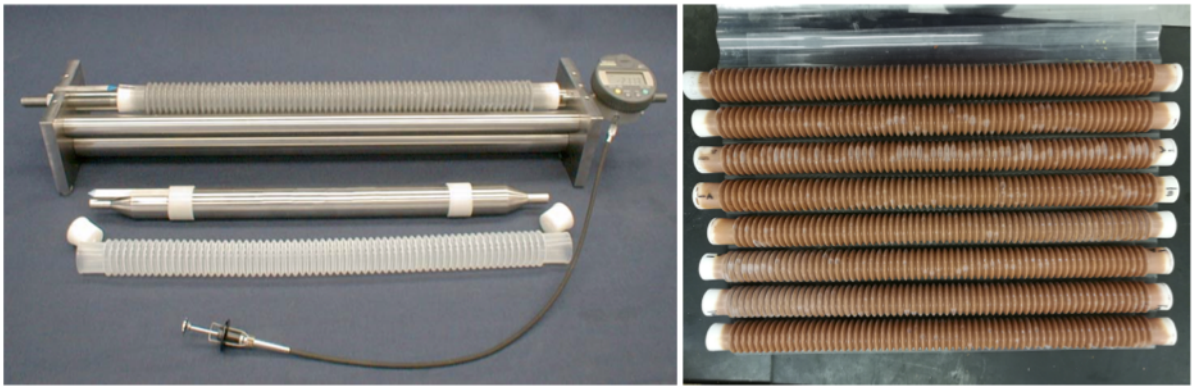

a) b)

Figure 4.17: a) Experimental setup for autogenous shrinkage test (after ASTM C1698 - 09 [34]) b) Picture of the samples.

erence bar and samples are marked in order to place the specimens in the same orientation during each measurement. Autogenous strain is then calculated as:

$$\epsilon_{autogenous}[\mu m/m] = \frac{L_t - L_0}{L_0} 10^6 \tag{4.23}$$

where L_t is the length of the specimen at time t.

Autogenous shrinkage test is undertaken at the time of final setting as indicated in the ASTM C1698 - 09 [34], avoiding the superposition of effects caused by chemical shrinkage. In fact, chemical shrinkage is calculated in the first moment of the reaction, since it is due to the chemical reaction between metakaolin and activating solution. Furthermore chemical shrinkage is tested with an apparatus that allows to read volume variations of 10 μl, while autogenous shrinkage is calculated as a length change. Hence the apparatus for the autogenous shrinkage test consists of a corrugated tube

which is 420 mm long, length that enable to read relative length changes in the order of μm.

4.3 Understanding ageing: a first approach

This Section introduces the methodology applied for long term experimental durability tests such as creep and drying shrinkage, as well as the construction of a model of N-A-S-H at the mesoscale level. Mesoscale models have been used in the cement literature to model long term deformations, as described in Section 2.2.1. In this Section a mesoscale model is developed for the analysis of the mesoporous network of geopolymers, which the experiments show to have significant impact on the long-term mechanics of these materials.

4.3.1 Long term behaviour: drying shrinkage and creep

Three samples for each Si:Al ratio (mix described in Section 4.2.1) have been cast and tested for the creep test (two samples used as control specimens, and one test for creep). The samples, shown in Fig. 4.18, are cylindrical measuring 80 mm in length and 39 mm in diameter. After casting, the specimens are placed inside a sealed container for 2 days, to prevent excessive moisture loss. Then the samples are demoulded and kept in sealed bags to avoid fast loss of evaporable water for 28 days. After the total 30 days of curing, the surfaces of each sample are flattened with a circular saw to ensure a uniform distribution of applied load during the creep test. Additionally, drying shrinkage at constant relative humidity has been tested at the University of Bologna.

Long-term test in environmental conditions. The reference standard for creep testing, BS ISO 1920-9:2009 [99], states that to consider possible dimension changes not caused by the applied load for the creep test, one sample has to be kept unloaded as a control specimen. Hence, two samples for each Si:Al (1.5, 1.75, 2) are tested for drying shrinkage in ambient conditions (RH ca. 50% and T=23℃), as part of the creep test described in the following paragraph. The top and bottom surfaces of each samples are covered with duct tape to replicate the same conditions of exposure of the creep samples. Weight loss and length change are tracked for 10 months at the Structural laboratory of the Georgia Institute of Technology (USA); for each sample,

measures are taken three times and the average is calculated. Data are then analysed plotting length change versus time. Furthermore the drying shrinkage strain (ϵ_{DS}) is calculated as:

$$\epsilon_{DS} = \frac{L_f - L_0}{L_0} \tag{4.24}$$

with L_f and L_0 being the final length and initial length of the sample.

Creep. One sample for each Si:Al ratio (1.5, 1.75, 2) has been tested for creep, after the initial 30 days of curing described previously. Creep tests involved long-term monitoring, over 10 months, and one loading frame for each sample. For this reason only three samples were tested. The setup is described in Fig. 4.18 and involves a spring loaded system that is able to keep constant load for the whole duration of the test. The applied load is checked periodically (every week for the first month, then once a month). The load is initially applied and then corrected during the test (to keep it constant) using a hydraulic load cell connected to a hydraulic pump and placed on the plate on top of the specimen (the plate weight is considered as part of the applied load). After each correction of the load, the bolts above the steel plate are tightened to keep the load constant, so that the load cell can be removed until the next time that the load is checked. The bolts below the plate are instead kept loose. In this setup the only plate that is moving during the test is the plate in between the springs and the sample, due to the creep deformation. Hence, the creep displacement is measured with a Westward dial gauge attached to the steel plate at the bottom of the specimen, and measuring the distance between the plate underneath the springs and the steel plate at the bottom of the specimen. The compressive load applied during the creep test is taken as one third of the average failure load at 30 days, on cylindrical samples cast on the same day as the creep specimens.

On the day of first loading, the initial displacement is immediately recorded, providing the so-called elastic strain $\epsilon_{elastic}$. During the whole duration of the test the displacement of the creep specimen is read off the dial gauge and, on the same date, the length of the control specimens is measured with a calliper. The frequency of the measurements is chosen as per BS ISO 1920-9:2009 [99]: at 2 and 6 hours after loading, then once a day for a week, then once a week for a month, and then once a month. The test is carried out in a controlled environment, at RH ca. 50% and T=23°C, in the Structural laboratory of the Georgia Institute of Technology.

Based on the collected data, the basic creep strain ϵ_{creep} is obtained by subtracting

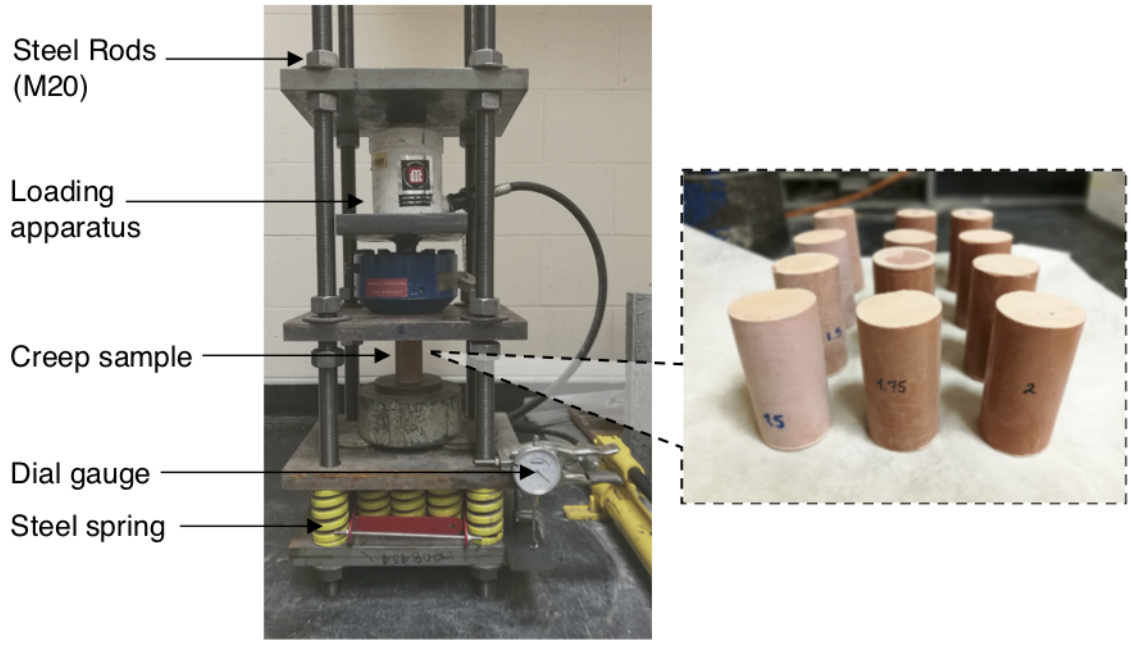

Figure 4.18: Setup for the creep test.

drying shrinkage strain ϵ_{DS} (measured on the control sample) and the initial elastic strain $\epsilon_{elastic}$ from the total strain ϵ_{tot} :

$$\epsilon_{creep} = \epsilon_{tot} - \epsilon_{DS} - \epsilon_{elastic} \tag{4.25}$$

In addition, creep modulus (*C*), creep compliance (*J*) and creep coefficient (ϕ) are calculated to quantitatively compare results from different mix designs.

$$\epsilon_{creep} = \frac{\sigma}{C}\ln(t) \tag{4.26}$$

$$J = \frac{\epsilon_{creep}}{\sigma} \tag{4.27}$$

$$\phi = \frac{\epsilon_{creep}}{\epsilon_{elastic}} \tag{4.28}$$

where σ is the applied stress. In Eq. 4.26 *C* can be calculated from the gradient of ϵ_{creep} plotted versus ln (t), and dividing said gradient by the stress σ.

Drying shrinkage at constant relative humidity. Four samples of metakaolin geopolymer for each Si:Al ratio (1.5, 1.75, 2) are prepared according to the mix design described in Section 4.2.1, and are subjected to different drying conditions at constant ambient temperature (T=23°C). The samples are cast on prismatic moulds (25x25x285 mm), as shown in Fig. 4.19 b, and equipped with a gauge stud at each end. The first

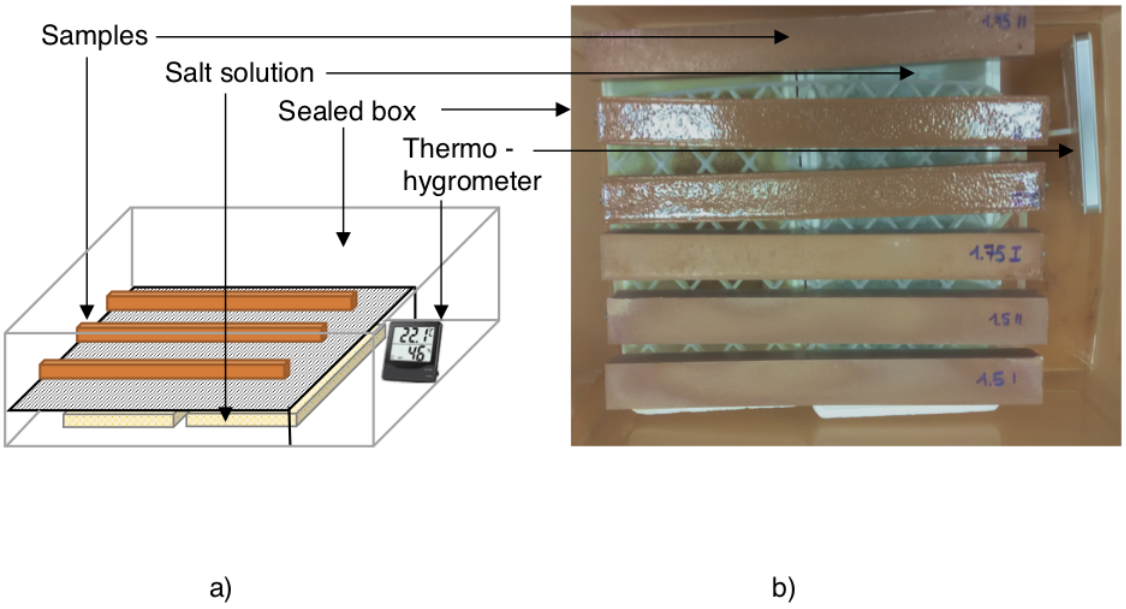

Figure 4.19: a) Setup for the drying shrinkage test b) Picture of the samples in the sealed box.

two days after casting consist in curing the samples at environmental conditions in a sealed box (RH=50% and T=23°C) prior to demoulding. The specimens are then placed into two sealed boxes (two samples per type in each box), following the setup displayed in Fig. 4.19. The relative humidity in each box is regulated with drying salt and monitored with a digital thermo - hygrometer. The first box contained silica gel, to set the internal humidity to less than 10% (very dry conditions; the hygrometer cannot measure below 10% RH), while the second box contained potassium carbonate, setting the RH to ca. 40% [153]. The samples are placed on a grid to allow uniform drying conditions. Weight loss and length change have been tracked for more than 50 days following ASTM C490/C490M-11 [97]. This test has been carried out at the University of Bologna.

4.3.2 Mesoscale model of the N-A-S-H gel

The results of the creep and drying shrinkage tests will show that an important role is played by the microstructure and pore structure of the samples with different chemical compositions. The pore structure cannot be analysed using the molecular model presented in Section 4.1, because the molecular model covers length-scales only up to 1-2 nm, whereas the pore networks develops over hundreds of nanometres. This Section therefore presents the methodology to construct a model that can simulate the structure and mechanics of geopolymers at the scale of ca. 500 nm, as previously done in the field of C-S-H mesoscale modelling (see Section 2.2.1). A way to construct such a model is to simulate the aggregation of polydisperse nanoparticles, that interact mechanically via effective potentials obtained from molecular simulations. An advantage of this approach is that chemistry-dependent properties can be extracted from the molecular model presented in Section 4.1, and the resulting structure and properties at the larger mesoscale will reflect the impact of the molecular structure. This Section has been the focus of a conference paper titled *Towards a mesoscale model of geopolymers: interaction potential from the molecular scale* [35], and presented at the EURO-C conference in February 2018.

Mesoscale model construction. The mesoscale model is developed using the software LAMMPS [137]. The starting point is an empty simulation box of predefined dimensions, into which particles are added randomly. The range of possible particle sizes is chosen to be consistent with the characteristic size of solid domains observed by microscope images, presented in Section 2.1.4. As a result, the N-A-S-H gel is modelled as an aggregate of nanoparticles with sizes ranging from 5 to 50 nm, leading to a resulting network of mesopores whose sizes range from 2 to 50 nm. The process to construct the model structures, such as the one in Fig. 4.20, is the following:

1. Several hundreds of particles characterised by one specific size (from here onward defined as *group*), are added instantaneously and randomly in the empty simulation box. The filling procedure is repeated for group of particles with different sizes: this differs and turns out to be computationally more efficient than other space-filling algorithms where particles are added one at a time [154, 155].

2. Each filling step is followed by energy minimisation using the conjugate gradient method (Polak-Ribiere version) implemented in LAMMPS [137]; particle interactions are explained below.

3. When the system is sufficiently dense to be mechanically stable (viz. not to collapse into a denser aggregate if NPT equilibration at constant pressure is carried out), the configuration is further stabilised by applying a pre-compressive stress to the box, followed by energy minimisation. The stress is then released by expanding the simulation box until zero pressure is recovered.

4. The entire process (partial space filling, compression, and relaxation back to zero pressure) is repeated until the desired packing density is obtained.

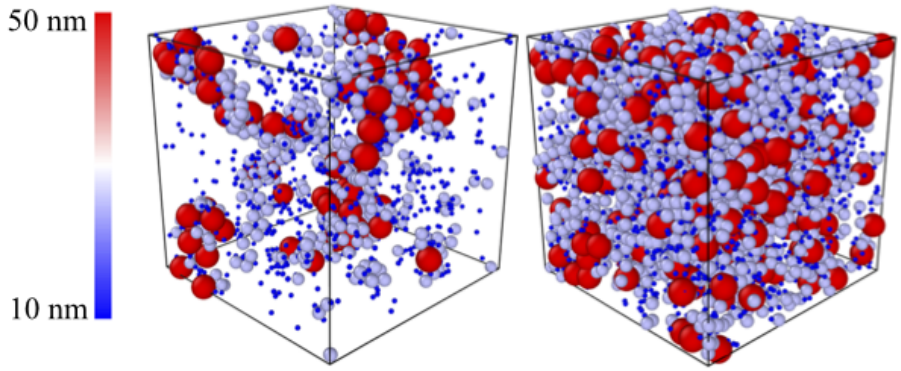

Figure 4.20: Snapshot of the packing process (after Lolli et al. [35]).

Interaction potentials between particles. In this model, similarly to Masoero's et al. [157] mesoscale model of C-S-H, the interaction between nanoparticles is defined reproducing the same behaviour as a continuous molecular structure of N-A-S-H. Hence, the interaction between two nanoparticles is the same as the behaviour inside the nanoparticle, and no assumption is made on the presence of physical interfaces between nanoparticles. This type of model can be assumed as a discretised homogenous structure, similarly to how the Discrete Element Method is used to model buildings. This hypothesis has been verified for C-S-H, where mechanical properties calculated at the mesoscale matched experimental results. Hence, the same approach has been followed for the mesoscale model of N-A-S-H gel. The functional form of the effective interactions between nanoparticles is assumed to be a particle-size-dependent generalised Lennard-Jones (Mie potential [156]), developed by Masoero et al. [157] to simulate the mesoscale mechanics of calcium silicate hydrates:

$$U_{ij}(r_{ij}) = 4\epsilon(\sigma_i, \sigma_j)\left[\left(\frac{\overline{\sigma}_{ij}}{r_{ij}}\right)^{2\alpha} - \left(\frac{\overline{\sigma}_{ij}}{r_{ij}}\right)^{\alpha}\right] \tag{4.29}$$

$U_{ij}(r_{ij})$ is the interaction energy between two particles i and j at a distance r_{ij} from one another and with diameters σ_i and σ_j. The depth of the energy well is governed by the parameter $\epsilon(\sigma_i, \sigma_j)$ and α determines the narrowness of the energy well. $\overline{\sigma}_{ij}$ is the average diameter of the two particles. Assuming $\epsilon(\sigma_i, \sigma_j)$ proportional to $\overline{\sigma}_{ij}$ is analogous to consider the Young's modulus uniform in the system [17], and as a consequence the ratio $\epsilon(\sigma_i, \sigma_j)/\overline{\sigma}_{ij}$ is a constant representing a unit pressure. Thus, pressure, strength and elastic moduli, having dimension of force per unit area are scale invariant. The cutoff employed for the different particle size combination is calculated as follows:

$$cutoff = \frac{3(\sigma_{max} + \sigma_{min})}{2} \tag{4.30}$$

with σ_{max} and σ_{min}, respectively the maximum and minimum diameter of the particles in the simulation. Shear forces are not transferred between particles. Following the same calculation explained by Masoero et al. [157] it is possible to express:

$$\epsilon(\sigma_i, \sigma_j) = f(\alpha) M \beta_{ij}(\sigma_i, \sigma_j) {\overline{\sigma}_{ij}}^3 \tag{4.31}$$

where *M* is the indentation modulus. $\beta = \sigma_i\sigma_j/{\overline{\sigma}_{ij}}^2$ is a corrective factor accounting for the fact that the contact surface area between two particles of different size typically differs from the average cross sectional area of the two particles. $f(\alpha)$ is a numerical constant that depends on the mapping between interaction potential and linear elastic properties. A detailed explanation of $f(\alpha)$ can be found in Masoero et al. [157], while the value of $f(\alpha)$ used for the simulations in this dissertation will be introduced in Section 5.3.2.

M is obtained as the initial slope of the axial stress versus axial strain graph at the molecular scale, when the simulation box is not allowed to contract nor expand in the directions perpendicular to the direction of loading. In a Lennard-Jones potential, α controls the distance corresponding at the maximum interaction force between two particles. This distance, divided by the average diameter $\overline{\sigma}_{ij}$, is the deformation at failure ϵ_{ult} as shown in Eq. 4.32. Therefore, by calculating ϵ_{ult} from molecular simulation, it is possible to obtain α applying Eq. 4.32 (see Masoero et al. [157] for the derivation of the equation).

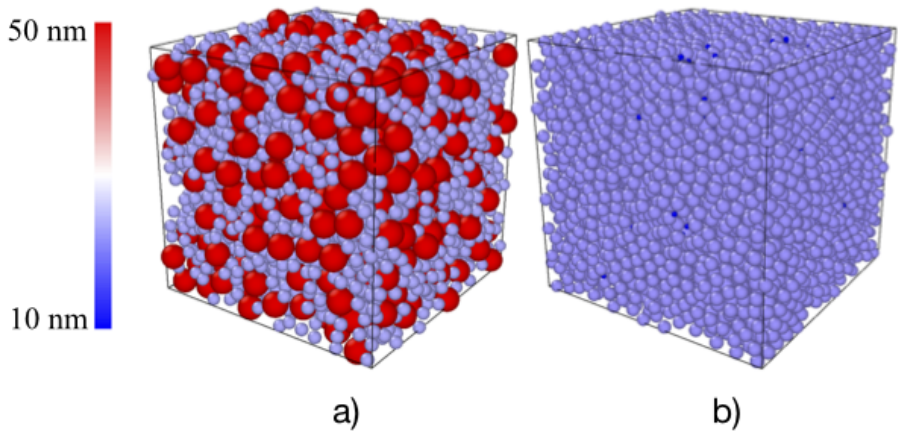

Figure 4.21: a) Mesoscale model set with preference for big particles b) Mesoscale model set with preference for small particles.

$$\epsilon_{ult} = \frac{\sqrt[\alpha]{\frac{4\alpha+2}{\alpha+1}} + \sqrt[\alpha]{2}}{\sqrt[\alpha]{2}} \tag{4.32}$$

Therefore, the potential in Eq. 4.29 is entirely determined by two molecular-scale mechanical parameters only: ϵ_{ult} and M.

Pore size distribution. The model construction described in the previous paragraph, allows to obtain a set of structures with different packing densities, therefore with different porosities. All these structures have chemistry-dependent mechanical properties resulting from interaction potentials whose parameters can be calculated from molecular scale simulations. This framework allows simulating a variety of structures observed experimentally. In particular, in this dissertation the focus is kept on two packing fractions, representing low density and high density N-A-S-H gel considered with different particle size range. To clarify, Fig. 4.21 shows two types of high density N-A-S-H gel obtained from two particle size distribution. In fact, both packing densities are obtained either from structures where preference is given to large solid nanoparticles (Fig. 4.21 a.), or from structure where preference is given to small particles (Fig. 4.21 b.). The former are obtained by imposing a preference for big particles (diameter 50 nm) over small ones, in the space filling algorithm, whereas the latter results from setting a preference for smaller particles, with a diameter of 10 and 25 nm. The pore size distribution was then simulated for each packing fraction with the open

source software Zeo++ [139], using the method by Pinheiro et al. [140], which is based on the Voronoi tessellation. The parameters used for the sampling are a probe radius of 0.2 nm and a number of Monte Carlo samples per unit cell equal to 5000. These variables results from a sensitivity analysis that considered three different probe radii (0.1 nm, 0.2 nm and 0.5 nm) as well as different MC samples varying from 1000 to 50000. The results are described in Section 5.3.2.

5

Results

Contents

5.1 Molecular scale model

This Section presents results to clarify the impact of disorder at the molecular level on mechanical and structural features of the N-A-S-H gel. The methodology described in Section 4.1 allowed building different types of models. Siliceous structures, containing only SiO_2 molecules, represented the baseline for three main categories of N-A-S-H molecular models, and analyses on these baseline structures are presented in Section 5.1.1. The baseline structure are the Si-O only preliminary structures built as described in Fig. 4.9. The procedure outlined in Section 4.1.2 led to structures that ranged from fully amorphous, to completely crystalline and to defective structures. The results address structural analysis first (X-Ray Diffraction, X-Ray Pair distribution function and density), and then mechanical properties (elastic modulus and large strain tensile behaviour). The content of this Section is from a paper recently published in ACS Applied Materials and Interfaces, titled *Atomistic Simulations of Geopolymer Models: The Impact of Disorder on Structure and Mechanics*, Lolli et al. [31].

5.1.1 Siliceous baseline structures: bond angle, bond length, ring distributions, and micropores.

Fig. 5.1 shows the distributions of internal (O-Si-O) and external bond angles (Si-O-Si). The internal angle quantifies the distortion of the silicate tetrahedra, whereas the external angle measures the relative orientation of tetrahedra in the short range (first neighbour). Longer-range topological information will be discussed later in terms of ring analysis. For a perfectly tetrahedral Si-O coordination, the O-Si-O internal angle distribution is expected to display a sharp peak at 109° [29]. This is indeed the result for the crystalline model structure in Fig. 5.1. Amorphous and defective structures have a very similar distribution of O-Si-O angles, with a spread of angles around the average 109°, which is probably a consequence of the overall disorder. Nevertheless, the standard deviation is limited, which indicates that the tetrahedra are only weakly distorted, without edge-sharing tetrahedra, as also confirmed by visual inspection of the configurations.

The distribution of external Si-O-Si angles shows that the crystalline structure has wider angles compared to the defective and amorphous structures, and that these latter two have similar distributions. Experiments shows that the T-O-T[1] angles in poly-

[1] T is a generic term to indicate either Si or Al as centre of a tetrahedron

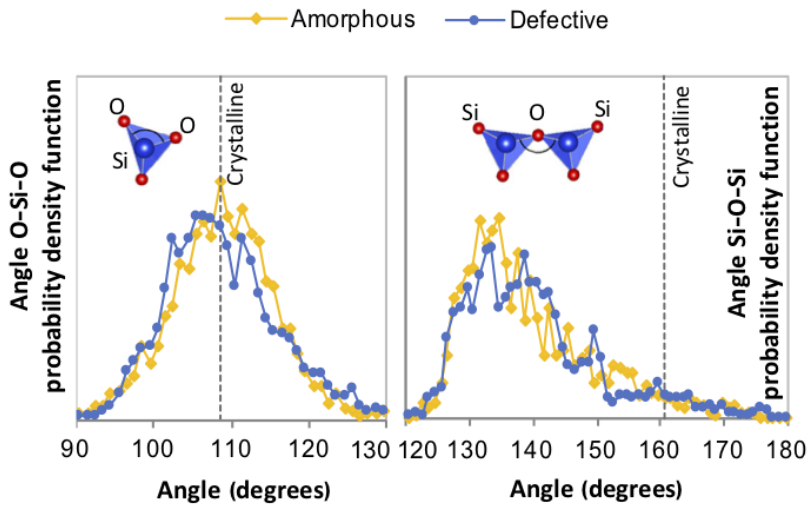

Figure 5.1: Internal (O-Si-O) and external (Si-O-Si) bond angle distributions for the three siliceous baseline structures. The area under the curve is normalised to the same constant.

merised SiO_2 and AlO_2 can range between 120° and 180° [158, 159], which agrees with Fig. 5.1. The smaller angles of the amorphous and defective structures compared to the crystalline structure suggest that the formers may be folded to some extent, which should result into higher densities. This is confirmed by the density values of the siliceous structures calculated at zero pressure. The densities of the amorphous and defective structures are similar to each other and respectively equal to 2.28 g/cm^3 and 2.13 g/cm^3, whereas the crystalline structure has a lower density of 1.66 g/cm^3. The similar density of the amorphous and defective structures leads also to a very similar total energy per mole of Si, which means that they are equally probable in thermodynamic terms (as expected, the crystalline structure has instead a much lower energy, and thus it is more thermodynamically stable).

The Si-O bond length distribution in Fig. 5.2 corroborates the result that the disordered structures are denser than the crystalline, in that the mode of the distributions for the amorphous and defective structures are shifted to the left (and thus the bonds are shorter) compared to the bond length value of the crystalline structure.

The angle analysis in Fig. 5.1, the bond angles in Fig. 5.2, densities and molar energy, highlight some differences between crystalline and disordered structures, but do not indicate any appreciable difference between defective and amorphous structures. Such a difference emerges instead in the pore structure and topology of the structure over larger length scales. The ring analysis in Fig. 5.3 provides one such

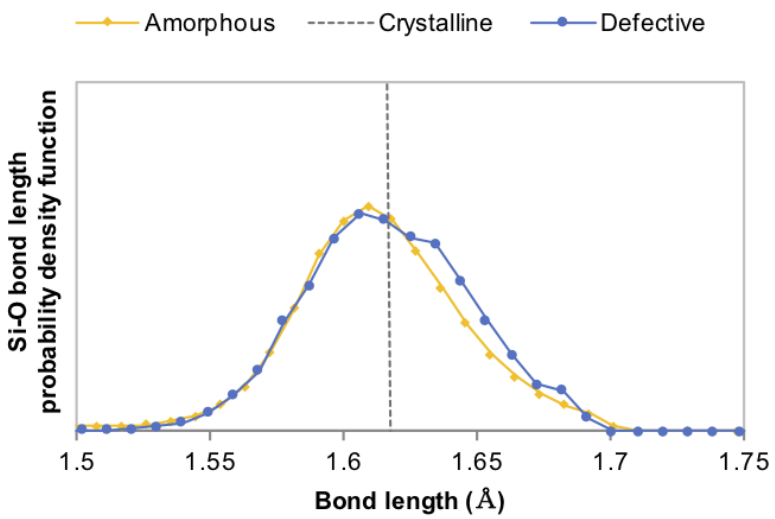

Figure 5.2: Bond length analysis of the three siliceous baseline structures (time-averaged over 50 timesteps).

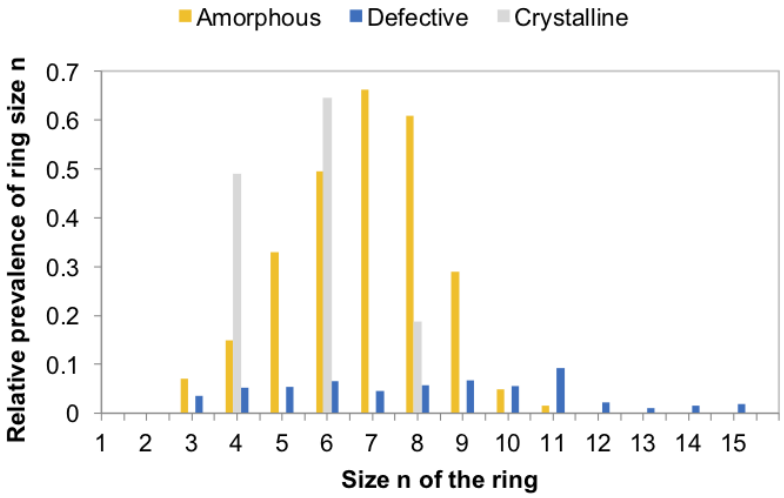

Figure 5.3: Ring size distribution of the siliceous baseline structures. The sum of all histograms is equal to the number of Si atoms in the simulation cell.

topological measure. The ring analysis of the crystalline structure is in good agreement with results in the zeolite literature, with prevalence of rings with size 4, 6, and 8 nodes [160]. The ring distributions of the amorphous and defective structures display a wider range of ring sizes, indicative of the greater medium-range disorder in these structures. Rings of odd size appear in both, and the range of possible sizes is significantly broader in the defective structure compared to the amorphous one, despite a

similar size of the simulation cell and a similar number of atoms in the structure (see Table 4.1). The differences in ring size distribution between the amorphous and the defective structures might impact their mechanical performance. On one hand, larger rings at the expense of smaller ones may indicate the presence of nanopores, which would decrease mechanical properties. On the other hand, large rings might provide long-range correlations and improve the large-strain mechanics of the system.

Fig. 5.4 shows the pore size distribution of the crystalline structure, correctly peaked around a diameter of 6.5 Å, which is the characteristic size of the sodalite cage shown in the snapshot. As expected, the pores of the crystalline structure are fully interconnected. The amorphous structure, instead, has non-interconnected, smaller pores, with average size peaked around 4 Å. The presence of small pores is consistent with the presence of small rings with size 3 in Fig. 5.3. The defective structure shows a pore structure that is indeed intermediate between those of the crystalline and of the amorphous structures. The pores are still interconnected to some extent, although less than in the crystalline structure (see snapshot in Fig. 5.4). Furthermore, the pore size distribution displays both a primary peak at ca. 4.5 Å, close to that of the amorphous structure, and a secondary peak at 6.5 Å, which indicates some persisting features of the original crystal structure from which the defective one was obtained. The impact of all these structural features on mechanical properties will be discussed later in Section 5.1.5.

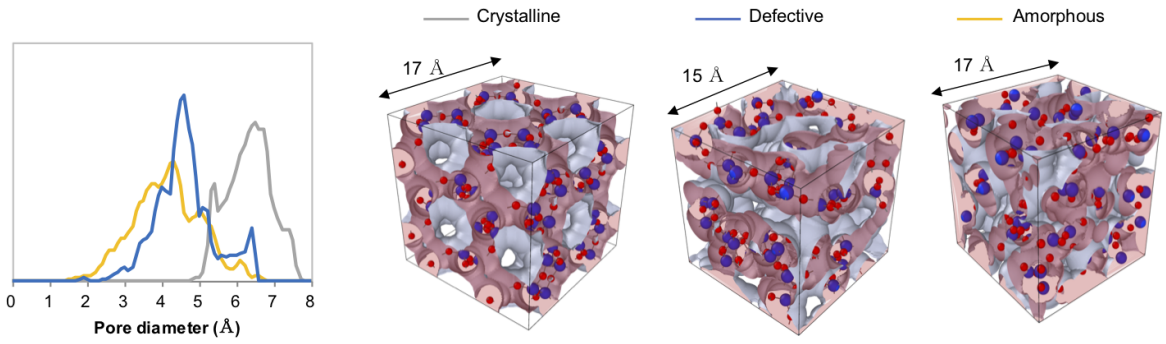

Figure 5.4: Pore size distribution and snapshots of the porosity of the siliceous structures. All snapshots are obtained using OVITO [33].

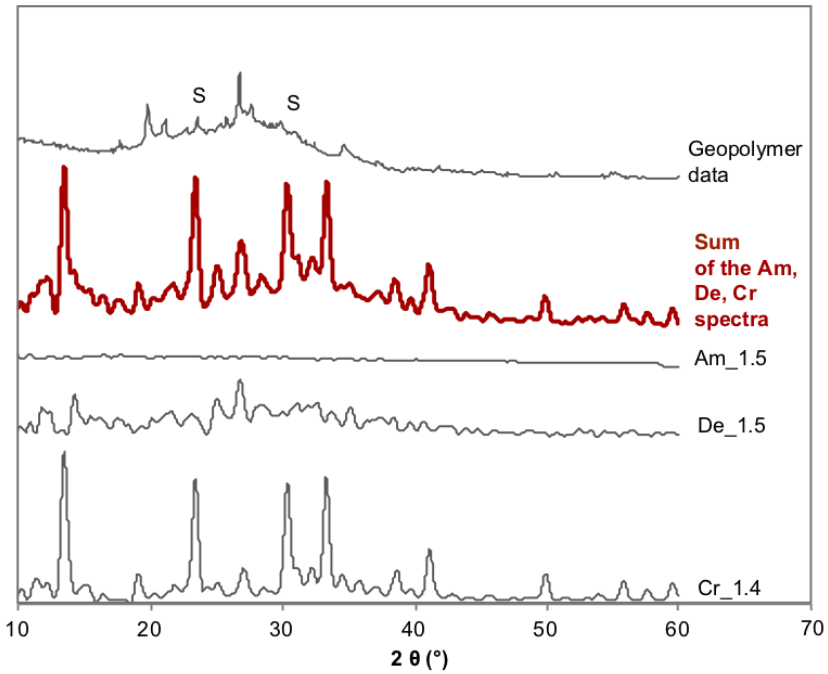

Figure 5.5: Simulation of X-ray diffractograms for three molecular models with Si:Al = 1.4 (crystalline structure) and Si:Al = 1.5 (amorphous and defective structures) and experimental XRD for a metakaolin geopolymer paste with Si:Al = 1.5. The metakaolin used is synthesised in the laboratories of Centro Ceramico (BO, Italy). Theoretical peaks for a siliceous sodalite structure [36]. All simulated X-ray diffraction are at room temperature and ambient pressure. Legend: S = theoretical sodalite peaks.

5.1.2 X-ray diffraction (XRD)

Fig. 5.5 shows the comparison between experimental X-ray diffraction data and simulations, highlighting the effect of molecular disorder on the calculated XRD patterns of structures with comparable Si:Al ratios of 1.4-1.5. The experimental diffractogram is from a metakaolin-based geopolymer paste with Si:Al = 1.5 cured at 23°C for 28 days. The simulations are not expected to precisely match the experimental spectrum, because structural disorder, defects, and impurities at all scales will introduce or smoothen features in the XRD signals, and this cannot be fully described by a molecular model only. However, two key features can be targeted and discussed in relation to the model molecular structures presented here: the broad peak that emerges at 2θ= 20°- 30°, which is typical of disordered alkali aluminosilicate gels, and the sodalite-related peaks at 2θ= 24° and 32°. In the simulated X-Ray diffraction patterns, the increased degree of order from the amorphous to the crystalline structure is appreciable: the amorphous structure does not display meaningful peaks; the crystalline struc-

ture displays sharp peaks typical of sodalite; the defective structure shows an overall disordered character but with sharper peaks (sodalite and quartz peaks at 2θ=27°) compared to the amorphous structure. The red curve in Fig. 5.5 is the results of the summation of the three spectra of crystalline, amorphous and defective structure, considering that the sample has an equal amount of the three systems. The resulting pattern presents a broad peak between 2θ=25° and 2θ=40° which is clearly due to the contribution of the defective structure, while the amorphous system just adds a background noise. As a result, the defective structure better captures the coexistence of amorphous and crystalline features emerging from the experiments.

Fig. 5.6 shows that altering the Si:Al ratio has a very small impact on the overall XRD signal. By decreasing the Si:Al ratio (thus increasing the number of Al, Na, and H_2O) the sodalite peaks slightly shift towards smaller values of the 2θ angle. This is true irrespective of the level of disorder, but it is most visible from the crystalline structure, whose results are therefore shown in Fig. 5.6. The shift is due to the swelling of the simulation box caused by the additional water. Since three H_2O molecules for each Na atom are considered, and since one Na atom is added for each Al atom, the structure with Si:Al 2 (indicate as Cr_2 in Fig. 5.6) contains less water, and consequently the crystalline planes are closer and the peaks are shifted towards higher values of the angles.

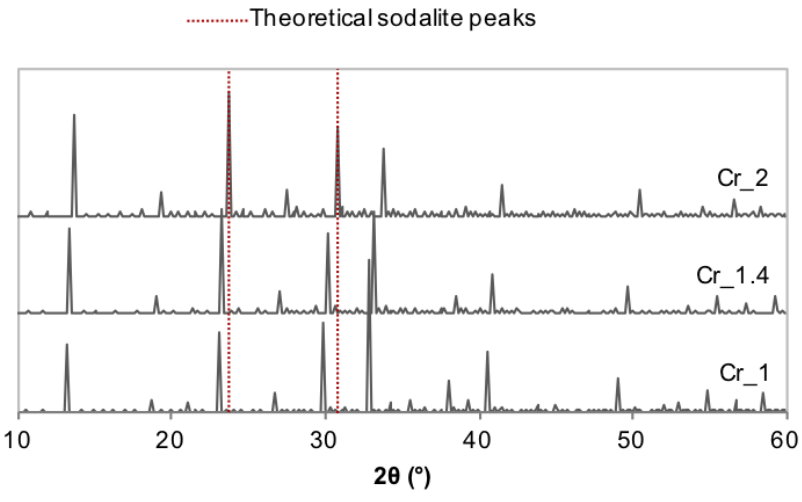

Figure 5.6: Simulated X-ray diffraction patterns of the three crystalline structures, varying Si:Al and showing the effect of the added water and Na. The curve for Cr_1.4 here is the same one as in Fig. 5.5, but here the spectrum is shown without peak broadening.

5.1.3 X-ray pair distribution function (PDF)

X-ray pair distribution functions *g(r)* allows to calculate the probability to find an atom A at the distance r of another atom B. X-ray pair distribution functions from simulations and experiments are compared in Fig. 5.7. The experimental data were discussed up to the first-neighbour peaks, hence the analysis of the simulations here are focused on the same peaks.

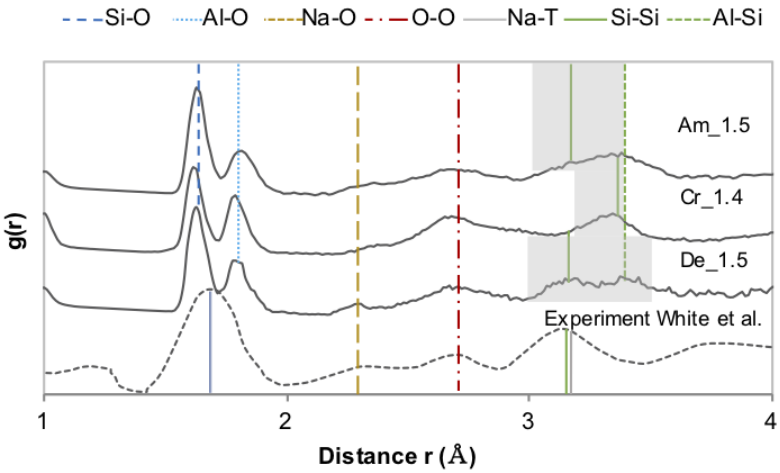

Figure 5.7: X-ray pair distribution function of metakaolin-based geopolymers. Comparison between experiments [37] and simulations on structures with Si:Al = 1.4 and 1.5. T: tetrahedral (Si or Al).

All the model structures, irrespective of their degree of disorder, capture two of the experimental peaks in Fig. 5.7:

- *T-O peak ($r \approx 1.7$ Å)*. The X-ray pair distribution functions obtained from the simulations discern between peaks associated with Si and Al tetrahedra, whereas the experiment displays a single broader peak. This difference may be due to two factors combined: the limited resolution of the experiment compared to the molecular model, and the possibility that the force field in the simulations might slightly overconstrain the interatomic distances to their equilibrium positions compared to the experiment. As expected, the level of disorder does not affect significantly these peaks in the simulations, because they depend only on the tetrahedral coordination of Al and Si with O.

- *O-O peak ($r \approx 2.7$ Å)*. All the simulations display and correctly locate the first O-O peak, which depends on the relative position of neighbouring tetrahedra as well

as on the location of water molecules.

Conversely, two of the experimental peaks in Fig. 5.7 are captured only by the defective model structure:

- *Na-O peak ($r \approx 2.3$ Å).* The defective structure is the only one clearly capturing this peak. In sodalite-based zeolites, the cations tend to occupy the center of ring structures; it is likely that the fact that the Na-O peak emerges only in the defective structure is related to its broader distribution of ring sizes compared to the amorphous and crystalline structures (see Fig. 5.3).

- *Na-T and T-T peaks (r ca. 3.2 Å).* The experiment indicates a single broad peak encompassing all the Na-T and T-T first neighbour peaks, and centred at ca. 3.1 Å. The crystalline structure displays a similar cumulative peak but shifted towards 3.3 Å. The amorphous structure displays a broader peak between 3 and 3.5 Å, resulting from the convolution of a broad Na-T peak, a Si-Si peak centred at 3.1 Å, and a sharp Si-Al peak at 3.3 Å. The defective structure is similar to the amorphous one, to some extent, but the Al-Si peak at 3.3 Å is less sharp and broader, whereas the Si-Si peak at 3.1 Å is more marked. As a result, the overall PDF shows the presence of a clearer peak at 3.1 Å, as in the experiment. This indicates that the positions of the peaks at ca. 3.2 Å are sensitive to the level of disorder, and that the intermediate disorder in the defective structure goes in the right direction of reducing the intensity of the Al-Si peak while increasing the intensity of the Si-Si peak. The agreement with the experiment leaves room for improvement, in that even in the defective structure the Si-Si and Si-Al peaks have similar intensity, whereas the experiment shows a prevalent peak at 3.1 Å (Si-Si). However, this limited difference in some T-T distances is not expected to cause significant inaccuracy in the skeletal density and mechanical properties that will be computed later in this Section.

5.1.4 Wet skeletal density

The wet skeletal density includes the so-called structural water, defined and discussed in Section 4.1.2; the simulations in this work predict wet skeletal densities between ca. 2.2 and 2.3 g/cm^3, which are in line with literature results (see Table 5.1). Fig. 5.8 shows the trend of density as a function of the Al:Si molar ratios (for a clearer

Table 5.1: Skeletal density of metakaolin geopolymers considering structural water (Wet ρ_{sk}). These literature data were obtained by He-pycnometry tests [40], comparing nominal density and pore volume [41] and from simulations on a fully glassy model structure [42].

Literature data	Si:Al molar ratio	Wet ρ_{sk} [g/cm^3]
Šmilauer et al., 2011 [40]	1.22	2.372
Duxson et al., 2007 [41]	1.15 - 1.65	1.8 - 1.7
Sadat et al, 2016 [42]	1-2	2.03 - 2.50

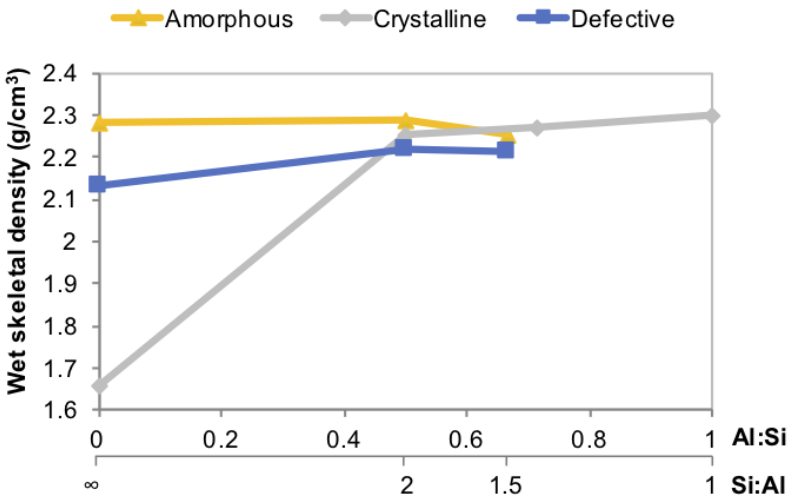

Figure 5.8: Simulated wet skeletal density as function of the Al:Si and Si:Al ratio.

representation of the results, this figure is discussed in terms of Al:Si ratio and not in terms of Si:Al ratio, which is the more common terms to indicate aluminium content in geopolymers). A higher Al:Si ratio implies a larger number of Na and water molecules in the structure, to keep the molar ratios Al:Na:H_2O to 1:1:3 as explained in Section 4.1.2. The skeletal densities at Al:Si = 0 coincide with the densities of the siliceous baseline structures computed in Section 5.1.1. The density of the crystalline structure increases significantly with the Al:Si ratio. This is due to the presence of relatively large pores, with width of ca. 6.5 Å (see pore size distribution in Fig. 5.4), which can accommodate Na and H_2O molecules, hence additional mass, without increasing the volume of the simulation cell. On the opposite hand, the amorphous structure has only small pores, therefore the addition of Na and H_2O, when the Al:Si is increased,

requires some swelling of the structure. This compensation effects leads to similar densities at different Al contents for the amorphous structure. The defective structure sits in between the other two: a moderate addition of Al, viz. at Al:Si $<$ 0.5 (so Si:Al $>$ 2) causes an increase of density akin to the crystalline structure, although less marked because only a few larger pores with width of ca. 6.5 Å are present in the defective structure (see Fig. 5.7). Increasing further the Al:Si ratio, instead, requires the defective structure to swell, hence the density remains constant and even decreases slightly for Al:Si $>$ 0.5, similar to the trend displayed by the amorphous structure in the same range of Al:Si ratios.

5.1.5 Mechanical properties: elastic modulus

Fig. 5.9 shows the elastic moduli *E* of all the model structures in this dissertation, averaged over the three Cartesian axes. The values obtained are in agreement with literature data, summarised in Table 5.2. Using nanoindentation, Němeček et al. [161] measured an elastic modulus of ca. 18 GPa for a N-A-S-H geopolymerisation product: these measurements, however, include mesopores with size of several nanometres, which are not described by the molecular simulations presented here. To extrapolate the experimental nanoindentation results to an equivalent elastic modulus without mesopores, one can consider the gel solid fraction of 0.6 [40] indicated by the same experiment. Extrapolation to zero mesoporosity (viz. a solid fraction of 1) using either the self-consistent or the Mori Tanaka homogenisation schemes (see Constantinides et al. [162]) are shown in Table 5.2. The simulation results in the present paper are indeed in line with the extrapolated nanoindentation results. Table 5.2 also shows that literature results from molecular simulations on zeolites, such as chlorosodalite [164] and

Table 5.2: Literature data for the elastic modulus [GPa], from *simulations and **experiments.

	E [GPa]
**Němeček et al., 2011 [161] - Mori Tanaka	44$\pm$12
**Němeček et al., 2011 [161] - Self consistent	88$\pm$23
*Sadat et al., 2016 [42] - glassy model structure	60 - 90
*Sanchez-Valle et al., 2005 [163] - analcime	75
*Williams et al., 2006 [164] - chlorosodalite	85

analcime, [163] are in the same range, as well as results from previous MD simulations of glassy geopolymer gels [42].

In Fig. 5.9, the moduli of the crystalline structure are clearly the largest, followed by the defective structure and then closely by the amorphous ones. This indicates that the level of structural disorder has an important impact on the elastic moduli at the molecular scale. The chemical composition, here quantified by the Si:Al ratio, also plays a role. Literature data from macroscale experiments indicate that E increases with Si:Al [41]. An analogous, albeit weak, trend emerges also from the simulations, with the crystalline structure showing a clear increase going from Si:Al 1 to 1.5, and the amorphous and defective structures showing a mild increase from Si:Al 1.5 to 2. On the other hand, one should note that the experimental measurements are on macroscopic samples, thus the trend in E may be affected by heterogeneities at larger length scales (e.g. microstructural characteristics) that molecular simulations alone cannot describe. The wet skeletal density appears not to be a good predictor of trends in

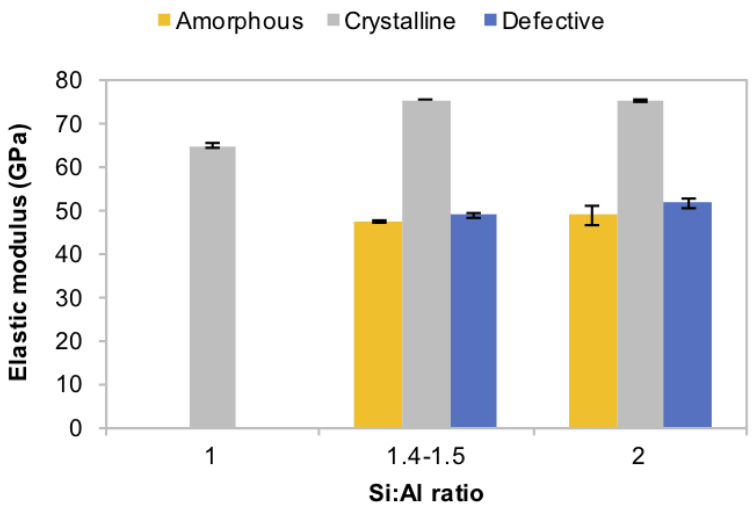

Figure 5.9: Young's elastic moduli as functions of the Si:Al ratio. Each elastic modulus is averaged over the three Cartesian directions.

elastic moduli, unlike often observed in materials with similar chemical compositions at the macroscale, for which higher density typically implies higher moduli. Indeed, by comparing Fig. 5.9 with Fig. 5.8 one can appreciate that an increase in Si:Al ratio (Fig. 5.8 read from right of left) corresponds to a decrease of density, whereas Fig. 5.9 shows that the Young's modulus increases. This means that for these geopolymer models, chemistry and topology at the molecular scale are more important than density in

determining the elastic properties, providing possible targets for material optimisation working up from the nanoscale.

5.1.6 Mechanical properties: large-strain tensile behaviour

Fig. 5.10 a. illustrates the complete stress-strain graph for all the structures with Si:Al 1.4-1.5. All the structures sustain stress in the order of several GPa and strain in the order of 0.1-0.5 before leaving the initial linear elastic regime. This is typical for material structures at the molecular scale [111, 113], while defects at larger scales are responsible for the experimentally observed typical values of macroscopic strength in the order of tens of MPa, and corresponding strain at the elastic limit in the order of fractions of the percent. The defective and amorphous structures display a similar mechanical behaviour, which is markedly different from that of the crystalline structure. The crystalline structure undergoes brittle failure and has a higher ultimate tensile stress compared to the amorphous and defective structures. These latter, instead, are more ductile, i.e. they sustain a high stress for a wide range of strain (from 0.1 to 0.2 - 0.25) without sudden drops of the stress itself. In particular, the defective structures can sustain larger stress and strain compared to the amorphous structure. This implies a better ability to prevent crack propagation and failure (viz. fracture toughness): a property that can significantly impact the durability of the material. The different

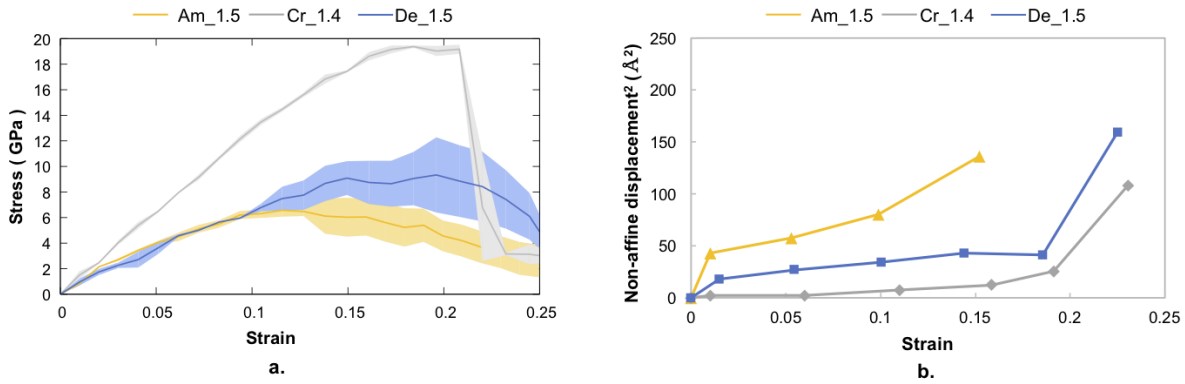

Figure 5.10: a) Stress-strain response under tensile load. Curves obtained from molecular dynamics simulations. Am_1.5 (amorphous with Si:Al = 1.5), Cr_1.4 (crystalline with Si:Al = 1.4) and De_1.5 (defective with Si:Al = 1.5). b) Average non-affine displacement of the atoms in the backbone structure, as a function of applied strain.

mechanical response to strain can be characterised in more detail by looking at the

non-affine displacements (see definition in Section 4.1.3). Fig. 5.10 b. shows the accumulation of non-affine displacements as a function of applied strain, only for the Si, Al, Na and O atoms in the backbone solid structure (thus excluding the displacements of atoms pertaining to the water molecules), which are the atoms governing the overall mechanical behaviour. The accumulation of non-affine displacements is related to the development of irreversible deformations [165]. Typically, a small level of average non-affine displacement ($\overline{\delta}_{na}$) is already accumulated during the initial linear stress-strain response of the material, due to small irreversible rearrangements that have a negligible impact on the overall mechanics and elastic moduli [165]. All the model structures presented here show such an initial small increase of $\overline{\delta}_{na}$ during the linear elastic stage (strain $<$ 0.1). Instead, as expected, $\overline{\delta}_{na}$ increases sharply when the structures leave the linear regime and enter the regime of plastic deformations eventually leading to failure. Fig. 5.10 b shows that the crystalline structure accumulates the least non-affine displacement (almost zero through the whole linear elastic stage), whereas the amorphous structure has the largest $\overline{\delta}_{na}$ and the defective structure is in-between. This is a convincing trend because the ability to accumulate non-affine displacements is expected to increase with the level of disorder, whereas order and symmetry add constraints to be overcome for $\overline{\delta}_{na}$ to develop. The increase of $\overline{\delta}_{na}$ with the level of disorder, provides therefore a rationale for the trend of Young's elastic moduli and strength in Fig. 5.10 a, which are both decreasing with the level of disorder.

One final remark concerns the relationship between the structural descriptors quantified in Section 5.1.1, and the observed different stress strain curves between amorphous and defective structures in Fig. 5.10. The results presented in Section 5.1.1 have shown that the only topological feature distinguishing the amorphous structure from the defective one are the ring size distribution and the pore structure. This suggests that long-range correlations, extending from the molecular scale to the mesoscale of several nanometres, might play an important role in determining the large-strain and failure behaviour of geopolymers.

Overall, with due attention to the impact that features and defects at larger scale might have on large-strain mechanics, the results in Fig. 5.10 provide the necessary starting point for the development of new multi-scale models of geopolymer mechanics.

5.2 Volume changes during geopolymer formation

This Section presents experimental results obtained on geopolymers pastes with Si:Al ranging from 1.5 to 2. In particular the focus is on identifying which features can impact macroscale properties, such as porosity, and volume changes in the early age. Three groups of results are presented: microstructure, early hydration kinetics, and early age volume changes. To investigate the microstructure of geopolymers, different types of analyses have been undertaken. Imaging techniques allow visualising the structure at different levels of magnification (Section 5.2.1), while porosity tests are used to obtain an overview of the pore size distribution and organisation at all scales (Section 5.2.2). The reaction kinetics is quantified by calorimetry tests aimed at identifying the relationship between reaction rate and activating solution used in the mix design (Section 5.2.3). Finally, experimental results on volume changes occurring during the early stages of the geopolymerisation reaction are presented, alongside a theoretical interpretation of the observed chemical expansion, which combine findings from the molecular model and from the experimental results.

5.2.1 Imaging characterisation techniques (SEM, TEM, HIM)

Section 4.2.2 presented three different imaging techniques used to study the microstructure of geopolymers. These techniques are used to obtain results presented hereafter.

Scanning Electron Microscopy (SEM). SEM micrographs are performed at 28 days after casting (Fig. 5.11) and one year after casting (Fig. 5.12) (see Section 4.2.2 for details). Fig. 5.11 shows a comparison of geopolymer pastes with Si:Al 1.5 (left column) and with Si:Al 2 (right column). Each row of pictures is at a comparable level of detail, and from top to bottom the magnification increases from 200X to 30000X. At 200X magnification, and for both Si:Al ratios, one can appreciate the porous structure of the material. The pore structure is characterised by two types of porosity at the macroscale, one with smaller pores diffused in the solid matrix, and the other one characterised by large and round shaped macropores. At higher magnification, between 2000 and 9000X the diffused porosity is still evident, and shown in Fig. 5.11 II a. and b.. Round shaped inclusions are found in both geopolymers and on their surface one can distinguish the formation of a gel characterised by particles with sub-micrometric

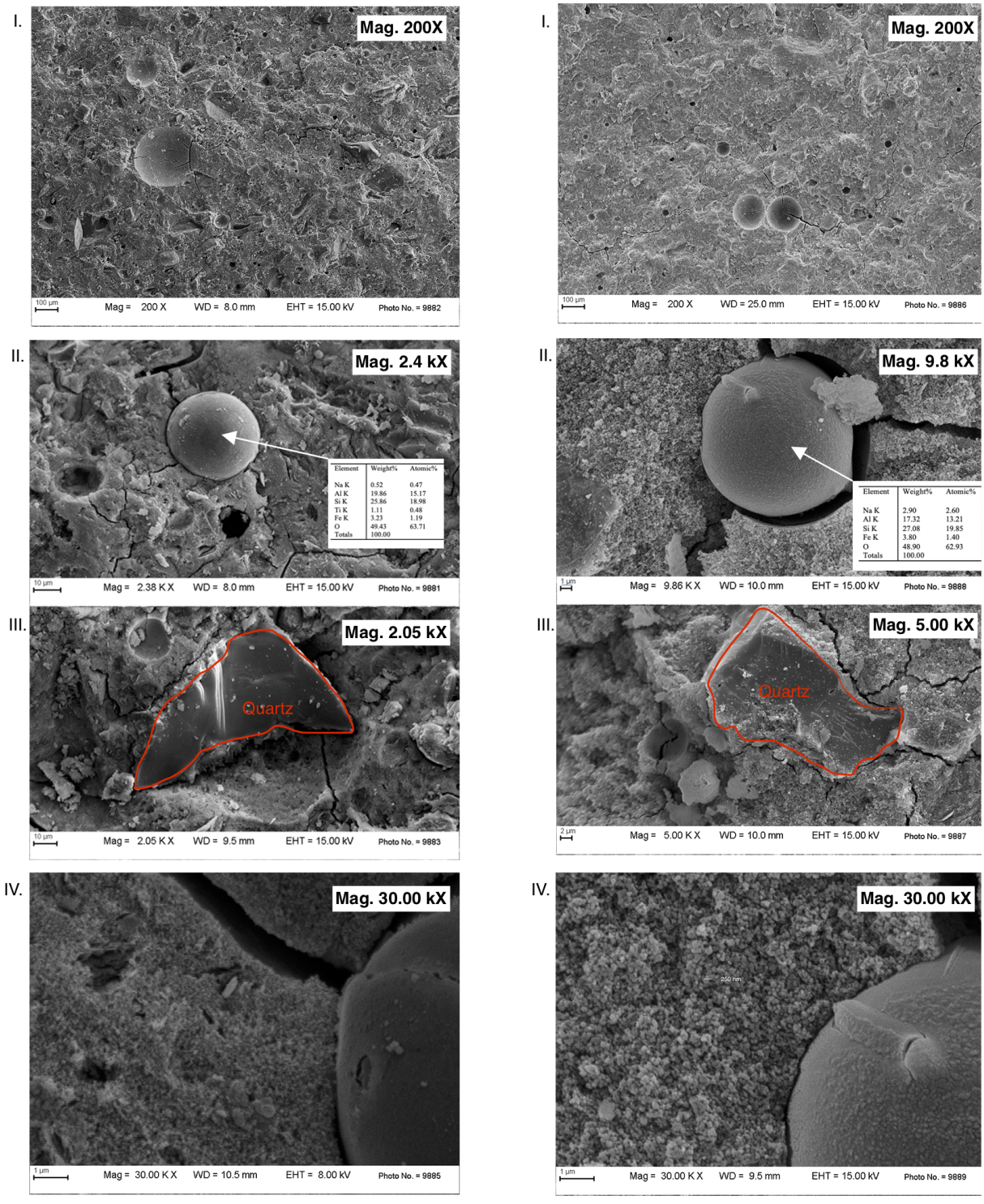

Figure 5.11: SEM micrographs of the geopolymers paste 28 days year after casting. From top to bottom Mag: 200X to 30000X a) Si:Al 1.5 b) Si:Al 2.

size, see Fig. 5.11 II a. and b.. In addition, crystalline particles with irregular shape are embedded in the geopolymer matrix, e.g. the quartz particles highlighted in Fig. 5.11 III a. and b., consistent with the high content of non-reactive impurities in the metakaolin raw material used to cast the samples (45% in weight, as shown in Section 4.2.1). Finally, the higher magnification, in Fig. 5.11 IV a. and b., shows the structure of the geopolymer N-A-S-H gel at the micrometre level and below, which is characterised by round granular texture and mesoporosity. The different Si:Al ratio effects the compactness of the final product. At 200X the paste with Si:Al 1.5 appears to be more porous than the paste with Si:Al 2. Namely, at the mesoscale, in Fig. 5.11 IV a. and b., the solid particles of the gel with Si:Al 1.5 appear to be smaller than for the Si:Al 2 gel, but this observation requires confirmation from techniques with better resolution, such as TEM and HIM images shown in later sections.

The presence of spherical macropores, in Fig. 5.11 I, is likely to be related to the round inclusions shown in Fig. 5.11 II. The chemical composition of these inclusions has been measured by Energy-dispersive X-ray spectroscopy (EDS), and the results are reported in the tables attached to the images. In both cases the main elements are silicon and aluminium, while sodium is less than 1% in wt., hence the particles are unreacted metakaolin. The round shape might be the result of flash calcination, which typically results in rounder particles compared to traditionally calcined metakaolin (as explained in Section 4.2.1). EDS also confirmed that the irregular shaped particles embedded in the geopolymer's matrix are quartz. On the other hand, Fig. 5.11 I a. and b. show that some spherical pores are significantly bigger than the average particle size of the metakaolin used (100-200μm vs 40 μm). It is possible however that some of the large spherical pores, especially those with diameter of ca. 100μm, are actually due to entrapped air bubbles.

All the SEM analyses discussed so far are taken at 28 days. SEM images are also taken after one year from casting, to measure whether significant changes of micro and meso structures should be expected during ageing. The images at one year involved not only samples with Si:Al 1.5 and 2, but also a sample with Si:Al 1.75. The results are shown in Fig. 5.12. At 200X, the images largely resemble those on the pastes at 28 days. Si:Al 1.5 displays diffused porosity, and a more homogenous pore size distribution, while Si:Al 2 has a more compact matrix with spherical macropores with diameter between 200 and 300 μm. At maximum magnification instead, 30000X, the granular gel is still visible at one year, but its particles appears to be bigger than at 28 days (300 nm for Si:Al 1.5 and ca. 50 nm for Si:Al 2, with Si:Al 1.75 displaying intermediate sizes).

This coarsening would be consistent with phenomena such as Ostwald ripening [2].

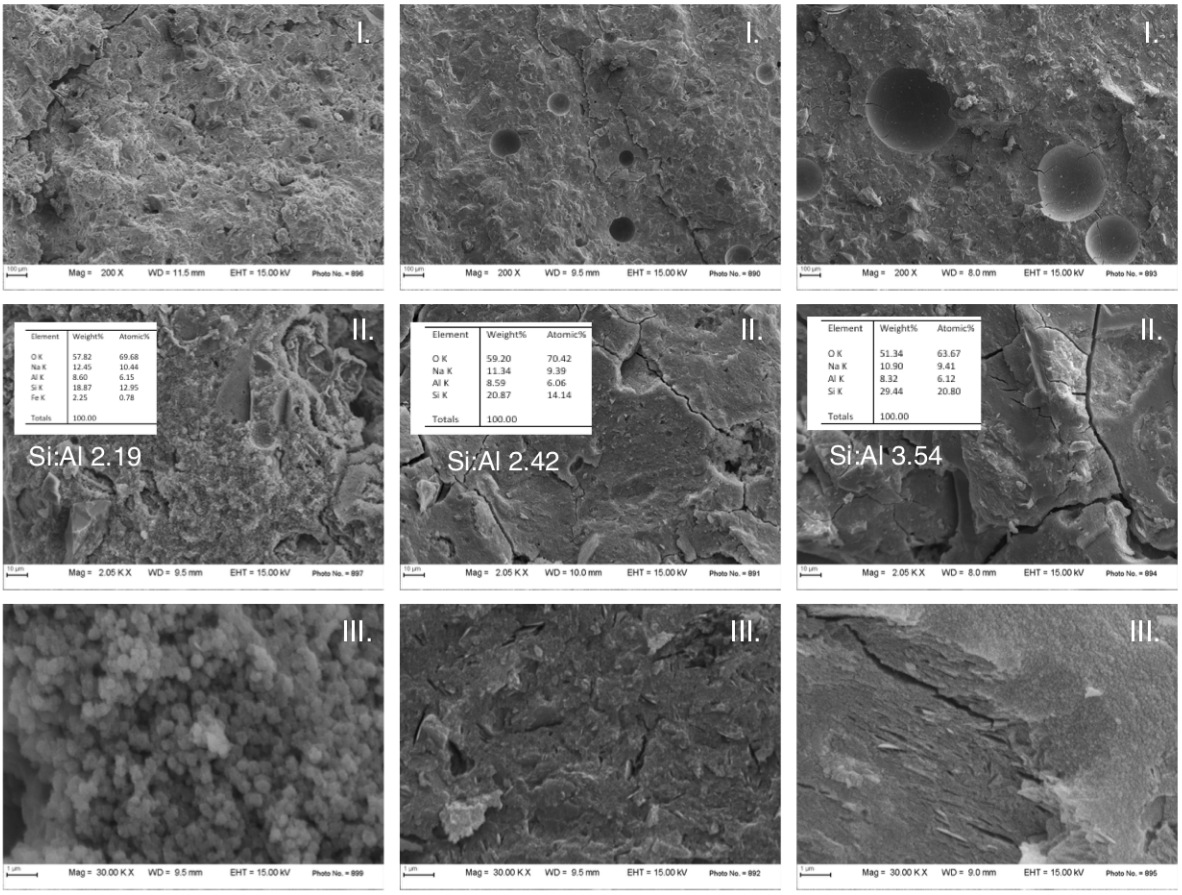

a) Si:Al 1.5 b) Si:Al 1.75 c) Si:Al 2

Figure 5.12: SEM micrographs of the geopolymers paste one year after casting. From top to bottom Mag: 200X to 30000X a) Si:Al 1.5 b) Si:Al 1.75 c) Si:Al 2.

Transmission Electron Microscopy (TEM) and Helium Ion Microscopy (HIM). These techniques allow exploring the details of the N-A-S-H gel at the nanoscale. TEM results are displayed in Fig. 5.13 where Si:Al 1.5 and 2 are compared at the same magnification (92000X). In this picture a particle of geopolymer paste is analysed to understand the mean size of the granular shape gel structure previously discussed in the SEM analysis. Si:Al 1.5 exhibits smaller particles, with sizes ranging between 15 and 50 nm, while Si:Al 2 has mean particles between 30 and 50 nm. Fig. 5.14

[2]Ostwald ripening is a phenomenon describing the change, e.g. coarsening, of solid particles via dissolution of smaller crystallites and growth of larger ones.

shows the HIM analysis on geopolymer paste with Si:Al 1.5, which provides a SEM-like picture of a surface of the N-A-S-H gel (as opposed to the TEM images which overlay on a single image features at different depths within the gel). The HIM image allows appreciating the porous interconnected structure, with pore diameters between 20 and 200 nm.

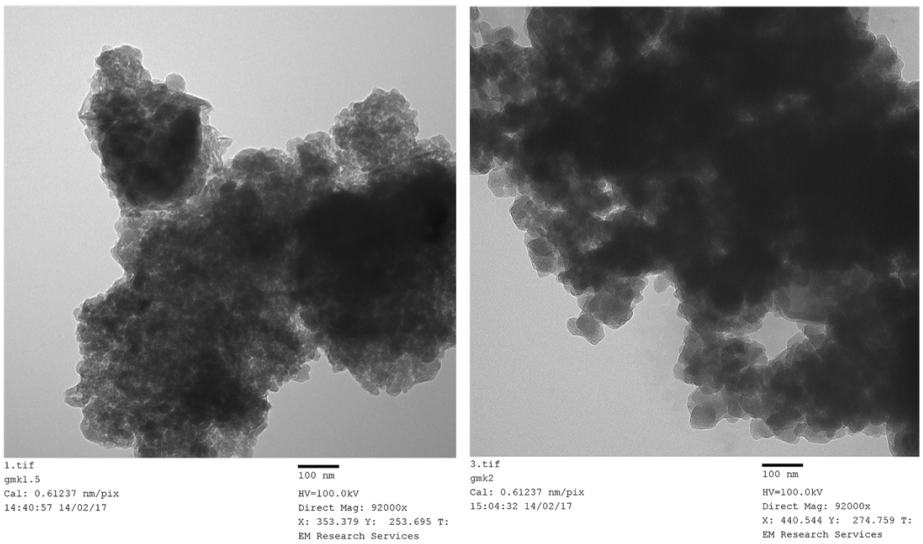

a) Si:Al 1.5 b) Si:Al 2

Figure 5.13: TEM micrographs of the geopolymers paste 14 days after casting. a) Si:Al 1.5 b) Si:Al 2.

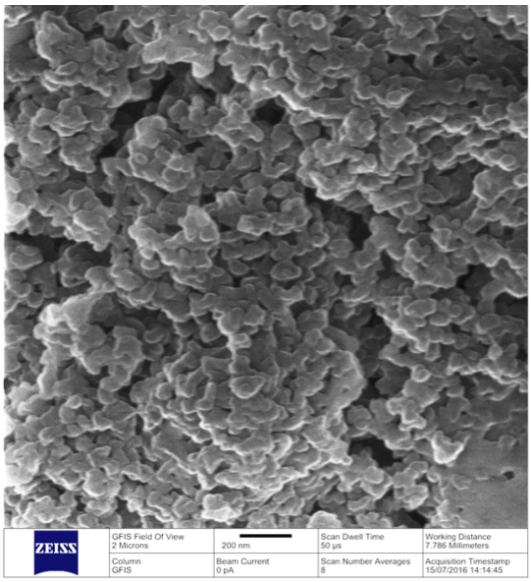

Figure 5.14: HIM micrographs of the geopolymers paste with Si:Al 1.5 28 days after casting.

5.2.2 Porosity study (isotherms, MIP, TGA)

This Section summarises all the results obtained analysing the porosity of metakaolin geopolymer pastes at different scales.

Water adsorption-desorption isotherms. Water adsorption-desorption isotherms obtained on different geopolymer pastes are displayed in Fig. 5.15. The methodology applied and described in Section 4.2.3 consisted of two successive cycles of desorption-adsorption, the first one displayed with a dotted line and the second one with a continuous line in Fig. 5.15. For clarity, the same test results are replicated in Fig. 5.16, with Fig. 5.16 a. showing only the first cycle and Fig. 5.16 b. only the second cycle. The adsorption curve does not change significantly from first to second cycle. By contrast, the desorption curve changes considerably, influencing the shape and extent of the hysteresis loop. The first desorption isotherm displays a plateau in

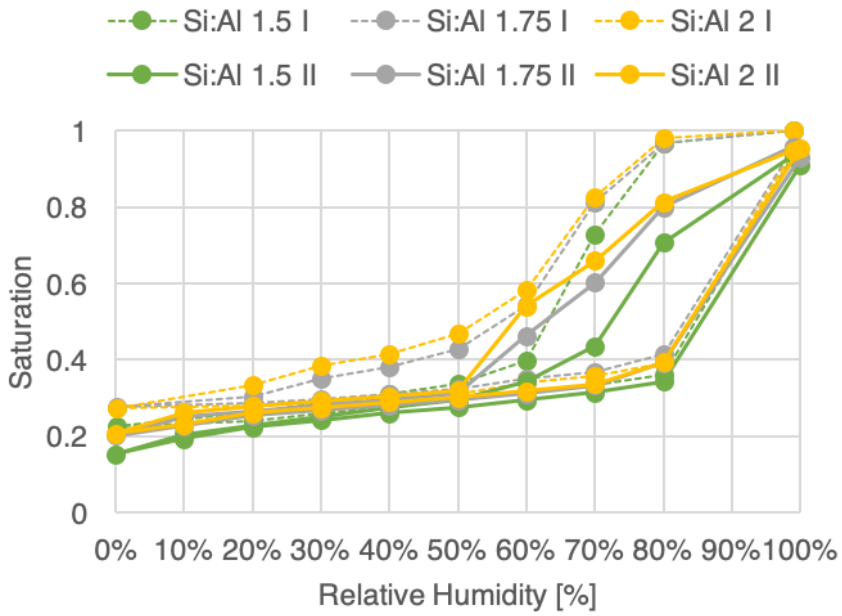

Figure 5.15: Overview of the complete water adsorption-desorption cycle.

desorption going from 100% to 80% RH, and the hysteresis involves the whole range of RH from 100% down to 0%. The second hysteresis loop instead closes at 50% RH, for all geopolymer pastes. For both cycles the point at 0% RH actually corresponds to the very small (although not strictly zero) humidity imposed by drying with silica gel. At this conventional 0% RH point, the saturation level does not reach zero because the

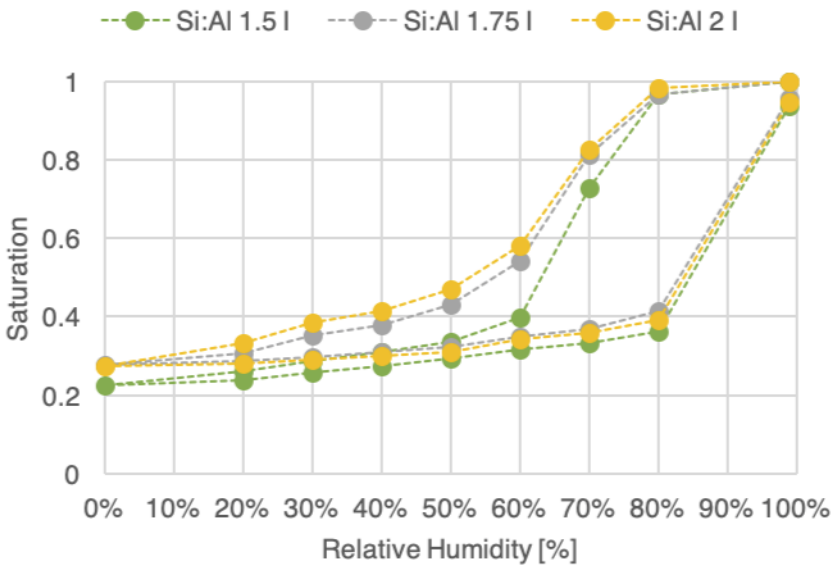

a) First isotherm

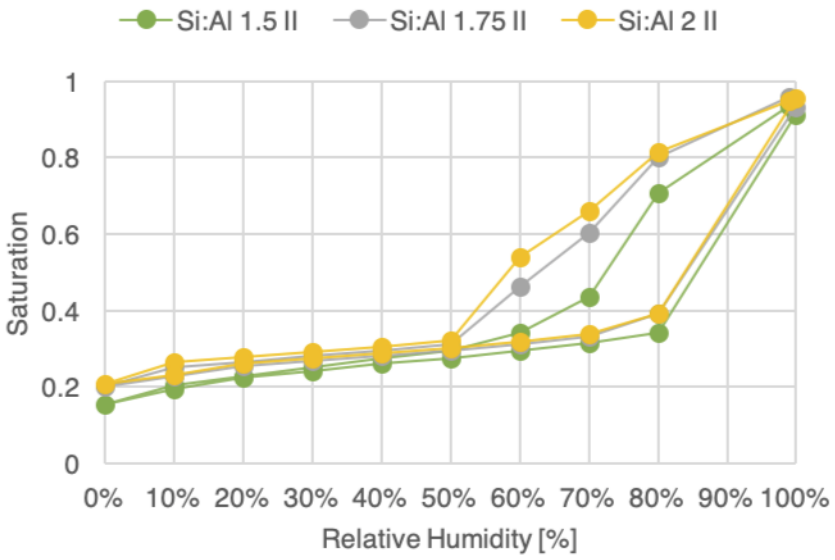

b) Second isotherm

Figure 5.16: a) First water adsorption-desorption isotherm b) Second adsorption-desorption isotherm.

reference dry mass was obtained by oven-drying the sample at 105 ℃, which removes more water from the structure than drying the samples with silica.

Considering the IUPAC classification [38], shown in Fig. 5.17 a., all the adsorption isotherms in Fig. 5.15 can be classified as Type IV. Type IV isotherms display a first

uptake at low RH, then an almost constant level of saturation at intermediate values of RH (between 10% and 50%) and finally a steep slope towards full saturation at higher RH. This adsorption behaviour is typical of mesoporous materials, hence from

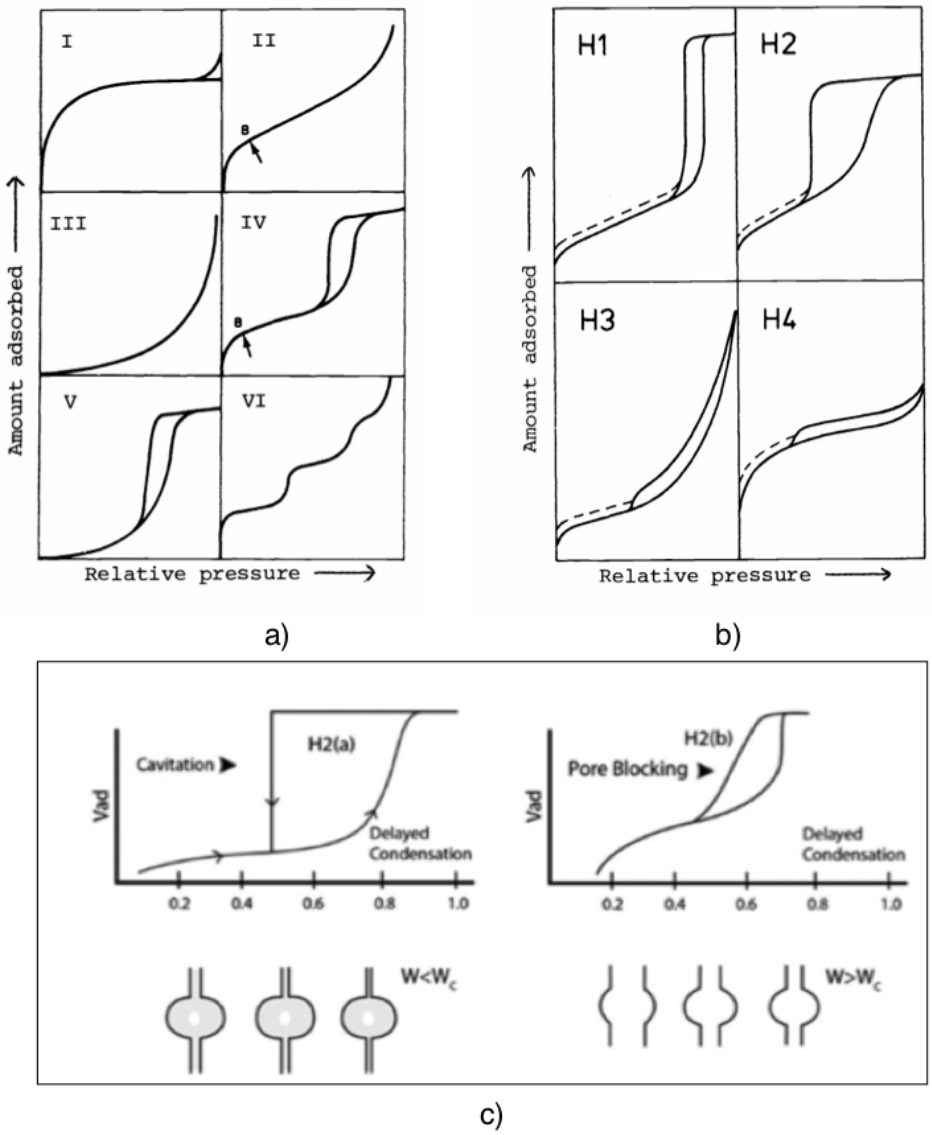

Figure 5.17: a) Types of adsorption-desorption isotherm (after IUPAC [38]). b) Type of hysteresis loop (after IUPAC [38]) c) Type H2 (a) and (b) hysteresis loop (after Thommes et al. [39]).

the similarity with the adsorption-desorption isotherms in Fig. 5.15, it can be concluded that the analysed geopolymers pastes are also mesoporous.

Additional information regarding the mechanism of pore emptying can be deducted from the shape of the hysteresis loop. All the adsorption isotherms in Fig. 5.15 present a hysteresis loop shape H2, as in Fig. 5.17b. This loop shape consists of desorption starting flat and sitting above adsorption at high RH, and then a sharp desorption at intermediate RH between 40% and 80%. A Type H2 hysteresis loop is typical of materials where the shape and size distributions of the pores are very polydisperse [166]. In such heterogeneous pore structures, pore blocking (also called the "ink bottle" effect) is typically the main obstable to equilibration during desorption, in which wide pores have access to the external environment only through narrow necks. During adsorption, the narrow necks saturate at low RH and the water can flow through them to progressively saturate also the wider pores deeper into the sample. However, during desorption, the wide pores cannot de-saturate until the narrow necks connecting them to the exterior get empty and provide a liquid-vapour interface, or until the partial pressure (or relative humidity) is sufficiently low to allow for cavitation within the wide pore considered as an isolated pore. This results in large pores desaturating at a lower RH than would be necessary if instead all the pores were directly connected with the exterior. Furthermore, H2 hysteresis loops can display different slopes in the desorption branch, as shown in Fig. 5.17c., which distinguish between two different mechanisms that may occur during evaporation [39, 166]: pore blocking and cavitation. In the case of the geopolymers samples tested here, the pore blocking effect is likely to be overcome before cavitation occurs, in that cavitation takes place in all pores more or less at the same RH of ca. 40%, whereas the desorption curves in Fig. 5.15 show progressive desaturation through a wide range of RH. The smaller extent of hysteresis during the second cycle of sorption is probably reflecting a coarsening of the pore structure. The desorption curve provides therefore information on the interconnectivity of the pore network.

The pore size distribution can be derived from the isotherm results, using the method presented in Section 4.2.3. However, to this end one must first decide on whether desorption or adsorption should be considered as a reference curve for the calculation of the pore size distribution. As discussed in Section 4.2.3, the theory to obtain pore size distribution is based on equations, e.g. Eq. 4.12, that assume equilibrium between the pore solution and RH in the environment. Therefore, the most appropriate branch to be chosen (adsorption vs. desorption) should be the branch where the corresponding distribution of water in the pore network is closer to equilibrium, i.e. corresponds to a lower free energy level. For materials with multiscale porosity, like geopolymers and cement paste, the adsorption isotherm is generally closer to equilibrium than the des-

orption isotherm [38]. Therefore the adsorption isotherms are used here to calculate pore size distributions.

The pore size distribution in Fig. 5.18 has been calculated with a model developed by Masoero et al. [149], and also considering the contribution of the Langmuir adsorption. Section 4.2.3 discussed the model in detail, highlighting the main parameters that determine the pore size distribution and that need to be fitted against the sorption isotherms. Namely, for the sorption isotherms obtained here, the model fit in Fig. 5.18 indicates a characteristic pore size for the dense domain equal to 3 nm, a characteristic pore size for the lose domain equal to 10 nm, and a packing fraction η = 0.69. The

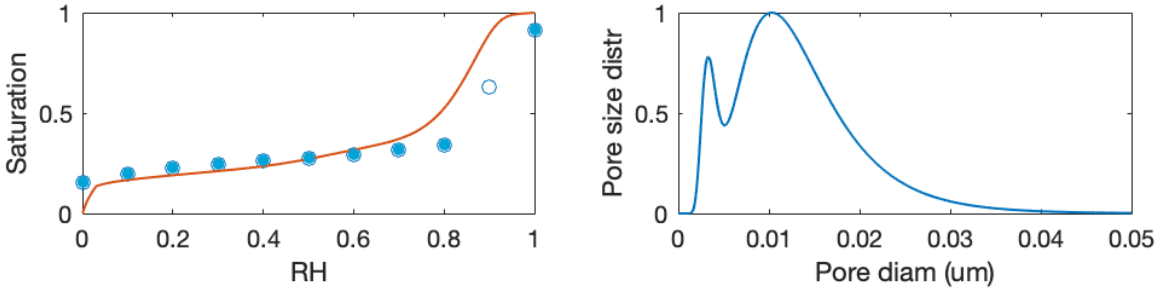

Figure 5.18: a) Comparison between experimental data points for Si:Al 1.5, blue circles, and modelling simulated isotherm (in red). The adsorption curve point at 90% is a linear interpolation between values at 80% and 100%, since it was not possible to measure this data experimentally (see Section 4.2.3). b) Pore size distribution obtained with the model.

resulting pore size distribution, in Fig. 5.18 b. displays two characteristic pore sizes of 3 and 10 nm, showing that wider pores occupy overall a larger fraction of the total mesoporosity. The two curves in Fig. 5.18 a. are in good agreement up to 70% RH, corresponding to a pore diameter of 8 nm, while the last three points at high RH are not captured. This means that the pore size distribution obtained with this model might underestimate the size of the largest mesopores. Additionally, water adsorption-desorption test cannot provide an appropriate characterisation of the macropores, like those shown in the SEM images previously discussed, hence the pore size distribution obtained in Fig. 5.18 b. will have to be integrated with MIP.

The pore size distribution in Fig. 5.18 is only for Si:Al 1.5. However, Fig. 5.16 shows that the Si:Al ratio does not have an important effect on the adsorption isotherm, and thus all the samples irrespective of their Si:Al ratio should have a similar pore size distribution. The Si:Al ratio affects instead the desorption branch, which is controlled by

the connectivity of the pore network. Increasing the Si:Al ratio widens the hysteresis in the RH range between 50% and 80%, leading to the conclusion that a higher Si:Al ratio creates a pore network where pore blocking is more significant. This is in line with literature results on metakaolin geopolymer pastes obtained through nitrogen adsorption [10].

Mercury Intrusion Porosimetry (MIP). The MIP test has been used to analyse the pore size distribution of the geopolymer pastes between 10 and 100 nm, which are still in the range of mesopores but difficult to characterise by vapour sorption. Exploring these range of mesopores by MIP will support the development of the mesoscale model presented in Sections 4.3.2 and 5.3.2. Fig. 5.19 shows the evolution of pore size distributions from MIP test results at 5, 7 and 14 days after casting. At all these ages,

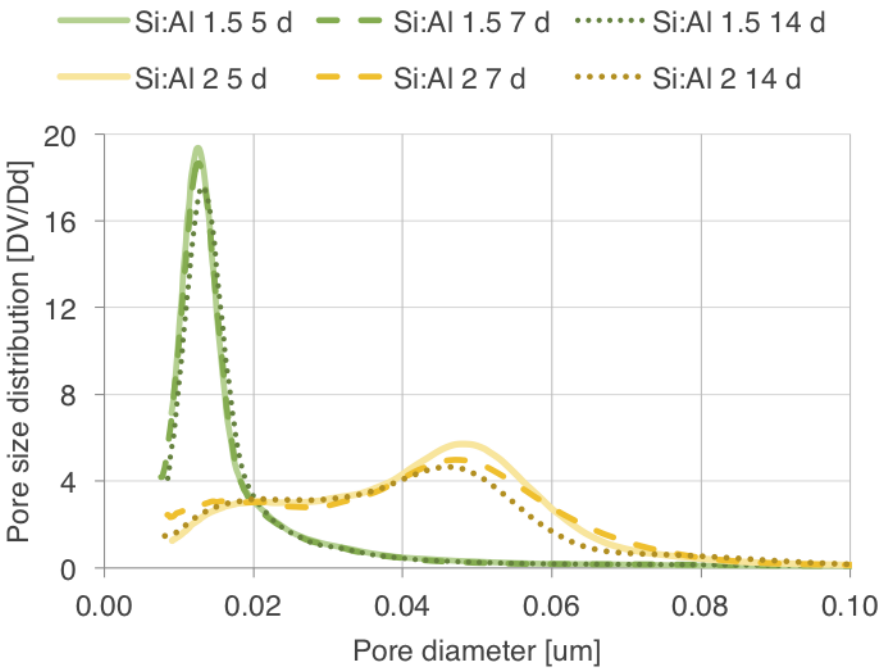

Figure 5.19: Pore size distribution obtained with MIP test at 5, 7 and 14 days after casting for Si:Al 1.5 and 2.

the samples with Si:Al 1.5 display a main peak centred at 15 nm, whereas the pastes with Si:Al 2 display two peaks, one centred at 18 nm and the other one at 50 nm. The only appreciable effects of sample age concern the samples with Si:Al 2, with the peak at 50 nm moving to 45 nm. This may be caused by ongoing reaction and product

forming inside the pore.

The MIP test also quantifies the total volume of pores in the sample, hence the total porosity. The test results show that the porosity does not change significantly with age during the first two weeks (ranging between 30 to 31% for Si:Al 1.5 and between 34 to 36% for Si:Al 2). The fact that the two pastes have a similar total porosity is in line with the SEM observations. For the samples with Si:Al 1.5 it is possible to compare the MIP results with the HIM observation in Fig. 5.14. The HIM micrograph shows a pore network characterised by pores with diameter between 20 to 200 nm, while the MIP pore size distribution of the sample with Si:Al 1.5 shows pores up to 40 nm. Hence, while some pore sizes are detected by both tests, specifically between 20 and 40, the MIP does not seem to capture pores with diameter over 40 nm and under 100 nm (upper limit of the test). This might mean that, while visible in the HIM pictures, pores with size between 40 and 100 nm occupy overall a much smaller volume compared to smaller pores. More data would be required to confirm the result.

TGA. Thermogravimetric Analysis is performed to qualitatively classify the water in the geopolymer matrix on the basis of how strongly it is bound to the solid structure. This qualitative classification will later be related to volume changes during the geopolymerisation reaction. Fig. 5.20 shows the results of the TGA tests, in which the amount of mass loss is assumed to coincide with water loss, together with a classification proposed by Kuenzel et al. [12]. The evaporable amount is considered to fully leave the structure at a temperature of 250℃, although this is known to depend on the testing conditions to some extent (e.g. a heating rate of 10℃/minute might prevent the complete evaporation of water at temperatures below 250℃) [12]. According to Kuenzel et al.'s work, water can be subdivided into three categories related to the degree of bonding with the solid structure. "Free water" and "interstitial water" correspond to two types of evaporable water in the structure. Comparing the graphs in Fig. 5.20, all the pastes experience the highest fraction of mass loss below 250℃, as highlighted by the differential thermogravimetric analysis (DTG) results in red: this corresponds to the loss of evaporable water. In particular Si:Al 1.5 loses 13.9% of its mass, Si:Al 1.75 10.05%, and Si:Al 2 10% in weight. These findings are in line with literature results reporting an inverse correlation between increase of Si:Al and mass loss of the samples [41]. In particular, the main difference between samples occurs in the temperature range between 125℃ and 200 ℃, while all mix designs experience the same mass loss up to a heating temperature of 125 ℃ and over 200 ℃.

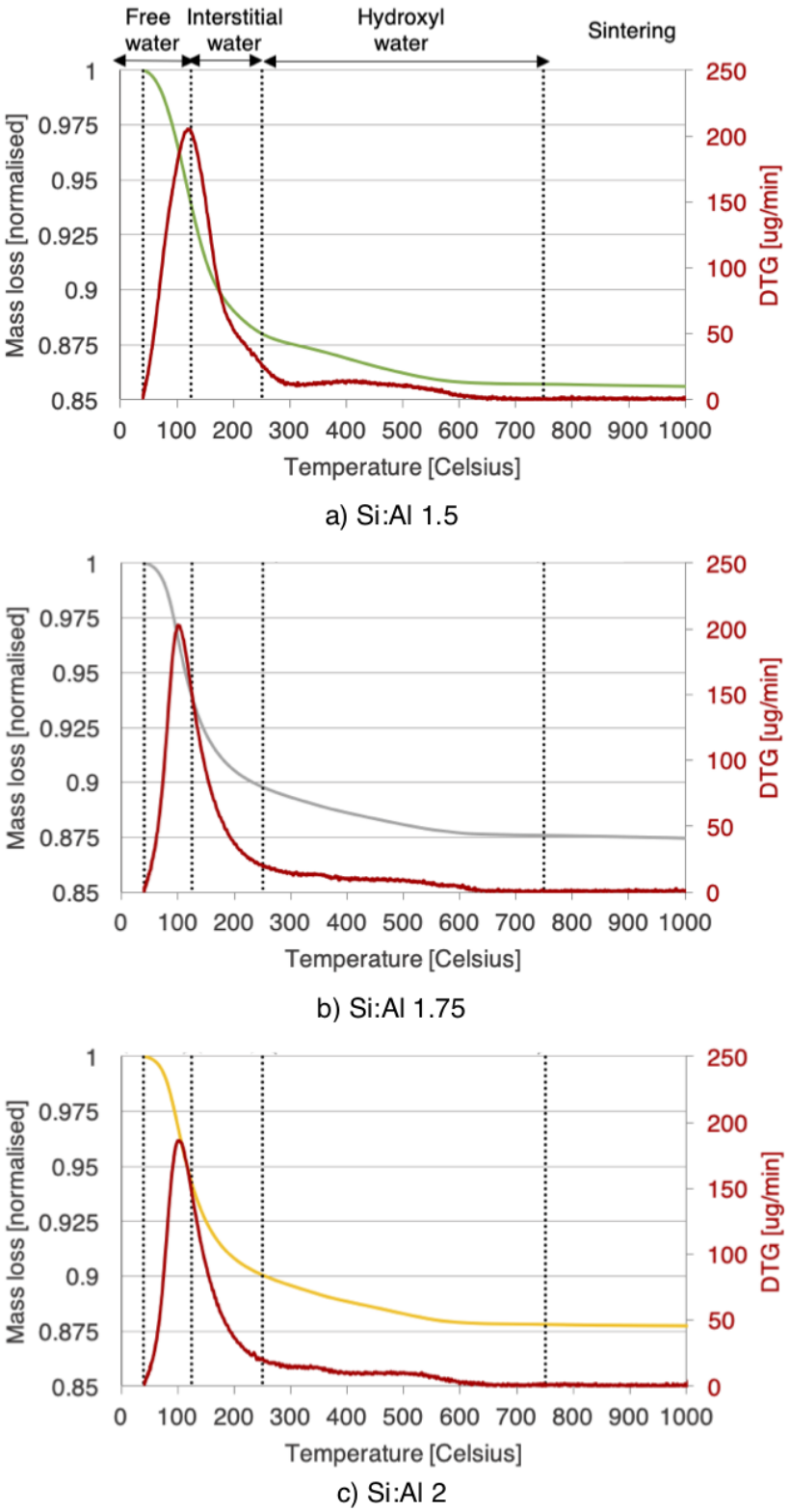

Figure 5.20: TGA results and classification of the type of water in the geopolymer structure. Results are presented from top to bottom for Si:Al 1.5 (a), 1.75 (b) and 2 (c) respectively.

The geopolymer paste with Si:Al 1.5 experiences a mass loss that is almost twice as large as that of the pastes with Si:Al 1.75 and 2 in the 125-200 ℃ temperature range. There is not a noticeable difference between Si:Al 1.75 and 2. The porosity values obtained with the MIP test at 14 days showed comparable results between the paste with Si:Al 1.5 and 2, with a porosity ranging between 30% (Si:Al 1.5) and 35% (Si:Al 2). This results from MIP seem to contradict with the observation of different evaporable water contents from TGA. However, the MIP results consider pore sizes only up to 100 nm, while the difference in the TGA results could be due to evaporable water in pores larger than that. The SEM at one year in Fig. 5.12 I. shows indeed a different characteristic macropore size for Si:Al 1.5 compared to 1.75 and 2, but the overall average porosity at the macroscale is difficult to quantify by visual observations. Previous works confirm the results discussed here, showing that between 100 and 300 ℃ metakaolin geopolymer samples lose the largest amount of water and, as a consequence, display the largest amount of drying shrinkage [41].

5.2.3 Reaction kinetics by calorimetry

The experimental results in Fig. 5.21 have been obtained with isothermal calorimetry test at 25° C on the three geopolymers pastes with Si:Al equal to 1.5, 1.75, and 2.

Fig. 5.21 displays the rate of reaction and, in the inset, the cumulative heat released during the geopolymerisation. Two distinctive peaks of rate are highlighted for all Si:Al ratios. The first exothermic peak appears immediately after the casting for all mixes, while the second peak occurs after several hours from mixing and its magnitude decreases with the Si:Al ratio. Zhang et al. [167] assigned these peaks to the different stages of the geopolymerisation, the first peak marking the dissolution of the metakaolin, and the second one being related to the formation and organisation of the N-A-S-H product. The second peak has higher intensity when decreasing Si:Al ratio, and the reaction happens rapidly. It is known in the literature [55] that an activating solution based on sodium silicate restrains and retards the formation of the geopolymer gel, partially hindering the formation of additional crystalline phases. This is due to the lower concentration of available Na^+ ions, and thus lower pH in solutions of sodium silicate compared to solutions of sodium hydroxide only. For the pastes used in this work, Si:Al 1.5 is activated with a mix of sodium hydroxide and commercial sodium silicate solution, while Si:Al 2 is activated only with the same commercial sodium sili-

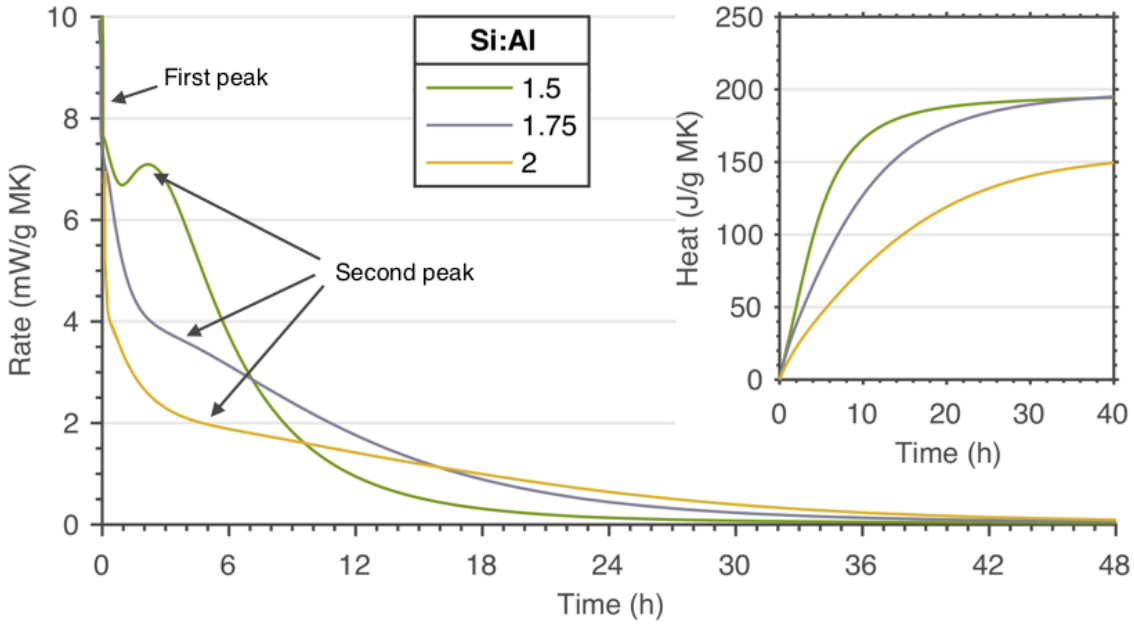

Figure 5.21: Isothermal calorimetry tests. Rate of the reaction as a function of time. The inset shown the cumulative heat released during the reaction.

cate solution (see Table 4.3). As a result the concentration of sodium hydroxide in the activating solution is higher for Si:Al 1.5 providing an increased alkalinity. Hence, the pH of the solution used for Si:Al 1.5 is higher than the other two mixes. Consistently with the second peak of rate getting smaller, the setting time in Table 4.6 increases with the Si:Al ratio. Therefore, adding more silicate in the activating solution retards the reaction, affecting the mechanical properties at early age.

The cumulative heat released during the geopolymerisation reaction (inset in Fig. 5.21) is comparable at 40 hours for Si:Al 1.5 and 1.75, whereas the samples with Si:Al 2 have released 25% less heat at 40 hours. This is also consistent with the lower reactivity of pastes with Si:Al 2. The same trend has been observed by Zhang et al. [167], who reported cumulative heat released ranging between 286 and 390 J/g MK. These values from Zhang et al. are higher than the heat release shown in the inset of Fig. 5.21, but the type of metakaolin used here has a high amount of unreactive material, which interferes with the extent of the reaction and with the heat released when normalised per gram of raw material, as it is in Fig. 5.21.

5.2.4 Chemical expansion: experiments and modelling

This Section discusses the results of the chemical shrinkage experiments presented in Section 4.2.5. The results are then interpreted through a theoretical model that considers the different reactants and products in the geopolymerisation reaction. Fig. 5.22 shows the experimental results of chemical expansion over time for the three geopolymer pastes considered here. All mix designs display an overall expansive behaviour, meaning that the volume of the geopolymerisation product is larger than the volume of the reactants. Specifically, the results indicate that the measured chemical expansion is inversely proportional to the Si:Al molar ratio in the geopolymer mix, with the maximum chemical expansion for the mix with Si:Al 1.5 equal to 15 μl/g MK, 8.5 μl/g MK for Si:Al 1.75, and 4 μl/g MK for Si:Al 2. Additionally, while the volume of the Si:Al 1.5 and 1.75 samples stabilises after 30 hours, Si:Al=2 starts to shrink again after 46 hours.

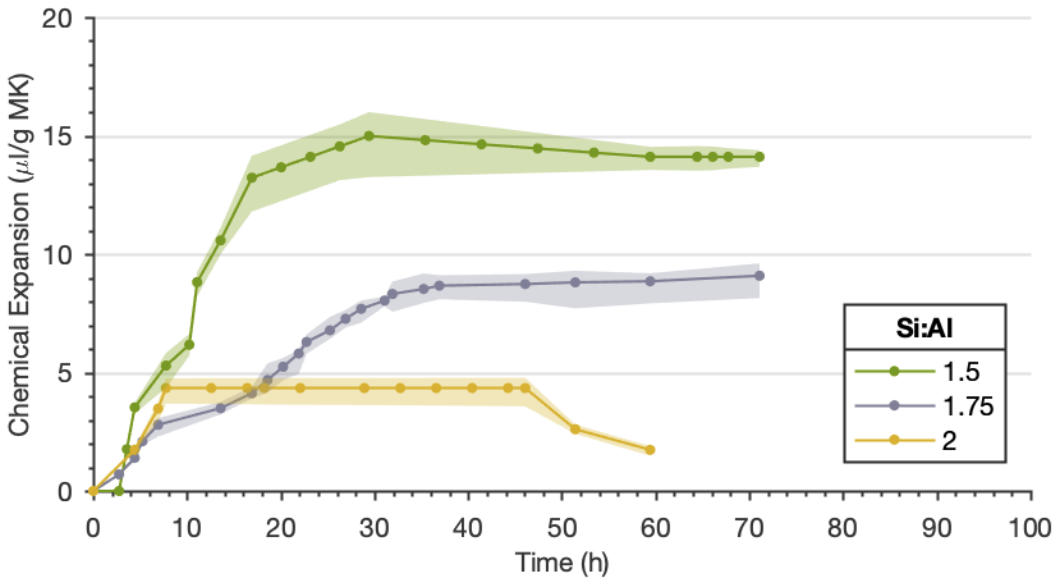

Figure 5.22: Chemical expansion versus time. Dots represent the averaged measurements over four tests for each mix design, and the shaded area indicates the standard error.

The expansive behaviour is uncommon for cementitious materials, as materials based on calcium silicate hydrates normally display chemical shrinkage. Hence, the chemical expansion observed here for the geopolymer mixes could be of technological value, in particular if this expansion eventually contrasts the macroscopic autogenous shrinkage that may cause cracking. The literature lacks experimental data on both the chemical and autogenous shrinkage of geopolymers, so this dissertation will address

both of these gaps: in Section 5.2.5, by presenting experimental results on autogenous shrinkage, and here by providing a model-based explanation to build confidence on the chemical expansion results shown in Fig. 5.22.

The chemical expansion results in Fig. 5.22 can be analysed with the theoretical model introduced in Section 4.2.5. The model will help explain which components of the reaction are the main responsible ones for the expansive behaviour. To this end, it is sufficient to consider one sample only with Si:Al 1.5. The effect of Si:Al ratio on the results will be discussed later in this section. As previously introduced in Section 4.2.5, the amount of water in the N-A-S-H gel at the molecular scale is not exactly defined, hence several hypothesis have been considered here to clarify the extent to which such water controls the chemical expansion. Eq. 5.1 describes the starting point of this study, under the initial assumption of H_2O:Na = 3 of structural water in the N-A-S-H product, viz. β=3.

$$\begin{aligned} &1\mathrm{Al_2O_3}\cdot 2\,\mathrm{SiO_2}\,(\mathrm{mk}) + 1\,\mathrm{Na_2O}\cdot 0.87\,\mathrm{SiO_2}\cdot 12.3\,\mathrm{H_2O}\,(\mathrm{solution}) + 3.02\,\mathrm{SiO_2}(\mathrm{quartz}) \longrightarrow \\ &2\,\mathrm{Na}(\mathrm{AlO_2}\cdot 1.5\,\mathrm{SiO_2})\cdot 3\,\mathrm{H_2O}\,(\mathrm{N{-}A{-}S{-}H}) + 6.3\,\mathrm{H_2O}\,(\mathrm{solution}) + 3.02\,\mathrm{SiO_2}(\mathrm{quartz}) \end{aligned} \tag{5.1}$$

The amount of chemical expansion depends on the difference between molar volume of reactants and products. The molar volume is obtained applying Eq. 4.17, starting from the density and molar weight of each component of the geopolymerisation. Referring to Eq. 5.1 it is possible to calculate the contribution of each reaction component to the balance of molar volumes, using Table 4.5 for the N-A-S-H density and Fig. 4.16 for the density of the solution. Table 5.3 summarises the results obtained for α=1, i.e. when the geopolymerisation reaction is 100% complete. The results in Table 5.3 indicate that a geopolymer paste with Si:Al 1.5 and β = 3, at full reaction (α=1) should display a chemical shrinkage of 20.17 cm^3 per mol of metakaolin, which corresponds to 90.84 μl/g MK. This result is in contrast with the experimental results of expansion obtained in Fig. 5.22, but the chemical shrinkage prediction is consequent to the choice of β = 3. Considering instead a different value of β it is possible to match the experimental expansion, as shown hereafter.

Table 5.4 shows the same calculation, but this time assuming β = 1.5. The different assumption of water content in the N-A-S-H leads to a different chemical formula, molar weight and density (computed with the molecular model in Section 5.1) for the N-A-S-H products and solution. These differences, compared to the values in Table 5.3,

Table 5.3: Example of molar volume calculations considering Si:Al =1.5, β=3, and α=1 . Legend: MW=molecular weight, MV= molar volume. The MV of 1 mole of product are the following: N-A-S-H = 101.10 cm^3/mol, SiO_2 = 22.67 cm^3/mol, H_2O = 18.02 cm^3/mol.

Reactants	**Chem. formula**	**MW** [g/mol]	**Density** [g/cm^3]	**MV tot.** [cm^3/mol]
Metakaolin	$Al_2O_3 \cdot 2\,SiO_2$	222.13	2.55	87.11
Solution	$Na_2O \cdot 0.87\,SiO_2 \cdot 12.3\,H_2O$	335.84	1.35	248.77
Inert	$3.02\,SiO_2$	60.08	2.65	68.58
				404.46
Products α**=1**	**Chem. formula**	**MW** [g/mol]	**Density** [g/cm^3]	**MV tot.** [cm^3/mol]
N-A-S-H	$2Na(AlO_2 \cdot 1.5SiO_2) \cdot 3H_2O$	222.24	2.198	202.21
Inert	$3.02\,SiO_2$	68.58	2.65	68.58
Solution	$6.3\,H_2O$	18.02	1.00	113.49
				384.29

are highlighted in orange in Table 5.4. Changing from β=3 to β=1.5 has a direct consequence on the total molar volume of the solution. In addition, the density of the N-A-S-H is also changing as described in Table 4.5 (value provided by dedicated molecular simulations and shown previously in Section 4.2.5). Hence, while the molar volume of the N-A-S-H decreases, the total molar volume of the solution increases more rapidly, suggesting that the volume occupied by the water inside the N-A-S-H product is smaller than the volume of the same quantity of water in bulk-like conditions in the pores.

Table 5.4 shows that a sample with Si:Al 1.5 and β = 1.5, fully reacted, should indeed display a chemical expansion of 3.44 cm^3/mol, which corresponds to 15.48 μl/g MK. This value is in line with the experimental result in Fig. 5.22 (15 μl/g MK), suggesting that H_2O:Na=1.5 may be considered as a good approximation for the molecular water content in geopolymers with Si:Al 1.5. This water content agrees with experimental results from the literature relating the Si:Al molar ratio to the molar water content of samples at the onset of drying shrinkage at room temperature [12]. Indeed, these literature results indicate that samples with Si:Al 1.6 start to display drying shrinkage when their water content decreases below H_2O:Na=2, whereas for samples with Si:Al 1.8 this happens when H_2O:Na=2.8, as shown in Fig. 2.12 c. Extrapolating the expected

Table 5.4: Example of molar volume calculations considering Si:Al =1.5, β=1.5, and α=1 . Legend: MW=molecular weight, MV= molar volume. The MV of 1 mole of product are the following: N-A-S-H = 86.64 cm^3/mol, SiO_2 = 22.67 cm^3/mol, H_2O = 18.02 cm^3/mol.

Products α**=1**	**Chem. formula**	**MW** [g/mol]	**Density** [g/cm^3]	**MV tot.** [cm^3/mol]
N-A-S-H	$2Na(AlO_2 \cdot 1.5SiO_2) \cdot 1.5H_2O$	195.21	2.253	173.27
Inert	$3.02\,SiO_2$	68.58	2.65	68.58
Solution	$9.3H_2O$	18.02	1.00	166.97
				408.82

value for Si:Al 1.5 the water content would be equal to 1.6 molecules of water per atom of sodium, close to the 1.5 indicated by the theoretical model and that could explain the measured chemical expansion.

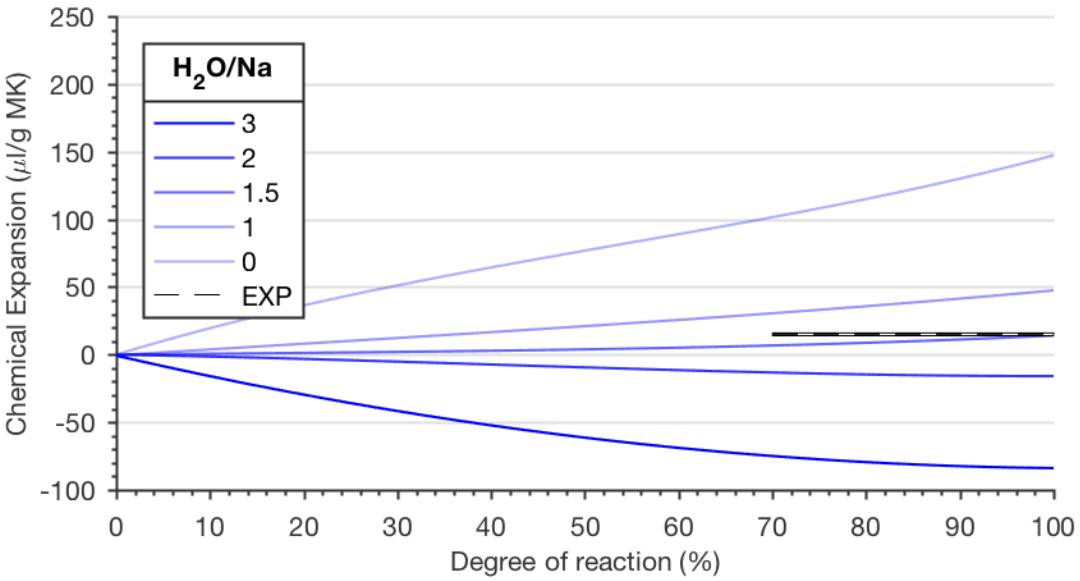

Figure 5.23: Chemical expansion as a function of the degree of reaction and H_2O/Na molar ratio. The experimental result in black corresponds to the chemical expansion measured in Fig. 5.22 and here is associated to a whole range of possible α, from 0.7 to 1, because of the uncertainty on the full geopolymerisation extent achieved during the chemical shrinkage experiment.

The model results discussed so far indicate that expansion is to be expected at full reaction (α=1) and that its extent is controlled by the amount of water in the skeletal structure of the geopolymer at the molecular scale. Fig. 5.23 shows how the chemical

expansion is predicted to evolve during the geopolymerisation reaction, i.e. when α increases from 0 to 1. The curves in Fig. 5.23 are obtained from the model referring to five different N-A-S-H structures with water content β ranging from 0 to 3. The trends in Fig. 5.23 are non linear, and showing more expansion as β diminishes. The non linearity reflects the nonlinear decrease of the density of the unreacted solution as the reaction proceeds, as previously shown in Fig. 4.16. Hence, Fig. 5.23 confirms that, for pastes with same Si:Al ratio, the amount of water in the molecular structure can be responsible for a wide range of possible extents of chemical expansion, with a theoretical chemical expansion of 150 μl/g MK when the molecular structure is assumed to be anhydrous (an unphysical but conceptually interesting limit behaviour), and with a chemical shrinkage of 90 μl/g MK when H_2O:Na molar ratio is equal to 3. The water content at the molecular scale has an impact both on the density of the N-A-S-H, and on the amount of water which remains available in the unreacted solution at the end of the reaction. In fact, the water that is not incorporated into the geopolymerisation product remains available in the paste as free water. As anticipated previously, the water confined in the molecular structure has a higher density than the water in the unreacted solution.

The theoretical model proposed here allows also to predict the dependence of chemical expansion on Si:Al ratio. This is quantified experimentally in Fig. 5.22, which shows that pastes with higher Si:Al ratios display less chemical expansion. The experiments in Kuenzel et al. [12] show that geopolymer samples with higher Si:Al also have higher water contents at the molecular level. Because the water in the N-A-S-H has a higher density than the water in the unreacted solution, on the basis of the chemical shrinkage model presented here, pastes with Si:Al 2 are expected to have a higher tendency to shrink than pastes with Si:Al 1.5.

Overall the theoretical model presented here provides an explanation for the extent of chemical expansion (or shrinkage) obtained experimentally, through an integrated approach which combines data from molecular dynamics simulations and experiments.

5.2.5 Autogenous shrinkage

Fig. 5.24 shows experimental results of autogenous shrinkage versus time. Samples with Si:Al 1.5 and Si:Al 1.75 show a first expansive behaviour followed by shrinkage after the first 1.5 days of measurements after setting. Instead, samples with Si:Al 2 display no strain for the first day, followed by shrinkage with a trend that is similar to the

other two mix designs. The initial expansion might result from the chemical expansion behaviour presented in the previous section, which followed a similar trend, viz. decreasing with the Si:Al ratio. The average values of autogenous strain at the end of the test are respectively: 50 μm/m expansion for Si:Al 1.5, 30μm/m shrinkage for Si:Al 1.75 and 260 μm/m of shrinkage for Si:Al 2. For traditional cement pastes based on calcium silicates, the literature reports values in the order of 1500-2000 μm/m of shrinkage depending on the type of cement [168, 169]. Hence, metakaolin geopolymers display much less autogenous shrinkage than calcium based cement paste, and this is good for applications where tightness against fluid permeation is crucial, for example in oil and gas well cementing. The literature lacks experimental data on autogenous shrinkage of metakaolin geopolymers, hence the results in Fig. 5.24 may only be compared with general observation on total shrinkage (autogenous and drying combined together into a single test that does not differentiate between them). Total shrinkage tests have indicated that increasing the Si:Al ratio causes an increase in the overall amount of shrinkage [13, 15].

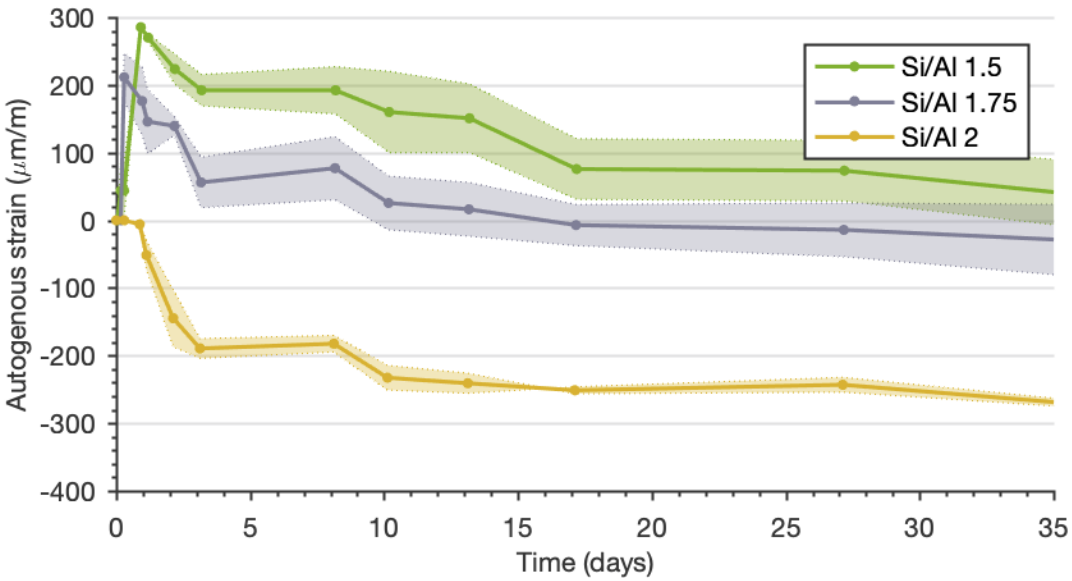

Figure 5.24: Autogenous strain versus time. Time equal to zero corresponds to the time of final setting (see Table 4.6), and the solid dots represent averaged measurements over four specimens for each mix design, while the shaded area indicates the standard error.

The curves shown in Fig. 5.24, suggest the presence of two competing processes, an expansive one that governs the first days of the reaction and a contracting one that dominates the following days. For traditional cements, autogenous shrinkage is ex-

plained with self desiccation caused by chemical shrinkage, but this is not applicable to geopolymers, as they undergo chemical expansion. The autogenous shrinkage of the geopolymers might instead have its origin in the intrinsic temporal evolution (viz. the ageing) of the geopolymerisation product. After the initial expansion, due to the formation of the geopolymerisation product, structural ageing might cause some of the pores in the N-A-S-H to collapse without significantly changing the molecular structure of the N-A-S-H itself. The pore collapse might be partly enabled by ripening processes at the mesoscale, resulting in coarsening of the mesostructures, observed in the SEM micrographs between 28 days and 1 year, as detailed in Section 5.2.1. If some of the mesopores close up causing a macroscopic autogenous shrinkage, then some water would need to be expelled from the sample, and indeed bleeding of water out of the samples was observed in the experiments reported here, with the samples with largest Si:Al displaying consistently maximum shrinkage and maximum bleeding. Overall this points to possible mechanism of autogenous shrinkage in geopolymer cements that is completely different from the autogenous shrinkage in traditional, self-desiccating, calcium-based cements. However, the theory presented here requires additional experiments to be confirmed.

5.3 Understanding ageing: first results

The early age behaviours discussed thus far (reaction kinetics and chemical and autogenous shrinkage) are signatures of nanoscale mechanisms that are also likely to influence the chemo-mechanical evolution of the material in the longer-term [170] hence, its durability. Similar to the results on early age shrinkage, the literature lacks data on long term drying shrinkage and creep of metakaolin geopolymers. This Section therefore introduces some first experimental investigations on long term properties of metakaolin geopolymers, in particular drying shrinkage tests and creep analysis up to more than 300 days after casting. Drying shrinkage has been tested both in environmental conditions, in a large humidity chamber with control of RH in the range of $50\pm$ 10% and T=23°C, and in boxes with salts to better control the humidity although for a shorter timescale only, respectively below 10% RH and ca. 40% RH. Creep has been tested in environmental conditions.

The results shown hereafter suggest that chemical composition and mesopore structure play a key role in the creep and drying shrinkage behaviours, as already

studied in the field of traditional PC [19, 171]. Hence, the second part of this Sections will show some first steps undertaken to develop a nanoparticle model of geopolymers to link the mesopore structure with chemical composition, providing a starting point to investigate the basic mechanisms that might control the long term behaviour of geopolymers. In particular, this section shows the derivation of interactions forces from the molecular scale model (hence chemistry-dependent) and how these lead to the formation of different mesopore structures at the large scale of nanoparticle agglomerates.

5.3.1 Long term behaviour: drying shrinkage and creep

Drying shrinkage at constant relative humidity. Fig. 5.25 displays weight loss versus length loss for three mixes with different Si:Al ratios exposed to two different drying conditions, for 50 days. The first condition, in Fig. 5.25 a., consists in placing the samples in a severe drying environment, reaching relative humidity below 10% by using silica gel as a drying agent. The second condition is achieved using potassium carbonate as drying salt, which sets the RH to 40%$\pm$ 4%. For both conditions the results are similar, with a clear trend that relates an increase in Si:Al ratio with higher amount of shrinkage. The severe drying conditions created by the silica gel expectedly lead to a final shrinkage that is larger compared to the case of a milder drying with potassium carbonate. This result is expected since the increase of drying shrinkage is considered to be inversely proportional to the relative humidity. In particular, as RH increases, the water evaporation within the specimen decreases, resulting in reduced drying shrinkage [172]. Specifically at 50 days (end of the test), Si:Al 1.5 displays a drying shrinkage strain of 0.004 at RH below 10%, compared to 0.003 at RH of 40%. The sample with Si:Al 2 instead shrinks by 0.032 at RH below 10%, compared to 0.028 at RH of 40%.

Fig. 5.25 a. and b. also show that the relationship between shrinkage strain and saturation is similar irrespective of the external humidity (and thus of the final strain at equilibrium). This similarly in trends is expected because, at a given saturation degree, the water in samples with same Si:Al is likely to occupy pores of similar size, irrespective of the external RH towards which the sample is evolving. This means that, for the same saturation degree, the position and curvature of the liquid-vapour menisci will be similar as well, and this is what is likely to control the drying shrinkage behaviour. Hence, the same saturation degree (proportional to the weight loss) should provide a

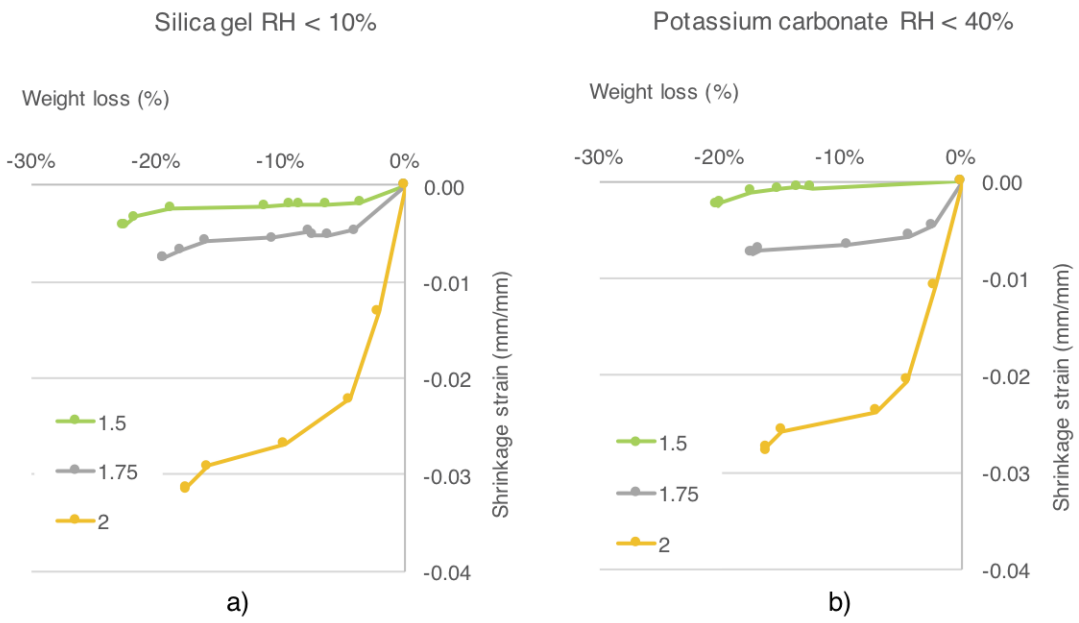

Figure 5.25: a) Weight loss versus drying shrinkage for samples exposed to silica gel (internal RH below than 10%) b) Weight loss versus drying shrinkage for samples exposed to potassium carbonate gel (internal RH below than 40%). The error is not displayed in the graph since it is always less than or equal to 0.001 mm/mm, hence below the width of the dots.

similar shrinkage strain as in Fig. 5.25. This result indicates that the drying shrinkage of metakaolin geopolymers is probably controlled by capillary pressure, as for traditional PC pastes.

Finally, Fig. 5.25 indicates that the weight loss is higher for samples with lower Si:Al ratios. This is in good agreement with the results in Sections 5.2.2 (in particular TGA results), 5.2.4 and 5.2.5, whereby samples with a lower Si:Al ratio have less water bound in the molecular structure of N-A-S-H, and thus more water occupying pores and able to evaporate upon reduction of RH within the ranges explored here (evaporable water).

Drying shrinkage of control creep specimens. Drying shrinkage in environmental conditions has been carried out on the control specimens cast for the creep test. The logarithmic plot in Fig. 5.26 shows that the results of the drying shrinkage do not display an asymptotic trend. This indicates that the drying shrinkage is a long-term

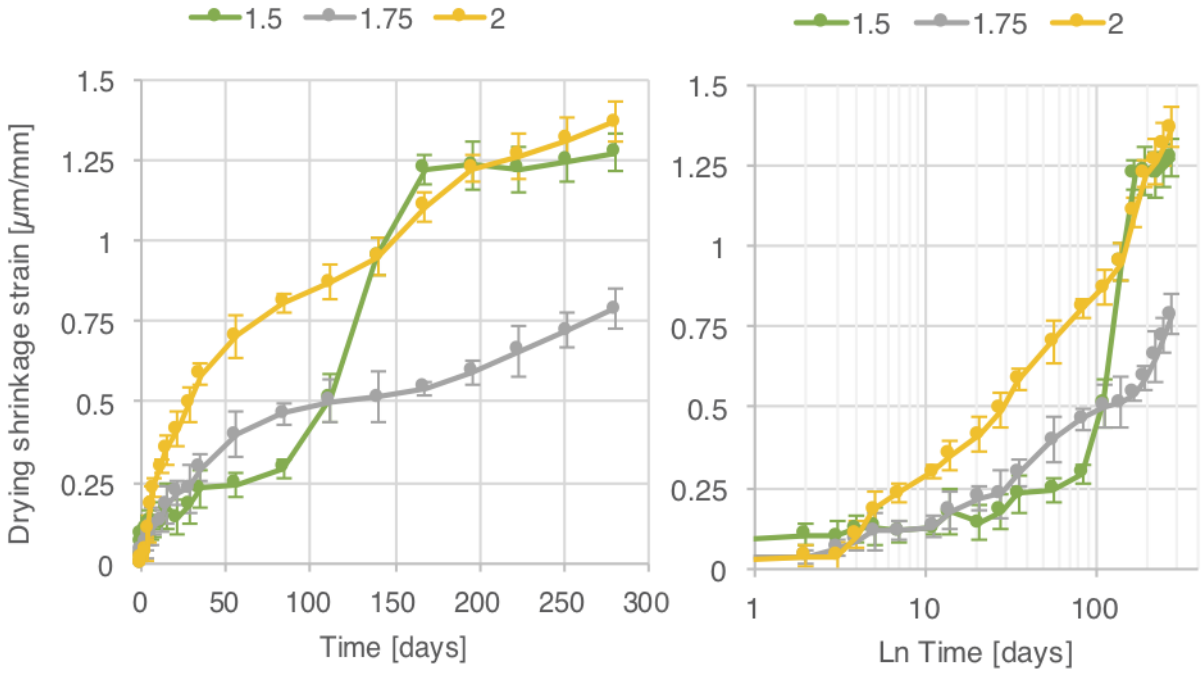

Figure 5.26: Drying shrinkage strain versus time, averaged over three samples for each mix design. Day zero represents the first day of testing, after 28 days of curing the samples in sealed bags.

phenomenon, which does not stabilise even after one year exposure at constant RH. Over the full duration of the analysis, Si:Al 2 undergoes the greatest amount of shrinkage with a shrinkage strain at 280 days equal to 1.366 μm/mm, followed by Si:Al 1.5 with 1.272 μm/mm and Si:Al=1.75 with 0.786 μm/mm. All mix designs display less drying shrinkage than ordinary cement paste: Bissonnette et al. [172], report drying shrinkage strain between 2.5 and 3 μm/mm after 300 days of testing an ordinary cement paste with water to cement ratio between 0.35 and 0.50 [172].

Fig. 5.26 shows that during the first 80 days of the test, a lower Si:Al ratio implies a smaller amount of drying shrinkage, which is in line with reported literature observations on metakaolin geopolymers [13, 15], and also agrees qualitatively with the results in Fig. 5.25. However, from day 80, the Si:Al 1.5 sample shows a considerable increase in drying shrinkage strain, reaching a final shrinkage that is comparable to the shrinkage of the sample with Si:Al 2. This acceleration of shrinkage of the paste with Si:Al 1.5 is shown consistently by both samples used to obtain the curve in Fig. 5.26, as indicated by the small error bars. From the observations in Sections 5.2.2, 5.2.4,

5.2.5, Si:Al 1.5 has less structural water at the molecular scale than Si:Al 2, and this has been identified as one of the causes of the formation of overall expansive products in the first day of the reaction. This expansion might be counteracting the contraction caused by desiccation, retarding the drying shrinkage of sample Si:Al 1.5, observed in Fig. 5.26. However, it is still unclear why this mitigation effect continues for more than 100 days, while the autogenous shrinkage strain, shown in Fig. 5.24, reverses its trend after one day. Another possible cause of the unusual shrinkage behaviour of the samples with Si:Al 1.5 might relate to a different saturation level or capillary pressure, however these are unlikely to explain the behaviour since all samples present similar sorption isotherms, as shown in Fig. 5.15. A third possible reason might have to do with permeability. Si:Al 1.5 displayed a mean pore size smaller then Si:Al 2, as shown in Fig. 5.19. The smaller pores could delay the drying of the sample, with Si:Al 1.5 samples displaying a retarded shrinkage compared to the other pastes. Despite these possible interpretations, the mechanisms causing acceleration of the shrinkage in the samples with Si:Al 1.5 are still not clear, and further experiments will be required to understand the origin of this unusual behaviour. Additional experiments on drying shrinkage and autogenous shrinkage should be performed on at least a new set (3 samples) of metakaolin geopolymer pastes with the same mix design. Furthermore, a comparison with geopolymer pastes cast with a different type of metakaolin, but with the same Si:Al ratio might be useful to understand the impact of the raw material. These additional data might confirm or deny the behaviour observed here.

Creep. Only one sample for each mix design has been tested for creep (see Section 4.3.1 for details), hence the plots presented in this Section do not show standard errors. Table 5.5 summarises the test parameters for each specimen. The applied load is equal to one third of the average failure load at 30 days (see Section 4.3.1), hence the applied stress is different for each mix design. The increase in compressive strength with the increase in Si:Al ratio is known in the literature, therefore the trend of applied stress in Table 5.5 is expected.

Fig. 5.27 displays the evolution of total strain with time for the three metakaolin geopolymer pastes, highlighting all the contributions to the total strain measured during the test. As indicated in Section 4.3.1 the basic creep strain is calculated with Eq. 4.25, repeated here for clarity:

$$\epsilon_{creep} = \epsilon_{tot} - \epsilon_{DS} - \epsilon_{elastic} \tag{5.2}$$

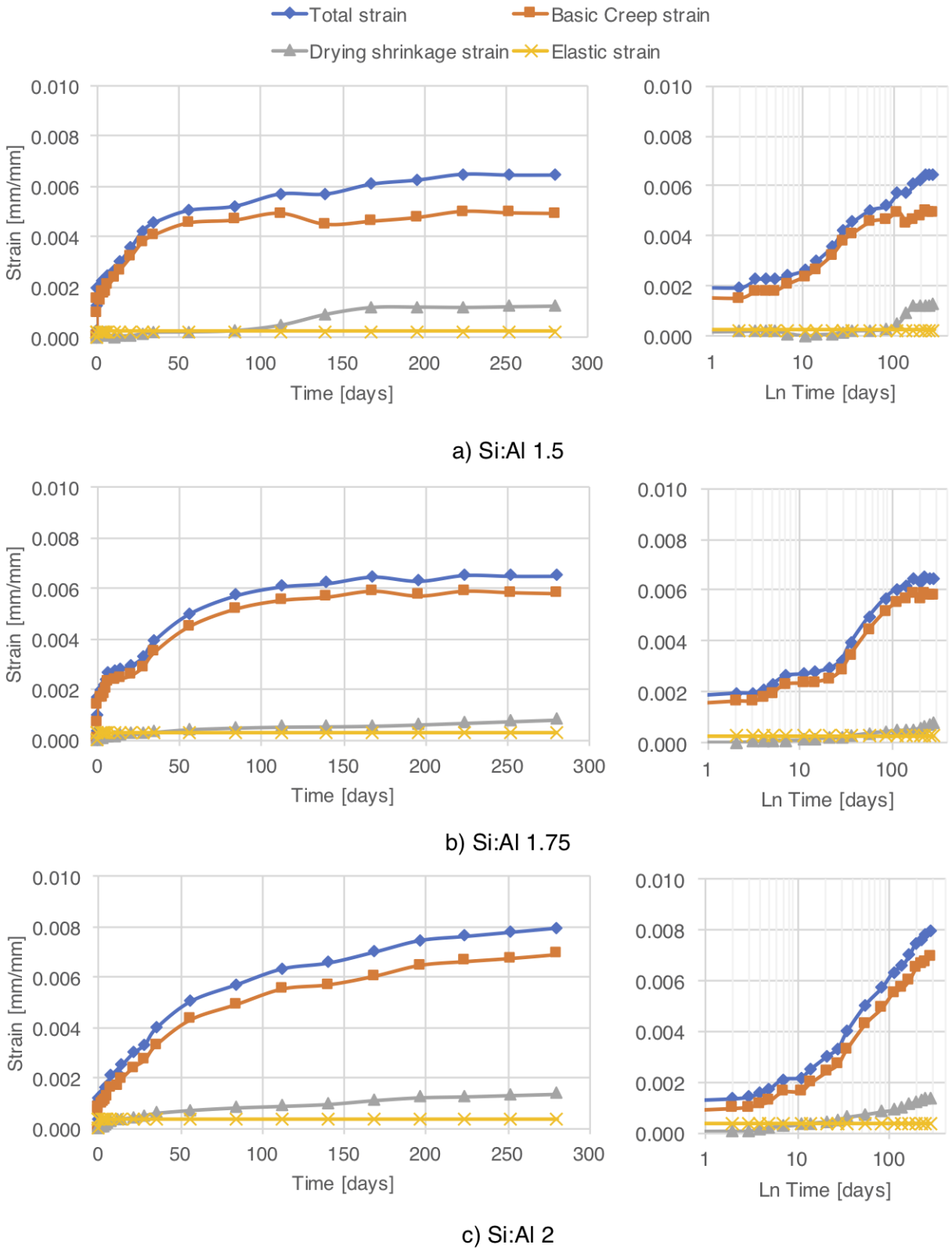

Figure 5.27: Different components of the creep strain versus time.

Table 5.5: Loading parameters for the creep test.

Si:Al ratio	Applied load [kN]	Mean diameter [mm]	Applied stress [MPa]
1.5	7.27	38.87	6.12
1.75	7.52	38.97	6.31
2	8.47	38.87	7.14

Fig. 5.27 shows that while Si:Al 1.5 and 1.75 seem to stabilise their basic creep deformation at the end of the test, reaching an asymptotic value, the basic creep deformation of Si:Al 2 continues to increase logarithmically beyond one year of testing. PC pastes also experience long-term logarithmic creep. Fig. 5.27a. also shows that the basic creep of samples with Si:Al 1.5 decreases between 100 and 150 days, in correspondence to the acceleration of shrinkage shown in Fig. 5.26. Instead, Fig. 5.27b. and c., show a more predictable behaviour without considerable fluctuations for the samples with Si:Al 1.75 and 2.

The results in Fig. 5.27 depend on the level of stress, hence cannot differentiate whether the increase of strain with Si:Al ratio is intrinsic to the material (i.e. a material property) or contextual to the higher stress level in samples with Si:Al 2 (see Table 5.5). In Section 4.3.1 three measures have been introduced to normalise the results: creep modulus, creep coefficient and creep compliance. These measures allow a comparison of the Si:Al ratio effect on the geopolymers creep behaviour irrespective of the level of applied stress.

Fig. 5.28 illustrates the creep compliance of each sample versus time. The final creep compliance for all sample is similar and ranges from 0.8 to 0.99 1/GPa increasing with the Si:Al ratio. On the other hand, as already pointed out in relation to Fig. 5.27, the compliance of samples with Si:Al 1.5 and 1.75 tends to an asymptote at 180 days whereas that of Si:Al 2 continues to increase logarithmically, hence longer-term measurements would be required in order to confirm whether the compliance of all samples will be the same past one year and weather eventually the sample with Si:Al 2 will also display a horizontal asymptote or not. Fig. 5.28 also shows that the compliance of sample with Si:Al 2 is initially smaller than that of the other samples, and only after 100 days it reaches values that are comparable to those of the samples with Si:Al 1.5 and Si:Al 1.75.

Fig. 5.29 displays the calculated creep coefficients as functions of time. The trend

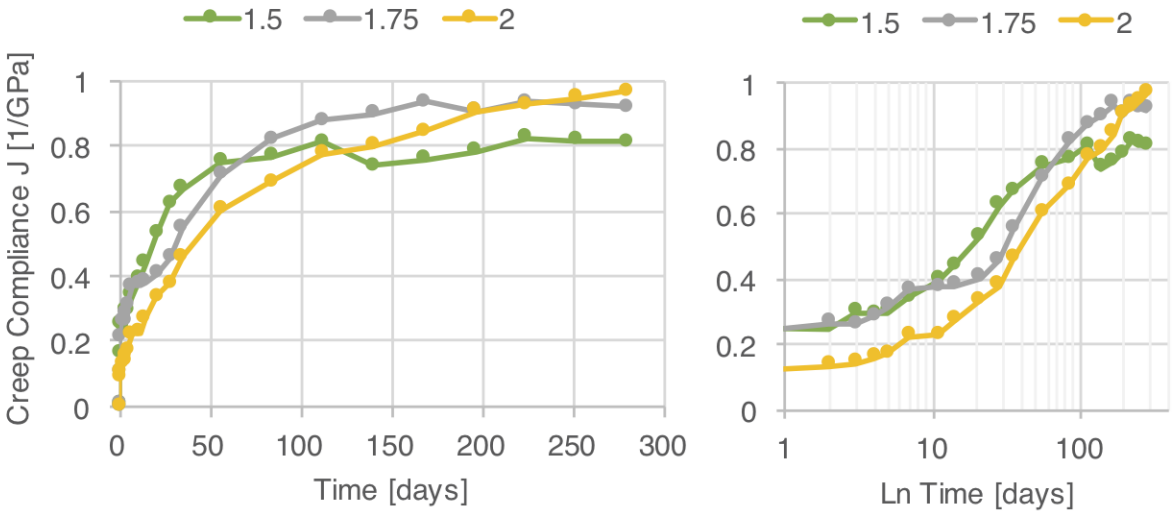

Figure 5.28: Creep compliance versus time.

displayed in this figure is opposite to the trend in Fig. 5.27, meaning that higher Si:Al corresponds to less creep. The evolution of the coefficient is quite different for the three samples: Si:Al 1.5 displays a constant creep coefficient already at 100 days, Si:Al 1.75 after 160 days, while the creep coefficient of the sample with Si:Al 2 keeps increasing logarithmically in time for the whole duration of the test. In addition, at early age the sample with Si:Al 1.5 displays a higher coefficient than samples with higher Si:Al ratio.

The creep modulus values in Table 5.6 range from 12.25 GPa to 10.20 GPa. These values are comparable to the results obtained on cement paste by Irfan-ul-Hassan et al. [173], ranging from 8.99 GPa to 12.9 GPa. The results in Table 5.6 show a creep modulus that decreases while increasing the Si:Al ratio, in accordance with the trends in Fig. 5.27 where samples with higher Si:Al ratio displayed more basic creep. Hence, from the creep modulus results to a higher Si:Al ratio corresponds a higher creep deformation. This result is opposite to the conclusion drawn from the creep coefficient. However, it should be noted that the creep modulus is calculated considering only the results from day 10 until then end of the test, and indeed Fig. 5.29 shows that the gradient of the coefficient versus time at later ages, e.g. after 100 days, is indeed greater in the samples with Si:Al 2. This means that, overall, samples with low Si:Al shrink faster in the short term (as shown by the slope of the creep coefficient), while samples with high Si:Al show a persistent logarithmic increment of creep in the long term. This might cause durability issues, since it is not clear whether the creep deformation will

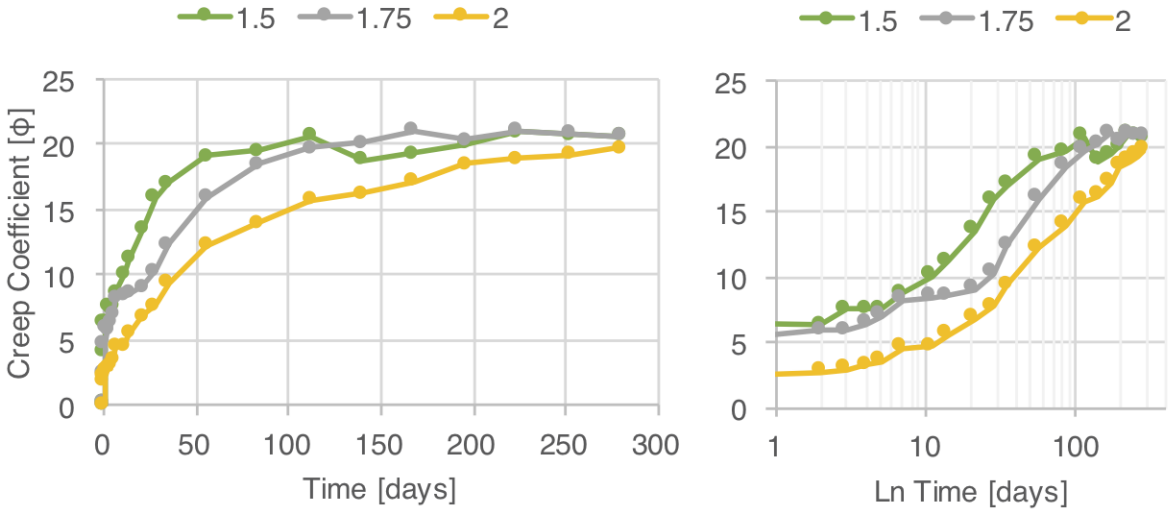

Figure 5.29: Creep coefficient versus time.

eventually stabilise to an asymptotic value or not.

Table 5.6: Gradient and creep modulus for the three mix designs.

Si:Al ratio	Gradient (G)	Creep modulus (C) [GPa]
1.5	0.0005	12.25
1.75	0.0006	10.51
2	0.0007	10.20

As mentioned in the literature review (Section 2.1.4), there is currently no literature available on the creep mechanisms or experiments of metakaolin geopolymer pastes. The results presented here are first, though only preliminary investigation, since only one sample per type is tested here. The only data available in the literature are for fly ash geopolymer concretes, which showed a basic creep strain of 200 μm/m [104], hence one order of magnitude lower than the metakaolin geopolymer pastes tested. This is an expected result considering that concretes usually undergo less creep than pastes, due to aggregates counteracting the deformation.

Nevertheless, at least one correlation can be discussed, concerning the relationship between the creep behaviour and the porosity of geopolymers. For ordinary calcium-silicate based cement pastes, a higher porosity usually correlates with higher creep.

This seems to hold also for the geopolymers paste studied here, as Si:Al 2 has an average porosity of 36%, while Si:Al 1.5 has 32%, and the sample with Si:Al 2 displays indeed higher creep than the sample with Si:Al 1.5.

The creep behaviour of geopolymers is expected to be mainly influenced by the mesoporosity (as is already known for PC pastes [174]) and by the chemical composition (Si:Al ratio). Consequently, the model proposed in the following Section will focus on porosity and eventually provide a complementary pathway to start understanding and predicting the long-term behaviour of geopolymers, despite the current shortage of experimental data in the literature.

5.3.2 Mesoscale model of the N-A-S-H gel

This Section presents first results from a new mesoscale model of the N-A-S-H product, idealised as an agglomerate of polydisperse nanoparticles interacting mechanically *via* effective interaction potentials. The model construction process is described in Section 4.3.2, together with an explanation of the parameters necessary to define the interaction potentials. In particular, Section 4.3.2, shows that the interaction potentials between particles can be entirely determined by two mechanical parameters at the molecular scale: the ultimate strain at which the molecular structure of N-A-S-H fails under tension (ϵ_{ult}) and the nanoindentation modulus *M*. These parameters are obtained in this Section and used to obtain interactions leading to nanoparticle agglomerates, whose pore size distributions are measured and compared to experimental results in previous Sections. The first part of this Section has been published in a conference paper titled *Towards a mesoscale model of geopolymers: interaction potential from the molecular scale* [35], and presented at the EURO-C conference in February 2018.

Mechanical parameters from the molecular model Sections 4.1 and 5.1 describe the molecular model of geopolymers based on fully polymerised defective structures. There, these molecular structure have been subjected to tensile strain using LAMMPS [137], obtaining stress strain curves that allow calculating here the indentation modulus (*M*) and the strain at failure ϵ_{ult} to parametrise interaction potentials at the mesoscale. Fig. 5.30 shows the stress - strain curves obtained from the defective molecular model with Si:Al 2, calculated in Section 5.1. The ultimate tensile strain, viz. the strain corresponding to the maximum tensile stress, defined as a reference to

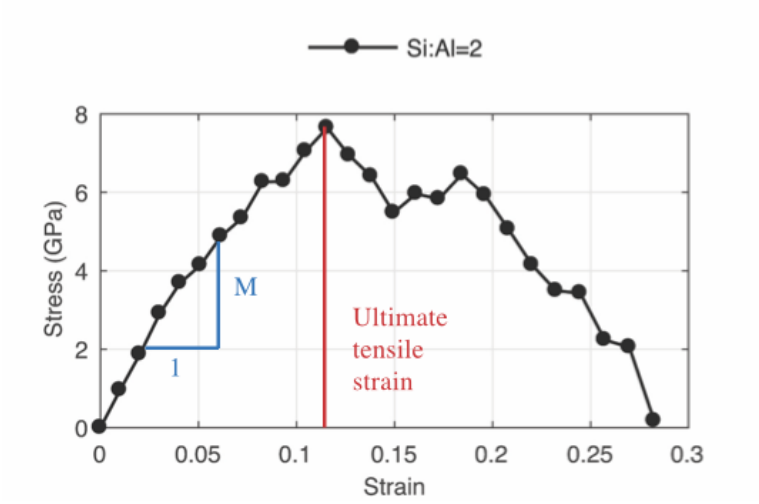

Figure 5.30: Stress strain graphs for the defective structure with Si:Al 2 [35].

calculate the parameter α is ϵ_{ult} =11.47%. The indentation modulus M is 75.18 GPa.

Interaction potential parameters.

Table 5.7: Interaction potential parameters depending on the particle size [35].

M [GPa]	α	σ_i **[Å]**	σ_j **[Å]**	$\overline{\sigma_{ij}}$ **[Å]**	$\epsilon(\sigma_i, \sigma_j)$ **[eV]**
75.18	6	50	50	50	1,035
75.18	6	50	100	75	3,107
75.18	6	50	500	275	56,973
75.18	6	50	1000	525	217,536
75.18	6	100	100	100	8,287
75.18	6	100	500	300	124,306
75.18	6	100	1000	550	455,790
75.18	6	500	500	500	1,035,888
75.18	6	500	1000	750	3,107,665

Table 5.7 collects interaction potential parameters for different particle sizes identified as most characteristic for the mesoscale model (from 5 to 100 nm), as highlighted by the imaging experiments, in Section 4.3.2. α = 6 leads to $f(\alpha)$= 0.0154, with $f(\alpha)$ depending on the mapping between interaction potential and elastic properties (more details in Eq. 4.31). Fig. 5.31 illustrates two curves of interaction potentials, one be-

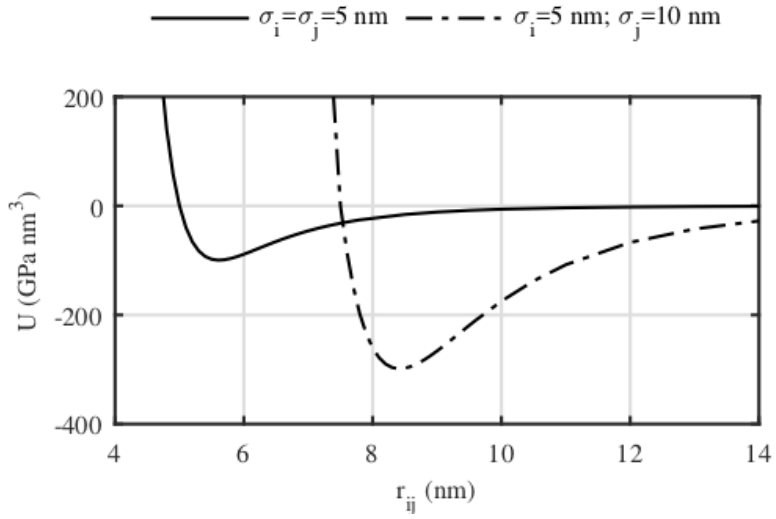

Figure 5.31: Interaction potential between two particles with same diameter of 5 nm and between two particles with different sizes.

tween particles with same size equal to 5 nm, and the other one between particles with different size (5 and 10 nm). The curves are obtained using the parameters in Table 5.7 and following the procedure described in Section 4.3.2. The depth of the potential well, i.e. the cohesion between particles, expectedly increases with the average size of the interacting particles.

Fig. 5.32 compares the effective forces computed from the derivative of the Lennard-Jones potential in Fig. 5.31 (see Eq. 4.29 in Section 4.3.2), and from the stress-strain graph in Fig. 5.30 integrated over the contact area between two particles with diameter of 2 nm. The figure shows that the initial slope of the force-displacement curve, which is related to the indentation modulus *M*, is indeed well captured by the generalised Lennard-Jones potential in Eq. 4.29. Also the interparticle distance corresponding to the maximum interaction force, which is related to the strain at failure ϵ_{ult}, is well captured. On the other hand, the effective Lennard-Jones potential underestimates the interaction force over most of the interaction range, hence the functional form in Eq. 4.29 may not be the optimum one to describe the large strain behaviour of geopolymers at the mesoscale. In this investigation, however, this is not an important issue because the focus is not on large-strain mechanical properties, but rather on the pore structure of undeformed mesostructures. To this end, a correct description of stress stemming from small strains (controlled by the indentation modulus) may be important, whereas forces at large strain are irrelevant. For studies where large-strain behaviour may be

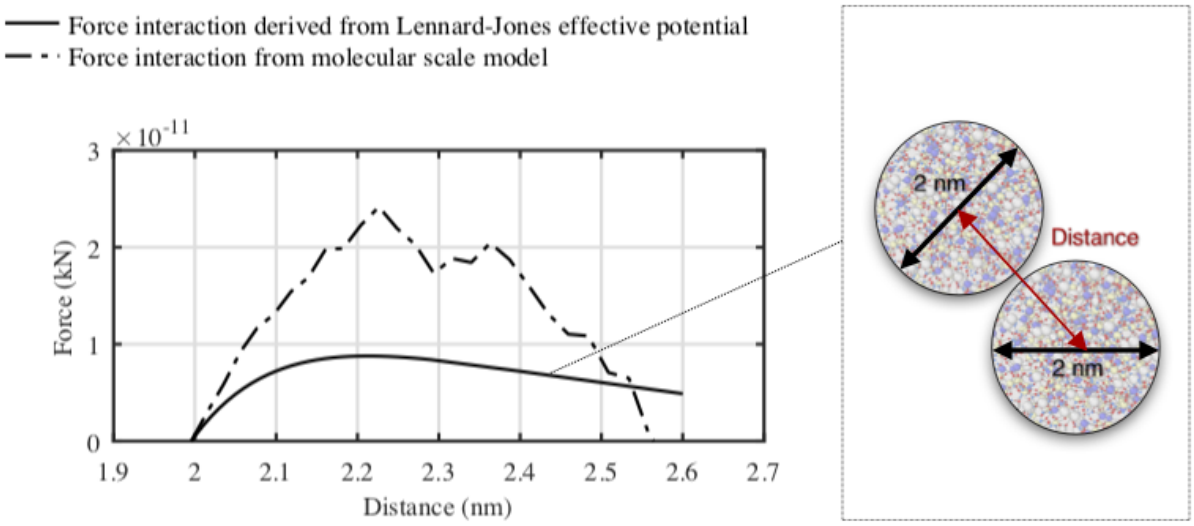

Figure 5.32: Force distance relationship obtained from the molecular model with Si:Al =2 and from the derivative of the effective interaction potential. The average particle size used is equal to 2 nm.

important, a viable alternative approach would be to directly tabulate in LAMMPS the interaction force and energy as functions of interparticle distance, as obtained from the molecular simulations. However, for this dissertation the Lennard Jones potential is preferred because it is more computationally efficient.

Pore size distribution. To build the mesostructural model, particles are added into a simulation box, and interact with the other particles via the previously described potentials and forces. The structures emerging from this aggregation process can be tuned to have different porosity ranges and different pore size distributions, trying to match the experimentally measured ones. In order to analyse the effect of different particle size distributions on the overall pore structure, two different packing fractions have been studied, as described in Section 4.3.2. Fig. 5.33 illustrates, from top to bottom, the two models at similar packing fractions (η, or solid fraction, namely the ratio between volume occupied by the solid nanoparticles and the volume of the simulation cell, including the pores between the particles). The model on the left column is built setting a preference for bigger particles over smaller ones. The upper snapshot represents a packing fraction η=0.28, hence a porosity ϕ=0.72, while the bottom one a packing fraction η=0.52, and a porosity ϕ=0.48. The model on the right column is built instead preferring small particles over bigger ones.

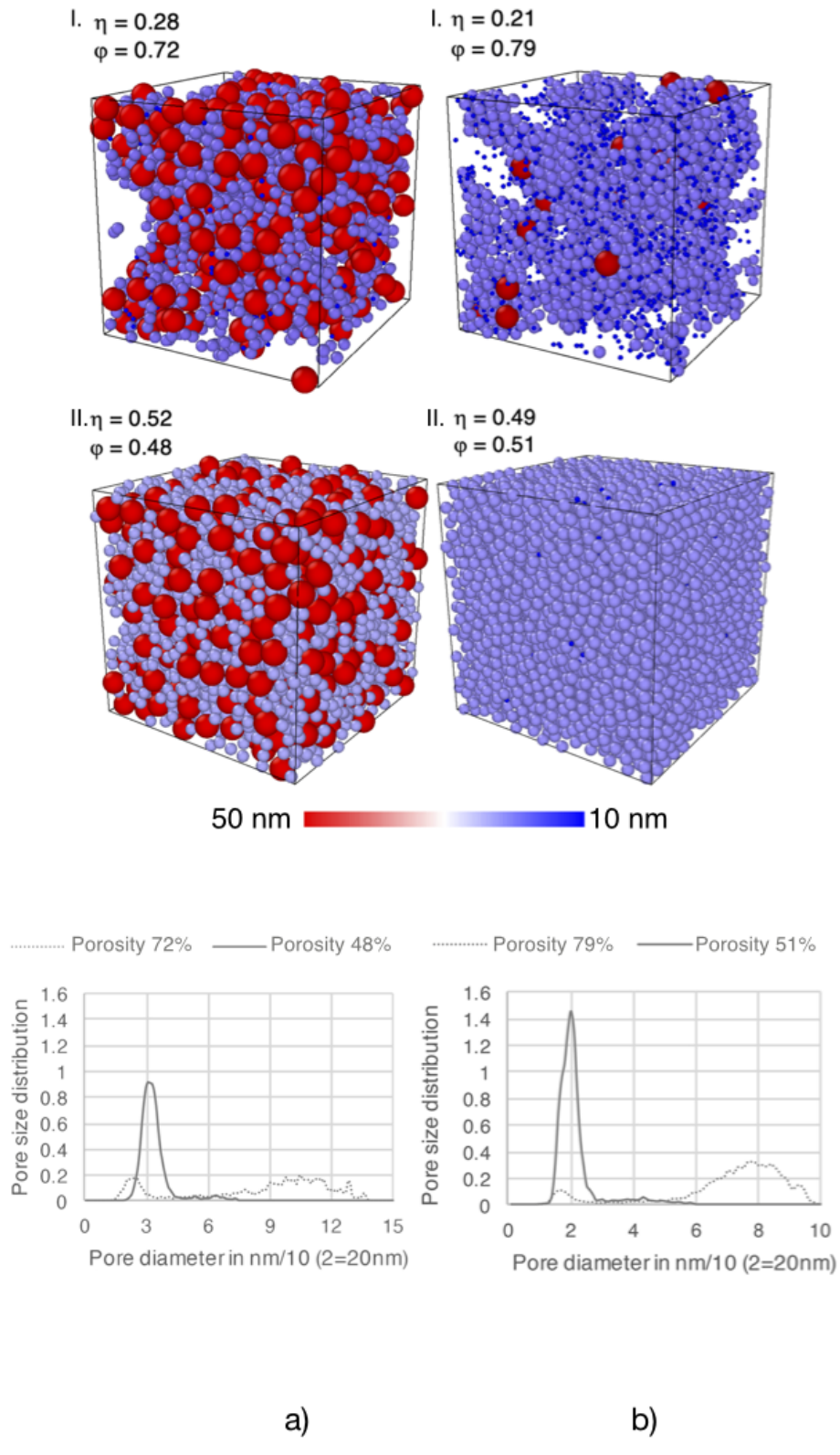

Figure 5.33: Snapshots of the two models with different packing fraction.

Also in this case the snapshot in the top row shows a porosity of ϕ=0.79, while the bottom one has a packing fraction η=0.49, and a porosity ϕ=0.51. The two packing fractions have been chosen to represent different densities of the N-A-S-H gel, which can be found in the same geopolymer paste in different polymerisation sites, or in pastes with different Si:Al ratio. Alternatively, the two packing fractions may as well describe the evolution of the N-A-S-H gel over time, with the structures with lower packing fraction representing N-A-S-H at an earlier stage of formation.

To study the effect of the gel density on the pore structure of the N-A-S-H, pore size distributions are simulated as described in Section 4.3.2 and displayed at the bottom of Fig. 5.33. The pore size distribution on the right hand side, shows the evolution of pore sizes going from a porosity of 79% to a porosity of 51%. The pore size distributions at 79% porosity displays two peaks: a broad one for pore sizes between 60 and 100 nm, centred at 77 nm, and a second peak at 15 nm. In the denser structure with 51% porosity, the broad peak disappears, while the peak centred at 15 nm shifts slightly towards 20 nm, increasing its magnitude, which indicates that many more pores per unit volume have now this characteristic size. On the left side, the results on the model obtained setting a preference for bigger particles over smaller ones, show the evolution of the pore distribution from a porosity of 72% to a porosity of 48%. The more porous structure displays one broad peak between 60 and 150 nm, centred at 115 nm, and a second peak at 20 nm. When densifying the structure to a porosity of 48% the broad peak disappears, while the peak centred at 20 nm shifts slightly towards 30 nm, also in this case, increasing its intensity.

The same behaviour has been observed in models of mesoporous calcium silicate hydrate in PC pastes, where a densification of the gel over time has been shown to correspond to progressively smaller average pore diameters. For C-S-H this has been explained with a progressive precipitation of newly formed solid hydration product in the gel pores [18]: a process that continues for months and years [149, 175].

The pore size distributions obtained with the mesoscale models can be compared with the MIP results in Fig. 5.19. The characteristic pore size obtained with MIP is 10 nm for Si.Al 1.5 and between 18 and 50 nm for Si:Al 2, with a single peak for Si:Al 1.5 and two peaks for Si:Al 2. The packing fraction obtained with MIP for both Si:Al 1.5 and Si:Al 2 is ca. 0.69. The simulated pore size distributions of the denser configurations, irrespectively of the particle size distributions, display similar characteristics: a main peak between 20 and 30 nm and smaller peaks between 40 and 60 nm. The actual value of 10 nm obtained with MIP is smaller than the simulated result in Fig. 5.33, but

consistent if considering the densification of the structure over time, which likely cause a shift of the main peak towards smaller average diameters.

The mesoscale models presented in this Section are a first quantitative description of the N-A-S-H geopolymerisation product, at scales that are intermediate between the molecular scale of atomistic simulations, and the macroscale of engineering models. The mesoscale models developed here have been obtained leveraging on mechanical properties obtained at the molecular scale. This type of model allows studying different types of densities of the N-A-S-H gel, which can represent different stage of the evolution of the geopolymer binding phase over time.

However, more research is required, e.g. on the type of interaction potential used. The generalised Lennard-Jones functional form of the interaction potential which has been presented, captures some key features of the mechanics at the molecular scale, but significantly underestimate the interaction forces at the mesoscale.

6

Conclusion

Contents

The literature review in Chapter 2 showed the interest in geopolymers within the scientific community, highlighting challenges that still have to be met to consider geopolymers as a valuable alternative to traditional cement. This dissertation discussed and addressed some of the open research questions, in particular those relating to the early-age behaviour of geopolymer cements. The pathway outlined in this dissertation is to leverage nanoscale modelling as a toolkit to better understand the macroscopic behaviour of geopolymers and, looking forwards, to nano-engineer these more sustainable alternatives to the current calcium-based cements. The main contributions of this research are summarised as follows:

1. **Development of a new molecular model of the geopolymerisation product (N-A-S-H)**:
   Understanding the molecular structure of sodium-aluminium-silicate-hydrate (N-A-S-H) geopolymers is the first necessary step in modelling and predicting the mechanics of these new cements. The existing molecular models of N-A-S-H in the literature are based on the assumption of an amorphous structure, but fail to capture the entirety of available experimental results at the molecular scale. The present dissertation instead has shown that multiple experimental observations can be explained by modelling N-A-S-H at the molecular scale as defective structures with a level of order that is intermediate between crystalline and amorphous. The resulting defective structures, with a range of chemical compositions, quantified by the Si:Al molar ratio, have been analysed in terms of structural and mechanical properties, and compared to fully amorphous and fully crystalline models with analogous chemical compositions, showing that the defective models indeed better match the experimental results. The main findings are:

   - In terms of XRD spectrum, the defective structure displays both an amorphous character and sharp peaks that are typical of crystalline features, in accordance with experimental results.
   - In terms of X-ray pair distribution function, only the defective structure captures the Na-O peak at 2.3 Ådisplayed in the experimental results. Also, the defective structure is the one that best captures the position and intensity of the Si-Si peak, at 3.1 Å.
   - A structural feature that distinguishes the defective structure from the amorphous and crystalline ones is the ring size distribution, which measures the topology of the aluminosilicate chains over the length of several nanometres.

Other measures that focus only on first or second neighbour molecules, such as bond lengths and angles, show a significant difference between crystalline and amorphous or defective, but are unable to distinguish between amorphous and defective structures. This means that the experimental observations mentioned above, regarding XRD and X-Ray PDF, are impacted by the structural topology extending beyond the molecular scale, and above the nanometre.

- The Young's moduli obtained during the simulated mechanical tests are between 45 and 75 GPa, which is in the range of experimental results from the literature. The moduli of the crystalline structures are the largest, followed by the defective structure and then closely by the amorphous ones. A clear correlation emerged between the degree of order and the modulus, whereas the density is shown not to correlate with the modulus.
- The structural disorder in the defective and amorphous structures reduces the maximum tensile stress that can be sustained, but it also leads to a more ductile behaviour which is desirable in mechanical applications. In particular, the defective structure is superior in that it combines higher strength and ductility compared to the fully amorphous one. Interestingly, this suggests that the longer-range correlations evidenced by the ring size distribution in the defective structure, being the only feature distinguishing the defective from the amorphous structures, might indeed play an important role in determining the large strain behaviour and failure mechanisms of the N-A-S-H.

The approach to obtain the molecular structures in this dissertation is general and transferrable, and may be used to model geopolymers derived from other precursors or activating solutions, *e.g.* low-calcium fly ash and potassium-based solutions. Even if complemented with additional chemical features, e.g. impurities, and directed towards other applications, the approach presented here would retain its ability to link chemistry and molecular structure with mechanical performance.

2. **Quantification and explanation of geopolymer volume changes at early ages**: A key new finding is that geopolymer pastes display chemical expansion, i.e. the volume of the products is larger than the volume of the reactants in the geopolymerisation reaction. This is an opposite behaviour compared to calcium-based cements, and a property that might be exploited to reduce autogenous and des-

iccation induced shrinkage at the macroscale, hence reducing the risk of cracking both at early age and with implications for durability too. For the first time the extent of the chemical expansion of geopolymer pastes has been quantified, and validated through a theoretical model which combines newly obtained experimental results, with data made accessible by the molecular model of the N-A-S-H product. Additionally, a quantification of autogenous shrinkage is also presented for the first time, and discussed in relation to the chemical expansion results. The main findings are:

- All the analysed samples, irrespective of their Si:Al molar ratio, undergo chemical expansion. The extent of the expansion is inversely proportional to the Si:Al ratio.
- The amount of structural water at the molecular scale, i.e. water that is strongly physisorbed in the cages and rings of the molecular structures of N-A-S-H, is responsible for controlling the extent of chemical shrinkage or expansion. The confined structural water has a higher density than the free water in the bulk. Hence, a higher water content in the molecular structure, corresponds to less expansion in the geopolymer paste during the formation of the N-A-S-H.
- The experimental observation that samples with higher Si:Al undergo less chemical expansion can be explained by the different water contents in the molecular structure of the N-A-S-H. The amount of such water is proportional to the increase in Si:Al molar ratio, hence samples with a lower Si:Al ratio have more structural water and thus tend to experience less chemical expansion or even chemical shrinkage. Indeed, the TGA results, presented in Section 5.2.2, showed that samples with high Si:Al ratio have more evaporable water, which is consistent with a lower content of structural water (hence more chemical expansion) at high Si:Al.
- Newly obtained data on autogenous shrinkage in Section 5.2.5 show an expansive behaviour followed by shrinkage. This behaviour is not unusual and presents similarities to PC pastes, but for the geopolymers this shrinkage cannot be explained as a result of the self-dessication. In traditional cements, self-dessication is the consequence of chemical shrinkage, but geopolymer pastes present chemical expansion instead. Hence, a different mechanism has been proposed here, that the ageing of N-A-S-H leads

to a closure of pores and mesopores (without significant changes of the molecular structure) which causes the experimentally observed autogenous shrinkage and bleeding of water out of the sample at the macroscale.

The last part of this dissertation is more explorative and presents first investigations of long-term behaviours that are key to engineering the durability of geopolymer cements. In particular, drying shrinkage and creep have been measured experimentally. The results on drying shrinkage indicate that samples with higher Si:Al ratios display more drying shrinkage and that all mix designs display less drying shrinkage than ordinary cement paste. The creep results instead are the first results of metakaolin geopolymers creep in the literature. They indicate that samples with a higher Si:Al ratios display more basic creep, and a consistently lower creep modulus, in the range of the creep modulus of traditional cement paste. The creep coefficient for the lowest Si:Al ratio equal to 1.5 stabilises in the early age (100 days), while the highest Si:Al ratio does not stabilise its behaviour in the test timeframe (one year).

Finally, to analyse the mesoporosity of geopolymers a first nanoparticle-based model of the mesopore structure of N-A-S-H is proposed, aiming to provide a pathway for the future development of a multi-scale analysis and understanding of geopolymer cement. An interaction potential for nanoparticle-based models of geopolymers has been developed starting from mechanical parameters obtained by molecular scale simulations. This multiscale approach allows preserving mechanical features of the molecular scale while obtaining porous structure that can reproduce some of the experimental results that are not accessible by molecular models only in particular the pore size distributions obtained from MIP and water sorption. The proposed approach to construct mesoporous structure of geopolymers can therefore be exploited in the sense of multi-scale modelling, to help identify which fundamental mechanisms control the chemo-mechanical stability and durability of these materials, and how these mechanisms are affected by chemical composition and processing [117, 149]. With additional experimental support, future investigations may lead to simulations to explain the relationship between creep behaviour and mesopore structure of metakaolin geopolymers.

6.1 Future work

The contributions of this dissertation can be used as a baseline to continue the ongoing research on geopolymers. Due to the modelling and experimental character

of the presented work, several pathways could be followed. A brief overview follows:

- **Molecular simulations.** The molecular model of the N-A-S-H geopolymerisation product might be used as a baseline to study several types of molecular models, through the addition of chemical compounds. Some examples are: PFA geopolymers (thought the addition of calcium), the effect of chloride ingress, nuclear waste encapsulation (through the addition of radioactive isotopes).

- **Mesoscale model.** Different polydispersities might be modelled to represent different type of mesostructures found experimentally. Additionally, the mesoscale model can be used to study long term properties, such as explaining the relationship between creep behaviour and mesopore structure of metakaolin geopolymers.

- **Experiments on long term behaviour.** Additional tests on the long term performance of geopolymers are needed to confirm the results obtained, and increase confidence in their application as structural materials. These tests might be performed both on geopolymer pastes, for a direct comparison, as well as on geopolymer mortars and concrete.

Ultimately, this would enable the simulation-guided optimisation of geopolymer cements, and the generation of confidence in their long-term performance. A better understanding of geopolymers durability, may be key to the commercialisation of geopolymer cements. Indeed, as highlighted in the Literature Review, the production of alkali activated materials in general, and of geopolymers in particular, involves less CO_2 emissions than traditional cement, but extended data on their durability are still lacking. A rigorous quantification of their performance in the long term could make an important difference between their success or their failure in the construction sector, assuming that other commercialisation barriers, such as supply chain and standardisation, will be overcome too.

7

Appendix

ACS APPLIED MATERIALS & INTERFACES

Research Article

Cite This: ACS Appl. Mater. Interfaces 2018, 10, 22809−22820

www.acsami.org

Atomistic Simulations of Geopolymer Models: The Impact of Disorder on Structure and Mechanics

Francesca Lolli,[†] Hegoi Manzano,[‡] John L. Provis,[§] Maria Chiara Bignozzi,[¶] and Enrico Masoero*[,†]

[†]School of Engineering, Newcastle University, Newcastle Upon Tyne NE1 7RU, U.K.

[‡]Condensed Matter Physics Department, University of the Basque Country (UPV/EHU), Bilbao 48940, Spain

[§]Department of Materials Science and Engineering, University of Sheffield, Sheffield S10 2TN, U.K.

[¶]Dipartimento di Ingegneria Civile, Chimica, Ambientale e dei Materiali, University of Bologna, Bologna 40131, Italy

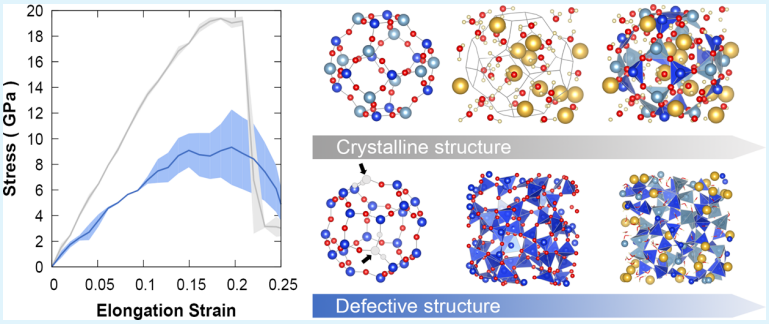

ABSTRACT: Geopolymers are hydrated aluminosilicates with excellent binding properties. Geopolymers appeal to the construction sector as a more sustainable alternative to traditional cements, but their exploitation is limited by a poor understanding of the linkage between chemical composition and macroscopic properties. Molecular simulations can help clarify this linkage, but existing models based on amorphous or crystalline aluminosilicate structures provide only a partial explanation of experimental data on the nanoscale. This paper presents a new model for the molecular structure of geopolymers, in particular for nanoscale interfacial zones between crystalline and amorphous nanodomains, which are crucial for the overall mechanical properties of the material. For a range of Si−Al molar ratios and water contents, the proposed structures are analyzed in terms of skeletal density, ring structure, pore structure, bond-angle distribution, bond length distribution, X-ray diffraction, X-ray pair distribution function, elastic moduli, and large-strain mechanics. Results are compared with experimental data and with other simulation results for amorphous and crystalline molecular models, showing that the newly proposed structures better capture important structural features with an impact on mechanical properties. This offers a new starting point for the multiscale modeling of geopolymers.

KEYWORDS: *geopolymers, atomistic simulation, molecular structure, mechanical properties, XRD, X-ray PDF, sodalite*

1. INTRODUCTION

Geopolymers, or more appropriately low-calcium alkali-activated aluminosilicate cement, are inorganic solids obtained from aluminosilicate precursors such as calcined clays, e.g., metakaolin $2SiO_2{\cdot}Al_2O_3$, or industrial byproducts, e.g, pulverized fuel ash or ground granulated blast furnace slag. These precursors are activated with alkaline aqueous solutions, usually based on sodium and potassium, which induce the dissolution of the precursors and the polymerization of AlO_2 and SiO_2 tetrahedra into a three-dimensional network on the molecular scale. Some water remains physisorbed while the cations (Na^+ or K^+) are bound ionically, providing positive charges that maintain overall neutrality and allow for the Al to be tetracoordinated. The macroscopic outcome of this reaction is analogous to the hydration of a cement paste, viz. the setting of a hard binding phase. This so-called "geopolymerization" reaction,[1] however, is fundamentally different from the hydration of traditional portland cements, and indeed the production of geopolymer binders causes significantly less CO_2 emissions compared to portland cement.[2] It is for this reason that geopolymers appeal to the construction industry, along with their good mechanical strength as well as thermal and acid resistance.[3] On the other hand, the exploitation of geopolymer cements is still limited by the inability to predict and control their durability. This calls for a better understanding of the linkage between chemical composition and degradation mechanisms.[4] Molecular simulations and nanoscale modeling provide a possible pathway to address this challenge.

Received: March 8, 2018
Accepted: June 13, 2018
Published: June 13, 2018

DOI: 10.1021/acsami.8b03873
ACS Appl. Mater. Interfaces 2018, 10, 22809−22820

Table 1. Three Molecular Structures Studied Here: Amorphous (Am), Crystalline (Cr), and Defective (De)[a]

name	Si−Al molar ratio	chemical formula	cell volume (nm^3)	atoms in the simulation cell	water content (atom %[b])
Am_1.5	1.5	$3SiO_2{\cdot}2Al_2O_3{\cdot}2Na_2O{\cdot}6H_2O$	41.26	4324	51.4
Am_2	2	$4SiO_2{\cdot}2Al_2O_3{\cdot}2Na_2O{\cdot}6H_2O$	38.73	3914	47.4
Cr_1	1	$2SiO_2{\cdot}2Al_2O_3{\cdot}2Na_2O{\cdot}6H_2O$	54.25	6144	56.3
Cr_1.4	1.4	$2.8SiO_2{\cdot}2Al_2O_3{\cdot}2Na_2O{\cdot}6H_2O$	50.07	5496	52.4
Cr_2	2	$4SiO_2{\cdot}2Al_2O_3{\cdot}2Na_2O{\cdot}6H_2O$	52.53	4856	47.4
De_1.5	1.5	$3SiO_2{\cdot}2Al_2O_3{\cdot}2Na_2O{\cdot}6H_2O$	44.95	4480	51.4
De_2	2	$4SiO_2{\cdot}2Al_2O_3{\cdot}2Na_2O{\cdot}6H_2O$	46.03	3840	45.0

[a]The Na/Al/H_2O molar ratio is set to 1:1:3 for all structures. [b]The total number of H and O atoms in water molecules divided by the total number of atoms in the cell.

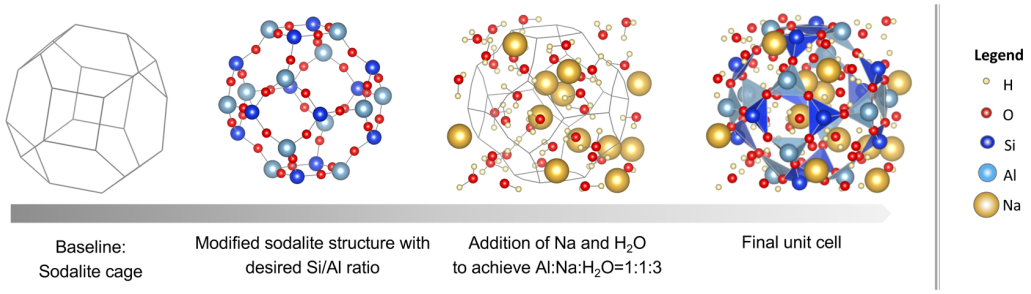

Figure 1. Simplified schematic of the construction process for a crystalline structure. All snapshots are obtained using VESTA.[24]

In the field of traditional cement science, molecular models of key hydration products[5−7] have provided a starting point for a multiscale modeling approach that is now starting to clarify the nanoscale origin of degradation mechanisms such as creep and shrinkage.[8−10] The multiscale modeling of geopolymers is less developed, with the first molecular simulations having been carried out only very recently.[11,12] Molecular models used in some geopolymer simulations today are based on fully amorphous (glassy) structures. Experimental characterization of these material does indeed show features that are typical of amorphous molecular structures: a broad peak in X-ray diffraction (XRD) at 2θ = 25°−35°, amorphous regions in transmission electron microscopy (TEM) images, and an X-ray pair distribution function (PDF) with only low intensity peaks beyond 5 Å atomic correlation distance.[13] On the other hand, the same experiments also show features that are typical of crystalline (or partially crystalline) structures: XRD peaks corresponding to faujasite, sodalite, and zeolite A (especially in samples prepared at high temperatures, e.g., 85 °C[14]), corresponding short-range peaks in the X-ray PDF,[13] and crystalline domains in TEM images.[15] To reconcile these data, geopolymers are sometimes described as nanocrystalline zeolitic networks within an amorphous aluminosilicate binding gel: the so-called "pseudocrystalline" model.[16] This leads to two possible scenarios:

1 if one considers the geopolymer as a uniform phase on the molecular scale, then this phase must be intermediate between amorphous and crystalline;
2 if one refers to the pseudo-nanocrystalline model, then the interfacial zones between nanocrystals and amorphous gel must be intermediate between the two and are likely to significantly impact the overall composite mechanics.

Both of these scenarios call for a representation of geopolymer molecular structures intermediate between glassy and crystalline, which is the objective of this paper.

This paper presents a new molecular model to describe the geopolymerization product of sodium silicate-activated metakaolin, hereafter referred to as N−A−S−H (sodium−aluminum−silicate−hydrate). The model is based on a defective crystal structure, obtained by creating vacancies into a sodalite cage and rearranging atoms to respect Loewenstein's principle[1] and full Q^4 polymerization of Al and Si tetrahedra, as indicated by experimental data.[17,18] Skeletal density, ring structure, pore structure, bond-angle distribution, bond length distributions, XRD, X-ray PDF, and mechanical properties (tensile stress−strain curves and non-affine displacements) are computed for a range of Si−Al molar ratios and water contents and then compared with available experimental data. Fully amorphous and fully crystalline model structures are also analyzed to assess the impact of disorder on the molecular scale.

2. METHODOLOGY

2.1. Siliceous Baseline Structures. Geopolymer molecular structures are created with different chemical compositions, described by Si−Al molar ratios of 1, 2, and 1.4−1.5, as shown in Table 1.

To consider different levels of disorder, three types of structure are built: a fully crystalline, a fully amorphous, and a defective crystal structure. The starting point is to construct a baseline structure containing only Si and O atoms: not including Al and Na in the initial baseline structures enables a clearer characterization of their skeletal structures. Adding Al and Na causes structural distortions, mainly because the Na cations tend to find their equilibrium positions at the center of the sodalite rings, altering the (Si,Al)−O−Si bond angles via electrostatic interactions. The Si−O baseline structures are first energy-minimized at T = 0 K and P = 1 atm, using the Polak−Ribiere version of the conjugate gradient method implemented in LAMMPS.[19] The baseline structures are then characterized using ISAACS,[20] quantifying in particular the bond length, bond angle, ring distributions, and pore size distribution. The

DOI: 10.1021/acsami.8b03873
ACS Appl. Mater. Interfaces 2018, 10, 22809−22820

ring distribution is computed using the King's shortest path criterion, with a ring being a closed path of nodes (Si atoms) and links (Si−O−Si bonds) connected in sequence without overlap.[20] The pore size distributions are obtained using the method by Pinheiro et al.,[21] with a probe radius of 0.1 Å (after checking convergence starting from a probe radius of 1 Å and progressively reducing it). This method is based on Voronoi tessellation and is implemented in the open source package Zeo++.[22]

2.2. Introduction of Al, Na, and Water. To convert the Si−O-only structures into model N−A−S−H structures (crystalline, amorphous, and defective), Si atoms are substituted by Al and Na atoms, and water molecules are added with initially random positions using the software Packmol,[23] as shown in Figure 1. Periodic boundary conditions are applied in all three directions, and the principles followed for all structures are as follows:

1 The number of added Na atoms is equal to the number of Al atoms in the structure, to satisfy charge neutrality, because Al is tetracoordinated and thus the Al-centered tetrahedron carries a net negative charge in the structure.
2 Three molecules of water (hereafter referred to as "structural water") are added for each Na atom. Structural water is defined as the minimum amount of water below which the material will undergo microstructural changes leading to drying shrinkage and microcracks. Drying shrinkage experiments have shown that extensive shrinkage deformations start only when the H_2O/Na molar ratio decreases below 3. Such a threshold ratio of ca. 3 has emerged from experiments in which geopolymer samples with Si−Al = 1.15−2.15 and H_2O/Na molar ratio = 5.5 were dried at 150 °C.[25] The drying caused a weight loss between 20 and 40% of the initial sample weight that, given the stoichiometry of the tested samples, was found to be consistent with a molar ratio H_2O/Na = 3.3−4.4 for water that is still present in the geopolymer at 150 °C. Similarly, Kuenzel et al.[26] ran a series of drying shrinkage experiments on geopolymer samples showing that, irrespective of the initial amount of water in the mix, extensive shrinkage started only when the residual water content decreased below H_2O/Na = 3. Thus, H_2O/Na = 3:1 is considered to be a reasonable estimation of structural water content in the N−A−S−H skeleton.
3 Loewenstein's principle is always respected, meaning that two Al tetrahedra cannot be linked by a single oxygen bond, and therefore each Al tetrahedron is always linked to four Si tetrahedra.[1] In reality, Na-based geopolymers display some Al−O−Al bonds but to such a small extent (e.g., 0.18% of T−O−T total bonds for Si−Al = 1.15[27]) that imposing a complete absence of Al−O−Al bonds leads to model structures that are more statistically relevant than what would be obtained if this constraint were removed.
4 No edge-sharing Al tetrahedra. When creating amorphous or defective structures with Al and Si tetrahedra, e.g., via heating−quenching or packing simulations, some tetrahedra often get linked to each other twice via two oxygen bonds.[11] This leads to a significant stretching of some O−T−O angles, which is thermodynamically unfavorable and unphysical when considering a room-temperature, hydrous structure. This may have a significant effect on the prediction of mechanical properties.
5 Full Q^4 polymerization, to obtain structures that are most statistically relevant, in agreement with the results of Al and Si nuclear magnetic resonance experiments.[17,18]

2.3. Structural and Mechanical Characterization. The N−A−S−H structures are first relaxed via energy minimization, using the Polak−Ribiere version of the conjugate gradient method in LAMMPS.[19] The structures are then equilibrated at P = 1 atm and T = 300 K via 1 ns of molecular dynamics (MD) in the NPT ensemble, also performed using LAMMPS (Verlet time integration scheme and an integration timestep of 0.1 fs). The NPT simulations are followed by 1 ns in the NVT ensemble, to verify the stability of potential energy and pressure. All simulations employed the ReaxFF interaction potential.[28] In ReaxFF, the interatomic bonding expressions are both bond-distance- and bond-order-dependent, and the atomic charges to compute the long-range Coulombic interaction are calculated on the fly by a charge equilibration method. As a result, ReaxFF is a very flexible force field and can reproduce chemical reactions for a wide range of structures. For instance, the same set of parameters can be used for the study of glasses and crystals with good accuracy.[29,30] The force field parameters used in this work are based on the Si/O/H[31] set, extended with Al/O/H[32] parameters for the study of aluminosilicate frameworks, and improved with a posteriori specific parameterization of the Si−O−Al angles and proton stability on aluminosilicate rings.[33] These parameters have been previously used to investigate silicalite and H-ZSM-5 aluminosilicate zeolites, their thermal stability, and their acid site chemistry.[32−34] In addition, the Si/O/H subset has been shown to reproduce the structural features of amorphous (sodium) silicate glasses.[35,36] To verify the ability of the chosen parameters to produce realistic elastic properties of aluminosilicates, the elastic tensor of faujasite has been computed, a sodalite-based zeolite with structural resemblance to geopolymers. The NaX faujasite analogue structure[37] was minimized using ReaxFF, and its elastic properties were obtained from the elastic tensor coefficients.[38] The unit cell parameters are in good agreement with the experimental ones, with a limited difference in volume (1.4%, as shown in Table 2). The cubic symmetry is broken because of the finite size effect of the simulation box and the consequent irregular distribution of Na counterions. The bulk modulus (K) of the zeolite is in very good agreement with the experimental measurement[39] and density functional theory simulations,[40] as shown in Table 2.

Table 2. Comparison between Literature Data on Faujasite and Parameters Obtained in This Study as Part of the Validation of the ReaxFF Potential

Faujasite	lattice parameters (Å)	K (GPa)
obtained values	a = 24.93	
	b = 25.16	36
	c = 25.56	
literature data	$a = b = c$ = 25.10	38.7,[39] 35[40]

The equilibrated N−A−S−H structures are then analyzed in terms of structural features and mechanical properties. The XRD patterns were simulated using the CrystalDiffract 6.5.0 program.[41] The patterns were generated using an instrumental

DOI: 10.1021/acsami.8b03873
ACS Appl. Mater. Interfaces 2018, 10, 22809−22820

peak broadening of 0.5° full width at half-maximum. ISAACS is used to compute the Fourier transform of the structure factor obtained using the Debye equation,[20] thus producing the X-ray pair distributions. Mechanical tests are simulated with LAMMPS[19] through tensile deformation of each simulation box by 1% of its length per step until rupture: strain increments in this range are typical in molecular simulations, where the absence of macroscopic defects enables significantly higher strain and stress levels compared to similar tests performed on the macroscale.[29] This increment has been chosen following a sensitivity analysis of different deformation steps (varying from 0.1 to 2.5% of the corresponding length of the box). After each deformation step, the structures have been relaxed via energy minimization (Polak−Ribiere version of the conjugate gradient method in LAMMPS[19]). The simulation box dimensions are kept fixed on the plane perpendicular to the loading direction: this generates a uniaxial strain scenario similar to that in nanoindentation or in atomic force microscope indentation experiments.[42] The simulated tests lead to stress−strain curves akin to those in Figure 2, from which one can compute elastic

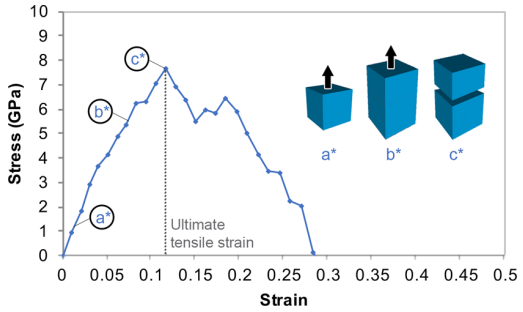

Figure 2. Stress−strain graphs for a defective structure obtained through MD simulation.

moduli, strength, and modulus of toughness. The strength is the maximum stress attained during the deformation process. The modulus of toughness is the area under the stress−strain curve; it quantifies the energy required to take a unit volume of material to complete failure. The elastic moduli quantify the amount of stress that produces a unit strain in the small-deformations regime, viz. when the strain tends to zero. The initial gradient of the stress−strain curve in Figure 2 is the so-called indentation modulus M, which is an elastic modulus related to the Young's elastic modulus E and Poisson's ratio ν by[43]

$$E = \frac{M(1+\nu)(1-2\nu)}{(1-\nu)} \tag{1}$$

Equation 1 assumes that the material is homogeneous, isotropic, and linear elastic: all of these conditions apply to the model structures in this paper, when the strain tends to zero. For the uniaxial strain scenario considered in this paper, the Poisson's ratio relates the stress in the loading direction i with the stress in its perpendicular directions j and k:[44]

$$\sigma_{jj} = \frac{\nu}{1-\nu}\sigma_{ii}; \qquad \sigma_{kk} = \frac{\nu}{1-\nu}\sigma_{ii} \tag{2}$$

Equation 2 allows computing the Poisson's ratio from the stresses in all three directions, these latter being tracked by LAMMPS at each step of the deformation process. The average magnitude of nonaffine displacements $\bar{\delta}_{na}$ has also been computed as

$$\bar{\delta}_{na} = \frac{\sum_i^N |r_i(\varepsilon) - r_{i,aff}(\varepsilon)|}{N} \tag{3}$$

where N is the number of atoms in the simulation box, r_i is the position of atom i at the strain level ε after energy minimization at that strain level, and the affine $r_{i,aff}$ is the position that the same atom i would have had at the same strain level ε if no minimization was ever performed during the tensile deformation test. Nonaffine displacements typically correlate with the onset and accumulation of plastic deformations and hence with the ductility or brittleness of the structure.[45]

2.4. Additional Details Depending on the Level of Disorder. *2.4.1. Crystalline Structures.* The crystalline structures built for this work are based on a simple sodalite framework which is common in zeolites[46] (see Figure 1). Indeed, experiments on geopolymers obtained from a metakaolin precursor show that, under certain conditions, faujasite and/or zeolite A can be formed,[47] whose basic building unit is the sodalite cage.[48−52]

2.4.2. Amorphous Structures. The starting structure for the amorphous N−A−S−H product is an amorphous SiO_2 glass developed by Sheikholeslam et al.[36] This has been preferred over the amorphous N−A−S−H model structures available in the literature[11] because the former satisfies all constraints that we listed in Section 2.2, in particular the Loewenstein's principle, the absence of edge-sharing tetrahedra, and the full Q^4 polymerization of tetrahedra. A simple Monte Carlo program has been written and used to substitute Si with Al while respecting Loewenstein's principle. Only two Si−Al

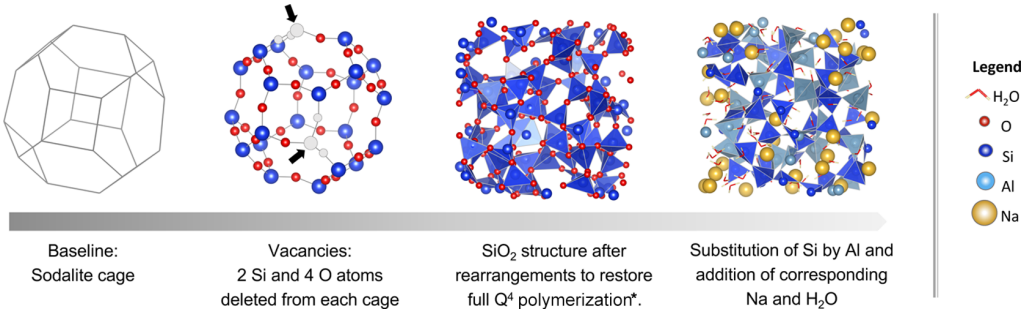

Figure 3. Simplified scheme of the construction process for a defective structure. All snapshots are obtained using VESTA.[24] *Some Si atoms are not visualized as tetrahedra because of the boundary conditions.

DOI: 10.1021/acsami.8b03873
ACS Appl. Mater. Interfaces 2018, 10, 22809−22820

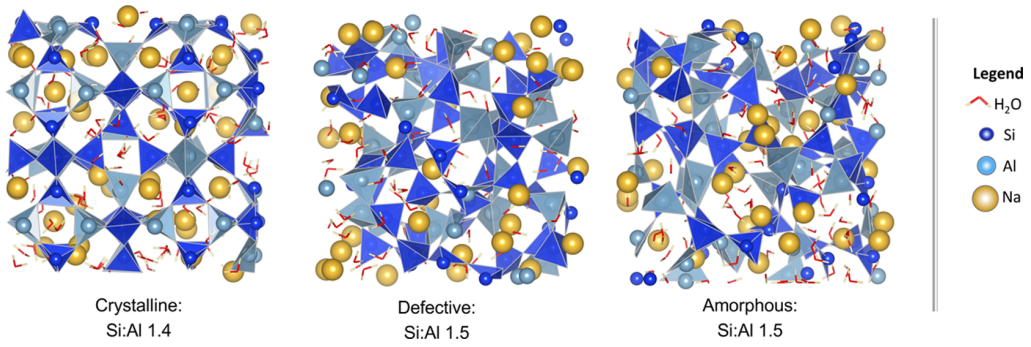

Figure 4. Structures with Si−Al = 1.4−1.5 and different degrees of disorder. The organization of Al and Si tetrahedra is highlighted. All snapshots are obtained using VESTA.[24]

molar ratios (1.5 and 2) were created; Si−Al = 1 was not achievable because of the disordered topology.

2.4.3. Defective Structures. The design process for the defective structure is described in Figure 3. The starting structure is the crystalline siliceous sodalite (without Al) equilibrated at P = 1 atm. Two SiO_2 molecules are randomly deleted from the sodalite framework to create vacancies; this is followed by MD simulations at P = 1 atm (NPT ensemble, 0.01 ns) and then in the NVT ensemble (0.01 ns). This leads to a defective structure with some O atoms left with dangling bonds. To restore full Q^4 polymerization, individual atoms are slightly displaced by hand and then the NPT equilibration is repeated until full polymerization is recovered. At this stage of the structure preparation, the simulations are performed at T = 1000 K to accelerate and enable a more effective relaxation of the structure before inducing next alterations. Subsequently, the final structures are equilibrated to 300 K for 2 ns, as explained in Section 2.3, before proceeding to any further characterization. This preparation protocol has the advantage of leading to structures with defects that nevertheless present some traces of the original crystal. Other preparation approaches, such as quenching, would lead to structures that are significantly more disordered than the intermediate level of disorder targeted here. The desired Si−Al ratio is obtained with the same substitution procedure as for the amorphous structures.

Overall, seven different model structures of N−A−S−H have been created and analyzed: three crystalline, two amorphous, and two defective. Figure 4 shows the equilibrated structures with similar Si−Al molar ratios and with the organization of tetrahedra highlighted. An increasing degree of disorder is noticeable from left to right in Figure 4.

3. RESULTS

3.1. Siliceous Baseline Structures: Bond Angle, Bond Length, Ring Distributions, and Pore Structure. Figure 5 shows the distributions of internal (O−Si−O) and external bond angles (Si−O−Si). The internal angle quantifies the distortion of the tetrahedra, whereas the external angle measures the relative orientation of tetrahedra in the short range (first neighbor). Longer-range topological information will be discussed later in terms of ring analysis. For a tetrahedral Si−O coordination, the O−Si−O internal angle distribution is expected to display a sharp peak at 109°.[20] This is indeed the result for the crystalline model structure in Figure 5. The amorphous and defective structures have a very similar distribution of O−Si−O angles, with a limited standard

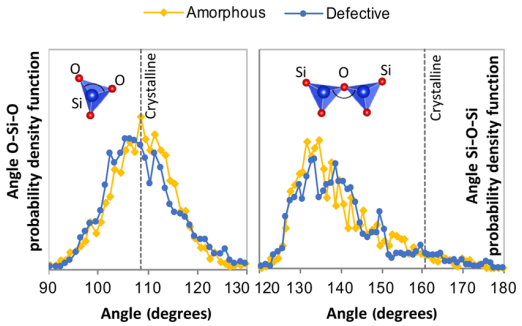

Figure 5. Internal (O−Si−O) and external (Si−O−Si) bond-angle distributions for the three siliceous baseline structures. The area under the curve is normalized to the same constant.

deviation, probably a consequence of the overall disorder. This indicates that the tetrahedra are only weakly distorted and that there are no edge-sharing tetrahedra, as also confirmed by visual inspection of the configurations.

The distribution of external Si−O−Si angles shows that the crystalline structure has wider angles compared to the defective and amorphous structures and that these latter two have similar distributions. Experiments show that the T−O−T angles in polymerized SiO_2 and AlO_2 can range between 120° and 180°,[53,54] which agrees with Figure 5. The smaller angles of the amorphous and defective structure compared to the crystalline structure suggest that the formers may be folded to some extent, which should result in higher densities. This is confirmed by the density values of the siliceous structures calculated at zero pressure. The densities of the amorphous and defective structures are similar to each other and, respectively, equal to 2.28 and 2.13 g/cm^3, whereas the crystalline structure has a lower density of 1.66 g/cm^3.

The Si−O bond length distribution in Figure 6 corroborates this point: the modes of the distributions for the amorphous and defective structures are shifted to the left compared to the bond length value of the crystalline structure. These shorter bonds are consistent with the disordered siliceous structures being denser than the crystalline one.

The angle analysis in Figure 5 highlights some differences between crystalline and disordered structures but does not indicate any appreciable difference between defective and amorphous structures. Such a difference emerges instead from the pore structure and topology of the structure over larger length scales. The ring analysis in Figure 7 provides one such topological measure. The ring analysis of the crystalline

DOI: 10.1021/acsami.8b03873
ACS Appl. Mater. Interfaces 2018, 10, 22809−22820

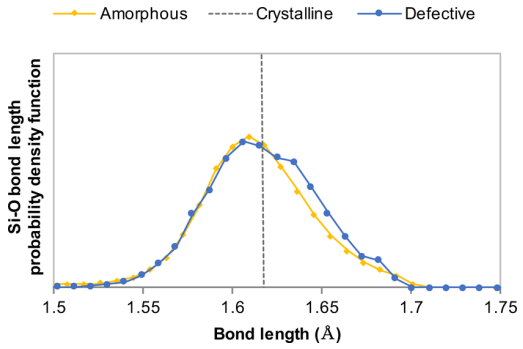

Figure 6. Bond length analysis of the three siliceous baseline structures (time averaged over 50 timesteps).

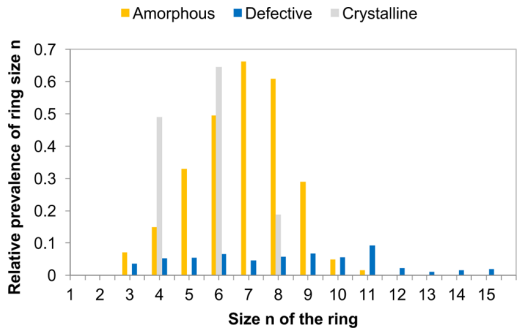

Figure 7. Ring size distribution of the siliceous baseline structures. The sum of all histograms is equal to the number of Si atoms.

structure is in good agreement with results in the zeolite literature, with prevalence of rings with size 4, 6, and 8 nodes.[55] The ring distributions of the amorphous and defective structures display a wider range of ring sizes, indicative of the greater medium-range disorder in these structures. Rings of odd size appear in both, and the range of possible sizes is significantly broader in the defective structure compared to the amorphous one, despite a similar size of the simulation cell and a similar number of atoms in the structure (see Table 1). The differences in ring size distribution between the amorphous and the defective structures may impact their mechanical performance. On the one hand, larger rings at the expense of smaller ones may indicate the presence of nanopores, which would decrease the density and mechanical properties. On the other hand, the formation of large rings may provide long-range correlations that may improve the large-strain mechanics of the system. It is also useful to note that the amorphous and defective structures have a very similar total energy per mole of Si, which means that they are equally probable in thermodynamic terms (as expected, the crystalline structure has instead a much lower energy).

Figure 8 shows the pore size distribution of the crystalline structure, correctly peaked around a diameter of 6.5 Å, which is the characteristic size of the sodalite cage shown in the snapshot. As expected, the pore structure of the crystalline structure is fully interconnected. The amorphous structure, instead, has a fragmented pore structure with smaller diameters, peaked around 4 Å. The presence of small pores is related to the presence of small rings with size 3 in Figure 7. The defective structure shows a pore structure that is indeed intermediate between the crystalline and amorphous structures. The pores are still interconnected to some extent, although less than that in the crystalline structure (see the snapshot in Figure 8). Furthermore, the pore size distribution displays both a primary peak at ca. 4.5 Å, close to that of the amorphous structure, and a secondary peak at 6.5 Å, which indicates some persisting features of the original crystal structure from which the defective one was obtained. The relationship between ring size distribution, pore structure, skeletal density, and mechanical properties will be discussed.

3.2. X-ray Diffraction. Figure 9 shows the comparison between experimental XRD data and simulations, highlighting

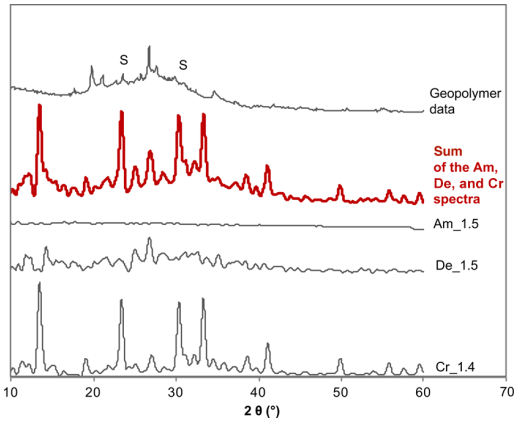

Figure 9. Simulation of X-ray diffractograms for three molecular models with Si−Al = 1.4 (crystalline structure) and Si−Al = 1.5 (amorphous and defective structures) and experimental XRD for a metakaolin geopolymer paste with Si−Al = 1.5. The metakaolin used is synthesized in the laboratories of Centro Ceramico (BO, Italy). Theoretical peaks for a siliceous sodalite structure.[57] All simulated XRD patterns are at room temperature and ambient pressure. Legend: S = theoretical sodalite peaks.

the effect of molecular disorder on the calculated XRD patterns of structures with comparable Si−Al ratios of 1.4−1.5. For all

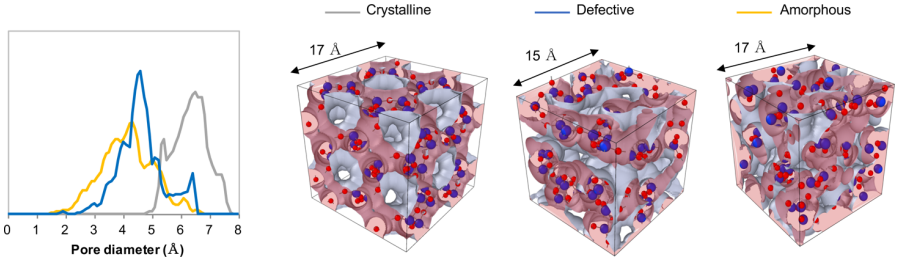

Figure 8. Pore size distribution and snapshots of the porosity of the siliceous structures. All snapshots are obtained using OVITO.[56]

DOI: 10.1021/acsami.8b03873
ACS Appl. Mater. Interfaces 2018, 10, 22809−22820

patterns, a peak broadening has been applied as explained in the Methodology. The experimental spectrum is from a metakaolin-based geopolymer paste with Si−Al = 1.5 cured at 23 °C for 28 days. The simulations are not expected to precisely match the experimental spectrum because the geopolymer is clearly not a pure crystal; thus, structural disorder, defects, and impurities at all scales will introduce or smoothen features in the XRD signals which cannot be fully described by a molecular model only. However, two key features can be targeted and discussed in relation to the model molecular structures presented here: the broad peak that emerges at $2\theta = 20°-30°$, which is typical of disordered alkali aluminosilicate gels, and the sodalite-related peaks at $2\theta = 24°$ and 32°. From the simulated XRD pattern, the increased degree of order from the amorphous to the crystalline structure is appreciable: the amorphous structure does not display meaningful peaks; the crystalline structure displays sharp peaks typical of sodalite; and the defective structure shows an overall disordered character but with sharper peaks (sodalite and quartz peaks at $2\theta = 27°$) compared to the amorphous structure. The red curve in Figure 9 is the result of the summation of the three spectra of crystalline, amorphous, and defective structure, considering that the sample has an equal amount of the three systems. The resulting pattern presents a broad peak between $2\theta = 25°$ and $2\theta = 40°$, which is clearly due to the contribution of the defective structure, while the amorphous system just adds a background noise. As a result, the defective structure better captures the coexistence of amorphous and crystalline features emerging from the experiments consistently with the two scenarios depicted in the Introduction.

Figure 10 shows that altering the Si−Al ratio has a very small impact on the overall XRD signal. By decreasing the Si−Al

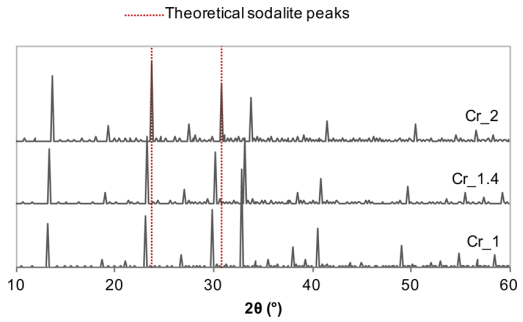

Figure 10. Simulated XRD patterns of the three crystalline structures, with varying Si−Al, showing the effect of the added water and Na. The curve for Cr_1.4 here is the same one as in Figure 9, but here the spectrum is shown without peak broadening.

ratio (thus increasing the number of Al, Na, and H_2O), the sodalite peaks slightly shift toward larger values of the 2θ angle. This is true irrespective of the level of disorder, but it is most visible from the crystalline structure, whose results are therefore shown in Figure 10. The shift is due to the swelling of the simulation box caused by the additional water. Because three H_2O molecules for each Na atom are considered and because one Na atom is added for each Al atom, Cr_2 contains less water and consequently the crystalline planes are closer and the angle is shifted toward higher values.

3.3. X-ray PDF. X-ray PDFs from simulations and experiments are compared in Figure 11. The experimental

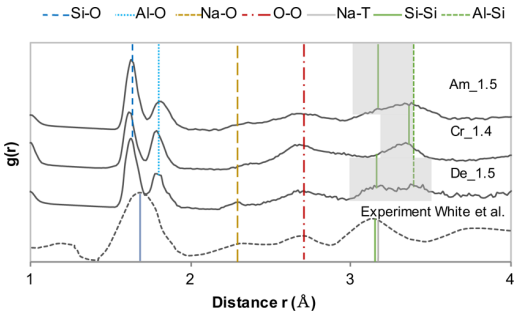

Figure 11. X-ray PDF of metakaolin-based geopolymers. Comparison between experiments[13] and simulations on structures with Si−Al = 1.4 and 1.5. T: tetrahedral (Si or Al).

data were discussed up to the first-neighbor peaks; hence, the analysis of the simulations here is focused on the same peaks. All model structures, irrespective of their degree of disorder, capture two of the experimental peaks in Figure 11.

- T−O peak ($r \approx 1.7$ Å). The X-ray PDF obtained from simulation discerns the peaks associated with Si and Al tetrahedra, whereas the experiment displays a single broader peak. This difference may be due to two factors combined: the limited resolution of the experiment compared to the molecular model and the possibility that the force field in the simulations might slightly overconstrain the interatomic distances to their equilibrium positions compared to the experiment. As expected, the level of disorder does not affect significantly these peaks in the simulations because they depend only on the tetrahedral coordination of Al and Si with O.
- O−O peak ($r \approx 2.7$ Å). All simulations display and correctly locate the first O−O peak, which depends on the relative position of neighboring tetrahedra as well as on the location of water molecules.

Conversely, two of the experimental peaks in Figure 11 are captured only by the defective model structure:

- Na−O peak ($r \approx 2.3$ Å). The defective structure is the only one clearly capturing this peak. In sodalite-based zeolites, the cations tend to occupy the center of ring structures; it is likely that the fact that the Na−O peak emerges only in the defective structure is related to its broader distribution of ring sizes compared to the amorphous and crystalline structures (see Figure 7).
- Na−T and T−T peaks ($r \approx 3.2$ Å). The experiment indicates a single broad peak encompassing all Na−T and T−T first neighbor peaks and centered at ≈3.1 Å. The crystalline structure displays a similar cumulative peak but shifts toward 3.3 Å. The amorphous structure displays a broader peak between 3 and 3.5 Å, resulting from the convolution of a broad Na−T peak, a Si−Si peak centered at 3.1 Å, and a sharp Si−Al peak at 3.3 Å. The defective structure is similar to the amorphous, to some extent, but the Al−Si peak at 3.3 Å is less sharp and broader, whereas the Si−Si peak at 3.1 Å is more marked. As a result, the overall PDF clearly shows the presence of a peak at 3.1 Å, as in the experiment. This indicates that the positions of the peaks at ca. 3.2 Å are sensitive to the level of disorder and that the intermediate disorder in the defective structure goes in

DOI: 10.1021/acsami.8b03873
ACS Appl. Mater. Interfaces 2018, 10, 22809−22820

the right direction of reducing the intensity of the Al−Si peak while increasing the intensity of the Si−Si peak. The agreement with the experiment leaves room for improvement, in which even in the defective structure, the Si−Si and Si−Al peaks have a similar intensity, whereas the experiment shows a prevalent peak at 3.1 Å (Si−Si). However, this limited difference in some T−T distances is not expected to cause any significant inaccuracy in the skeletal density and mechanical properties that will be evaluated next in this paper.

3.4. Wet Skeletal Density. The wet skeletal density includes the so-called structural water (see Methodology); the simulations in this work predict wet skeletal densities between ∼2.2 and ∼2.3 g/cm^3, which are in line with literature results (see Table 3). Figure 12 shows the trend of density as a function of the Al−Si (and Si−Al) molar ratios. The higher the Al−Si ratio is, the more the Na and thus water molecules are added to the structure (to keep the molar ratios Al/Na/H_2O to 1:1:3 as explained in Section 2.2). The values at Al−Si = 0 coincide with the densities of the siliceous baseline structures computed in Section 3.1. The density of the crystalline structure increases significantly with the Al−Si ratio, which is due to the presence of large pores, with a width of ca. 6.5 Å (see the pore size distribution in Figure 8). These pores can accommodate Na and H_2O molecules and hence additional mass, without any significant increase of the volume of the structure. On the other hand, the amorphous structure has only narrow pores; therefore, the addition of Na and H_2O, when the Al−Si is increased, requires some swelling of the structure. This compensation effect leads to similar densities at different Al contents, and even a slight decrease, as the Al−Si increases (because of the lower density of water compared to Al and Si). The defective structure sits in between the other two: a moderate addition of Al, viz. at Al−Si < 0.5 (so Si−Al > 2), causes an increase of density similar to that of the crystalline structure, although less marked, because only several "large" pores with a width of ca. 6.5 Å remain in the defective structure (see Figure 11). Further increasing the Al−Si ratio instead requires the defective structure to swell; hence, the density stabilizes and even decreases slightly for Al−Si > 0.5, similar to the trend displayed by the amorphous structure in the same range of Al−Si ratios.

Table 3. Skeletal Density of Metakaolin Geopolymers Considering Structural Water (Wet ρ_{sk})[a]

literature data	Si−Al	wet ρ_{sk} (g/cm^3)
Šmilauer et al., 2011[58]	1.22	2.372
Duxson et al., 2007[25]	1.15−1.65	1.8−1.7
Sadat et al., 2016[11]	1−2	2.03−2.50

[a]The literature data were obtained by He-pycnometry tests,[58] by comparing nominal density and pore volume,[25] and from simulations on a fully glassy model structure.[11]

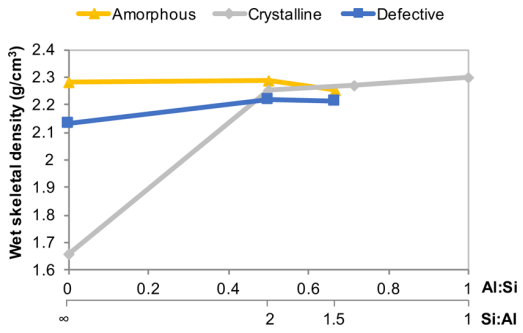

Figure 12. Wet skeletal density as a function of the Al−Si and Si−Al ratios.

3.5. Mechanical Properties: Elastic Modulus. Figure 13 shows the elastic moduli of all model structures in this paper,

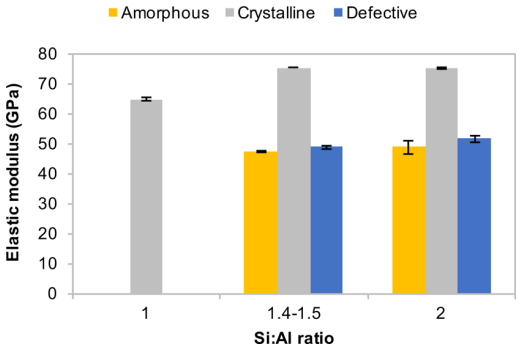

Figure 13. Young's elastic moduli as a function of the Si−Al ratio. Each elastic modulus is averaged over the three Cartesian directions.

averaged over the three Cartesian axes. The moduli of the crystalline structure are clearly the largest, followed by the defective structure and then closely by the amorphous ones. This indicates that the level of structural disorder has an important impact on the elastic moduli on the molecular scale. The chemical composition, here quantified by the Si−Al ratio, also plays a role. Literature data from macroscale experiments indicate that E increases with Si−Al.[25] An analogous, albeit weak, trend emerges overall from the simulations, with the crystalline structure showing a clear increase going from Si−Al = 1 to 1.5 and the amorphous and defective structures showing a mild increase from Si−Al = 1.5 to 2. On the other hand, one should note that the experimental measurements are on macroscopic samples; thus, the trend in E may be affected by heterogeneities on larger length scales (e.g., microstructural characteristics) that molecular simulations cannot describe. The wet skeletal density instead appears not to be a good predictor of trends in elastic moduli, unlike often observed in materials with similar chemical compositions on the macroscale. Indeed, by comparing Figure 13 with Figure 12, one can immediately appreciate that an increase in Si−Al ratio (Figure 12, read from right of left) corresponds to a decrease, whereas Figure 13 shows that the Young modulus increases. This means that the chemistry and topology on the molecular scale play an important role in determining the elastic properties of the geopolymer binder on a corresponding length scale, providing possible targets for material optimization working up from the nanoscale.

Table 4 summarizes the data on Young's modulus available in the literature. Using nanoindentation, Němeček et al.[59] measured an elastic modulus of ∼18 GPa for a N−A−S−H geopolymerization product: these measurements, however, include mesopores with a size of several nanometers, which are not described by the molecular simulations presented here. To extrapolate the experimental nanoindentation results to an equivalent elastic modulus without mesopores, one can consider the gel solid fraction of 0.6[58] indicated for the same experiment. Extrapolation to zero mesoporosity (viz. a solid

DOI: 10.1021/acsami.8b03873
ACS Appl. Mater. Interfaces 2018, 10, 22809−22820

Table 4. Literature Data for the Elastic Modulus (GPa) from *Simulations and **Experiments

	E (GPa)
**Němeček et al., 2011[59]—Mori Tanaka	44 ± 12
**Němeček et al., 2011[59]—self-consistent	88 ± 23
*Sadat et al., 2016[11]—glassy model structure	60−90
*Sanchez-Valle et al., 2005[61]—analcime	75
*Williams et al., 2006[60]—chlorosodalite	85

fraction of 1) using both the self-consistent and Mori Tanaka homogenization schemes (see Constantinides and Ulm[42]) is shown in Table 4. The simulation results in the present paper are indeed in line with the extrapolated nanoindentation results. Table 4 also shows that literature results from molecular simulations on zeolites, such as chlorosodalite[60] and analcime,[61] are also in the same range, as well as results from previous MD simulation of glassy geopolymer gels.[11]

3.6. Mechanical Properties: Large-Strain Tensile Behavior. Figure 14a illustrates the complete stress−strain graph for all structures with Si−Al = 1.4−1.5. All structures sustain stress on the order of several GPa and strain on the order of 0.1−0.5 before leaving the initial linear elastic regime. This is typical for material structures on the molecular scale,[5,29] whereas defects on larger scales are responsible for the experimentally observed typical values of macroscopic strength on the order of tens of MPa and corresponding strain at the elastic limit in the order of fractions of the percent. The defective and amorphous structures display a similar mechanical behavior, which is markedly different from that of the crystalline structure. The crystalline structure undergoes a brittle rupture and has a higher ultimate tensile stress compared to the amorphous and defective structures. These latter, instead, are more ductile; that is, they sustain a high stress for a wide range of strain (from 0.1 to 0.2−0.25) without sudden drops of the stress itself. In particular, the defective structures can sustain larger stress and strain compared to the amorphous structure. This implies a better ability to prevent crack propagation and failure, viz. fracture toughness, a property that can significantly impact the durability of the material. The different mechanical response to strain can be characterized in more detail by looking at the nonaffine displacements (see the description in Section 2.3). Figure 14b shows the accumulation of nonaffine displacements as a function of applied strain, only for the Si, Al, Na, and O atoms in the backbone solid structure, which are the depositories of mechanical strength. The accumulation of nonaffine displacements is related to the development of irreversible deformations.[45] Typically, a small level of nonaffine displacement ($\overline{\delta}_{na}$) is already accumulated during the initial linear stress−strain response of the material because of small irreversible rearrangements that have a negligible impact on the overall mechanics and elastic moduli.[45] All model structures presented here show such an initial small increase of $\overline{\delta}_{na}$ during the linear elastic stage (strain < 0.1). Instead, as expected, $\overline{\delta}_{na}$ increases sharply when the structures leave the linear regime and enter the regime of plastic deformations, eventually leading to failure. Figure 14b shows that the crystalline structure accumulates the least nonaffine displacement (almost zero through the whole linear elastic stage), whereas the amorphous structure has the largest $\overline{\delta}_{na}$ and the defective structure is in-between. This is a convincing trend because the ability to accumulate nonaffine displacements is expected to increase with the level of disorder, whereas order and symmetry add constraints to be overcome for $\overline{\delta}_{na}$ to develop. The loss of constraints and hence the better mobility (in response to strain) of atoms in the backbone structure, evidenced by the increase in $\overline{\delta}_{na}$ with the level of disorder, provide a rationale for the trend of Young elastic moduli and strength in Figure 14a, which are both decreasing with the level of disorder.

The results presented in Section 3.1 have shown that the only topological feature distinguishing the amorphous structure from the defective one is the ring analysis and the pore structure. This suggests that long-range correlations extending from the molecular scale to the mesoscale of several nanometers may play an important role in determining the large-strain and failure behavior of geopolymers. However, as for the elastic modulus results discussed earlier, structural features at even larger scales (microstructure) are also likely to significantly impact the large-strain behavior of the material. The results in Figure 14 therefore should be regarded as the necessary starting point for new multiscale models of geopolymer mechanics.

4. CONCLUSIONS

A new molecular model of the geopolymerization product (N−A−S−H), obtained by creating vacancies in a sodalite cage, is described in this paper. The resulting defective structures have been constructed with a range of Si−Al ratios

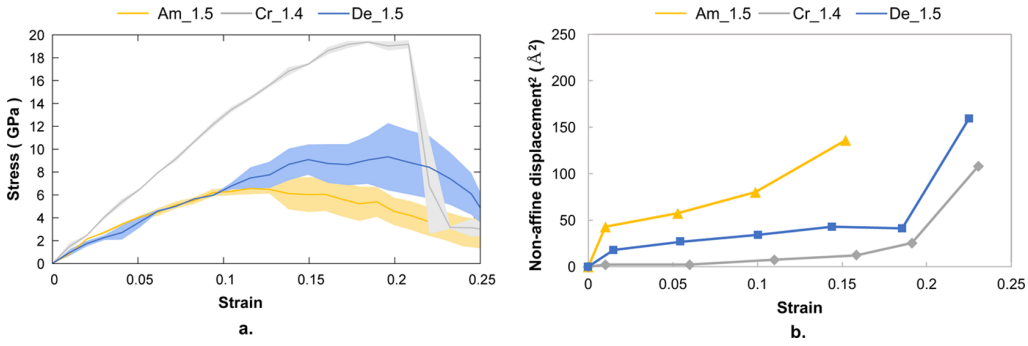

Figure 14. (a) Stress−strain response under tensile load. Curves obtained from MD simulations with strain applied in steps of 1%. Am_1.5 (amorphous with Si−Al = 1.5), Cr_1.4 (crystalline with Si−Al = 1.4), and De_1.5 (defective with Si−Al = 1.5). Each curve is obtained as the average from three repetitions; the shaded areas show the maximum and minimum stresses obtained from the repetitions. (b) Nonaffine displacement as a function of applied strain for the Si, Al, Na, and O atoms in the backbone solid structure.

DOI: 10.1021/acsami.8b03873
ACS Appl. Mater. Interfaces 2018, 10, 22809−22820

and have been analyzed in terms of structure and mechanical properties. The same analyses have also been carried out for fully amorphous and fully crystalline model structures with analogous chemical compositions. All structures, irrespective of their level of disorder, respected a set of crystallographic constraints including Loewenstein's principle, full Q^4 polymerization, and absence of edge-sharing tetrahedra. The main findings are as follows:

- The crystalline structure significantly differs from both the amorphous and defective ones in terms of bond angle, bond length, and ring size distributions and the pore structure analysis. By contrast, only the ring size distribution distinguishes the amorphous from the defective structures.
- In terms of XRD spectrum, the defective structure combines an overall amorphous character, namely, a broad halo peak over a wide range of $2\theta = 20°-30°$ angles with sharp peaks that are typical of crystalline features.
- In terms of X-ray PDF, several peaks are captured by all structures irrespective of their level of disorder. However, only the defective structure captures the Na−O peak at 2.3 Å. Also, the defective structure is the one that best captures the position and impact of the Si−Si peak, at 3.1 Å, on the overall signal. This result may be a consequence of the unique character of the ring size distribution for the defective structure, where rings can be much larger compared to those in the amorphous and crystalline structures.
- The wet skeletal densities of all model structures in this paper are in the range of experimental results from the literature. The trends of density with content in aluminum have been explained based on the pore size distribution of the baseline siliceous structures. In particular, the filling large pores (ca. 6.5 Å in width) with water and sodium in the crystalline structure and, to a lesser extent, in the defective structure explain the trend of increasing density with increasing Al−Si ratio.
- In terms of the mechanics, the initial linear elastic stress−strain behavior is characterized by Young moduli between 45 and 75 GPa, which are in the range of experimental results. The moduli are largest for the crystalline structure and lowest for the amorphous one, showing a mildly increasing trend with increasing Si−Al ratio. Density instead is shown not to be correlated with modulus: the degree of order and chemical composition play a more important role. The mechanical behavior at large strain indicates that the crystalline structure is the strongest, that is, it can sustain the highest tensile load, but its failure is brittle, which is an important drawback, in which it favors crack initiation and propagation. The structural disorder in the amorphous and defective structures reduces the maximum tensile stress that can be sustained, but it also leads to a more ductile behavior, which is desirable in mechanical applications. In particular, the defective structure is superior, in which it combines higher strength and ductility compared to the fully amorphous one. The analysis of nonaffine displacements indicates that structural disorder enables more mobility of the atoms in the T−O backbone structure, when tensile strain is applied. This provides a rationale for the observed detrimental effect of disorder on Young moduli and strength.

The molecular models presented here refer to N−A−S−H obtained from a high-purity metakaolin precursor activated with typical sodium-based solutions. The approach to obtain those structures, however, is general and transferrable to modelling geopolymers from other precursors or activating solutions, e.g., low-calcium fly ash and potassium-based solutions. Even if complemented with additional chemical features, e.g., impurities, and directed toward other application-specific geometries, the approach presented here would retain its ability to link chemistry and molecular structure with mechanical performance. By linking chemical composition with structural features, density, and mechanical properties, this paper is a starting point for the development of larger scale models of geopolymers. Multiscale models are the key to clarify which fundamental mechanisms control the chemo-mechanical stability and durability of these materials and how these mechanisms are affected by chemical composition and processing.[8,62,63] Ultimately, this will enable the simulation-guided optimization of geopolymer cements, the generation of confidence in their long-term performance, and the development of adequate design standards to support the deployment of these more sustainable cements in the construction sector.

AUTHOR INFORMATION

Corresponding Author

*E-mail: enrico.masoero@newcastle.ac.uk.

ORCID

Francesca Lolli: 0000-0003-4610-3171
Hegoi Manzano: 0000-0001-7992-2718
John L. Provis: 0000-0003-3372-8922
Enrico Masoero: 0000-0003-1791-6640

Notes

The authors declare no competing financial interest.

ACKNOWLEDGMENTS

The contributions of J.L.P. were funded by the European Research Council under the European Union's Seventh Framework Programme (FP7/2007-2013)/ERC Grant Agreement #335928 (GeopolyConc). H.M. acknowledges the financial support from the Departamento de Educación, Política Lingüística y Cultura del Gobierno Vasco (IT912-16), and the ELKARTEK project.

REFERENCES

(1) Davidovits, J. Geopolymers. *J. Therm. Anal.* **1991**, *37*, 1633−1656.

(2) Habert, G.; Ouellet-Plamondon, C. Recent Update on the Environmental Impact of Geopolymers. *RILEM Tech. Lett.* **2016**, *1*, 17−23.

(3) Pacheco-Torgal, F.; Abdollahnejad, Z.; Camões, A. F.; Jamshidi, M.; Ding, Y. Durability of Alkali-Activated Binders: A Clear Advantage over Portland Cement or an Unproven Issue? *Constr. Build. Mater.* **2012**, *30*, 400−405.

(4) Provis, J. L.; Duxson, P.; Van Deventer, J. S. J.; Lukey, G. C. The Role of Mathematical Modelling and Gel Chemistry in Advancing Geopolymer Technology. *Chem. Eng. Res. Des.* **2005**, *83*, 853−860.

(5) Manzano, H.; Moeini, S.; Marinelli, F.; van Duin, A. C. T.; Ulm, F.-J.; Pellenq, R. J.-M. Confined Water Dissociation in Microporous Defective Silicates: Mechanism, Dipole Distribution, and Impact on Substrate Properties. *J. Am. Chem. Soc.* **2012**, *134*, 2208−2215.

DOI: 10.1021/acsami.8b03873
ACS Appl. Mater. Interfaces 2018, 10, 22809−22820

(6) Papatzani, S.; Paine, K.; Calabria-Holley, J. A Comprehensive Review of the Models on the Nanostructure of Calcium Silicate Hydrates. *Constr. Build. Mater.* **2015**, *74*, 219−234.
(7) Hajilar, S.; Shafei, B. Nano-Scale Investigation of Elastic Properties of Hydrated Cement Paste Constituents using Molecular Dynamics Simulations. *Comput. Mater. Sci.* **2015**, *101*, 216−226.
(8) Pinson, M. B.; Masoero, E.; Bonnaud, P. A.; Manzano, H.; Ji, Q.; Yip, S.; Thomas, J. J.; Bazant, M. Z.; Van Vliet, K. J.; Jennings, H. M. Hysteresis from Multiscale Porosity: Modeling Water Sorption and Shrinkage in Cement Paste. *Phys. Rev. Appl.* **2015**, *3*, 064009.
(9) Ioannidou, K.; Krakowiak, K. J.; Bauchy, M.; Hoover, C. G.; Masoero, E.; Yip, S.; Ulm, F.-J.; Levitz, P.; Pellenq, R. J.-M.; Del Gado, E. Mesoscale Texture of Cement Hydrates. *Proc. Natl. Acad. Sci. U.S.A.* **2016**, *113*, 2029−2034.
(10) Bauchy, M.; Wang, M.; Yu, Y.; Wang, B.; Krishnan, N. M. A.; Masoero, E.; Ulm, F.-J.; Pellenq, R. Topological Control on the Structural Relaxation of Atomic Networks under Stress. *Phys. Rev. Lett.* **2017**, *119*, 035502.
(11) Sadat, M. R.; Bringuier, S.; Asaduzzaman, A.; Muralidharan, K.; Zhang, L. A Molecular Dynamics Study of the Role of Molecular Water on the Structure and Mechanics of Amorphous Geopolymer Binders. *J. Chem. Phys.* **2016**, *145*, 134706.
(12) White, C. E.; Provis, J. L.; Proffen, T.; van Deventer, J. S. J. Molecular Mechanisms Responsible for the Structural Changes Occurring during Geopolymerization: Multiscale Simulation. *AIChE J.* **2012**, *58*, 2241−2253.
(13) White, C. E.; Page, K.; Henson, N. J.; Provis, J. L. In Situ Synchrotron X-ray Pair Distribution Function Analysis of the Early Stages of Gel Formation in Metakaolin-Based Geopolymers. *Appl. Clay Sci.* **2013**, *73*, 17−25.
(14) Fernàndez-Jimènez, A.; Monzó, M.; Vicent, M.; Barba, A.; Palomo, A. Alkaline Activation of Metakaolin and Fly Ash Mixtures: Obtain of Zeoceramics and Zeocements. *Microporous Mesoporous Mater.* **2008**, *108*, 41−49.
(15) Kriven, W. M.; Gordon, M.; Bell, J. L. Geopolymers: Nanoparticulate, Nanoporous Ceramics Made Under Ambient Conditions. *Microsc. Microanal.* **2004**, *10*, 404−405.
(16) Provis, J. L.; Lukey, G. C.; van Deventer, J. S. J. Do Geopolymers Actually Contain Nanocrystalline Zeolites? A Reexamination of Existing Results. *Chem. Mater.* **2005**, *17*, 3075−3085.
(17) Duxson, P.; Provis, J. L.; Lukey, G. C.; Separovic, F.; van Deventer, J. S. J. 29Si NMR Study of Structural Ordering in Aluminosilicate Geopolymer Gels. *Langmuir* **2005**, *21*, 3028−3036.
(18) Favier, A.; Habert, G.; Roussel, N.; d'Espinose de Lacaillerie, J.-B. A Multinuclear Static NMR Study of Geopolymerisation. *Cem. Concr. Res.* **2015**, *75*, 104−109.
(19) Plimpton, S. Fast Parallel Algorithms for Short-Range Molecular Dynamics. *J. Comput. Phys.* **1995**, *117*, 1−19.
(20) Le Roux, S.; Petkov, V. ISAACS - Interactive Structure Analysis of Amorphous and Crystalline Systems. *J. Appl. Crystallogr.* **2010**, *43*, 181−185.
(21) Pinheiro, M.; Martin, R. L.; Rycroft, C. H.; Jones, A.; Iglesia, E.; Haranczyk, M. Characterization and Comparison of Pore Landscapes in Crystalline Porous Materials. *J. Mol. Graphics Modell.* **2013**, *44*, 208−219.
(22) Willems, T. F.; Rycroft, C. H.; Kazi, M.; Meza, J. C.; Haranczyk, M. Algorithms and Tools for High-Throughput Geometry-Based Analysis of Crystalline Porous Materials. *Microporous Mesoporous Mater.* **2012**, *149*, 134−141.
(23) Martínez, L.; Andrade, R.; Birgin, E.; Martínez, J. PACKMOL: A Package for Building Initial Configurations for Molecular Dynamics Simulations. *J. Comput. Chem.* **2009**, *30*, 2157−2164.
(24) Momma, K.; Izumi, F. VESTA 3 for Three-Dimensional Visualization of Crystal, Volumetric and Morphology Data. *J. Appl. Crystallogr.* **2011**, *44*, 1272−1276.
(25) Duxson, P.; Lukey, G. C.; van Deventer, J. S. J. Physical Evolution of Na Geopolymer Derived from Metakaolin up to 1000 C. *J. Mater. Sci.* **2007**, *42*, 3044−3054.
(26) Kuenzel, C.; Vandeperre, L. J.; Donatello, S.; Boccaccini, A. R.; Cheeseman, C. Ambient Temperature Drying Shrinkage and Cracking in Metakaolin-Based Geopolymers. *J. Am. Ceram. Soc.* **2012**, *95*, 3270−3277.
(27) Duxson, P. The Structure and Thermal Evolution of Metakaolin Geopolymers, Ph. D. thesis, Department of Chemical and Biomolecular Engineering, The University of Melbourne, 2006.
(28) Senftle, T. P.; Hong, S.; Islam, M. M.; Kylasa, S. B.; Zheng, Y.; Shin, Y. K.; Junkermeier, C.; Engel-Herbert, R.; Janik, M. J.; Aktulga, H. M.; Verstraelen, T.; Grama, A.; van Duin, A. C. T. The ReaxFF Reactive Force-Field: Development, Applications and Future Directions. *npj Comput. Mater.* **2016**, *2*, 15011.
(29) Manzano, H.; Masoero, E.; Lopez-Arbeloa, I.; Jennings, H. M. Shear Deformations in Calcium Silicate Hydrates. *Soft Matter* **2013**, *9*, 7333−7341.
(30) Manzano, H.; Masoero, E.; Lopez-Arbeloa, I. M.; Jennings, H. Mechanics and Physics of Creep, Shrinkage, and Durability of Concrete: A Tribute to Zdeňk P. Bažant. *Proceedings of the 9th Int. Conf. On Creep, Shrinkage, and Durability Mechanics, CONCREEP*, 2013; pp 86−97.
(31) Fogarty, J. C.; Aktulga, H. M.; Grama, A. Y.; van Duin, A. C. T.; Pandit, S. A. A Reactive Molecular Dynamics Simulation of the Silica-Water Interface. *J. Chem. Phys.* **2010**, *132*, 174704.
(32) Joshi, K. L.; van Duin, A. C. T. Molecular Dynamics Study on the Influence of Additives on the High- Temperature Structural and Acidic Properties of ZSM - 5 Zeolite. *Energy Fuels* **2013**, *27*, 4481−4488.
(33) Joshi, K. L.; Psofogiannakis, G.; Van Duin, A. C. T.; Raman, S. Reactive Molecular Simulations of Protonation of Water Clusters and Depletion of Acidity in H-ZSM-5 Zeolite. *Phys. Chem. Chem. Phys.* **2014**, *16*, 18433−18441.
(34) Bai, C.; Liu, L.; Sun, H. Molecular Dynamics Simulations of Methanol to Olefin Reactions in HZSM-5 Zeolite Using a ReaxFF Force Field. *J. Phys. Chem. C* **2012**, *116*, 7029−7039.
(35) Yu, Y.; Wang, B.; Wang, M.; Sant, G.; Bauchy, M. Reactive Molecular Dynamics Simulations of Sodium Silicate Glasses - Toward an Improved Understanding of the Structure. *Int. J. Appl. Glass Sci.* **2016**, *8*, 276−284.
(36) Sheikholeslam, S. A.; Manzano, H.; Grecu, C.; Ivanov, A. Reduced Hydrogen Diffusion in Strained Amorphous SiO2: Understanding Ageing in MOSFET Devices. *J. Mater. Chem. C* **2016**, *4*, 8104−8110.
(37) Porcher, F.; Souhassou, M.; Dusausoy, Y.; Lecomte, C. The Crystal Structure of a Low-Silica Dehydrated NaX Zeolite. *Eur. J. Mineral.* **1999**, *11*, 333−344.
(38) Manzano, H.; Dolado, J.; Ayuela, A. Elastic Properties of the Main Species Present in Portland Cement Pastes. *Acta Mater.* **2009**, *57*, 1666−1674.
(39) Baimpos, T.; Giannakopoulos, I. G.; Nikolakis, V.; Kouzoudis, D. Effect of Gas Adsorption on the Elastic Properties of Faujasite Films Measured using Magnetoelastic Sensors. *Chem. Mater.* **2008**, *20*, 1470−1475.
(40) Bryukhanov, I. A.; Rybakov, A. A.; Larin, A. V.; Trubnikov, D. N.; Vercauteren, D. P. The Role of Water in the Elastic Properties of Aluminosilicate Zeolites: DFT Investigation. *J. Mol. Model.* **2017**, *23*, 68.
(41) Palmer, D. C. *CrystalDiffract User's Guide*; CrystalMaker Software Ltd, 2015.
(42) Constantinides, G.; Ulm, F.-J. The Nanogranular Nature of C-S-H. *J. Mech. Phys. Solids* **2007**, *55*, 64−90.
(43) Galin, L. A.; Moss, H.; Sneddon, I. N. *Contact Problems in the Theory of Elasticity*, North Carolina State Univ Raleigh School of Physical Sciences and Applied Mathematics, 1961.
(44) Timoshenko, S. *Theory of Elasticity*, 3rd ed.; EngineeringSocietiesMonographs; McGraw-Hill: New York, 1969.
(45) Masoero, E.; Del Gado, E.; Pellenq, R. J.-M.; Yip, S.; Ulm, F.-J. Nano-Scale Mechanics of Colloidal C−S−H Gels. *Soft Matter* **2014**, *10*, 491−499.

DOI: 10.1021/acsami.8b03873
ACS Appl. Mater. Interfaces 2018, 10, 22809−22820

(46) Database of Zeolite Structures. http://www.iza-structure.org/databases/. accessed (April 20, 2018).
(47) Duxson, P.; Lukey, G. C.; van Deventer, J. S. J. Evolution of Gel Structure during Thermal Processing of Na-Geopolymer Gels. *Langmuir* **2006**, *22*, 8750−8757.
(48) Slavík, R.; Bednařík, V.; Vondruška, M.; Skoba, O.; Hanzlíček, T. Proof of Sodalite Structures in Geopolymers. *3rd Meeting on Chemistry and Life*, 2005.
(49) Oh, J. E.; Moon, J.; Mancio, M.; Clark, S. M.; Monteiro, P. J. M. Bulk Modulus of Basic Sodalite, Na8 [AlSiO4] 6 (OH) 2· 2H2O, a possible Zeolitic Precursor in Coal-Fly-Ash-Based Geopolymers. *Cem. Concr. Res.* **2011**, *41*, 107−112.
(50) Walling, S. A.; Bernal, S. A.; Gardner, L. J.; Kinoshita, H.; Provis, J. L. Phase Formation and Evolution in Mg (OH) 2−Zeolite Cements. *Ind. Eng. Chem. Res.* **2018**, *57*, 2105−2113.
(51) Sturm, P.; Gluth, G. J. G.; Simon, S.; Brouwers, H. J. H.; Kühne, H.-C. The Effect of Heat Treatment on the Mechanical and Structural Properties of One-Part Geopolymer-Zeolite Composites. *Thermochim. Acta* **2016**, *635*, 41−58.
(52) Alzeer, M.; MacKenzie, K. J. D. Synthesis and Mechanical Properties of New Fibre-Reinforced Composites of Inorganic Polymers with Natural Wool Fibres. *J. Mater. Sci.* **2012**, *47*, 6958−6965.
(53) Louisnathan, S. J.; Hill, R. J.; Gibbs, G. V. Tetrahedral Bond Length Variations in Sulfates. *Phys. Chem. Miner.* **1977**, *1*, 53−69.
(54) Yuan, X.; Cormack, A. N. Si-O-Si Bond Angle and Torsion Angle Distribution in Vitreous Silica and Sodium Silicate Glasses. *J. Non-Cryst. Solids* **2003**, *319*, 31−43.
(55) Baerlocher, C.; Meier, W. M.; Olson, D. *Atlas of Zeolite Framework Types*, 5th ed.; Elsevier: Amsterdam, New York, 2001.
(56) Stukowski, A. Visualization and Analysis of Atomistic Simulation Data with OVITO−the Open Visualization Tool. *Modell. Simul. Mater. Sci. Eng.* **2009**, *18*, 015012.
(57) Treacy, M. M. J.; Higgins, J. B. *Collection of Simulated XRD Powder Patterns for Zeolites*, 5th ed.; Elsevier: Oxford, 2007.
(58) Šmilauer, V.; Hlaváček, P.; Škvára, F.; Šulc, R.; Kopecký, L.; Němeček, J. Micromechanical Multiscale Model for Alkali Activation of Fly Ash and Metakaolin. *J. Mater. Sci.* **2011**, *46*, 6545−6555.
(59) Němeček, J.; Šmilauer, V.; Kopecký, L. Nanoindentation Characteristics of Alkali-Activated Aluminosilicate Materials. *Cem. Concr. Compos.* **2011**, *33*, 163−170.
(60) Williams, J. J.; Evans, K. E.; Walton, R. I. On the Elastic Constants of the Zeolite Chlorosodalite. *Appl. Phys. Lett.* **2006**, *88*, 021914.
(61) Sanchez-Valle, C.; Sinogeikin, S. V.; Lethbridge, Z. A. D.; Walton, R. I.; Smith, C. W.; Evans, K. E.; Bass, J. D. Brillouin Scattering Study on the Single- Crystal Elastic Properties of Natrolite and Analcime Zeolites. *J. Appl. Phys.* **2005**, *98*, 053508.
(62) Shvab, I.; Brochard, L.; Manzano, H.; Masoero, E. Precipitation Mechanisms of Mesoporous Nanoparticle Aggregates: Off-Lattice, Coarse-Grained, Kinetic Simulations. *Cryst. Growth Des.* **2017**, *17*, 1316−1327.
(63) Masoero, E.; Cusatis, G.; Di Luzio, G. C−S−H gel densification: The impact of the nanoscale on self-desiccation and sorption isotherms. *Cem. Concr. Res.* **2018**, *109*, 103−119.

DOI: 10.1021/acsami.8b03873
ACS Appl. Mater. Interfaces 2018, 10, 22809−22820

36th Cement and Concrete Science Conference
Cardiff, 5th & 6th September 2016
Paper Number P005

Experiments and nanoscale simulations of geopolymers: porosity and molecular structure.

F. Lolli, E. Masoero,
School of Civil Engineering and Geosciences, Newcastle University
F. Cucinotta
School of Chemistry, Newcastle University
M. C. Bignozzi, S. Manzi
DICAM, Scuola di Ingegneria e Architettura - Università di Bologna, Italy

ABSTRACT

Cement production is responsible for approximately 9.5% of global anthropogenic CO_2 emissions and as a consequence the increasing attention to sustainability issues has promoted research in alternative materials to cement paste, such as geopolymers. Current studies on geopolymers mainly focus on mechanical strength but research on their long-term mechanical performance and durability is still limited. Reducing the uncertainties around geopolymer durability requires a better understanding of the microstructural features and microscopic mechanisms that govern their chemo-mechanical behaviour. This can be pursued using simulations based on High Performance Computing (HPC), as previously experienced in the field of traditional cement. The aim of this study is to combine results from experimental analysis with HPC-based theoretical understanding of the fundamental mechanisms of material's reactivity and ageing. The molecular structure of N-A-S-H (sodium aluminosilicate hydrate) geopolymer is considered as a model of metakaolin geopolymers. First results on molecular simulations based on a simplified crystalline version of N-A-S-H with hydrosodalite structure and Al/Si = 1 are discussed. The simulations indicate a path to develop a more fundamental understanding of Na-Si and Na-OH concentration effect on the porous structure and on the skeletal density.

1. INTRODUCTION

Growing demand for more sustainable alternatives to cementitious materials has increased research in materials such as geopolymers, which are aluminosilicate sources (e.g. metakaolin) activated with alkali solutions. Understanding their long term properties will allow to evaluate their consequent success on large scale applications: for this reason durability study of geopolymer (GP) cements was defined as a key issue by the Rilem Technical Committee 224-AAM.

For a wider comprehension of mechanical properties of porous materials the nanoscale study is crucial, in particular to understand molecular structure of the solid and mesoporous network between 2 and 50 nm. Models at this scale have already proved to be successful in the field of traditional cement science, allowing to study the relationship between pore structure and water adsorption of an ordinary cement paste (Pinson et al., 2015) and to provide structural parameters to be used for a continuum model of reversible drying shrinkage. Theoretical modelling and simulation of geopolymers is still in a primitive state compared to traditional cement. The only molecular model of geopolymers available in literature (Sadat et al., 2016) was built considering the amorphous binder as aluminosilicate structure balanced with Na-cations, without considering structural water in the skeleton. The main problem for this simulation was that the final molecular structure displayed Al-O-Al bonds and adjacent edge-sharing AlO_4 tetrahedra, not respecting the Lowensteins' rule (Moloy et al., 2004).

Understanding the nanoscale origin and ultimately controlling the strength and long-term performance of geopolymers require a new synergy between experiments and molecular models. This study is a first step in combining models and simulations to analyse the durability of metakaolin geopolymers and it focuses on the acquisition of microstructural experiments data (Section 2) both with direct test on the mesopore structure and literature research on skeletal properties at the molecular scale. For the experiments MIP test (Mercury Intrusion Porosimetry) has been performed because durability of geopolymers is strictly linked to their porosity: compressive strength and elasticity depend on the total volume of pores, migration mechanism and migration rate vary depending on pore size. Results on the skeletal structure will then be considered to develop a first simple molecular model that includes structural water (Section 3). The molecular model is built to capture the structure and mechanical behaviour of N-A-S-H geopolymer at the nanoscale between 1 and 2 nm. The response of the molecular model to varying parameters such as concentration of activators and water content is presented.

2. Microstructure experiments

Porosity analysis: procedure and results. The geopolymer pastes analysed in this study were synthesized from flash calcined metakaolin (MK Argicem, Argeco, Toulouse, FR). The particle size distribution of the powder, performed at Centro Ceramico, Bologna, IT (Mastersizer 2000, Malvern Instruments) displays an average particle size of 40 µm (see Figure 1).

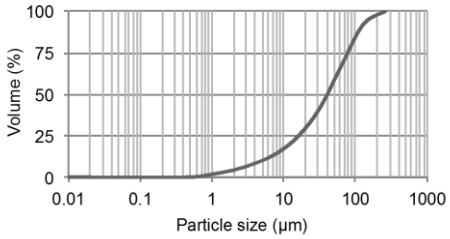

Figure 1. Particle size distribution MK Argicem**.**

To achieve Si/Al=1 and Si/Al=1.5 molar ratio, two different activating solutions were used: sodium hydroxide 8M (27.35% in weight of NaOH pellet, Sigma Aldrich and 72.65% of H_2O) and a commercial sodium silicate solution (Reoflux B, Ingessil S.r.l, Verona, IT: 29.01% in weight of SiO_2, 14.71% Na_2O and 56.28% of H_2O). Geopolymer samples were prepared as follows using the mix designs in Table 1: (a) mix of the activating solutions followed by a static phase of 30 minutes to achieve equilibrium; (b) addition of metakaolin and water followed by hand mix for 3 minutes to obtain an homogeneous paste; (c) transfer of the paste into a silicon mould which was gently wobbled for 5 minutes to remove entrained air. Samples have been sealed and cured a 60°C for the first 24 hours and then stored at room temperature (20±2°C and R.H.~55%) and sealed in plastic bags to avoid a fast loss of water.

Table 1. Mix design. Numbers used as suffix in the name of the sample describe the Si/Al ratio.

	GMK-A 1	GMK-A 1.5
Metakaolin (g)	500	500
NaOH 8M (g)	345	175.4
Na-Si solution (g)	0	225
Si/Al (mol/mol)	1	1.5

The porosity of the samples was investigated (Table 2). For the open porosity liquid water sorption (LWS) and mercury intrusion porosimetry (MIP) were used. LWS provides the total mass of water by a sample that is initially immersed in water for 24 hours and then dried at 100°C for 24 hours. These tests were performed on 4x2x1cm prisms and the absorbed water is expressed as a weight fraction relative to the dry mass of the sample. The MIP test (Carlo Erba 2000 with macropore unit 120, Fison Instruments) explores a wide range of pores. The test was carried out on 1 g samples cut from the prisms and dried under vacuum (mercury surface tension = 0.48 N/m, contact angle =141.3°).

Table 2. Result summary from MIP and LWS. Each data is an average of three tested samples.

	GMK-A 1	GMK-A 1.5
Average pore size - MIP (µm)	1.418	0.071
Total porosity – MIP (% vol)	41.59	34.49
Water absorbed - LWS (% wt)	31.07	28.20

Both MIP and water sorption indicate a more porous structure for GMK with Si/Al=1. Figure 2 shows result of MIP test: all the samples exhibit the same monodisperse trend describing a porosity which is characteristic of metakaolin geopolymers. The quantity of intruded mercury (i.e. the total open pore volume) is between 250 and 300 mm^3 per gram of geopolymer while characteristic pore size changes by one order: 1.4 µm vs 0.071 µm for GMK-A with Si/Al of 1 and 1.5 respectively.

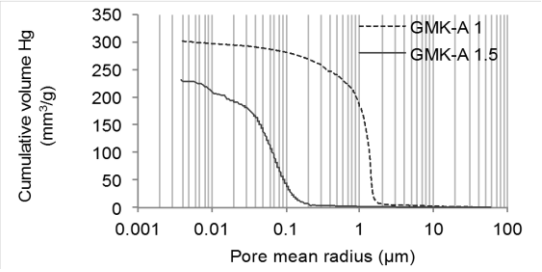

Figure 2. Cumulative pore volume measured by MIP. Each dataset is an average of three tested samples.

Data obtained for GMK-A 1.5 agree with results reported in literature, contrary to GMK-A 1 results. Němeček et al., 2011, studied metakaolin geopolymers with Si/Al molar ratio equal to 1.23, cured at 80°C for 12 hours; MIP test shows an average pore size of ~0.08 µm. Analogous results were achieved by Bignozzi et al., 2013 reporting an average pore size of 0.069 µm for metakaolin geopolymer with Si/Al = 1.36, cured at ambient temperature.

Skeletal properties. Reference data summarised in Table 3 were identified as target to test the validity of the results obtained with the molecular model. Skeletal density is important because density typically correlates with strength and reduced creep deformations, but also because it provides a necessary starting point to describe the solid part of a geopolymer in any nanoscale model. Available results regarding skeletal density of metakaolin geopolymers at the molecular scale are still scarce and vary from 1.7 to ~2.4 g/cm^3. Šmilauer et al., 2011, detected skeletal density with He-picnometry test. Duxson et al., 2007, obtained it comparing pore volume and nominal density, showing that the skeletal density increases with decreasing Si/Al ratio.

Table 3. Wet skeletal density (Wet ρsk) of MK GP from the literature (i.e. skeletal density considering also structural water). Young modulus at the molecular scale.

	Si/Al (mol/mol)	Wet ρsk (g/cm^3)	E mol. (GPa)
(Šmilauer et al., 2011)	1.22	2.372	25.48
(Duxson et al., 2007)	1.15 – 1.65	1.8-1.7	/

The amount of structural water in the GP skeleton is difficult to measure directly but some reasonable assumptions can be made to estimate it. For example, here the structural water was identified considering the minimum amount of water below which the sample starts to lose integrity and experience microstructural changes, typically manifesting themselves as drying shrinkage. Duxson et al., 2007 reported that drying at 150°C led to weight loss due to evaporable water between 20% and 40% of the initial weight for sample with Si/Al molar ratio between 1.15 and 2.15. Considering the initial mix design described by Duxson et al., 2007 (H_2O/Na=5.5 molar ratio) and 20-40% of water loss, the amount of water still present inside the skeleton is H_2O/Na=3.3 - 4.4 (molar ratio). On a similar line, Kuenzel et al., 2012 calculated the molar water content of samples just before they started to undergo drying shrinkage. They observed that, independently of the amount of initial water in the mix design, shrinkage started when the residual water content was equal to ~3 mol for Si/Al=2 metakaolin geopolymers with molar ratio of Na/Al equal to 1. Thus H_2O:Na=3:1 was considered as a reasonable estimation of structural water content in the GP skeleton

4. Molecular model

Model design. As a baseline molecular model a crystalline zeolite structure was considered. Experiments on MK show that, under certain conditions, faujasite is formed (Duxson et al., 2006) whose basic building cage is sodalite. Thus the model is based on a sodalite structure with desired Al/Si ratio, with addition of Na-cations to satisfy charge neutrality and structural water. Wet skeletal density, Young modulus, XRD (X-Ray Diffraction), PDF (Pair Distribution Function) of the resulting structure are calculated and compared to experimental results. Molecular dynamic simulations were performed using LAMMPS (Plimpton, 1995). PDF were obtained using ISAAC (Le Roux and Petkov, 2010). This simulation was run considering 8 cages for a total of ~700 atoms interacting through Reax FF potential (Chenoweth et al., 2008). The process followed was: (a) minimization for 1000 ts at T=300K and P=1atm in NPT ensemble; (b) NVT for 1000 ts at T=300K; (c) length changing of the box in one direction followed by 4 cycles of minimization letting the box relax in the other two dimensions.

Molecular dynamics (MD) simulation results. Table 4 summarizes results for wet skeletal density and Young modulus obtained with the simulation. Wet skeletal density achieved is in line with the range identified in literature (1.7 – 2.4 g/cm^3) and confirms the trend underlined by Duxson et al., 2007: decreasing while increasing silicon content.

Table 4. MD results - Young modulus and wet skeletal density.

	E_x mol. (GPa)	E_y mol. (GPa)	E_z mol. (GPa)	Wet ρsk (g/cm^3)
Si/Al =1	72	71	72	2.30
Si/Al = 1.4	69	65	69	2.23

It is worth to mention that MD simulation can overestimate the E modulus. This is because the size of the simulated cells is ~2 nm not allowing to model microstructural defects such as voids and pores, and the elastic modulus of MK-geopolymers is largely depending on mesopores and macropores and unreacted source materials (Duxson et al., 2005). On the other hand molecular simulation on zeolite structures such as analcime (Sanchez-Valle et al., 2005) and chlorosodalite (Williams et al., 2006) reported results in line with the present work with E modulus values between 75 and 85 GPa. In addition, first results on bulk modulus show values in the range of ~150 GPa increasing while increasing Al content.

XRD diffractograms of the two modelled crystalline structures are shown in Figure 3. The two main peaks at ~24.6° 2ϑ and ~ 32° 2ϑ are typical of the sodalite cage but it is possible to notice a slight shifting of the 2ϑ angle with increasing water content, probably due to an increasing pressure that stretches the bond lengths (since 3 H_2O molecules for each Na atom are considered, and the Na balances the Al, Si/Al 1.4 contains less water).

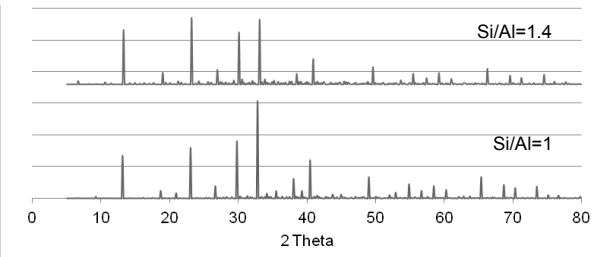

Figure 3. MD results - XRD diffractograms for Si/Al=1 and 1.4.

The PDF provides a quantitative measure of structural changes involved during the MK-geopolymerisation process. In Figure 4 atom-atom correlations are identified for Si/Al=1 and 1.4 and compared with in situ X-ray PDF from experiments (White et al., 2013). Predictably, the most evident difference between MD and experimental results is that both MD crystalline samples show sharp peaks at distances larger than 5 Å while the experimental sample reaches a plateau that is typical for amorphous materials (White et al., 2013). In addition r-correlation atom-atom are increased with higher water content.

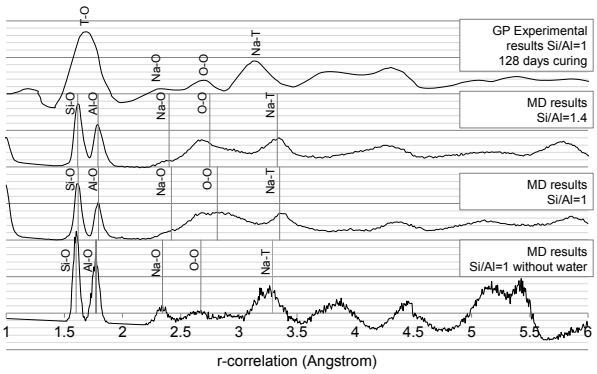

Figure 4. Comparison between PDF from experimental results (White et al., 2013) and from simulation results on configurations with Al/Si = 1, with and without water. Legend: T: tetrahedra (Si or Al), Si: silicon, Al: aluminium, O: Oxigen, Na: sodium.

5. Conclusions

To conclude, mechanical properties and porous structure are influenced by Si/Al molar ratio and water content. In particular, porosity increases when decreasing Si/Al and consequently increasing water content. At the nanoscale skeletal density shows the same trend and a higher water content affects the nanoscale structure increasing the r-correlation in the PDF analysis.

Future developments of this study will consider a disordered structure with the same Si/Al ratio in order to find the most representative molecular model for the experiments and compute the interaction potentials needed for the mesoscale.

One of the final objectives of this project is, in fact, to build a mesoscale model (between 1nm and 1μm) for metakaolin geopolymer to capture their mechanical behaviour.

References

Bignozzi, M. C., Manzi, S., Lancellotti, I., Kamseu, E., Barbieri, L. and Leonelli, C., 2013. Mix-design and characterization of alkali activated materials based on metakaolin and ladle slag. Applied Clay Science, 73: 78-85.

Chenoweth, K., van Duin, A. C. T. and Goddard, W. A., 2008. ReaxFF Reactive Force Field for Molecular Dynamics Simulations of Hydrocarbon Oxidation. The Journal of Physical Chemistry A, 112(5): 1040-1053.

Duxson, P., Lukey, G.C., van Deventer, J.S.J., 2006. Evolution of Gel Structure during Thermal Processing of Na-Geopolymer Gels. Langmuir, 22(21): 8750-8757.

Duxson, P., Lukey, G.C., van Deventer, J.S.J., 2007. Physical evolution of Na-geopolymer derived from metakaolin up to 1000 °C. Journal of Materials Science, 42(9): 3044-3054.

Duxson, P., Provis, J. L., Lukey, G. C., Mallicoat, S. W., Kriven, W. M. and van Deventer, J. S. J., 2005. Understanding the relationship between geopolymer composition, microstructure and mechanical properties. Colloids and Surfaces A: Physicochemical and Engineering Aspects, 269(1–3): 47-58.

Kuenzel, C., Vandeperre, L.J., Donatello, S., Boccaccini, A.R., Cheeseman, C., 2012. Ambient Temperature Drying Shrinkage and Cracking in Metakaolin-Based Geopolymers. Journal of the American Ceramic Society, 95(10): 3270-3277.

Le Roux, S., Petkov, V., 2010. ISAACS - interactive structure analysis of amorphous and crystalline systems. Journal of Applied Crystallography, 43(1): 181-185.

Moloy, E.C., Cygan, R.T., Bonhomme, F., Teter, D.M., Navrotsky, A., 2004. Molecular Simulations of Anhydrous $Na_6[Al_6Si_6O_{24}]$ Sodalite. Chemistry of Materials, 16(11): 2121-2133.

Němeček, J., Šmilauer, V., Kopecký, L., 2011. Nanoindentation characteristics of alkali-activated aluminosilicate materials. Cement and Concrete Composites, 33(2): 163-170.

Pinson, M. B., Masoero, E., Bonnaud, P. A., Manzano, H., Ji, Q., Yip, S., Thomas, J. J., Bazant, M. Z., Van Vliet, K. J. and Jennings, H. M., 2015. Hysteresis from Multiscale Porosity: Modeling Water Sorption and Shrinkage in Cement Paste. Physical Review Applied, 3(6).

Plimpton, S., 1995. Fast Parallel Algorithms for Short-Range Molecular Dynamics. Journal of Computational Physics, 117: 1-19.

Provis, J.L., Duxson, P., Van Deventer, J.S.J., Lukey, G.C., 2005. 7th World Congress of Chemical Engineering The Role of Mathematical Modelling and Gel Chemistry in Advancing Geopolymer Technology. Chemical Engineering Research and Design, 83(7): 853-860.

Sadat, M. R., Bringuier, S., Muralidharan, K., Runge, K., Asaduzzaman, A. and Zhang, L., 2016. An atomistic characterization of the interplay between composition, structure and mechanical properties of amorphous geopolymer binders. Journal of Non-Crystalline Solids, 434: 53-61.

Sanchez-Valle, C., Sinogeikin, S. V., Lethbridge, Z. A. D., Walton, R. I., Smith, C. W., Evans, K. E. and Bass, J. D., 2005. Brillouin scattering study on the single-crystal elastic properties of natrolite and analcime zeolites. Journal of Applied Physics, 98(5): 053508.

White, C.E., Page, K., Henson, N.J., Provis, J.L., 2013. In situ synchrotron X-ray pair distribution function analysis of the early stages of gel formation in metakaolin-based geopolymers. Applied Clay Science, 73: 17-25.

Williams, J.J., Evans, K.E., Walton, R.I., 2006. On the elastic constants of the zeolite chlorosodalite. Applied Physics Letters, 88(2): 021914.

Šmilauer, V., Hlaváček, P., Škvára, F., Šulc, R., Kopecký, L. and Němeček, J., 2011. Micromechanical multiscale model for alkali activation of fly ash and metakaolin. Journal of Materials Science, 46(20): 6545-6555.

Towards a mesoscale model of geopolymers: interaction potential from the molecular scale.

F. Lolli & E. Masoero
School of Engineering
Newcastle University, Newcastle upon Tyne, United Kingdom

ABSTRACT: Geopolymers are alumino-silicate hydrates obtained by reaction of an alumino-silicate source (e.g. metakaolin or fly ash) with alkali solution. Geopolymer-based binders are less environmentally impacting than ordinary cement, but their implementation in the construction field is still limited and requires a better understanding of the nanoscale origin of their mechanical properties. This understanding can be advanced with new simulations based on interaction-driven aggregation of nanoparticles, similar to what has happened in the last decade in the field of traditional cement science. This paper introduces a pathway to develop such a model starting from recent molecular models of geopolymers, which allow to compute the interaction potentials needed for the larger mesoscale. Interaction potential parameters are presented in this work as a function of different particle sizes, targeting experimentally-observed ranges of particle sizes and porosity. Overall, this work opens new opportunities to understand the linkage between mesostructure and engineering properties of geopolymers, with the aim of supporting their commercialisation as alternative cements and, in this way, contributing to the development of a greener economy.

1 INTRODUCTION

Geopolymers are synthesised mixing alumino-silicate precursors (*e.g.* metakaolin, GGBS or fly ash) with highly alkaline solution, usually based on sodium or potassium. The alkali cations in solution (the focus in this work will be on sodium, *e.g.* Na^+) balance the anions of the raw material and start the geopolymerisation with a first dissolution of Si and Al atoms from the source material. The geopolymerisation process continues with two other main stages: reorganisation and polycondensation. The final result is a porous material with cementitius properties (Duxson et al. 2007). The macroscale mechanical properties of geopolymers are governed by the sodium-alumino silicate gel (N-A-S-H) formed during the geopolimerisation. The N-A-S-H is a cohesive matrix that can be modelled as an aggregate of nanoparticles and mesopores (*viz.* pores with characteristic size between 2 and 50 nm, Rouquerol et al. 1994). These heterogeneities have a primary role for the development of mechanical properties at the macroscale and this has already been shown by various authors working on the mesoscale modelling of ordinary cement hydrates (Masoero et al. 2012, Ioannidou et al. 2016, Yu and Lau 2015). Furthermore mesopores are crucial in controlling the interaction between the material and water in the environment, with key implications for transport properties and durability (Pinson et al. 2015).

A popular class of mesoscale models, in the field of modelling cementitious binders, is based on the aggregation of mechanically interacting nanoparticles. The key input of these simulations are the effective interaction potentials between particles, to be obtained from atomistic simulations at the smaller molecular scale (Bonnaud et al. 2016). These interactions are functions $U(r)$ of potential energy, depending on the distance between nanoparticles (r), or otherwise defined in terms of interaction force $F(r) = -dU(r)/dr$. A pathway to compute such $U(r)$ interactions is to start from stress-strain curves derived from molecular simulations of solid phases subjected to deformation. This approach has been followed in the field of traditional cement science (Masoero et al. 2012), where effective interaction potentials obtained from the stress-strain response of molecular models at the nanometre scale (Pellenq et al. 2009 and Manzano et al. 2013) have led to realistic predictions of

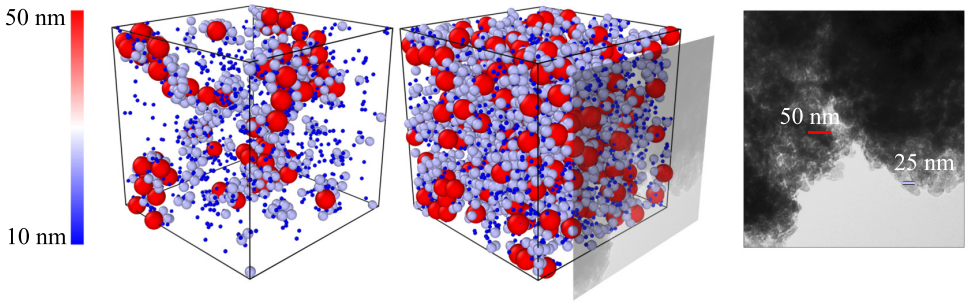

Figure 1: a) Snapshots of the packing process. b) Transmission Election Microscope micrograph of geopolymer metakaolin paste.

mechanical properties at the larger mesoscale of *ca.* 500 nm. In the field of alkali activate materials the only mesoscale model to date has been developed by Yang and White (2016). In this model the coarse-grained units represent individual molecules rather than nanoparticles and the focus is on simulating the sequence of chemical reactions during polimerisation rather than on capturing mechanical properties. Nanoparticle-based simulation of geopolymer mechanics are still to be developed, especially because effective interactions $U(r)$, as well as the molecular-scale inputs required for them, are still missing.

This paper introduces a methodology to derive effective interactions potentials and to obtain model structures for N-A-S-H geopolymers at the mesoscale between the nanometre and the micrometre. The N-A-S-H gel is represented as an aggregate of nanoparticles randomly added to an initially empty simulation box using an efficient space filling algorithm. The effective interaction potential chosen is a modified Lennard-Jones which allows to model particles polydispersity, and which is parametrised from stress-strain curves derived from new molecular simulations of geopolymer mechanics.

2 METHODOLOGY

2.1 *Mesoscale model construction*

The mesoscale model is developed using the software LAMMPS (Plimpton 1995). The starting point is an empty simulation box of predefined dimensions, in which particles are added randomly. The range of possible particle sizes is chosen to be consistent with experimental results described in Section 3.1. The process to construct the model structures, such as the one in Fig. 1 a., is the following:

1. Particles with various diameters are added in groups of many hundreds at a time: this differs and turns out to be computationally more efficient than other space-filling algorithms where particles are added one at a time (Masoero et al. 2014, Ioannidou et al. 2014).

2. Each filling step is followed by energy minimisation using the conjugate gradient method (Polak-Ribiere version) implemented in LAMMPS (Plimpton 1995); particle interactions are explained in Section 2.2.

3. When the system is sufficiently dense to display mechanical stability, the configuration is further stabilised by applying a pre-compressive stress to the box, followed by energy minimisation. The stress is then released by expanding the simulation box until zero pressure is recovered.

4. The entire process (partial space filling, compression, and relaxation back to zero pressure) is repeated until the desired packing density is obtained.

2.2 *Interaction potentials between particles*

The functional form of the effective interactions between nanoparticles is assumed to be a particle-size-dependent generalised Lennard-Jones (Mie potential, Avendano et al. 2011), developed by Masoero et al. (2014) to simulate the mesoscale mechanics of calcium silicate hydrates:

$$U_{ij}(r_{ij}) = 4\epsilon(\sigma_i,\sigma_j)\left[\left(\frac{\overline{\sigma}_{ij}}{r_{ij}}\right)^{2\alpha} - \left(\frac{\overline{\sigma}_{ij}}{r_{ij}}\right)^{\alpha}\right] \qquad (1)$$

$U_{ij}(r_{ij})$ is the potential energy of an interaction between two particles i and j at a distance r_{ij} from one another and with diameters σ_i and σ_j. The depth of the energy well is governed by the parameter $\epsilon(\sigma_i,\sigma_j)$ and α determines the narrowness of the energy well. $\overline{\sigma}_{ij}$ is

Table 1: Interaction potential parameters depending on the particle size.

M	α	σ_i	σ_j	$\overline{\sigma_{ij}}$	$\epsilon(\sigma_i, \sigma_j)$
GPa		Å	Å	Å	eV
75.18	6	50	50	50	1,035
75.18	6	50	100	75	3,107
75.18	6	50	500	275	56,973
75.18	6	50	1000	525	217,536
75.18	6	100	100	100	8,287
75.18	6	100	500	300	124,306
75.18	6	100	1000	550	455,790
75.18	6	500	500	500	1,035,888
75.18	6	500	1000	750	3,107,665

the average diameter of the two particles. Shear forces are not transferred between particles. Following the same calculation explained by Masoero et al. (2014) and adapted to the results obtained with a molecular model of geopolymers (see Section 2.3) it is possible to identify:

$$\epsilon(\sigma_i, \sigma_j) = f(\alpha) M \beta_{ij}(\sigma_i, \sigma_j) \overline{\sigma}_{ij}{}^3 \tag{2}$$

where M is the indentation modulus, *viz.* the initial slope of the axial stress versus axial strain graph obtained at the molecular scale, when the simulation box is not allowed to contract nor expand in the directions perpendicular to the direction of loading (see Section 2.3). β is a corrective factor for the different size of the two interacting particles. $f(\alpha)$ is a numerical constant that depends on the mapping between interaction potential and linear elastic properties (Masoero et al. 2014). α is calculated considering the ultimate strain obtained with the same stress-strain curve from the molecular scale and applying Eq. 3.

$$\epsilon_{ult} = \frac{\sqrt[\alpha]{\frac{4\alpha+2}{\alpha+1}} + \sqrt[\alpha]{2}}{\sqrt[\alpha]{2}} \tag{3}$$

Therefore, the potential in Eq. 1 is entirely determined by two molecular-scale mechanical parameters only: ϵ_{ult} and M.

2.3 *Reference mechanical parameters from the molecular model*

At the molecular scale geopolymers are constituted by sodium-aluminate-silicate hydrate (N-A-S-H), characterised by a nanocrystalline network embedded in an amorphous alumino-silicate gel (Provis, Lukey, & van Deventer 2005). This definition finds its origin in experimental evidence showing features typical of both amorphous and crystalline structures. X-Ray diffraction (XRD) of metakaolin geopolymers is characterised by a broad hump corresponding to 2θ= 25° to 35° which is typical of amorphous materials, but the same experiment identifies also crystalline zeolites peaks corresponding to sodalite and faujasite (Fernández-Jiménez et al. 2008). In the X-ray pair distribution function the amorphous region is identified with broad peaks beyond 5 Å r-correlation function (White et al. 2013), but at shorter distance higher peaks are typical of crystalline domains. A molecular model that could be used to extract mechanical properties and inform the mesoscale potential in Eq. 1 has been developed only very recently by Sadat et al. (2016). This model, however, assumes a fully amorphous molecular structure of geopolymer and therefore, in this paper, another reference molecular structure is used in order to compute mechanical properties. This structure, recently developed by the authors of the present paper (details in a separate paper, currently under preparation), is intermediate between crystalline and amorphous and built by introducing defects into a crystalline structure of the sodalite type. Two different structures are developed, with Si:Al molar ratios of 1.5 and 2. The desired Si:Al ratio is obtained starting from a Si-only defective sodalite framework and substituting Si with Al while respecting the Lowenstein's rule and avoiding the formation of edge-sharing O-Si-O or O-Al-O tetrahedra. Na atoms and water molecules are packed randomly using Packmol (Martinez et al. 2009) applying periodic conditions in all three directions. The resulting structures respect charge neutrality: Na cations balance Al negative charges and Al tetrahedra are linked to four Si tetrahedra (Davidovits 1991). The fully polymerised defective structures are then analysed and subjected to large-strain tensile test to obtain stress-strain curves shown in Section 3 using LAMMPS (Plimpton 1995). During the simulation, each deformation step imposes an extension of 1% of the length in one direction, until rupture. From these tests it has been possible to calculate the indentation modulus (M) and the strain at failure ϵ_{ult} required to parametrise the mesoscale potential, as per Section 2.2.

3 RESULTS

3.1 *Definition of the particle size distribution*

Geopolymers are widely described as mesoporous materials (Provis et al. 2015, Duxson et al. 2006), *viz.* materials with pore diameters between 2 and 50 nm

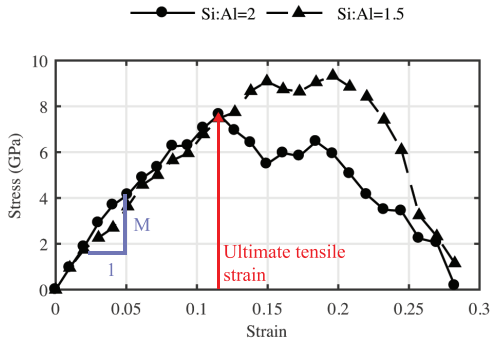

Figure 2: Stress strain graphs for two molecular structure with different Si:Al ratio.

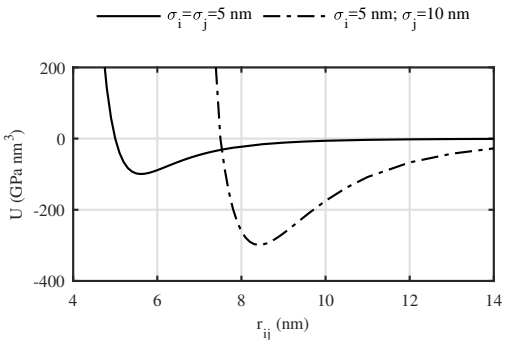

Figure 3: Interaction potential between two particles with same diameter of 5 nm and between two particles with different sizes.

as per IUPAC classification. Benavent et al. (2016) analysed the pore structure of geopolymers with different techniques, such as small-angle X-ray scattering, BET and MIP. Results describe a mean pore size between 5 and 15 nm, with a mesoporous network mainly open with only 1.2% to 2.7% of closed porosity, depending on the type of activator used. On the same line Kriven et al. (2004) studied the geopolymer gel with Transmission Electron Microscopy (TEM) identifying particles and pores in the order of 5 to 10 nm. Fig. 1 b. shows a TEM micrograph of a metakaolin geopolymer paste in which it is possible to distinguish the amorphous geopolymer matrix with a grain size ranging between 10 and 50 nm. Therefore the N-A-S-H gel can be described as an aggregate of nanoparticles ranging from 5 to 50 nm with a mesoporous network ranging from 2 to 50 nm.

3.2 *Mechanical parameters at the molecular scale*

Fig. 2 shows the stress - strain curves obtained from the molecular model of the defective structures with Si:Al 1.5 and 2. The mechanical behaviour displayed is similar for both structures with a ductile rupture, *i.e.* the tensile stress doesn't present a sudden drop after reaching its maximum value (strength). The ultimate tensile strain, *viz.* the strain corresponding to the maximum tensile stress, defined as a reference to calculate the parameter α is ϵ_{ult} =11.47%. The indentation modulus M is 75.18 GPa for the structure with Si:Al = 2.

3.3 *Interaction potential parameters*

Table 1 collects interaction potential parameters for different particle sizes identified as most characteristic for the mesoscale model (from 5 to 100 nm). α = 6 leads to $f(\alpha)$= 0.0154. Fig. 3 illustrates two curves for interaction potential between particles with same size and with different size. The depth of the potential well for particles with same size is lower than for particles with different size. This is due to the fact that the depth correlates to the strength of the interaction and a deeper potential well indicates that more energy is

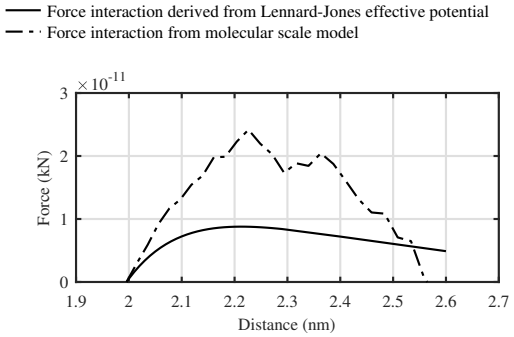

Figure 4: Force distance relationship obtained from the molecular model with Si:Al =2 and from the derivative of the effective interaction potential.

required in order to deform the structure. Fig. 4 compared the effective forces computed as the derivative of the Lennard-Jones potential in Eq. 1, and the integral of the stress-strain graph at the molecular scale over the contact area between two particles with diameter of 2 nm. The figure shows that the initial slope of the force-displacement curve, which is related to the indentation modulus M, is indeed well captured by the generalised Lennard-Jones functional form in Eq. 1. Also the interparticle distance corresponding to the maximum interaction force, which is related to the strain at failure ϵ_{ult}, is well captured. On the other hand, the effective Lennard-Jones potential underestimates force over most of the interaction range, hence the functional form in Eq. 1 may not be the optimum one to describe the mechanical interactions in a nanoparticle-based model of geopolymer. This indicates that the Lennard-Jones potential is not the optimum solution for this fitting. A possible alternative could be to develop a suitable effective potential in LAMMPS, obtained by directly tabulating the interaction force and energy as a function of interparticle distance obtained from the molecular simulations.

4 CONCLUSIONS

In this work a first polydisperse mesoscale model of geopolymers is presented. This model is based on mechanical properties obtained at the molecular scale.

The effective pair interaction potentials are computed between particles ranging from 5 to 100 nm, with particle size distribution based on experimental results at different scales. It is also shown that a generalised Lennard-Jones functional form of the interaction potential captures some key features of the mechanics at the molecular scale, but it would also significantly underestimate the interaction forces at the mesoscale. By linking molecular scale mechanics with mesoscale structure and properties, the proposed model allows investigating the role of particle size distributions and different packing densities for a range of Si:Al molar ratios, types of activators, and water contents. The effective interactions presented here create the conditions to simulate for the first time the mechanical behaviour of geopolymer binders at the mesoscale, with the aim of providing fundamental informations on the failure mechanism and deformations of these materials.

REFERENCES

Avendano, C., T. Lafitte, A. Galindo, C. S. Adjiman, G. Jackson, & E. A. Muller (2011). Saft-γ force field for the simulation of molecular fluids. 1. a single-site coarse grained model of carbon dioxide. *The Journal of Physical Chemistry B 115*(38), 11154–11169.

Benavent, V., F. Frizon, & A. Poulesquen (2016). Effect of composition and aging on the porous structure of metakaolin based geopolymers. *Journal of Applied Crystallography 49*(6), 2116–2128.

Bonnaud, P. A., C. Labbez, R. Miura, A. Suzuki, N. Miyamoto, N. Hatakeyama, A. Miyamoto, & K. J. Van Vliet (2016). Interaction grand potential between calcium-silicate-hydrate nanoparticles at the molecular level. *Nanoscale 8*, 4160–4172.

Davidovits, J. (1991). Geopolymers. *Journal of thermal analysis 37*(8), 1633–1656.

Duxson, P., A. Fernández-Jiménez, J. L. Provis, G. C. Lukey, A. Palomo, & J. S. J. van Deventer (2007). Geopolymer technology: the current state of the art. *Journal of Materials Science 42*(9), 2917–2933.

Duxson, P., G. C. Lukey, & J. S. J. van Deventer (2006). Evolution of gel structure during thermal processing of na-geopolymer gels. *Langmuir 22*(21), 8750–8757.

Fernández-Jiménez, A., M. Monzó, M. Vicent, A. Barba, & A. Palomo (2008). Alkaline activation of metakaolin and fly ash mixtures: Obtain of zeoceramics and zeocements. *Microporous and Mesoporous Materials 108*(13), 41–49.

Ioannidou, K., K. J. Krakowiak, M. Bauchy, C. G. Hoover, E. Masoero, S. Yip, F.-J. Ulm, P. Levitz, R. J.-M. Pellenq, & E. Del Gado (2016). Mesoscale texture of cement hydrates. *Proceedings of the National Academy of Sciences 113*(8), 2029–2034.

Ioannidou, K., R. J.-M. Pellenq, & E. Del Gado (2014). Controlling local packing and growth in calcium-silicate-hydrate gels. *Soft Matter 10*, 1121–1133.

Kriven, W. M., M. Gordon, & J. L. Bell (2004). Geopolymers: Nanoparticulate, nanoporous ceramics made under ambient conditions. *Microscopy and Microanalysis 10*(S02), 404–405.

Manzano, H., E. Masoero, I. Lopez-Arbeloa, & H. M. Jennings (2013). Shear deformations in calcium silicate hydrates. *Soft Matter 9*(30), 7333–7341.

Martinez, L., R. Andrade, E. Birgin, & J. Martinez (2009). Packmol: A package for building initial configurations for molecular dynamics simulations. *Journal Of Computational Chemistry 30*(13), 2157–2164.

Masoero, E., E. Del Gado, R. J.-M. Pellenq, F.-J. Ulm, & S. Yip (2012, Oct). Nanostructure and nanomechanics of cement: Polydisperse colloidal packing. *Phys. Rev. Lett. 109*, 155503.

Masoero, E., E. Del Gado, R. J.-M. Pellenq, S. Yip, & F.-J. Ulm (2014). Nano-scale mechanics of colloidal c-s-h gels. *Soft Matter 10*, 491–499.

Masoero, E., H. M. Jennings, F.-J. Ulm, E. Del Gado, H. Manzano, R. J.-M. Pellenq, & S. Yip (2014). Modelling cement at fundamental scales: From atoms to engineering strength and durability. In *Computational Modelling of Concrete Structures, Vol 1*.

Pellenq, R. J.-M., A. Kushima, R. Shahsavari, K. J. Van Vliet, M. J. Buehler, S. Yip, & F.-J. Ulm (2009). A realistic molecular model of cement hydrates. *Proceedings of the National Academy of Sciences 106*(38), 16102–16107.

Pinson, M. B., E. Masoero, P. A. Bonnaud, H. Manzano, Q. Ji, S. Yip, J. J. Thomas, M. Z. Bazant, K. J. Van Vliet, & H. M. Jennings (2015). Hysteresis from multiscale porosity: Modeling water sorption and shrinkage in cement paste. *Phys. Rev. Applied 3*, 064009.

Plimpton, S. (1995). Fast parallel algorithms for short-range molecular dynamics. *Journal of Computational Physics 117*, 1–19.

Provis, J. L., G. C. Lukey, & J. S. J. van Deventer (2005). Do geopolymers actually contain nanocrystalline zeolites? a reexamination of existing results. *Chemistry of Materials 17*(12), 3075–3085.

Provis, J. L., A. Palomo, & C. Shi (2015). Advances in understanding alkali-activated materials. *Cement and Concrete Research 78, Part A*, 110–125.

Rouquerol, J., D. Avnir, C. W. Fairbridge, D. H. Everett, J. M. Haynes, N. Pernicone, J. D. F. Ramsay, K. S. W. Sing, & K. K. Unger (1994). Recommendations for the characterization of porous solids (technical report).

Sadat, M. R., S. Bringuier, A. Asaduzzaman, K. Muralidharan, & L. Zhang (2016). A molecular dynamics study of the role of molecular water on the structure and mechanics of amorphous geopolymer binders. *The Journal of Chemical Physics 145*(13), 134706.

White, C. E., K. Page, N. J. Henson, & J. L. Provis (2013). In situ synchrotron x-ray pair distribution function analysis of the early stages of gel formation in metakaolin-based geopolymers. *Applied Clay Science 73*, 17–25.

Yang, K. & C. E. White (2016). Modeling the formation of alkali aluminosilicate gels at the mesoscale using coarse-grained monte carlo. *Langmuir 32*(44), 11580–11590.

Yu, Z. & D. Lau (2015). Nano- and mesoscale modeling of cement matrix. *Nanoscale Research Letters 10*(1), 1–6.

A defective crystal model for the molecular structure of geopolymers: disorder, structure, and mechanics.

Francesca Lolli, Enrico Masoero.

School of Engineering, Newcastle University, Newcastle Upon Tyne NE1 7RU, U.K.

ABSTRACT

Geopolymers represent a sustainable alternative to cementitious materials, since they can be obtained from waste products. Chemically speaking, their binding phase is constituted by sodium-alumino-silicate-hydrates (N-A-S-H), through the reaction of an alumino-silicate source with a sodium silicate solution. The adaptation of geopolymers in the construction field is still limited by insufficient understanding of their long-term properties and chemo-mechanical stability. Reducing these uncertainties requires an integrated approach between modelling and experimental verification. However, the existing models, based on solely amorphous or crystalline structures, are not always in agreement with experimental results. For this reason, a defective crystalline structure is proposed as a baseline geopolymer cell, featuring both amorphism and crystallinity. This novel structure is created by inducing vacancies to a sodalite crystalline cage, then reorganised while respecting the Loewenstein's principle, thereby achieving a full polymerisation of Al and Si tetrahedra. Molecular simulation results of this novel structure are compared to a pure amorphous glass and a sodalite crystal, showing better correspondence to experimental results. Specifically, verification is done by computing the effect of Si:Al molar ratio and water content on a range of structural and mechanical properties such as skeletal density, ring structure, bong-angle distribution, X-ray diffraction and X-ray pair distribution function. The simulation results confirm the necessity of a defective structure able to detect both order and disorder in geopolymers experiments, which suggests a heterogeneous material with both crystalline and amorphous features. The proposed defective molecular model serves as a baseline for multiscale understanding of geopolymer structure.

1. INTRODUCTION

Geopolymers, also more appropriately defined as low-calcium alkali activated cements, are the product of the reaction between an aluminosilicate precursor (flash calcined clay, e.g. metakaolin, or by-products such as pulverised fuel ash or slag) and an alkali activated solution (usually sodium silicate or potassium silicate). Geopolymers have similar macroscale properties to Portland cement, but with the advantage of entailing 35%-45% lower CO_2 emissions compared to traditional cements (Habert & Ouellet-Plamondon 2016).

The geopolymerisation process is very different from the hydration of cement paste. The alkaline solution dissolves the precursor releasing aluminate and silicate monomers, which condensate into oligomeric structures eventually forming a three-dimensional aluminosilicate structure. In this final structure, cations (Na^+ or K^+) provide a positive charge that balances the negative charge of the tetra-coordinated aluminium, and some water molecules remain physisorbed. Provis et al. 2005 described the molecular structure of geopolymers as pseudo-zeolitic, in the sense that they feature zeolite nano-crystals embedded in an amorphous gel. This model is supported by experiments on the characterisation of geopolymers, which indicated both crystalline domains (frequently zeolite-type structures, such as zeolite A, faujasite and sodalite) and amorphous domains (White et al. 2013, Fernández-Jiménez et al. 2008, Kriven, Gordon & Bell 2004). The relationship between chemical compositon and level of disorder at the molecular scale as well as the implications of different level of disorder on the physical and mechanical properties of the material are still not understood. Molecular modelling, and molecular dynamic (MD) simulations can contribute to this current scientific discussion.

Molecular dynamic (MD) simulations of geopolymers are very recent and mainly based on completely amorphous and not fully polymerised structures (Kupwade-Patil et al. 2013, Sadat et al. 2016, Hou et al. 2018, Zhang et al. 2018). To the authors' knowledge, only two studies thus far have considered crystalline zeolite as a precursor to model the atomic structure (Bagheri et al. 2018, Lolli et al. 2018). This manuscript presents an atomistic model of the N-A-S-H structure (sodium aluminate silicate hydrates) based on defective sodalite. Model geopolymer structures are built by introducing some

degree of disorder in the highly ordered sodalite network, so that the final structures preserve nevertheless a certain level of crystallinity. The porous network at the nanoscale level is then analysed providing data that are useful to understand water diffusivity in the geopolymer matrix both at this scale and at the mesoscale. Additionally, the importance of molecular modelling as a tool to support experimental research and provide insights on the chemical and structural mechanisms responsible for macroscale properties, is discussed. Finally, a mesoscale model of geopolymer is obtained from molecular scale data, and an insight on the porous network at this scale is discussed.

2. THE DEFECTIVE SODALITE MOLECULAR MODEL OF GEOPOLYMERS

This section describes some key steps to construct model geopolymer structures for atomistic simulations based on defective sodalite geometries. The interested reader can find additional details, also including the construction of fully amorphous and fully crystalline model structure, in a recently published manuscript by the same authors (Lolli et al. 2018).

The defective model is built starting from a siliceous crystalline sodalite structure with only Si and O atoms, which is minimised at T=0 K and P=1 atm using LAMMPS (Plimpton et al. 2007) (Polak-Ribiere version of the conjugate gradient method) and the ReaxFF interaction potential (Chenoweth et al. 2008). To generate defects, two SiO_2 molecules have been randomly deleted, creating vacancies. The resulting intermediate structure is equilibrated *via* 0.01 ns of molecular dynamics (MD) at P=1 atm and T=300 K in the NPT ensemble, followed by 0.01 ns in the NVT ensemble. After this step, some O atoms presented dangling bonds, hence individual atoms are slightly displaced and NPT-MD simulations are run at P=1 atm and T=1000 K until full polymerisation is restored.

Two different Si/Al ratio are then analysed, 1.5 and 2, corresponding to the molar ratios that are experimentally known to produce optimum mechanical properties (Leonelli 2011, De Silva, Sagoe-Crenstil & Sirivivatnanon 2007, Zhang et al. 2013). To control the Si/Al ratio, some Si atoms are substituted with Al atoms. Aluminium is tetra coordinated, hence the structure is not significantly altered when introducing it in the place of Si. However, Al carries a net negative charge, thus sodium atoms are added in the same quantity as aluminium atoms (i.e. Na/Al =1) to restore charge neutrality.

To determine the water quantity, which could be considered as “structural water” i.e. water pertaining to the skeletal atomic structure of the N-A-S-H gel, realistic assumptions are made based on experimental results from the literature. In particular, here it is considered that structural water is the minimum amount of water needed to avoid large microstructural changes during drying (viz. drying shrinkage, which can cause microcracks). Duxson et al. 2007, analysed sodium activated geopolymer samples with Si/Al varying from 1.15 to 2.15 molar ratio, and with H_2O/Na = 5.5. Drying the samples at 150°C caused a mass loss between 20 and 40% of the initial mass of the sample, and analysing the stoichiometry of the mix design this corresponded to a residual H_2O/Na molar ratio between 3.3 and 4.4 even after the thermal treatment. Likewise, Kuenzel et al. 2012 studied ambient temperature drying shrinkage for geopolymer samples with varying initial water content and drying shrinkage started only when the residual water content was H_2O/Na=3 for geopolymers with Si/Al=2, regardless of the initial water content of the mix design. In the same work, it is also shown that the residual water content depends on the Si/Al ratio of the mix design, notably decreasing with the decrease of Si/Al. For the atomistic model investigated here, it is therefore decided to consider H_2O/Na=3 as simulation parameter for both the Si/Al ratios analysed.

The final geopolymer model structure presents Si:Al:Na:H_2O= 1.5-2:1:1:3 molar ratios, but other structural constraints have been defined. Al and Si atoms are all tetra coordinated, representing a fully polymerised structure, Al tetrahedra do not present edge-sharing, meaning that two tetrahedra cannot be linked with two oxygen bonds, and finally Loewenstein’s principle is always respected. Loewenstein’s principle states that two Al tetrahedra cannot be linked by a single oxygen bond. Lastly, the N-A-S-H structures are energy minimised using the Polak-Ribiere version of the conjugate gradient method, and then equilibrated *via* 1 ns of molecular dynamics at P=1 atm and T=300 K in NPT ensemble, followed by 1ns in NVT ensemble. A snapshot obtained with Vesta of the resulting defective N-A-S-H gel is shown in Figure 1a. In a previous work (Lolli et al. 2018) the molecular model has been used to provide insights into the impact of the structural organisation (studied through XRD, X-ray PDF, ring and bond length analysis) on the development of mechanical properties at the molecular scale. Here the focus is kept instead on the pore structure.

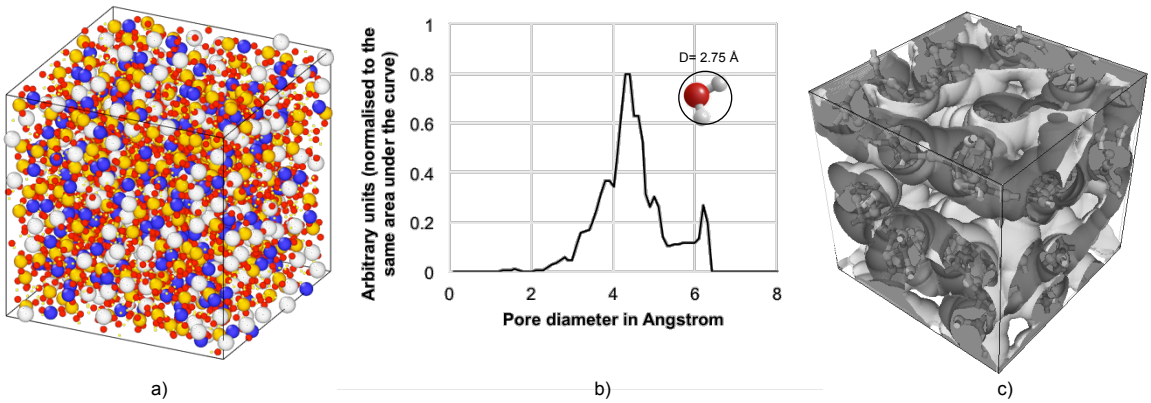

Figure 1. a) Snapshot of the defective molecular model with Si/Al = 1.5. b) Sensitivity analysis of the pore size distribution of the siliceous baseline structure c) Snapshot of the pore structure (light gray) within the defective siliceous baseline structure (dark gray).

The pore size distributions in Figure 1b is calculated with the open source software Zeo++ (Haranczyk et al. 2012), using Pinheiro et al. method (Pinheiro et al. 2013), based on the Voronoi tassellation. A probe radius of 0.15 Å was used to simulate the diameter of a water molecule (2.8 Å) and obtaining a pore size distribution accessible by water. It is possible to distinguish two main peaks, at 4.5 Å and 6.5 Å, the former typical of completely amorphous structures, and the latter describing the characteristic size of the sodalite cage. Figure 1c shows a snapshot of the porosity network of the defective siliceous baseline structure obtained with Ovito considering the pore surface as atoms radius. This three-dimensional model allows a clear visualisation of the geometry of the pore network and it is possible to identify a fully percolated structure, which may have implications for the diffusivity of water at the molecular scale and consequent durability issues at the macroscale. The previously mentioned reference paper (Lolli et al. 2018) presents an in depth analysis of structural features of the siliceous structures and of the mechanical properties of the N-A-S-H gel at the molecular scale. The present manuscript instead aims at clarifying the importance of molecular modelling for advances on material research, as explained in the following paragraphs.

3. MESOSCALE MODEL OF GEOPOLYMERS

Mesoscale structures can be modeled using molecular scale inputs, and this section summarizes the approach used by Lolli *et al.* (Lolli & Masoero 2018) to construct a mesoscale model of geopolymers and presents a porosity analysis at this scale.

The mesoscale model in Figure 2a, is built considering aggregated polydisperse nanoparticles interacting *via* effective interaction potentials, which are fully defined by two molecular scale mechanical parameters: the ultimate tensile strain ε_{ult} and the indentation modulus *M.* Both these parameters can be obtained from the molecular model described in Section 2. In addition to the interaction potentials, particles and pore size distribution have been defined analyzing literature and experimental data, defining target ranges of 5 to 50 nm for particle size distribution, and a mesoporous network from 2 to 50 nm (Lolli & Masoero 2018). Figure 2b shows the nanoscale structure of a metakaolin geopolymer paste with Si:Al = 1.5, in which the upper limit of the targeted range is displayed, showing particle and pores with a diameter of 50 nm.

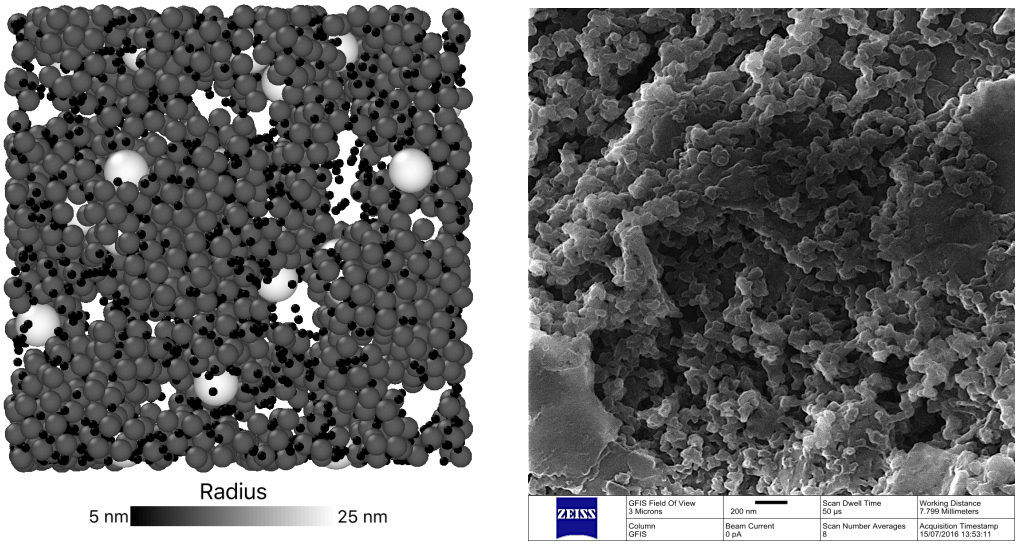

Figure 2. a) Snapshot of the mesoscale model from (Lolli and Masoero 2018). b) Helium Ion Microscopy image showing the polydisperse structure of the N-A-S-H gel at the nanoscale.

During the construction process particles of different radius are added randomly into an empty box (more details in Lolli & Masoero 2018), permitting to define a preferential size of particles during the filling process. This allowed to study the effect of different particle size distribution on the mesopores structure. Two filling limit cases have been considered; the first results from setting a preference for big particles (50 nm diameters) over smaller particles, while the second is built preferring particles with a diameter of 10 and 25 nm over 50 nm, in Figure 3. The two different filling steps represented in Figure 3a and b, display different packing fractions, therefore different densities of the N-A-S-H gel, which can be found in the same geopolymer paste in different polymerization sites. The two packing fraction may as well describe the evolution of the N-A-S-H gel over time. To study the effect of the gel density on the porosity of the N-A-S-H, pore size distributions are simulated using the open source software Zeo++ (Haranczyk et al. 2012), with the Pinheiro et al. method (Pinheiro et al. 2013) based on the Voronoi tassellation. To obtain the results displayed in Figure 3c the parameters for the sampling are: a probe radius of 0.2 nm and Monte Carlo samples per unit cell equal to 5000. These parameters are chosen after a sensitivity analysis that considered probe radii from 0.1 to 0.5 nm and Monte Carlo samples varying from 1000 to 50000. The results in Figure 3c show the evolution of the pore distribution from a porosity of 79% (Configuration I) to a porosity of 51% (Configuration II). Configuration I displays one broad peak from 60 to 100 nm and centered at 77 nm, and a second peak at 15 nm. When densifying the structure in Configuration II the broad peak disappears, while the peak centered at 15 nm shifts slightly to 20 nm, increasing its intensity.

The same behavior has been observed in the CSH, where a higher densification of the gel over time corresponds to progressively smaller average pore diameter. For CSH this is explained with a progressive precipitation of newly formed solid hydration product in the gel pores (Ioannidou et al. 2016), and it is a process that continues for months and years (Masoero et al. 2018, Jiang et al. 2019). For sodium silicate activated geopolymers, it is instead hypothesized a rapid densification, with full geopolymerisation completed in hours. On the contrary sodium hydroxide activated geopolymers, display the formation of new crystalline phases as a secondary products, days after the casting (Zhang et al. 2012).

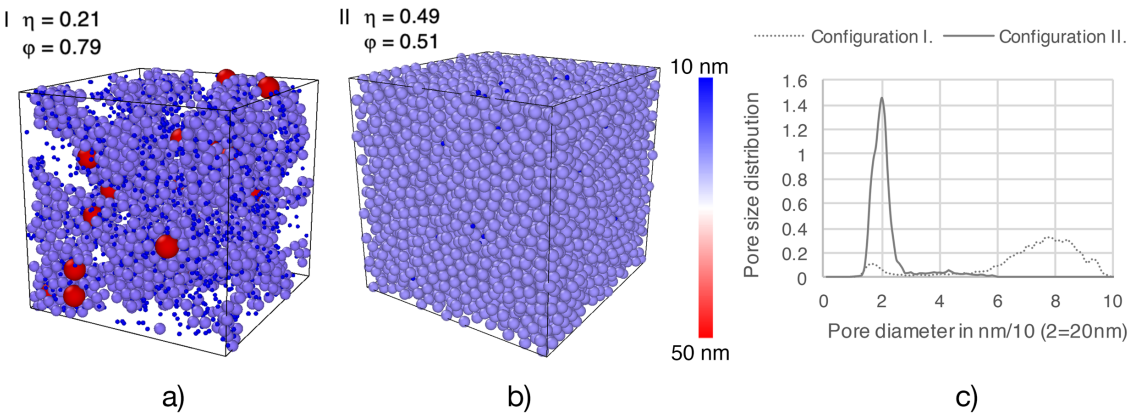

Figure 3. Mesoscale model with preference of small particles over big ones a) Configuration I. Filling algorithm stopped at a packing fraction of 21%. b) Configuration II. Filling algorithm stopped at a packing fraction of 49%. c) Pore size distribution of the two configurations.

4. IMPLICATIONS OF NANOSCALE MODELLING OF GEOPOLYMERS

The study of the porous network at different scales of both C-S-H and N-A-S-H gel is of fundamental importance for understanding their durability. In fact, durability is directly linked to mechanisms such as water transport inside materials. Creep and shrinkage for example are related to these mechanisms and experimental techniques available nowadays (e.g. proton NMR and quasi elastic neutron scattering) can only detect the presence of water in the nanopores. Therefore, the combination of these techniques with MD simulation can be useful to identify the direct correlation between water transport and degradation mechanisms, both through three-dimensional visualisation and simulation of mechanical tests.

Pinson et al. 2015, developed a mesoscale model of water sorption in the C-S-H, discussing the implications for transport properties caused by the interaction between cement and water. The authors reproduced the water sorption isotherms coupling the molecular model of C-S-H from Pellenq et al. 2009 with a mesoscale model. Hysteresis in water sorption isotherms depends on pore size distribution and pore connectivity, therefore the effect of both micropores and mesopores must considered. In Pinson et al 2015, a molecular model of C-S-H was crucial to distinguish the sorption effect due to the interaction between C-S-H and water in the nanopores from the interaction due to capillary forces in the gel pores, at the mesoscale. In addition, the distribution of pores in the matrix is also connected to volume changes due to drying shrinkage, hence with the same model Pinson et al. were able to simulate the shrinkage associated with sorption isotherms. Molecular modelling is also the starting point to simulate long term mechanical responses such as creep. Recent works applied quasi static shear (Masoero et al. 2013), oscillatory stress (Bauchy et al. 2015, Bauchy et al. 2017), and incremental stress-marching (ISM) (Morshedifard et al. 2018) to replicate viscoelastic deformations and creep, accelerating thermal fluctuation. These studies showed that the viscoelastic creep behaviour of C-S-H transitioned from asymptotic to logarithmic when the water content in the interlayer region was increased. The implications of the water content in the interlayers zones of C-S-H was also the focus of a study by Manzano et al. 2013. Comparing two different molecular models of C-S-H, the authors studied the effect of water content on the shear behaviour of C-S-H. The two models presented a different degree of molecular order: the first one was a glassy C-S-H (amorphous system) and the second one a highly-ordered C-S-H (tobermorite). Both systems were subjected to shear deformation and for both this deformation was concentrated in the water confined nanolayers, suggesting that the C-S-H gel can be modelled as composed by aggregated nanoparticles with water rich regions on their interfaces. All this shows that molecular models clarified the relation between nanostructure and mechanical properties of C-S-H.

The hypothesis of C-S-H gel as aggregate of interacting nanoparticles is at the basis of mesoscale models that use molecular scale inputs to model interactions (Bonnaud et al. 2016). The effective interaction potentials between particles *U(r)* are a function of the distance between particles, and a possible approach to compute such potentials is from stress-strain curves derived from molecular

simulations. Masoero et al. 2012 used this methodology to compute mechanical properties of C-S-H at the mesoscale (*ca*. 500 nm) leading to realistic results, function of packing fraction and polydispersity. Finally, molecular models together with experimental results were used by Shvab et al. 2017 to simulate different mechanism of C-S-H precipitation. Specifically, the simulated Boundary Nucleation and Growth mechanism displayed evolution rates comparable to literature results, indicating that this could be the most representative hypothesized growth mechanism for C-S-H. This indicates that molecular models can be used to upscale C-S-H models at the mesoscale, and understand gel formation mechanisms happening at different scales.

Finally, from a technological point of view, molecular dynamics simulations hold the promise of impacting the field of nuclear waste encapsulation. Ordinary Portland Cement is commonly used as a binder to immobilize different types of radioactive waste (Evans 2008, Young et al. 2013), but current studies on geopolymer indicate that metakaolin geopolymers could be used successfully as well (Geddes et al. 2018, Künzel 2013). Molecular model simulations could be employed to provide insights on the mechanisms that govern the retention of radionuclides in the cement matrix. Duque-Redondo et al. 2018 applied MD to simulate absorption and diffusivity of Cs-137 in the C-S-H gel pores, to determine which leaching mechanisms could cause the release of the contaminants in the environment. This ability to predict encapsulation as a function of chemical composition is an asset for the development of new, more sustainable and effective binders for the nuclear industry.

5. CONCLUSIONS

This manuscript has shown that N-A-S-H models can be used to provide insights on the pore structure of geopolymers at the molecular scale and at the mesoscale. The molecular scale model displayed a fully percolated pore structure with characteristic pore diameters typical of amorphous and crystalline structures. The mesoscale model showed that the densification of the structure entails changes in the pore size distribution toward one characteristic mean pore diameter. These findings provide a better understanding of the pore structure of geopolymers, therefore add new information useful to discuss the water diffusivity mechanisms in these materials, and consequently durability issues at the macroscale. Additionally, a literature review on the importance of molecular modelling as a reference for several types of simulations has been presented. Hence, analysis related to water transport mechanisms, leaching of different types of chemicals (e.g. radioactive isotopes) and carbon captures can be considered for future research. Molecular modelling is therefore a central support to the experimental research on geopolymers to promote and discuss the application of these materials in civil engineering.

6. REFERENCES

Bagheri, A., A. Nazari, J. G. Sanjayan & W. Duan (2018). *Molecular simulation of water and chloride ion diffusion in nanopores of alkali-activated aluminosilicate structures*. Ceramics International.

Bauchy, M., E. Masoero, F.-J. Ulm & R. Pellenq (2015). *Creep of bulk CSH: insights from molecular dynamics simulations.* In CONCREEP 10, pp 511-516.

Bauchy, M., M. Wang, Y. Yu, B. Wang, N. A. Krishnan, E. Masoero, F.-J. Ulm & R. Pellenq (2017). Topological control on the structural relaxation of atomic networks under stress. *Physical review letters,* Volume 119**,** pp 035502.

Bonnaud, P. A., C. Labbez, R. Miura, A. Suzuki, N. Miyamoto, N. Hatakeyama, A. Miyamoto & K. J. Van Vliet (2016). *Interaction grand potential between calcium–silicate–hydrate nanoparticles at the molecular level.* Nanoscale, Volume 8**,** pp 4160-4172.

Chenoweth, K., A. van Duin & W. Goddard (2008). *ReaxFF reactive force field for molecular dynamics simulations of hydrocarbon oxidation.* Journal Of Physical Chemistry A, Volume 112**,** pp 1040-1053.

De Silva, P., K. Sagoe-Crenstil & V. Sirivivatnanon (2007). *Kinetics of geopolymerization: role of Al_2O_3 and SiO_2.* Cement and Concrete Research*,* Volume 37**,** pp 512-518.

Duque-Redondo, E., Y. Kazuo, I. López-Arbeloa & H. Manzano (2018). *Cs-137 immobilization in CSH gel nanopores*. Physical Chemistry Chemical Physics, Volume 20, pp 9289-9297.

Duxson, P., G. C. Lukey & J. S. J. van Deventer (2007). *Physical evolution of Na-geopolymer derived from metakaolin up to 1000 °C.* Journal of Materials Science, Volume 42, pp 3044-3054.

Evans, N. (2008). *Binding mechanisms of radionuclides to cement*. Cement and concrete research, Volume 38, pp 543-553.

Fernández-Jiménez, A., M. Monzó, M. Vicent, A. Barba & A. Palomo (2008). *Alkaline activation of metakaolin–fly ash mixtures: Obtain of Zeoceramics and Zeocements*. Microporous and Mesoporous Materials, Volume 108, pp 41-49.

Geddes, D., X. Ke, S. Bernal, M. Hayes & J. Provis (2018). *Metakaolin-Based Geopolymers for Nuclear Waste Encapsulation.* In Calcined Clays for Sustainable Concrete, pp 183-188. Springer.

Habert, G. & C. Ouellet-Plamondon (2016). *Recent update on the environmental impact of geopolymers*. RILEM technical Letters, Volume 1, pp 17-23.

Haranczyk, M., C. Rycroft, R. Martin & T. Willems (2012). *Zeo++: High-throughput analysis of crystalline porous materials, v0. 2.2*. Lawrence Berkeley National Laboratoy, Berkeley.

Hou, D., Y. Zhang, T. Yang, J. Zhang, H. Pei, J. Zhang, J. Jiang & T. Li (2018). *Molecular structure, dynamics, and mechanical behavior of sodium aluminosilicate hydrate (NASH) gel at elevated temperature: a molecular dynamics study.* Physical Chemistry Chemical Physics, Volume 20, pp 20695-20711.

Ioannidou, K., K. J. Krakowiak, M. Bauchy, C. G. Hoover, E. Masoero, S. Yip, F.-J. Ulm, P. Levitz, R. J.-M. Pellenq & E. Del Gado (2016). *Mesoscale texture of cement hydrates.* Proceedings of the National Academy of Sciences, Volume 113, pp 2029-2034.

Jiang, Z., Y. Xi, X. Gu, Q. Huang & W. Zhang (2019). *Modelling of water vapour sorption hysteresis of cement-based materials based on pore size distribution*. Cement and Concrete Research, Volume 115, pp 8-19.

Kriven, W., M. Gordon & J. Bell (2004). *Geopolymers: nanoparticulate, nanoporous ceramics made under ambient conditions.* Microscopy and microanalysis, Volume 10, pp 404-405.

Kuenzel, C., L. J. Vandeperre, S. Donatello, A. R. Boccaccini & C. Cheeseman (2012) *Ambient Temperature Drying Shrinkage and Cracking in Metakaolin-Based Geopolymers.* Journal of the American Ceramic Society, Volume 95, pp 3270-3277.

Kupwade-Patil, K., F. Soto, A. Kunjumon, E. N. Allouche & D. S. Mainardi (2013). *Multi-scale modeling and experimental investigations of geopolymeric gels at elevated temperatures*. Computers & Structures, Volume 122, pp 164-177.

Künzel, C. (2013). *Metakaolin based geopolymers to encapsulate nuclear waste*. Imperial College London.

Leonelli, C. (2011). *Geopolimeri Polimeri Inorganici Chimicamente Attivati*.

Lolli, F., H. Manzano, J. L. Provis, M. C. Bignozzi & E. Masoero (2018). *Atomistic simulations of geopolymer models: the impact of disorder on structure and mechanics.* ACS applied materials & interfaces.

Lolli, F. & E. Masoero. 2018. *Towards a mesoscale model of geopolymers: Interaction potential from the molecular scale.* In Computational Modelling of Concrete Structures: Proceedings of the Conference on Computational Modelling of Concrete and Concrete Structures (EURO-C 2018), February 26-March 1, 2018, Bad Hofgastein, Austria, 87. CRC Press.

Manzano, H., E. Masoero, I. Lopez-Arbeloa & H. M. Jennings (2013). *Shear deformations in calcium silicate hydrates.* Soft Matter, Volume 9, pp 7333-7341.

Masoero, E., G. Cusatis & G. Di Luzio (2018). *C–S–H gel densification: The impact of the nanoscale on self-desiccation and sorption isotherms.* Cement and Concrete Research, Volume 109, pp 103-119.

Masoero, E., E. Del Gado, R. J. M. Pellenq, F. J. Ulm & S. Yip (2012). *Nanostructure and Nanomechanics of Cement: Polydisperse Colloidal Packing.* Phys. Rev. Lett., Volume 109.

Masoero, E., H. Manzano, E. Del Gado, R.-M. Pellenq, F.-J. Ulm & S. Yip. (2013). *Kinetic simulation of the logarithmic creep of cement*. In Mechanics and Physics of Creep, Shrinkage, and Durability of Concrete: A Tribute to Zdeňk P. Bažant, pp 166-173.

Morshedifard, A., S. Masoumi & M. A. Qomi (2018). *Nanoscale origins of creep in calcium silicate hydrates*. Nature communications, Volume 9, pp 1785.

Pellenq, R. J., A. Kushima, R. Shahsavari, K. J. Van Vliet, M. J. Buehler, S. Yip & F. J. Ulm (2009) *A realistic molecular model of cement hydrates.* Proc Natl Acad Sci USA, Volume 106, pp 16102-7.

Pinheiro, M., R. L. Martin, C. H. Rycroft, A. Jones, E. Iglesia & M. Haranczyk (2013). *Characterization and comparison of pore landscapes in crystalline porous materials.* Journal of Molecular Graphics and Modelling, Volume 44, pp 208-219.

Pinson, M. B., E. Masoero, P. A. Bonnaud, H. Manzano, Q. Ji, S. Yip, J. J. Thomas, M. Z. Bazant, K. J. Van Vliet & H. M. Jennings (2015). *Hysteresis from Multiscale Porosity: Modeling Water Sorption and Shrinkage in Cement Paste.* Physical Review Applied, Volume 3.

Plimpton, S., P. Crozier & A. Thompson (2007). *LAMMPS-large-scale atomic/molecular massively parallel simulator.* Sandia National Laboratories, Volume 18, pp 43.

Provis, J. L., G. C. Lukey & J. S. J. van Deventer (2005). *Do Geopolymers Actually Contain Nanocrystalline Zeolites? A Reexamination of Existing Results.* Chemistry of Materials, Volume 17, pp 3075-3085.

Sadat, M. R., S. Bringuier, K. Muralidharan, K. Runge, A. Asaduzzaman & L. Zhang (2016). *An atomistic characterization of the interplay between composition, structure and mechanical properties of amorphous geopolymer binders.* Journal of Non-Crystalline Solids, Volume 434, pp 53-61.

Shvab, I., L. Brochard, H. Manzano & E. Masoero (2017) *Precipitation mechanisms of mesoporous nanoparticle aggregates: off-lattice, coarse-grained, kinetic simulations.* Crystal Growth & Design, Volume 17, pp 1316-1327.

White, C. E., K. Page, N. J. Henson & J. L. Provis (2013). *In situ synchrotron X-ray pair distribution function analysis of the early stages of gel formation in metakaolin-based geopolymers.* Applied Clay Science, Volume 73, pp 17-25.

Young, A. J., P. Warwick, A. E. Milodowski & D. Read (2013). *Behaviour of radionuclides in the presence of superplasticiser.* Pp 32-43.

Zhang, M., N. A. Deskins, G. Zhang, R. T. Cygan & M. Tao (2018). *Modeling the Polymerization Process for Geopolymer Synthesis through Reactive Molecular Dynamics Simulations*. The Journal of Physical Chemistry C, Volume 122, pp 6760-6773.

Zhang, Z., J. L. Provis, H. Wang, F. Bullen & A. Reid (2013). *Quantitative kinetic and structural analysis of geopolymers. Part 2. Thermodynamics of sodium silicate activation of metakaolin*. Thermochimica Acta, Volume 565, pp 163-171.

Zhang, Z., H. Wang, J. L. Provis, F. Bullen, A. Redi & Y. Zhu (2012). *Quantitative kinetic and structural analysis of geopolymers. Part 1. The activation of metakaolin with sodium hydroxide*. Thermochimica Acta, Volume 539, pp 10.

Bibliography

[1] U. N. D. P. Division. (2018, May) World Urbanization Prospects 2018. Accessed 21-May-2018. [Online]. Available: https://esa.un.org/unpd/wup/

[2] W. Vienna. (2018, September) The Material Glow Analysis Portal. Accessed 20-September-2018. [Online]. Available: http://www.materialflows.net/visualisation-centre/

[3] J. S. van Deventer, J. L. Provis, P. Duxson, and D. G. Brice, "Chemical research and climate change as drivers in the commercial adoption of alkali activated materials," *Waste and Biomass Valorization*, vol. 1, no. 1, pp. 145–155, 2010.

[4] E. Chlor. (2018, August) The membrane cell process. Accessed 15-August-2018. [Online]. Available: http://www.eurochlor.org

[5] CEES. (2018, July) Soluble Silicates chemical, toxicological, ecological and legal aspects of production, transport, handling and application. Accessed 15-July-2018. [Online]. Available: http://www.cees-silicates.org/index.php/publications

[6] J. Davidovits, "Geopolymers," *J. Therm. Anal.*, vol. 37, no. 8, pp. 1633–1656, 1991. [Online]. Available: http://dx.doi.org/10.1007/BF01912193

[7] P. Duxson, A. Fernández-Jiménez, J. L. Provis, G. C. Lukey, A. Palomo, and J. S. van Deventer, "Geopolymer technology: the current state of the art," *Journal of materials science*, vol. 42, no. 9, pp. 2917–2933, 2007.

[8] J. Provis and J. Van Deventer, "Geopolymerisation kinetics. 2. reaction kinetic modelling," *Chemical Engineering Science*, vol. 62, no. 9, pp. 2318–2329, 2007.

[9] A. Fernández-Jiménez, A. Palomo, and M. Criado, “Microstructure development of alkali-activated fly ash cement: a descriptive model,” *Cement and concrete research*, vol. 35, no. 6, pp. 1204–1209, 2005.

[10] V. Benavent, F. Frizon, and A. Poulesquen, “Effect of composition and aging on the porous structure of metakaolin-based geopolymers,” *Journal of Applied Crystallography*, vol. 49, no. 6, pp. 2116–2128, 2016.

[11] T. da Silva Rocha, D. P. Dias, F. C. C. França, R. R. de Salles Guerra, L. R. d. C. de Oliveira *et al.*, “Metakaolin-based geopolymer mortars with different alkaline activators (na+ and k+),” *Construction and Building Materials*, vol. 178, pp. 453–461, 2018.

[12] C. Kuenzel, L. J. Vandeperre, S. Donatello, A. R. Boccaccini, and C. Cheeseman, “Ambient temperature drying shrinkage and cracking in metakaolin-based geopolymers,” *Journal of the American Ceramic Society*, vol. 95, no. 10, pp. 3270–3277, 2012.

[13] C. Ferone, F. Colangelo, G. Roviello, D. Asprone, C. Menna, A. Balsamo, A. Prota, R. Cioffi, and G. Manfredi, “Application-oriented chemical optimization of a metakaolin based geopolymer,” *Materials*, vol. 6, no. 5, pp. 1920–1939, 2013.

[14] D. Perera, O. Uchida, E. Vance, and K. Finnie, “Influence of curing schedule on the integrity of geopolymers,” *Journal of materials science*, vol. 42, no. 9, pp. 3099–3106, 2007.

[15] G. Samson, M. Cyr, and X. X. Gao, “Formulation and characterization of blended alkali-activated materials based on flash-calcined metakaolin, fly ash and ggbs,” *Construction and Building Materials*, vol. 144, pp. 50–64, 2017.

[16] R. J.-M. Pellenq, A. Kushima, R. Shahsavari, K. J. Van Vliet, M. J. Buehler, S. Yip, and F.-J. Ulm, “A realistic molecular model of cement hydrates,” *Proceedings of the National Academy of Sciences*, vol. 106, no. 38, pp. 16 102–16 107, 2009.

[17] E. Masoero, E. Del Gado, R.-M. Pellenq, F.-J. Ulm, and S. Yip, “Nanostructure and nanomechanics of cement: polydisperse colloidal packing,” *Physical review letters*, vol. 109, no. 15, p. 155503, 2012.

[18] K. Ioannidou, K. J. Krakowiak, M. Bauchy, C. G. Hoover, E. Masoero, S. Yip, F.-J. Ulm, P. Levitz, R. J.-M. Pellenq, and E. Del Gado, "Mesoscale texture of cement hydrates," *Proceedings of the National Academy of Sciences*, p. 201520487, 2016.

[19] M. B. Pinson, E. Masoero, P. A. Bonnaud, H. Manzano, Q. Ji, S. Yip, J. J. Thomas, M. Z. Bazant, K. J. Van Vliet, and H. M. Jennings, "Hysteresis from multiscale porosity: modeling water sorption and shrinkage in cement paste," *Physical Review Applied*, vol. 3, no. 6, p. 064009, 2015.

[20] A. Koleżyński, M. Król, and M. Żychowicz, "The structure of geopolymers–theoretical studies," *Journal of Molecular Structure*, vol. 1163, pp. 465–471, 2018.

[21] M. R. Sadat, S. Bringuier, K. Muralidharan, K. Runge, A. Asaduzzaman, and L. Zhang, "An atomistic characterization of the interplay between composition, structure and mechanical properties of amorphous geopolymer binders," *Journal of Non-Crystalline Solids*, vol. 434, pp. 53–61, 2016.

[22] D. Hou, Y. Zhang, T. Yang, J. Zhang, H. Pei, J. Zhang, J. Jiang, and T. Li, "Molecular structure, dynamics, and mechanical behavior of sodium aluminosilicate hydrate (nash) gel at elevated temperature: a molecular dynamics study," *Physical Chemistry Chemical Physics*, vol. 20, no. 31, pp. 20 695–20 711, 2018.

[23] A. Bagheri, A. Nazari, J. G. Sanjayan, P. Rajeev, and W. Duan, "Fly ash-based boroaluminosilicate geopolymers: Experimental and molecular simulations," *Ceramics International*, vol. 43, no. 5, pp. 4119–4126, 2017.

[24] P. Duxson, J. L. Provis, G. C. Lukey, and J. S. Van Deventer, "The role of inorganic polymer technology in the development of "green concrete"," *Cement and Concrete Research*, vol. 37, no. 12, pp. 1590–1597, 2007.

[25] M. Weil, K. Dombrowski, and A. Buchwald, "Life-cycle analysis of geopolymers," in *Geopolymers*. Elsevier, 2009, pp. 194–210.

[26] G. Habert, J. D. De Lacaillerie, and N. Roussel, "An environmental evaluation of geopolymer based concrete production: reviewing current research trends," *Journal of cleaner production*, vol. 19, no. 11, pp. 1229–1238, 2011.

[27] B. C. McLellan, R. P. Williams, J. Lay, A. Van Riessen, and G. D. Corder, “Costs and carbon emissions for geopolymer pastes in comparison to ordinary portland cement,” *Journal of cleaner production*, vol. 19, no. 9-10, pp. 1080–1090, 2011.

[28] G. Habert and C. Ouellet-Plamondon, “Recent update on the environmental impact of geopolymers,” *RILEM technical Letters*, vol. 1, pp. 17–23, 2016.

[29] S. Le Roux and V. Petkov, “Isaacs - interactive structure analysis of amorphous and crystalline systems,” *J. Appl. Crystallogr.*, vol. 43, no. 1, pp. 181–185, 2010. [Online]. Available: http://dx.doi.org/10.1107/S0021889809051929

[30] K. Momma and F. Izumi, “Vesta 3 for three-dimensional visualization of crystal, volumetric and morphology data,” *J. Appl. Crystallogr.*, vol. 44, pp. 1272–1276, 2011.

[31] F. Lolli, H. Manzano, J. L. Provis, M. C. Bignozzi, and E. Masoero, “Atomistic simulations of geopolymer models: the impact of disorder on structure and mechanics.” *ACS applied materials & interfaces*, 2018.

[32] A. Developpement. (2018, June) Le metakaolin. Accessed 12-June-2018. [Online]. Available: http://www.argeco.fr/le_metakaolin.php

[33] A. Stukowski, “Visualization and analysis of atomistic simulation data with ovito–the open visualization tool,” *Modelling Simul. Mater. Sci. Eng.*, vol. 18, no. 1, p. 015012, 2009.

[34] Standard.

[35] F. Lolli and E. Masoero, “Towards a mesoscale model of geopolymers: Interaction potential from the molecular scale,” in *Computational Modelling of Concrete Structures: Proceedings of the Conference on Computational Modelling of Concrete and Concrete Structures (EURO-C 2018), February 26-March 1, 2018, Bad Hofgastein, Austria*. CRC Press, 2018, p. 87.

[36] M. Treacy and J. Higgins, *Collection of Simulated XRD Powder Patterns for Zeolites*, 5th ed. Oxford: Elsevier, 2007.

[37] C. E. White, K. Page, N. J. Henson, and J. L. Provis, “In situ synchrotron x-ray pair distribution function analysis of the early stages of gel formation

in metakaolin-based geopolymers," *Appl. Clay Sci.*, vol. 73, pp. 17–25, 2013. [Online]. Available: http://www.sciencedirect.com/science/article/pii/S0169131712002268

[38] K. S. Sing, "Reporting physisorption data for gas/solid systems with special reference to the determination of surface area and porosity (recommendations 1984)," *Pure and applied chemistry*, vol. 57, no. 4, pp. 603–619, 1985.

[39] M. Thommes and K. A. Cychosz, "Physical adsorption characterization of nanoporous materials: progress and challenges," *Adsorption*, vol. 20, no. 2-3, pp. 233–250, 2014.

[40] V. Šmilauer, P. Hlaváček, F. Škvára, R. Šulc, L. Kopeckỳ, and J. Němeček, "Micromechanical multiscale model for alkali activation of fly ash and metakaolin," *J. Mat. Sci.*, vol. 46, no. 20, pp. 6545–6555, 2011. [Online]. Available: http://dx.doi.org/10.1007/s10853-011-5601-x

[41] P. Duxson, G. C. Lukey, and J. S. J. van Deventer, "Physical evolution of na geopolymer derived from metakaolin up to 1000 c," *J. Mat. Sci.*, vol. 42, no. 9, pp. 3044–3054, 2007. [Online]. Available: http://dx.doi.org/10.1007/s10853-006-0535-4

[42] M. R. Sadat, S. Bringuier, A. Asaduzzaman, K. Muralidharan, and L. Zhang, "A molecular dynamics study of the role of molecular water on the structure and mechanics of amorphous geopolymer binders," *The Journal of chemical physics*, vol. 145, no. 13, p. 134706, 2016.

[43] K. A. Komnitsas, "Potential of geopolymer technology towards green buildings and sustainable cities," *Procedia Engineering*, vol. 21, pp. 1023–1032, 2011.

[44] U. Nations. (2018, May) 68% of the world population projected to live in urban areas by 2050, says UN. Accessed 21-May-2018. [Online]. Available: https://www.un.org/development/desa/en/news/population/2018-revision-of-world-urbanization-prospects.html

[45] K. L. Scrivener, V. M. John, and E. M. Gartner, "Eco-efficient cements: Potential economically viable solutions for a low-co2 cement-based materials industry," *United Nations Environment Program*, 2016.

[46] W. C. S. Initiative. (2018, May) Getting the Numbers Right, Project Emissions Report 2014. Accessed 21-May-2018. [Online]. Available: https://wbcsdcement.org/pdf/CSI%20GNR%20Report%20final_updated%20Nov11_LR.pdf

[47] C. Ouellet-Plamondon and G. Habert, "Life cycle assessment (lca) of alkali-activated cements and concretes," in *Handbook of alkali-activated cements, mortars and concretes*. Elsevier, 2015, pp. 663–686.

[48] E. Commission. (2018, September) EU climate action. Accessed 1-September-2018. [Online]. Available: https://ec.europa.eu/clima/citizens/eu_en

[49] Statista. (2018, May) U.S. cement prices 2017. Accessed 21-May-2018. [Online]. Available: https://www.statista.com/statistics/219339/us-prices-of-cement/

[50] G. Institute. (2019, May) 70,000 tonnes Geopolymer Concrete for airport. Accessed 11-May-2019. [Online]. Available: https://www.geopolymer.org/news/70000-tonnes-geopolymer-concrete-airport/

[51] ——. (2019, May) World?s first public building with structural Geopolymer Concrete. Accessed 11-May-2019. [Online]. Available: https://www.geopolymer.org/news/worlds-first-public-building-with-structural-geopolymer-concrete/

[52] R. San Nicolas, M. Cyr, and G. Escadeillas, "Characteristics and applications of flash metakaolins," *Applied Clay Science*, vol. 83, pp. 253–262, 2013.

[53] B. Fabbri, S. Gualtieri, and C. Leonardi, "Modifications induced by the thermal treatment of kaolin and determination of reactivity of metakaolin," *Applied Clay Science*, vol. 73, pp. 2–10, 2013.

[54] B. R. Ilić, A. A. Mitrović, and L. R. Miličić, "Thermal treatment of kaolin clay to obtain metakaolin," *Hemijska industrija*, vol. 64, no. 4, pp. 351–356, 2010.

[55] J. L. Provis and J. S. J. van Deventer, *Alkali Activated Materials State-of-the-Art Report, RILEM TC 224-AAM*. Springer, 2014.

[56] A. M. Rashad, "Metakaolin as cementitious material: History, scours, production and composition–a comprehensive overview," *Construction and building materials*, vol. 41, pp. 303–318, 2013.

[57] J. L. Provis and J. S. J. Van Deventer, *Geopolymers: structures, processing, properties and industrial applications*. Elsevier, 2009.

[58] C. C. P. Association. (2018, June) Prospecting and mining. Accessed 10-June-2018. [Online]. Available: http://www.kaolin.com/ccpros.html

[59] B. G. Survey. (2018, June) Kaolin. Accessed 10-June-2018. [Online]. Available: https://www.bgs.ac.uk/downloads/start.cfm?id=1362

[60] D. Technologies. (2018, June) Advantages of the flash process. Accessed 12-June-2018. [Online]. Available: http://www.demeter-technologies.fr/calcination.avantages.php

[61] E. Parliament, "Directive 2010/75/EU of the European Parliament and of the Council of 24 November 2010 on industrial emissions (integrated pollution prevention and control)," European Parliament, Bruxelles, Standard, Nov. 2010.

[62] J. Provis, "Green concrete or red herring?–future of alkali-activated materials," *Advances in Applied Ceramics*, vol. 113, no. 8, pp. 472–477, 2014.

[63] J. Davidovits, "Mineral polymers and methods of making them, us patent 4,349,386," *USA patent*, vol. 4, 1982.

[64] P. Duxson, "The structure and thermal evolution of metakaolin geopolymers," Ph.D. dissertation, Department of Chemical and Biomolecular Engineering, The University of Melbourne, 2006.

[65] H. M. Jennings, J. Thomas, D. Rothstein, and J. Chen, "Cements as porous materials," *Handbook of Porous Solids*, pp. 2971–3028, 2002.

[66] R. Slavík, V. Bednařík, M. Vondruška, O. Skoba, and T. Hanzlíček, "Proof of sodalite structures in geopolymers," in *3rd Meeting on Chemistry and Life*. Česká společnost chemická, 2005.

[67] J. E. Oh, J. Moon, M. Mancio, S. M. Clark, and P. J. Monteiro, "Bulk modulus of basic sodalite, na8 [alsio4] 6 (oh) 2· 2h2o, a possible zeolitic precursor in coal-fly-ash-based geopolymers," *Cem. Concr. Res.*, vol. 41, no. 1, pp. 107–112, 2011.

[68] S. A. Walling, S. A. Bernal, L. J. Gardner, H. Kinoshita, and J. L. Provis, "Phase formation and evolution in mg (oh) 2–zeolite cements," *Ind. Eng. Chem. Res.*, vol. 57, no. 6, pp. 2105–2113, 2018.

[69] P. Sturm, G. Gluth, S. Simon, H. Brouwers, and H.-C. Kühne, "The effect of heat treatment on the mechanical and structural properties of one-part geopolymer-zeolite composites," *Thermochim. Acta*, vol. 635, pp. 41–58, 2016.

[70] M. Alzeer and K. J. MacKenzie, "Synthesis and mechanical properties of new fibre-reinforced composites of inorganic polymers with natural wool fibres," *J. Mater. Sci.*, vol. 47, no. 19, pp. 6958–6965, 2012.

[71] W. Loewenstein, "The distribution of aluminum in the tetrahedra of silicates and aluminates," *American Mineralogist: Journal of Earth and Planetary Materials*, vol. 39, no. 1-2, pp. 92–96, 1954.

[72] J. Tosspr-r, "A theoretical study of the molecular basis of the al avoidance rule and of the spectral characteristics of al-o-al linkages," *American Mineralogist*, vol. 78, pp. 911–920, 1993.

[73] G. Engelhardt, D. Hoebbel, M. Tarmak, A. Samoson, and E. Lippmaa, "29si-nmr-untersuchungen zur anionenstruktur von kristallinen tetramethylammonium-alumosilicaten und-alumosilicatlösungen," *Zeitschrift für anorganische und allgemeine Chemie*, vol. 484, no. 1, pp. 22–32, 1982.

[74] J. Davidovits, "Structural characterization of geopolymeric materials with xray diffractometry and mas nmr spectroscopy," in *Geopolymer*, vol. 88, 1988, pp. 149–166.

[75] H. Xu and J. S. van Deventer, "The effect of alkali metals on the formation of geopolymeric gels from alkali-feldspars," *Colloids and Surfaces A: Physicochemical and Engineering Aspects*, vol. 216, no. 1-3, pp. 27–44, 2003.

[76] P. Duxson, J. L. Provis, G. C. Lukey, F. Separovic, and J. S. J. van Deventer, "29si nmr study of structural ordering in aluminosilicate geopolymer gels," *Langmuir*, vol. 21, no. 7, pp. 3028–3036, March 2005.

[77] P. S. Singh, T. Bastow, and M. Trigg, "Structural studies of geopolymers by 29si and 27al mas-nmr," *Journal of Materials Science*, vol. 40, no. 15, pp. 3951–3961, 2005. [Online]. Available: http://dx.doi.org/10.1007/s10853-005-1915-x

[78] P. Duxson, G. Lukey, F. Separovic, and J. Van Deventer, "Effect of alkali cations on aluminum incorporation in geopolymeric gels," *Industrial & Engineering Chemistry Research*, vol. 44, no. 4, pp. 832–839, 2005.

[79] J. L. Provis, G. C. Lukey, and J. S. J. van Deventer, "Do geopolymers actually contain nanocrystalline zeolites? a reexamination of existing results," *Chem. Mater.*, vol. 17, no. 12, pp. 3075–3085, 2005. [Online]. Available: http://dx.doi.org/10.1021/cm050230i

[80] A. Fernàndez-Jimènez, M. Monzó, M. Vicent, A. Barba, and A. Palomo, "Alkaline activation of metakaolin and fly ash mixtures: Obtain of zeoceramics and zeocements," *Microporous Mesoporous Mater.*, vol. 108, no. 13, pp. 41–49, 2008. [Online]. Available: http://www.sciencedirect.com/science/article/pii/S1387181107001837

[81] W. M. Kriven, M. Gordon, and J. L. Bell, "Geopolymers: Nanoparticulate, nanoporous ceramics made under ambient conditions," *Microsc. Microanal.*, vol. 10, no. S02, pp. 404–405, 2004.

[82] Z. Bažant, "Thermodynamics of interacting continua with surfaces and creep analysis of concrete structures," *Nuclear engineering and design*, vol. 20, no. 2, pp. 477–505, 1972.

[83] G. W. Scherer, J. H. Prévost, and Z.-H. Wang, "Bending of a poroelastic beam with lateral diffusion," *International Journal of Solids and Structures*, vol. 46, no. 18-19, pp. 3451–3462, 2009.

[84] T. C. Powers and T. L. Brownyard, "Studies of the physical properties of hardened portland cement paste," in *Journal Proceedings*, vol. 43, no. 9, 1946, pp. 101–132.

[85] S. Lu, E. Landis, and D. Keane, "X-ray microtomographic studies of pore structure and permeability in portland cement concrete," *Materials and Structures*, vol. 39, no. 6, pp. 611–620, 2006.

[86] E. J. Garboczi, "Permeability, diffusivity, and microstructural parameters: a critical review," *Cement and concrete research*, vol. 20, no. 4, pp. 591–601, 1990.

[87] ISO, "ISO 15901-2:2006(en): Pore size distribution and porosity of solid materials by mercury porosimetry and gas adsorption Part 2: Analysis of mesopores and macropores by gas adsorption," International Organization for Standardization, Geneva, CH, Standard, Mar. 2006.

[88] J. Rouquerol, D. Avnir, C. Fairbridge, D. Everett, J. Haynes, N. Pernicone, J. Ramsay, K. Sing, and K. Unger, "Recommendations for the characterization of porous solids (technical report)," *Pure and Applied Chemistry*, vol. 66, no. 8, pp. 1739–1758, 1994.

[89] J. L. Provis, A. Palomo, and C. Shi, "Advances in understanding alkali-activated materials," *Cement and Concrete Research*, vol. 78, Part A, pp. 110–125, 2015. [Online]. Available: http://www.sciencedirect.com/science/article/pii/S0008884615001192

[90] P. Duxson, G. C. Lukey, and J. S. J. van Deventer, "Evolution of gel structure during thermal processing of na-geopolymer gels," *Langmuir*, vol. 22, no. 21, pp. 8750–8757, 2006. [Online]. Available: http://dx.doi.org/10.1021/la0604026

[91] A. Gharzouni, I. Sobrados, E. Joussein, S. Baklouti, and S. Rossignol, "Predictive tools to control the structure and the properties of metakaolin based geopolymer materials," *Colloids and Surfaces A: Physicochemical and Engineering Aspects*, vol. 511, pp. 212–221, 2016.

[92] E. Kamseu, L. B. Moungam, M. Cannio, N. Billong, D. Chaysuwan, U. C. Melo, and C. Leonelli, "Substitution of sodium silicate with rice husk ash-naoh solution in metakaolin based geopolymer cement concerning reduction in global warming," *Journal of cleaner production*, vol. 142, pp. 3050–3060, 2017.

[93] R. Pouhet and M. Cyr, "Formulation and performance of flash metakaolin geopolymer concretes," *Construction and Building Materials*, vol. 120, pp. 150–160, 2016.

[94] J. R. Gasca-Tirado, J. C. Rubio-Ávalos, M. Muñiz-Villarreal, A. Manzano-Ramírez, J. L. Reyes-Araiza, S. Sampieri-Bulbarela, C. Villaseñor-Mora, J. Pérez-Bueno, L. Apatiga, and V. A. Borrás, "Effect of porosity on the absorbed, reemitted and transmitted light by a geopolymer metakaolin base," *Materials Letters*, vol. 65, no. 5, pp. 880–883, 2011.

[95] E. Papa, V. Medri, S. Amari, J. Manaud, P. Benito, A. Vaccari, and E. Landi, "Zeolite-geopolymer composite materials: Production and characterization," *Journal of Cleaner Production*, vol. 171, pp. 76–84, 2018.

[96] ASTM, “ASTM C1608-17 Standard Test Method for Chemical Shrinkage of Hydraulic Cement Paste,” American Society for Testing and Materials, Standard, Jul. 2017.

[97] ——, “ASTM C490-11 Use of Apparatus for the Determination of Length Change of Hardened Cement Paste, Mortar, and Concrete,” American Society for Testing and Materials, Standard, Apr. 2014.

[98] G. Palumbo, A. Iadicicco, F. Messina, C. Ferone, S. Campopiano, R. Cioffi, and F. Colangelo, “Characterization of early age curing and shrinkage of metakaolin-based inorganic binders with different rheological behavior by fiber bragg grating sensors,” *Materials*, vol. 11, no. 1, p. 10, 2017.

[99] BSI, “BS ISO 1920-9:2009 - Determination of creep of concrete cylinders in compression.” International Organization for Standardization, Geneva, CH, Standard, Nov. 2009.

[100] G. Ranzi and R. I. Gilbert, *Time-dependent behaviour of concrete structures*. CRC Press, 2010.

[101] J. Brooks and A. Neville, “Predicting long-term creep and shrinkage from short-term tests,” *Magazine of concrete research*, vol. 30, no. 103, pp. 51–61, 1978.

[102] S. Wallah, “Creep behaviour of fly ash-based geopolymer concrete,” *Civil Engineering Dimension*, vol. 12, no. 2, pp. 73–78, 2010.

[103] R. Gilbert, “Creep and shrinkage models for high strength concrete–proposals for inclusion in as3600,” *Australian Journal of Structural Engineering*, vol. 4, no. 2, pp. 95–106, 2002.

[104] J. Shekhovtsova, M. Kovtun, and E. P. Kearsley, “Evaluation of short-and long-term properties of heat-cured alkali-activated fly ash concrete,” *Magazine of Concrete Research*, vol. 67, no. 16, pp. 897–905, 2015.

[105] A. Castel, S. Foster, T. Ng, J. Sanjayan, and R. Gilbert, “Creep and drying shrinkage of a blended slag and low calcium fly ash geopolymer concrete,” *Materials and Structures*, vol. 49, no. 5, pp. 1619–1628, 2016.

[106] *EN 1992-1-1 Eurocode 2: Design of concrete structures - Part 1-1: General rules and rules for buildings*, EN. Brussels: CEN, 2005.

[107] H. Lee, V. Vimonsatit, P. Chindaprasirt, T. Ngo, and P. Mendis, "Creep properties of cement and alkali activated fly ash materials using nanoindentation technique," *Construction and Building Materials*, vol. 168, pp. 547–555, 2018.

[108] M. A. Qomi, K. Krakowiak, M. Bauchy, K. Stewart, R. Shahsavari, D. Jagannathan, D. B. Brommer, A. Baronnet, M. J. Buehler, S. Yip *et al.*, "Combinatorial molecular optimization of cement hydrates," *Nature communications*, vol. 5, p. 4960, 2014.

[109] M. Bauchy, M. Wang, Y. Yu, B. Wang, N. A. Krishnan, E. Masoero, F.-J. Ulm, and R. Pellenq, "Topological control on the structural relaxation of atomic networks under stress," *Physical review letters*, vol. 119, no. 3, p. 035502, 2017.

[110] A. Morshedifard, S. Masoumi, and M. A. Qomi, "Nanoscale origins of creep in calcium silicate hydrates," *Nature communications*, vol. 9, no. 1, p. 1785, 2018.

[111] H. Manzano, S. Moeini, F. Marinelli, A. C. Van Duin, F.-J. Ulm, and R. J.-M. Pellenq, "Confined water dissociation in microporous defective silicates: mechanism, dipole distribution, and impact on substrate properties," *Journal of the American Chemical Society*, vol. 134, no. 4, pp. 2208–2215, 2012.

[112] A. C. Van Duin, S. Dasgupta, F. Lorant, and W. A. Goddard, "Reaxff: a reactive force field for hydrocarbons," *The Journal of Physical Chemistry A*, vol. 105, no. 41, pp. 9396–9409, 2001.

[113] H. Manzano, E. Masoero, I. Lopez-Arbeloa, and H. M. Jennings, "Shear deformations in calcium silicate hydrates," *Soft Matter*, vol. 9, no. 30, pp. 7333–7341, 2013.

[114] H. M. Jennings, "A model for the microstructure of calcium silicate hydrate in cement paste," *Cement and concrete research*, vol. 30, no. 1, pp. 101–116, 2000.

[115] P. A. Bonnaud, C. Labbez, R. Miura, A. Suzuki, N. Miyamoto, N. Hatakeyama, A. Miyamoto, and K. J. Van Vliet, "Interaction grand potential between calcium–silicate–hydrate nanoparticles at the molecular level," *Nanoscale*, vol. 8, no. 7, pp. 4160–4172, 2016.

[116] E. Masoero, H. Manzano, E. Del Gado, R.-M. Pellenq, F.-J. Ulm, and S. Yip, "Kinetic simulation of the logarithmic creep of cement," in *Mechanics and Physics*

of Creep, Shrinkage, and Durability of Concrete: A Tribute to Zdeňk P. Bažant, 2013, pp. 166–173.

[117] I. Shvab, L. Brochard, H. Manzano, and E. Masoero, "Precipitation mechanisms of mesoporous nanoparticle aggregates: off-lattice, coarse-grained, kinetic simulations," *Crystal Growth & Design*, vol. 17, no. 3, pp. 1316–1327, 2017.

[118] C. E. White, J. L. Provis, T. Proffen, and J. S. van Deventer, "Molecular mechanisms responsible for the structural changes occurring during geopolymerization: multiscale simulation," *AIChE Journal*, vol. 58, no. 7, pp. 2241–2253, 2012.

[119] C. E. White, J. L. Provis, G. J. Kearley, D. P. Riley, and J. S. van Deventer, "Density functional modelling of silicate and aluminosilicate dimerisation solution chemistry," *Dalton transactions*, vol. 40, no. 6, pp. 1348–1355, 2011.

[120] K. Yang and C. E. White, "Modeling the formation of alkali aluminosilicate gels at the mesoscale using coarse-grained monte carlo," *Langmuir*, vol. 32, no. 44, pp. 11 580–11 590, 2016.

[121] M. Zhang, N. A. Deskins, G. Zhang, R. T. Cygan, and M. Tao, "Modeling the polymerization process for geopolymer synthesis through reactive molecular dynamics simulations," *The Journal of Physical Chemistry C*, vol. 122, no. 12, pp. 6760–6773, 2018.

[122] K. Kupwade-Patil, F. Soto, A. Kunjumon, E. N. Allouche, and D. S. Mainardi, "Multi-scale modeling and experimental investigations of geopolymeric gels at elevated temperatures," *Computers & Structures*, vol. 122, pp. 164–177, 2013.

[123] A. Bagheri, A. Nazari, J. G. Sanjayan, and W. Duan, "Molecular simulation of water and chloride ion diffusion in nanopores of alkali-activated aluminosilicate structures," *Ceramics International*, 2018. [Online]. Available: http://www.sciencedirect.com/science/article/pii/S0272884218321291

[124] F. Puertas, M. Palacios, H. Manzano, J. Dolado, A. Rico, and J. Rodríguez, "A model for the cash gel formed in alkali-activated slag cements," *Journal of the European Ceramic Society*, vol. 31, no. 12, pp. 2043–2056, 2011.

[125] X. Wan, D. Hou, T. Zhao, and L. Wang, "Insights on molecular structure and micro-properties of alkali-activated slag materials: a reactive molecular dynamics study," *Construction and Building Materials*, vol. 139, pp. 430–437, 2017.

[126] M. R. Sadat, K. Muralidharan, and L. Zhang, “Reactive molecular dynamics simulation of the mechanical behavior of sodium aluminosilicate geopolymer and calcium silicate hydrate composites,” *Computational Materials Science*, vol. 150, pp. 500–509, 2018.

[127] ISO, “ISO 14040:2006 Environmental management Life cycle assessment Principles and framework,” International Organization for Standardization, Geneva, CH, Standard, Jul. 2006.

[128] K.-H. Yang, J.-K. Song, and K.-I. Song, “Assessment of CO_2 reduction of alkali-activated concrete,” *Journal of Cleaner Production*, vol. 39, pp. 265–272, 2013.

[129] EPSRC. (2018, July) Productive Nation. Accessed 2-July-2018. [Online]. Available: https://epsrc.ukri.org/about/plans/deliveryplan/prosperityoutcomes/productivity/

[130] M. Fawer, M. Concannon, and W. Rieber, “Life cycle inventories for the production of sodium silicates,” *The International Journal of Life Cycle Assessment*, vol. 4, no. 4, p. 207, 1999.

[131] G8. (2018, May) G8 Hokkaido Toyako Summit Leaders Declaration, Hokkaido Toyako, 8 July 2008. Accessed 21-May-2018. [Online]. Available: http://www.mofa.go.jp/policy/economy/summit/2008/doc/doc080714_en.html

[132] ASTM, “ASTM C1157-17 Standard Performance Specification for Hydraulic Cement,” American Society for Testing and Materials, Standard, Jun. 2017.

[133] BSI, “PAS 8820:2016, Construction materials - Alkali-activated cementitious material and concrete ? Specification,” British Standards Institute, Standard, Apr. 2016.

[134] A. Passuello, E. D. Rodríguez, E. Hirt, M. Longhi, S. A. Bernal, J. L. Provis, and A. P. Kirchheim, “Evaluation of the potential improvement in the environmental footprint of geopolymers using waste-derived activators,” *Journal of Cleaner Production*, vol. 166, pp. 680–689, 2017.

[135] R. T. Cygan, J.-J. Liang, and A. G. Kalinichev, “Molecular models of hydroxide, oxyhydroxide, and clay phases and the development of a general force field,” *The Journal of Physical Chemistry B*, vol. 108, no. 4, pp. 1255–1266, 2004.

[136] R. Shahsavari, R. J.-M. Pellenq, and F.-J. Ulm, “Empirical force fields for complex hydrated calcio-silicate layered materials,” *Physical Chemistry Chemical Physics*, vol. 13, no. 3, pp. 1002–1011, 2011.

[137] S. Plimpton, “Fast parallel algorithms for short-range molecular dynamics.” *J. Comput. Phys.*, vol. 117, pp. 1–19, 1995.

[138] H. Manzano, E. Masoero, I. Lopez-Arbeloa, and H. M. Jennings, “Mechanical behaviour of ordered and disordered calcium silicate hydrates under shear strain studied by atomic scale simulations,” in *Mechanics and Physics of Creep, Shrinkage, and Durability of Concrete: A Tribute to Zdeňk P. Bažant - Proceedings of the 9th Int. Conf. on Creep, Shrinkage, and Durability Mechanics, CONCREEP*, 2013, pp. 86–97.

[139] T. F. Willems, C. H. Rycroft, M. Kazi, J. C. Meza, and M. Haranczyk, “Algorithms and tools for high-throughput geometry-based analysis of crystalline porous materials,” *Microporous Mesoporous Mater.*, vol. 149, no. 1, pp. 134–141, 2012.

[140] M. Pinheiro, R. L. Martin, C. H. Rycroft, A. Jones, E. Iglesia, and M. Haranczyk, “Characterization and comparison of pore landscapes in crystalline porous materials,” *J. Mol. Graph. Model*, vol. 44, pp. 208–219, 2013.

[141] L. Martinez, R. Andrade, E. Birgin, and J. Martinez, “Packmol: A package for building initial configurations for molecular dynamics simulations,” *J. Comput. Chem.*, vol. 30, no. 13, pp. 2157–2164, 2009.

[142] D. C. Palmer, *CrystalDiffract User’s Guide*. CrystalMaker Software Ltd, 2015.

[143] L. A. Galin, H. Moss, and I. N. Sneddon, “Contact problems in the theory of elasticity,” North Carolina State University - Raleigh School of physical sciences and applied mathematics, Tech. Rep., 1961.

[144] S. Timoshenko, *Theory of Elasticity*, 3rd ed., ser. Engineering societies monographs. New York: McGraw-Hill, 1969.

[145] I. SC. (2019, May) Database of zeolite structures. Accessed 10-May-2019. [Online]. Available: http://america.iza-structure.org/IZA-SC/framework.php?STC=SOD

[146] S. A. Sheikholeslam, H. Manzano, C. Grecu, and A. Ivanov, “Reduced hydrogen diffusion in strained amorphous sio2: Understanding ageing in mosfet devices,” *J. Mat. Chem. C*, vol. 4, no. 34, pp. 8104–8110, 2016. [Online]. Available: http://dx.doi.org/10.1039/C6TC02647H

[147] R. Pouhet and M. Cyr, “Carbonation in the pore solution of metakaolin-based geopolymer,” *Cement and Concrete Research*, vol. 88, pp. 227–235, 2016.

[148] W. H. Bragg, W. L. Bragg *et al.*, “The reflection of x-rays by crystals,” *Proc. R. Soc. Lond. A*, vol. 88, no. 605, pp. 428–438, 1913.

[149] E. Masoero, G. Cusatis, and G. Di Luzio, “C–s–h gel densification: The impact of the nanoscale on self-desiccation and sorption isotherms,” *Cement and Concrete Research*, vol. 109, pp. 103–119, 2018.

[150] E. W. Washburn, “The dynamics of capillary flow,” *Physical review*, vol. 17, no. 3, p. 273, 1921.

[151] K. Scrivener, R. Snellings, and B. Lothenbach, *A practical guide to microstructural analysis of cementitious materials*. Crc Press, 2018.

[152] H. I. of Mineralogy. (2018, October) Quartz. Accessed 2-October-2018. [Online]. Available: https://www.mindat.org/min-3337.html

[153] O. Engineering. (2018, November) Equilibrium Relative Humidity Salt Solutions. Accessed 11-November-2018. [Online]. Available: https://www.omega.com/temperature/z/pdf/z103.pdf

[154] E. Masoero, E. Del Gado, R. J.-M. Pellenq, S. Yip, and F.-J. Ulm, “Nano-scale mechanics of colloidal c-s-h gels,” *Soft Matter*, vol. 10, pp. 491–499, 2014. [Online]. Available: http://dx.doi.org/10.1039/C3SM51815A

[155] K. Ioannidou, R. J.-M. Pellenq, and E. Del Gado, “Controlling local packing and growth in calcium-silicate-hydrate gels,” *Soft Matter*, vol. 10, pp. 1121–1133, 2014. [Online]. Available: http://dx.doi.org/10.1039/C3SM52232F

[156] C. Avendano, T. Lafitte, A. Galindo, C. S. Adjiman, G. Jackson, and E. A. Muller, “Saft-γ force field for the simulation of molecular fluids. 1. a single-site coarse grained model of carbon dioxide,” *The Journal of Physical Chemistry B*, vol. 115, no. 38, pp. 11 154–11 169, 2011.

[157] E. Masoero, H. M. Jennings, F.-J. Ulm, E. Del Gado, H. Manzano, R. J.-M. Pellenq, and S. Yip, “Modelling cement at fundamental scales: From atoms to engineering strength and durability,” in *Computational Modelling of Concrete Structures, Vol 1*, 2014.

[158] S. J. Louisnathan, R. J. Hill, and G. V. Gibbs, “Tetrahedral bond length variations in sulfates,” *Phys. Chem. Miner.*, vol. 1, no. 1, pp. 53–69, 1977. [Online]. Available: https://doi.org/10.1007/BF00307979

[159] X. Yuan and A. N. Cormack, “Si-o-si bond angle and torsion angle distribution in vitreous silica and sodium silicate glasses,” *J. Non-Cryst. Solids*, vol. 319, no. 1, pp. 31–43, 2003. [Online]. Available: http://www.sciencedirect.com/science/article/pii/S0022309302019609

[160] C. Baerlocher, W. M. Meier, and D. Olson, *Atlas of Zeolite Framework Types*, 5th ed. Amsterdam; New York: Elsevier, 2001.

[161] J. Němeček, V. Šmilauer, and L. Kopecký, “Nanoindentation characteristics of alkali-activated aluminosilicate materials,” *Cem. Concr. Compos.*, vol. 33, no. 2, pp. 163–170, 2011.

[162] G. Constantinides and F.-J. Ulm, “The nanogranular nature of c-s-h,” *J. Mech. Phys. Solids*, vol. 55, no. 1, pp. 64 – 90, 2007. [Online]. Available: http://www.sciencedirect.com/science/article/pii/S0022509606001062

[163] C. Sanchez-Valle, S. V. Sinogeikin, Z. A. D. Lethbridge, R. I. Walton, C. W. Smith, K. E. Evans, and J. D. Bass, “Brillouin scattering study on the single- crystal elastic properties of natrolite and analcime zeolites,” *J. Appl. Phys.*, vol. 98, no. 5, p. 053508, 2005.

[164] J. J. Williams, K. E. Evans, and R. I. Walton, “On the elastic constants of the zeolite chlorosodalite,” *Appl. Phys. Lett.*, vol. 88, no. 2, p. 021914, 2006.

[165] E. Masoero, E. Del Gado, R. J.-M. Pellenq, S. Yip, and F.-J. Ulm, “Nano-scale mechanics of colloidal c–s–h gels,” *Soft matter*, vol. 10, no. 3, pp. 491–499, 2014.

[166] K. A. Cychosz, R. Guillet-Nicolas, J. Garcia-Martinez, and M. Thommes, “Recent advances in the textural characterization of hierarchically structured nanoporous materials,” *Chemical Society Reviews*, vol. 46, no. 2, pp. 389–414, 2017.

[167] Z. Zhang, H. Wang, J. L. Provis, F. Bullen, A. Reid, and Y. Zhu, “Quantitative kinetic and structural analysis of geopolymers. part 1. the activation of metakaolin with sodium hydroxide,” *Thermochimica acta*, vol. 539, pp. 23–33, 2012.

[168] O. M. Jensen and P. F. Hansen, “Influence of temperature on autogenous deformation and relative humidity change in hardening cement paste,” *Cement and concrete research*, vol. 29, no. 4, pp. 567–575, 1999.

[169] P. Lura, O. M. Jensen, and K. van Breugel, “Autogenous shrinkage in high-performance cement paste: An evaluation of basic mechanisms,” *Cement and concrete research*, vol. 33, no. 2, pp. 223–232, 2003.

[170] S. Rahimi-Aghdam, E. Masoero, M. Rasoolinejad, and Z. P. Bažant, “Century-long expansion of hydrating cement counteracting concrete shrinkage due to humidity drop from selfdesiccation or external drying,” *Materials and Structures*, vol. 52, no. 1, p. 11, 2019.

[171] M. Bauchy, E. Masoero, F.-J. Ulm, and R. Pellenq, “Creep of bulk csh: insights from molecular dynamics simulations,” in *CONCREEP 10*, 2015, pp. 511–516.

[172] B. Bissonnette, P. Pierre, and M. Pigeon, “Influence of key parameters on drying shrinkage of cementitious materials,” *Cement and Concrete Research*, vol. 29, no. 10, pp. 1655–1662, 1999.

[173] M. Irfan-ul Hassan, B. Pichler, R. Reihsner, and C. Hellmich, “Elastic and creep properties of young cement paste, as determined from hourly repeated minute-long quasi-static tests,” *Cement and Concrete Research*, vol. 82, pp. 36–49, 2016.

[174] M. Vandamme and F.-J. Ulm, “Nanogranular origin of concrete creep,” *Proceedings of the National Academy of Sciences*, vol. 106, no. 26, pp. 10 552–10 557, 2009.

[175] Z. Jiang, Y. Xi, X. Gu, Q. Huang, and W. Zhang, “Modelling of water vapour sorption hysteresis of cement-based materials based on pore size distribution,” *Cement and Concrete Research*, vol. 115, pp. 8–19, 2019.